Investigating the Solid Oxide Fuel Cell Anode Degradation under Siloxane Contamination

by

Jiashen Tian

A Dissertation Presented in Partial Fulfillment
of the Requirements for the Degree
Doctor of Philosophy

Approved July 2022 by the
Graduate Supervisory Committee:

Ryan Milcarek, Chair
Christopher Muhich
Qiong Nian
Patrick Phelan
Liping Wang

ARIZONA STATE UNIVERSITY

August 2022

ABSTRACT

Siloxane, a common contaminant present in biogas, is known for adverse effects on cogeneration prime movers. In this work, the solid oxide fuel cell (SOFC) nickel-yttria stabilized zirconia (Ni-YSZ) anode degradation due to poisoning by siloxane was investigated. For this purpose, experiments with different fuels, different deposition substrate materials, different structure of contamination siloxane (cyclic and linear) and entire failure process are conducted in this study. The electrochemical and material characterization methods, such as Electrochemical Impedance Spectroscopy (EIS), Scanning Electron Microscope- Wavelength Dispersive Spectrometers (SEM-WDS), X-ray Photoelectron Spectroscopy (XPS), X-ray Diffraction (XRD), and Raman spectroscopy, were applied to investigate the anode degradation behavior. The electrochemical characterization results show that the SOFCs performance degradation caused by siloxane contamination is irreversible under bio-syngas condition. An equivalent circuit model (ECM) is developed based on electrochemical characterization results. Based on the Distribution of Relaxation Time (DRT) method, the detailed microstructure parameter changes are evaluated corresponding to the ECM results. The results contradict the previously proposed siloxane degradation mechanism as the experimental results show that water can inhibit anode deactivation. For anode materials, Ni is considered a major factor in siloxane deposition reactions in Ni-YSZ anode. Based on the results of XPS, XRD and WDS analysis, an initial layer of carbon deposition

develops and is considered a critical process for the siloxane deposition reaction. Based on the experimental results in this study and previous studies about siloxane deposition on metal oxides, the proposed siloxane deposition process occurs in stages consisting of the siloxane adsorption, initial carbon deposition, siloxane polymerization and amorphous silicon dioxide deposition.

ACKNOWLEDGEMENTS

Over the past four years, I am grateful for the chance to be a PhD student at Arizona State University. As a man who was born and grew up in the cold north, I believe Arizona provided me with an incredible living experience during my PhD period. The heat and sunshine in Arizona offered me tremendous energy and enthusiasm for research and study. Fortunately, at Arizona State University I also had the opportunity to meet many nice professors, university staff, lab mates and friends. I would not have been able to go through it without their assistance.

First, I would express my great thanks and gratitude to my advisor Dr. Ryan Milcarek who offered me the research assistant position in Combustion & Electrochemical Power Systems (CEPS) lab for my PhD degree. In this situation, I was able to devote 100% of my attention to my research project without any disturbance in the past four years. In this period, Dr. Milcarek mentored me to become a researcher and provided tremendous support in my research life. He guided me from academic writing and presenting to experiment setup with great patience. Apart from the research respective, what most touches me is I can feel he really wants his students to be successful. He really takes care about his students' improvement and is very willing to share and discuss his experiences. Working with him taught me how to manage my time effectively; how to develop good writing and reading habits and even how to have a good lifestyle including exercise in daily life. I also thank my committee members, Dr. Christopher Muhich, Dr. Qiong Nian

Dr. Patrick Phelan, Dr. Robert Wang, and Dr. Liping Wang for serving on my committee and giving me precious suggestions for my research. Additionally, I am thankful to Dr. Axel Wittmann and Dr. Emmanuel Soignard in Eyring material center for guiding and supporting me in the materials characterization area. Additionally, I am thankful to Dr. Peter Crozier, Dr. Ivan Ermanoski, Dr. Majid Minary, Dr. Rene Villalobos, Dr. Heather Emady and Fred Pena for the collaboration and guidance on my previous research projects.

In the past four years, I gained many wonderful memories of getting along with my lab mates in CEPS lab. I would like to thank Brent Skabelund particularly. We spend lots of tough and exciting time together in the lab. As a non-native student, I also gained lots of life skills from Brent including language and knowledge about the United States and Arizona, which helped me to live better here. I also want to expend my gratitude to my amazing and talented lab mates Cody Jenkins, Rhushikesh Ghotkar, Joe Elio, Saulo Valdivia-Leos, Derall Riley, Kristina Phillips, Danielle Caron, Kyle Horn and Abdul Khalid for the memorable experience working together. Moreover, I also express my thanks to graduate students who have provided their help to my research: Ashley Myles, Piyush Haluai, Dou Yan, Dr. Rui Dai, Dr. Wilson Kong.

Finally, I would also like to express my deepest thankfulness to my families and friends. I thank my parents for their unconditional support and sponsor for my graduate study in the United States which provides me a strong opportunity to succeed. And I am

very grateful for their sacrifices of family time in past few years. I would also thank my friends Hao Zhou and Yuan Gao. I appreciated your company especially in the pandemic period. I would not have survived in that hard time without your companionship and support.

For project funding, I thank the U.S. Department of Energy (award number DE-EE0007721) and City of Phoenix for sponsoring the material and my assistantship salary based upon this work. I also acknowledge the use of facilities within the Eyring Materials Center at Arizona State University supported in part by NNCI-ECCS-1542160.

TABLE OF CONTENTS

Page

LIST OF TABLES

Table Page

LIST OF FIGURES

Figure Page

Figure Page

Figure Page

Figure Page

Figure Page

Figure Page

NOMENCLATURE

AAL	Anode Active Layer
ASL	Anode Support Layer
ASR	Area Specific Resistance
AS-SOFCs	Anode Supported Solid Oxide Fuel Cells
CHP	Combined Heat and Power
CNLS	Complex Nonlinear Least Squares
D4	Octamethylcyclotetrasiloxane
D5	Decamethylcyclopentasiloxane
$D_{H2,H2O}$	Binary Diffusion Coefficient Between the H_2 and H_2O
$D_{H2,N2}$	Binary Diffusion Coefficient Between the H_2 and N_2
$D_{H2O,N2}$	Binary Diffusion Coefficient Between the H_2O and N_2
DRT	Distribution of Relaxation Time
e	Porosity
ECM	Equivalent Circuit Model
EDS	Energy-dispersive Spectrometer
EIS	Electrochemical Impedance Spectroscopy
F	Faraday Constant
FESEM	Field Emission Scanning Electron Microscope
FIB	Focused Ion Beam

FLW	Finite-length Warburg
I-V	Current-voltage
l	Regularization Parameter
L	Diffusion Length
L3	Octamethyltrisiloxane
L4	Decamethyltetrasiloxane
LSCF	Lanthanum Strontium Cobalt Ferrite, $(La_{0.60}Sr_{0.40})_{0.95}Co_{0.20}Fe_{0.80}O_{3-x}$
MFCs	Mass Flow Controllers
OCV	Open Circuit Voltage
P	Pressure of Anode Side Gas
PDMS	Polydimethylsiloxane
ppm	Parts Per Million
ppm_v	Parts Per Million Volume
R	Universal Gas Constant
RMSE	Residual Root-mean-square Error
RW	Gas Diffusion Resistance
sccm	Standard Cubic Centimeters Per Minute
SDC	Samarium Doped Ceria, $Sm_{0.20}Ce_{0.80}O_{2-X}$
SEM	Scanning Electron Microscope
SOFC	Solid Oxide Fuel Cell

t	Tortuosity
T	Temperature
TMS	Trimethylsilanol
TPB	Triple Phase Boundary
vol%	Volume Percent
V-t curve	Voltage Versus time curve
WDS	Wavelength-dispersive Spectrometer
wt%	Weight Percentage
WWTPs	Wastewater Treatment Plants
XRD	X-ray Diffractometer
YSZ	Yttria-stabilized Zirconia, $(ZrO_2)_{0.92}(Y_2O_3)_{0.08}$
χ_{H2}	Molar Fraction of the H_2
χ_{H2O}	Molar Fraction of the H_2O
χ_{N2}	Molar Fraction of the N_2

1 INTRODUCTION

1.1 Motivation

Currently, global energy consumption is continuously increasing with fossil fuels accounting for over 80 percent of the total [1]. Increasing energy consumption results in rising concentration of atmospheric greenhouse gases with fossil fuels accounting for the majority of the emissions. Besides increasing energy consumption and global climate change, energy security challenges also need consideration. Political instability and even wars, such as the 2022 Ukraine War, impact the global energy supply chain and cause a severe energy crisis [2]. Recovering energy from waste is considered one worthwhile solution to the global energy problems. Biogas as a byproduct of waste treatment systems can be generated from the anaerobic digestion process from wastewater treatment plants and landfills. Due to extensive distribution of the waste treatment systems, biogas can serve as a versatile renewable energy source for natural gas replacement and complement [3].

Among the more recently developed power generation technologies, biogas utilization as a fuel source of solid oxide fuel cells (SOFCs) has drawn increasing attention recently for its high efficiency and environmentally friendly characteristics [4–8]. A type of organosilicon chemical component — siloxanes — can be found in biogas as impurities in trace level whose source can originate from an industrial material polymeric dimethylsiloxanes [9–14]. As a result of direct biogas or bio-syngas utilization

in SOFCs, the stable silicon compounds from siloxanes deposit in the anode which is one of the main barriers for biogas utilization [10,15–17]. In this circumstance, scientific research is pursuing the investigation of the SOFCs' anode degradation under siloxane contamination.

1.2 Electrochemical Fundamentals of Solid Oxide Fuel Cells

1.2.1 Fundamentals

As the prime mover focused on this study, the solid oxide fuel cell, as an electrochemical device, can convert the chemical energy of a fuel to electrical power directly. Without the limitation of the Carnot cycle, the efficiency of fuel cells can be higher than combustion engines [18,19]. Similar to batteries, the operating principle of fuel cells depends on the combination of reactants to generate electricity with electrochemical reactions. Unlike batteries, instead of consuming themselves and requiring recharging, fuel can be supplied continuously [18]. Fuel cells have various advantages compared with conventional power generating systems in terms of their efficiency, size flexibility and environmental friendliness [20,21]. If hydrogen is used as the fuel, water is the only product on the anode side.

A SOFC consists of two porous electrodes (the anode and the cathode) and a dense ceramic electrolyte sandwiched between the two electrodes. On the cathode side, O_2 from air is reduced to O^{2-}. Then these O^{2-} ions travel through the YSZ electrolyte, which is an

O^{2-} ion conductor, towards the anode. The anode of a SOFC provides the sites for the fuel gas to react with the oxygen ions received from the electrolyte [19]. Electrochemical oxidation of fuel in the anode is believed to occur only at the triple phase boundary (TPB) region, where the electrode, the electrolyte and the gas phase meet, as shown in **Fig. 1.1**. The anode and cathode reaction equations are show in equation (1.1) and (1.2).

The anode reaction: $\frac{1}{2}O_2 + 2e^- \rightarrow O^{2-}$ (1.1)

The cathode reaction: $H_2 + O^{2-} \rightarrow H_2O + 2e^-$ (1.2)

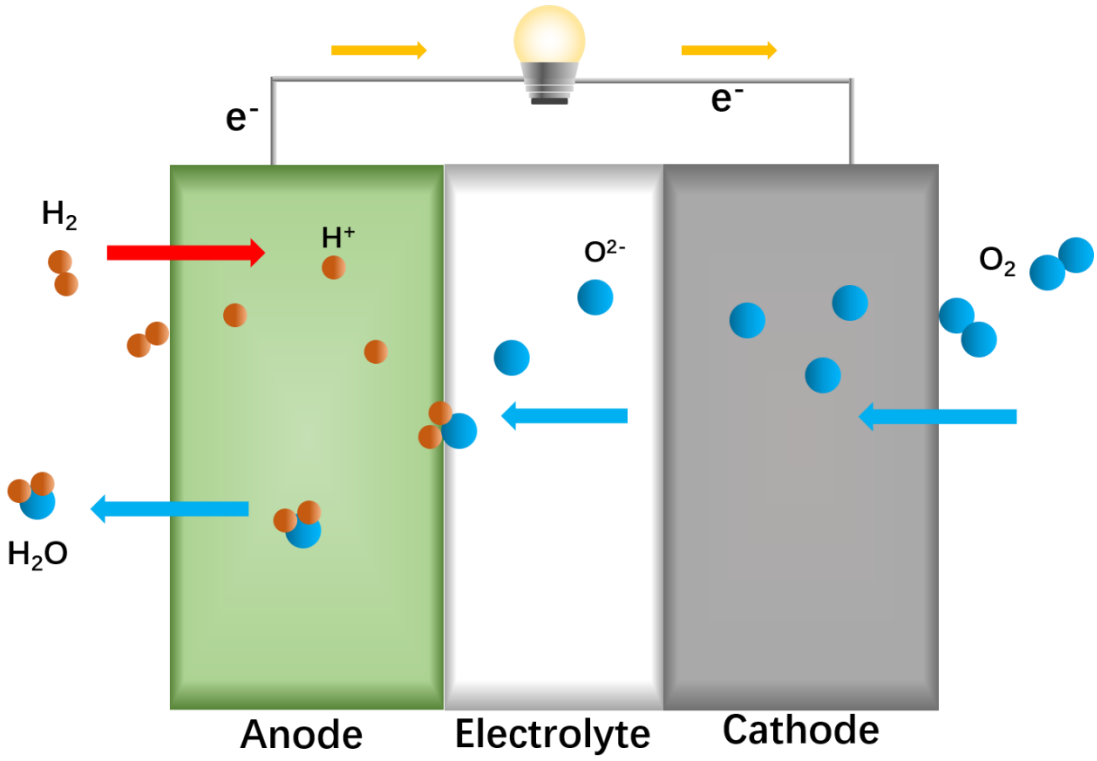

Figure 1.1 Schematic figure of SOFC operation.

1.2.2 Operating Conditions of SOFCs

SOFCs with fully stabilized zirconia (i.e., yttria stabilized zirconia, YSZ) as an

electrolyte material are wildly utilized. However, good oxygen conductivity requires high operating temperature (800 °C–1000 °C) [22]. High temperature operation provides advantages but is also a shortcoming. At high temperature the electrode materials can diffuse into the electrolyte and lower performance and ultimately influence the lifetime. Thus, lowering the operation temperature can be beneficial for the commercialization of SOFC systems [23]. As a result some studies have explored electrolyte materials that exhibit high ionic conductivity at lower operating temperatures (400 °C–800 °C) [24,25].

Several challenges exist for the electrodes and interfaces at lower operating temperatures. Instead of utilizing traditional Sr-doped $LaMnO_3$ (LSM) cathode, one effective way of reducing the operating temperature is to use perovskite cathode materials such as LSCF ($La_{0.6}Sr_{0.4}Co_{0.2}Fe_{0.8}O_3$) or BSCF ($Ba_{0.5}Sr_{0.5}Co_{0.8}Fe_{0.2}O_{3-\delta}$) which have higher electrocatalytic activity and oxygen permeability [26–28]. However, due to the incompatibility of the YSZ electrolyte and perovskite cathode, interfacial reactions should be prevented by applying a samaria-doped ceria (SDC) or gadolinium-doped ceria (GDC) buffer layer [29–31], which can reduce the direct contact between YSZ and the perovskite cathode.

1.2.3 The Ni-YSZ SOFC Anode

The anode must meet some essential requirements such as high electronic conductivity, electro catalytic activity, chemical and mechanical stability. Thermal compatibility with electrolyte and cathode is also a factor that should be considered. After

high temperature reduction, sufficient porosity which allows gas transport is also needed [32].

Ni-YSZ is the common anode material for the SOFC because of its low manufacturing cost. Ni and YSZ are compatible at high temperature and Ni provides excellent characteristics with high electronic conductivity and good catalytic activity for hydrogen/ oxygen reactions [33]. As a result, SOFCs made with Ni based anode have relatively high-power density compared with other materials. The thickness of the electrolyte can be reduced because of YSZ's outstanding mechanical strength and, at same time, operating temperature also can be reduced below 800 °C [18]. Thus, Ni-YSZ was selected as the anode utilized in this work.

1.2.4 SOFC Polarization

Due to irreversible losses, the voltage of a fuel cell is always less than the thermodynamically predicted ideal voltage, or reversible cell potential, which is shown in **Fig. 1.2** [34]. Known as polarization or over potential, these loss mechanisms consist of activation polarization (reaction rate loss), ohmic polarization (resistance loss) and concentration polarization (gas transport loss).

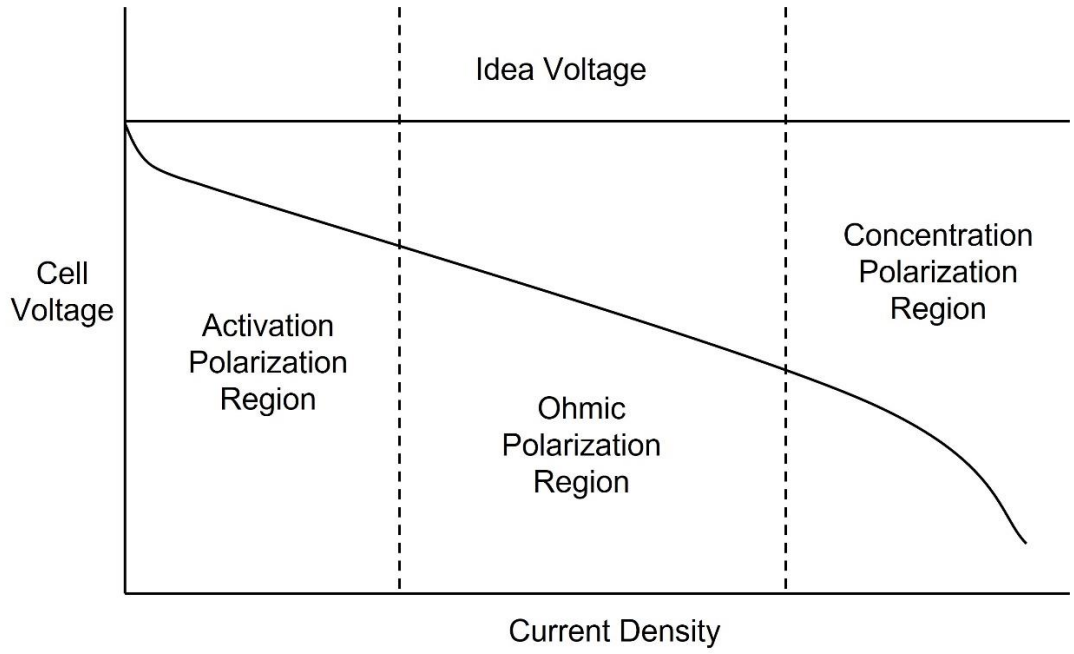

Figure 1.2 Schematic plot of voltage versus current density of a SOFC showing different types of polarization.

Different effects on the theoretical voltage of the fuel cell occur under polarization. Reaction rate losses are related to charge transfer processes, which depend on the electrode-electrolyte interfaces. Activation overpotential loss and current density are related with an exponential relationship. Ohmic losses result from the resistance to the charge transport through the electrodes and electrolyte. In SOFCs the electrolyte is the main contributor to the ohmic polarization. Higher ionic conductivity and a thinner electrolyte are methods to reduce the ohmic contribution. Gas transport losses are related to the transport of gaseous species through porous electrodes. Optimization of microstructure is a way to reduce this type of loss [18,21]. In this regard, the polarization curve was utilized for the SOFCs' performance evaluation in this work.

1.2.5 SOFC Anode Degradation

Anode degradation can be categorized into two groups: intrinsic and extrinsic degradation. Intrinsic degradation results from included constituents and structures that participate in the degradation process such as Ni-agglomeration, densification/sintering, nickel grain growth and impurities in raw materials. Extrinsic degradation occurs when a foreign material is introduced into the fuel cell contributing to degradation such as poisoning by impurities like sulfur, chlorine carbon and silicon. They are all considered as extrinsic sources of degradation [18,35].

From the degradation process perspective, the mechanisms can also be categorized into two types [36]. One type of degradation results in gradual performance decay such as intrinsic degradation, Ni-agglomeration and densification/sintering [37,38]. For external sources of contamination, like sulfur poisoning or carbon and siloxane deposition, which is the focus of this study, there is also the gradual/soft degradation period initially which is similar to the gradual degradation mechanism. However, an obvious and even sudden failure occurs after the gradual decay over a relatively short period of time.

1.2.6 Impedance Spectroscopy

Since 19th century, the research related to the frequency-dependent material characterization started to appear. Electrochemical impedance spectroscopy (EIS) and the related frequency response analysis are broad application alternating current (AC)

methods to investigate the physiochemical processes in the electrochemical devices and components. Oliver Heaviside et al. developed the mathematical foundation for the impedance spectroscopy and introduced some essential terms for the study such as conductance, impedance and admittance. He also developed the transmission line model for the transatlantic cable [39,40]. Then Nernst applied the electrochemical impedance spectroscopy to physical systems and measured dielectric constants for different aqueous electrolytes [39]. Warburg developed the mathematical equation for the impedance response corresponding to the diffusion process. The equivalent circuit with the capacitor and resistor was proposed and associated capacitance and resistance equations were developed as a function of frequency [39,41].

In the 1950s, impedance spectroscopy was applied to complicated reactions. The impedance response of porous and rough electrodes was simulated by transmission line models developed by de Levie [39,42]. For solid-state electrolytes, like those utilized by the SOFC, Bauerle investigated the polarization characterization of solid zirconia by AC method [43,44]. A more detailed electrochemical impedance spectroscopy development history can be found in Orazem's book [39].

As shown in **Fig. 1.3**, during the EIS measurement process an AC potential, as the small excitation signal, is applied to an electrochemical cell and then the AC current signal obtained through the cell can be utilized for the process analysis [45]. The sinusoidal potential excitation with different frequency and related current signal

response can also be utilized to separate the physicochemical processes with different speeds [44]. High frequencies correspond to short-time processes, while low frequencies connect to long-time processes. For instance, charging of the electrode-electrolyte interface occurs quickly in an electrochemical system and is associated with a high-frequency or short-time response. Diffusion is a slower process with a large time constant and a lower characteristic frequency as a result [39]. In this study, EIS was also utilized to identify and analyze the electrochemical processes during the SOFC anode degradation.

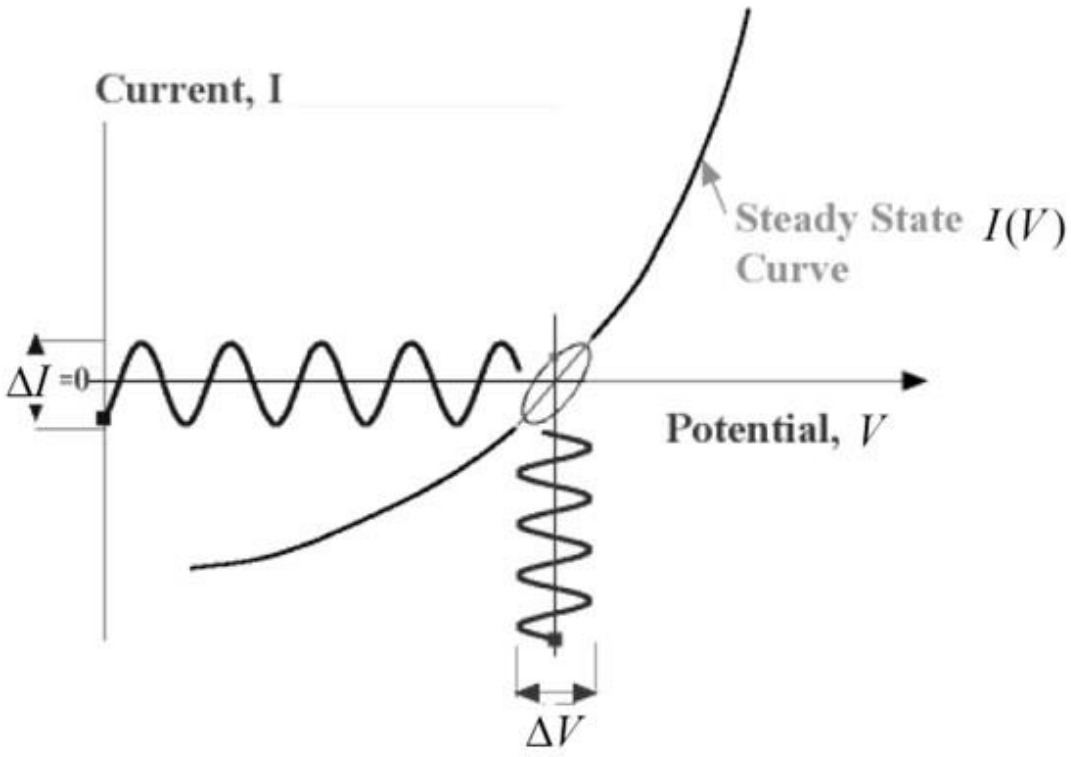

Figure 1.3 Lissajous figure of EIS test.

1.2.7 Distribution of Relaxation Times (DRT)

EIS can be utilized for physicochemical processes' separation based on the reaction speed. However, the overlap of the frequency response of different processes is still considered a barrier for the electrochemical characterization analysis. The distribution of relaxation times (DRT) method can serve as a powerful tool for impedance analysis. The high-resolution physicochemical processes' separation can be achieved by the relaxation processes deconvolution of an electrochemical system [46]. Shown in equation (1.3), the DRT function g(τ) can be calculated according to distinctive time constants from the impedance spectrum $Z_{DRT}(f)$.

$$Z_{DRT}(f) = R_{\infty} + \int_0^{\infty} \frac{g(\tau)}{1+i2\pi f\tau} d\tau \quad (1.3)$$

The basic idea for DRT was introduced by Schweidler over a century ago [44,47]. Although the idea of DRT was proposed a long time ago, due to the ill-posed problem the general calculation of the DRT is not easily accomplished [44]. Recently, two main methods have been applied to the DRT calculation. For the first method Fourier transformation of the imaginary part of the impedance spectrum creates a discrete value. However, extraordinarily high quality impedance data is necessary to fulfill the essential data extrapolation and filtering [44,48]. To overcome the problems in the Fourier transform method, Sonn combined the fitting of the real part of RC elements spectra with relative time constraints and Tikhonov regularization. It gives an effective approach for DRT calculation [44,49]. Simultaneously, Ciucci and his group developed a free

MATLAB embedded code for the DRT calculation [44,50]. The DRT method was used to separate the electrochemical processes from the EIS results.

1.2.8 Equivalent Circuit Modeling (ECM)

With the assistance of the DRT, the detailed physicochemical processes corresponding to the frequency response in spectra can be identified. Then the equivalent circuit model for the complex electrochemical system can be established with different electronic elements, which represent the corresponding physicochemical processes.

The common elements considered in an equivalent circuit model with both parallel and series configurations are listed below:

R_s: The ohmic resistance R_s is the intercept with the real axis at high frequency and represents the YSZ electrolyte bulk resistance and external circuit resistance.

L: Inductance is always utilized to explain high frequency response in impedance spectra. Especially for SOFC systems, its existence can be traced from the impedance of probes and cables.

RQ element: parallel combination of ohmic resistance (R) and constant phase element (Q). It represents the ionic and charge transport process in the anode or cathode.

W: Warburg-element represents the concentration loss polarization in the gas diffusion process through thick electrodes.

G: Gerischer element corresponds to the diffusion and reaction process in porous

electrodes. For the SOFC it is most commonly used to represent the polarization of mixed ionic and electronic conductive cathode such as YSZ-LSM cathode.

After establishment of the ECM, the exact value of each element can be obtained through the fitting of the impedance spectra with Complex Nonlinear Least Squares (CNLS) algorithm [51]. In this circumstance, the impedance spectra can be analyzed quantitatively and more details such as the microstructure and kinetic parameters can also be revealed [52]. The shortcoming of the ECM is that a certain circuit configuration needs to be given before modeling. In addition, the CNLS-fitting results are highly initial value dependent and the approximate initial fitting parameters of each individual element need to be estimated. The combination of DRT and ECM can significantly enhance the accuracy of the modeling results [53]. In this study, ECM provided a method to quantitatively analyze the electrochemical processes.

1.3 CHP and Wastewater Treatment Plants

Water and Wastewater Treatment Plants (WWTPs) in the United States collectively demand around 2-4% of the total U.S. energy consumption representing a total cost of around $4.7 billion annually [54]. To reduce the electric energy consumption of WWTPs biogas can be generated from sludge and utilized as a fuel for CHP [55]. In 2011, 43% of U.S. WWTPs generated biogas using anaerobic digestion, but only 3.3% utilized the biogas to generate electricity via cogeneration or combined heat and power (CHP) [55].

Many WWTPs flare biogas, limiting energy recovery from this renewable resource. In this situation, utilizing a CHP system with SOFCs as power generator is a method to improve the energy efficiency of WWTPs. One pioneer application for an integrated biogas fuel cell system is the DEMOSOFC project in which a 175 kW SOFC plant with an electrical efficiency of 53% was installed in SMAT Collegno WWTP in the Turin area, Italy. The SOFC plant can supply around 30% of the WWTP electrical consumption and almost 100% of the thermal requirement [5].

Currently, the main CHP prime movers in WWTPs are internal combustion engines and microturbines, which occupy the major market share at 69% and 17% in the United States, respectively [56]. Unfortunately, small and medium size internal combustion engines and microturbines have relatively lower electrical efficiency. For an internal combustion engine in the 100-1000 kW range, the efficiency ranges from 37-43%. In comparison, the efficiency of a 10-100 kW internal combustion engine drops to 28-37% [5]. The significant decrease in electrical efficiency has also been observed for the microturbine for rated power below 1000 kW [56]. According to Roostaei and Zhang [57], 73% of the WWTPs in the United States are small-scale plants whose wastewater treatment capacities are below 37,854 m^3 (10 million gallons) per day and account for 33.4% of total capacity. Considering the limited annual biogas production for these plants (< 10 GWh) the total prime movers power is less than 1000 kW generally [58]. For parallel generator systems, the single prime mover is even smaller. For these smaller

WWTPs, utilizing SOFCs as the prime mover in CHP systems can be competitive due to much higher electrical efficiency (~50%) compared with internal combustion engines and microturbines (~30%) [56]. This is shown in **Fig. 1.4**. Besides higher energy conversion efficiency, the SOFC is also an environmentally friendly technology which can reduce the NO_x, SO_x and particulate matter emissions to the atmosphere [59]. However, the impurities in biogas will cause degradation of the SOFC [60].

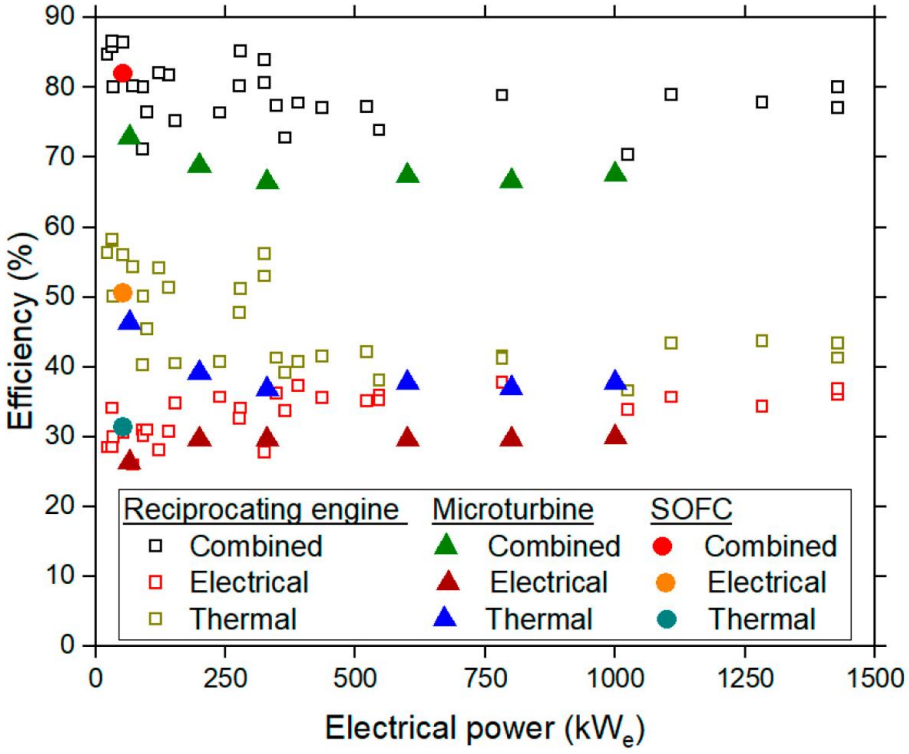

Figure 1.4 The relationship of prime movers' efficiency and size [56].

1.4 Biogas Fundamentals

Biogas is generated by natural degradation of organic material by microorganisms under anaerobic conditions. WWTPs utilize the anaerobic digestion process converting

organic material in waste water to biogas which is considered a renewable fuel that could be used to produce electricity, heat or as vehicle fuel [3]. The sources of biogas (landfills, WWTPs, farms), anaerobic digestion process, location, and season are all essential factors influencing the chemical composition of biogas. Biogas from sewage digesters usually contains from 55% to 65% methane, from 35% to 45% carbon dioxide and 1% nitrogen. Biogas from organic waste digesters usually contains from 60% to 70% methane, from 30% to 40% carbon dioxide and <1% nitrogen. In landfills methane content is usually from 45% to 55%, carbon dioxide from 30% to 40% and nitrogen from 5% to 15% [61]. Typically, biogas also contains hydrogen sulfide and other sulfur compounds, compounds such as siloxanes and aromatic and halogenated compounds. The main impurities of biogas include hydrogen sulfide (0.005-2 vol%), siloxanes (0-0.02 vol%), ammonia (< 1 vol%), and halogenated compounds (< 0.6 vol%) [62]. Most of these impurities, even at low concentrations, can potentially damage the prime mover of the CHP system [7,63].

1.5 Siloxane

The main siloxane species in biogas are classified as cyclic structure siloxanes, such as D4 (octamethylcyclotetrasiloxane) and D5 (decamethylcyclopentasiloxane), linear structure siloxanes, such as L3 (octamethyltrisiloxane) and L4 (decamethyltetrasiloxane), and other organosilicon compounds like TMS (Trimethylsilanol) [64]. As shown in **Fig.**

1.5, D5, D4 and L2 tend to have the highest concentrations among siloxanes in biogas from WWTPs [65]. The distributions of siloxane in different countries is shown in **Table 1.1**. Siloxanes in biogas mainly originate from the degradation of polydimethylsiloxanes (PDMS). PDMS is used as the antifoaming agent and lubricant in different areas such as crude oil refining, coking, steam cracking processes, medical equipment, adhesives, cosmetics and food industry [66,67]. During wastewater treatment siloxane is preferentially absorbed in the sludge flocs and volatizes at temperatures above 60 °C, which is common in the anaerobic digester [67]. Some of the siloxane compounds are more soluble in water and have higher vapor pressure (e.g., L2 and D3 siloxane) which makes them less likely to appear in biogas than others siloxanes (e.g., D4 and D5 siloxane) [67,68]. Anti-foaming agents, which are added to the anaerobic digester, are another common source of siloxane.

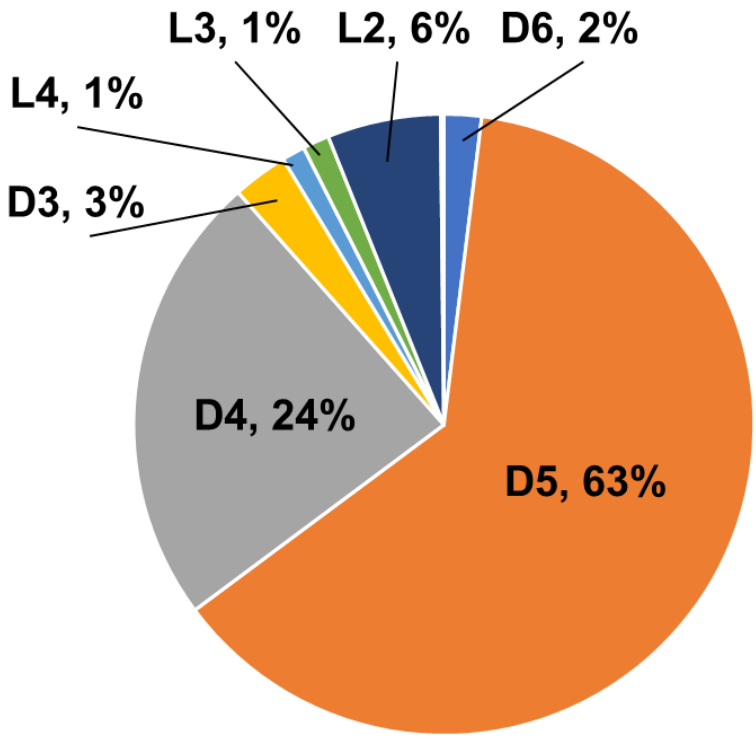

Figure 1.5 Siloxane Distribution in Biogas from WWTPs**.**

Table 1.1 WWTP biogas siloxane composition distribution in different countries

WWTPs	**D6**	**D5**	**D4**	**D3**	**L4**	**L3**	**L2**	**TMS**
Finland	0.11	0.56	0.05	0.00	0.06	0.01	0.01	0.00
Germany	0.00	0.40	0.40	0.02	0.01	0.00	0.00	0.03
U.S.	0.00	3.73	2.68	0.36	0.00	0.20	0.92	0.00
Italy	0.16	0.44	0.13	0.02	0.12	0.02	0.00	0.00
Spain	0.04	5.51	0.82	0.09	0.02	0.01	0.09	0.00
Austria	0.02	0.40	0.08	0.00	0.00	0.00	0.00	0.00
Average	0.06	1.84	0.69	0.08	0.04	0.04	0.17	0.0

1.6 The Siloxane Deposition Mechanism

1.6.1 Degradation of SOFC Anode Due to Siloxane

Among the impurities in biogas (hydrogen sulfide, siloxanes, ammonia and

halogenated compounds), CHP prime movers are especially vulnerable to siloxane [69–71]. For SOFCs, below 1 ppm hydrogen sulfide concentration is generally considered a safe operating condition for SOFCs [68]. However, H. Madi et al. [72] reported even ppb levels of siloxanes can cause fast degradation of SOFCs Ni-YSZ anode. The average siloxane concentration in biogas of German WWTPs has been reported as 0.98 ppm [15] while the concentration can be as high as 41 ppm in WWTPs according to other sources [73].

1.6.2 The Siloxane Deposition Mechanism for the Ni-YSZ Anode

Ni-YSZ is one of the most extensively applied SOFC anodes due to excellent electrochemical and physical properties, as discussed previously [33]. However, the mechanism of siloxane deposition in the Ni-YSZ SOFC anode has not been fully identified. K. Haga et al. [74] in 2008 assumed a two-step chemical reaction mechanism for D5 siloxane deposition. The two-step mechanism is shown in equation (1.4) and (1.5). In the first step, D5 undergoes a gas phase reforming reaction with water and converts the methyl groups to carbon monoxide and hydrogen. Then the remaining orthosilicic acid gas travels through the anode and decomposes to solid silicon dioxide and water (1.5).

$$[(CH_3)_2SiO]_5(g) + 25H_2O(g) \rightarrow 5Si(OH)_4(g) + 10CO(g) + 30H_2(g) \quad (1.4)$$

$$Si(OH)_4(g) \rightarrow SiO_2(s) + 2H_2O(g) \quad (1.5)$$

The mechanism proposed by K. Haga et al. was based on FESEM images and EDX

results where silicon element was overlapped with oxygen element in addition to chemical equilibrium calculations. In this case, the assumed Si deposition was reported as SiO_2, but not verified. Based on the assumed SiO_2 formation, anode poisoning by siloxane was classified as a deposition type mechanism [75] in which the Si accumulates in the anode. K. Haga et al. further claimed that silicon does not interact with Ni at 800 °C [76]. The researchers also proposed that the SiO_2 deposition in the anode would decrease the active TPB area leading to higher anode polarization and ohmic loss [74]. However, Si deposition was found to be most significant near the anode surface with some occurring within the anode [16,74,75]. Thus, more research is needed to understand the process of siloxane conversion and silicon deposition in SOFCs.

In later tests, Y. Kikuchi et al. found that SOFC polarization resistance increased significantly with siloxane deposition [16]. DRT analysis of EIS results indicated that mass transport, including surface gas diffusion of reactants, and charge transfer process were affected [16]. They also believed that the Si deposited on the anode surface decreased surface gas diffusion, while silicon deposition near the electrolyte interface decreased charge transfer by covering the Ni. Scanning transmission electron microscopy electron energy loss spectroscopy (STEM-EELS) indicated that the Si-O substance was SiO_2, but again, not definitively shown [16].

In a Solid Oxide Electrolysis Cell (SOEC) setup, Jenson showed SEM/EDS analysis of Ni+YSZ exposed to $Si(OH)_4$ evaporated from silicone [77]. Based on quantitative

analysis of the spectra, they concluded that Si/O atomic ratio was close to 0.5 which indicates an oxidized state that is most likely SiO_2. Overlapping of Y and Si in EDS profile is a potential concern with the analysis of results. In that study, Si deposition could only be observed within a range of 10 μm from the electrolyte layer [77]. A detailed TEM analysis with nanometer resolution showed Si did not penetrate the Ni [78]. Instead, the Si deposited on an Al impurity that was next to the Ni particle [78]. Hauch et al. investigated Si deposition from sealant materials and found that deposition only occurred in the 10 μm closest to the YSZ electrolyte [79]. H_2O and H_2 (50:50 flow rate ratio) were supplied to the anode whose thickness was over 300 μm. No explanation for the Si buildup near the electrolyte was given and the anode surface may not have been investigated. This may indicate the importance of oxygen in the Si deposition process. Based on these limited results, more research is needed to understand the siloxane conversion and silicon deposition processes in SOFCs.

1.6.3 Siloxane Degradation Mmechanism for Metal Oxides

The mechanism of siloxane deposition on certain metal oxides, like γ-alumina, was investigated previously for biogas cleaning [80]. It is well known that alumina is a good adsorbent of siloxane and has been utilized in industry for siloxane removal. Experimental results indicate that siloxane is first adsorbed to the surface of the metal oxide and the methyl radicals in siloxane form methane according to equation (1.6) [80].

$$Siloxane\ (g) + \ bAl_2O_3(s)_{active} \rightarrow \ silicated\ Al_2O_3(s)_{inert} + xCH_4 \quad (1.6)$$

Following the initial deposition other methyl groups in siloxane are converted to methane and replaced by hydroxyl groups. Eventually siloxane converts to amorphous crystal silicon dioxide [81]. Finocchio and Vaiss et al. [82,83] reported that in the siloxane chemical adsorption process, the surface hydroxyl groups on the metal oxide play an important role as shown in equation (1.7).

$$8OH(\gamma\text{–}Al_2O_3) + [SiO(CH_3)_2]_4 \rightarrow 4OH(\gamma\text{–}Al_2O_3) + Si_4O_8H(CH_3)_5(\gamma\text{–}Al_2O_3) + 3CH_4 \quad (1.7)$$

Inspired by the studies about the siloxane degradation mechanism on metal oxides, the entire siloxane deposition process in the SOFC anode should be reconsidered. To verify the previously proposed siloxane mechanism and to assess the possible siloxane chemical adsorption process, the siloxane deposition process needs to be analyzed comprehensively from four different aspects in the following chapters. In Chapter 2, siloxane poisoning of Ni-YSZ anode is investigated in different gas compositions which can provide hints for the possible reaction pathway. The influence of H_2, H_2O, CO and CO_2 on the D4 siloxane deposition process are assessed during long-term stability tests. In Chapter 3, considering the catalytic properties of anode materials, the siloxane deposition process was investigated on Ni, YSZ, ZrO_2 and Y_2O_3 pellets respectively. This analysis will elucidate the role of the anode material in the siloxane deposition process and offer a perspective for the siloxane tolerant anode development. Besides fuels and materials consideration, the influence of the structure of siloxane is investigated and

discussed in Chapter 4. Regarding the different properties of linear and cyclic siloxanes, comparison of their deposition processes may also provide an explanation for the siloxane deposition behavior. Most of the previous studies only focus on the anode degradation process, not the entire failure process of Ni-YSZ anode under siloxane contamination. In this circumstance, the failure process of anode is investigated in Chapter 5. Investigation on the anode failure process can also provide deeper understanding of the siloxane deposition and related anode degradation behaviors.

2 DEGRADATION OF THE SOFC NI-YSZ ANODE WITH DIFFERENT FUELS

2.1 Introduction

The previously proposed siloxane deposition mechanisms were introduced in the previous section. The fuels, operating temperature and siloxane concentrations for these studies provide important context for the results obtained. As shown by the summary of previous experiments in **Table 2.1**, the compositions of gases fed to the SOFC anode during siloxane contamination experiments tends to vary. For K. Haga and Kikuchi et al. experiments, besides H_2 and D5, only a small concentration of H_2O (3%) was added. However, in order to simulate syngas generated from biogas reforming, high concentrations of H_2O (~20%), CO (~10%) and CO_2 (~10%) were mixed with pure H_2 and D4 in the studies of H. Madi and D. Papurello et al. The experiments with syngas were meant to better simulate realistic operating conditions after reforming biogas. According to equation (1.4) from K. Haga et al., components like H_2O would have an obvious influence on the degradation process. In this regard, a study focused on how individual components of syngas impact the siloxane deposition process in SOFC anode is necessary. It will also aid in understanding the siloxane poisoning behavior of SOFC Ni-YSZ anode and provide a chance to verify the previously established theories. In order to compare with former studies, D4 was selected as siloxane contamination source. In this section, siloxane poisoning of Ni-YSZ anode is investigated in different gas compositions. The influence of H_2, H_2O, and CO on the D4 siloxane deposition process

are assessed during long-term stability tests. A more convincing siloxane deposition process can be revealed based on the experimental results.

Table 2.1 Summary of previous SOFC degradation studies due to siloxane [84]

Siloxane	Siloxane Conc. (ppm)	Temp. (°C)	Fuel	Anode	Ref
D5	10	800, 900, 1000	3% H_2O, 97%H_2	Ni-ScSZ	[74]
D5	60	800	3% H_2O, 97%H_2	Ni-ScSZ	[16]
D4	0.069, 0.1, 0.2, 0.25, 0.5, 1, 1.5, 2, 3	750	50% H_2, 20% H_2O, 20% CO, 10% CO_2	Ni-YSZ	[72]
D4	0.6, 3, 5	750	50% H_2, 20% H_2O, 20% CO, 10% CO_2	Ni-YSZ	[65]
D4	0, 0.111, 0.193, 0.47, 0.943, 1.447, 1,923	750	50.8% H_2, 19.9% H_2O, 19.5% CO, 9.1% CO_2, 0.7% CH_4	Ni-YSZ	[60]

2.2 Fabrication and Methods

The NiO+YSZ (60:40 w/w, Fuelcellmaterials) anode was prepared by dry pressing to prepare anode supported SOFCs (AS-SOFCs). The green body was then pre-sintering at 1100 °C for 4 hours. After pre-sintering, yttria-stabilized zirconia (YSZ, $(ZrO_2)_{0.92}(Y_2O_3)_{0.08}$, Fuelcellmaterials) electrolyte was prepared by wet powder spray and also pre-sintering after spray. Then samarium doped ceria (SDC, $Sm_{0.20}Ce_{0.80}O_{2-X}$, Fuelcellmaterials) buffer layer was deposited by wet powder spray. After wet powder spray, anode, electrolyte and buffer layer were co-sintered at 1400 °C in air for 4 hours.

A lanthanum strontium cobalt ferrite (LSCF, $(La_{0.60}Sr_{0.40})_{0.95}Co_{0.20}Fe_{0.80}O_{3-x}$, Fuelcellmaterials) + SDC (7:3 w/w) cathode was spray deposited onto the SDC buffer layer by wet powder spray and then sintered to 1100 °C for 2 hours [22,28]. The final anode thickness is ~380 μm, electrolyte thickness ~10 μm, buffer layer ~3 μm and cathode thickness ~17 μm. Silver paste was used for cathode current collector and the active area was 0.712 cm^2.

The fuel cell performance was measured by the I-V (current-voltage) method with 4-probe technique. The fuel cells open circuit voltage (OCV), polarization, power density, and operating voltage change at constant current density (V-t curve) were measured and recorded by the digital SourceMeter (Keithley 2460) interfaced with a computer.

An Electrochemical Impedance Analyzer (Solartron Analytical Energylab XM) was utilized to test the electrochemical impedance spectroscopy (EIS) of the fuel cells under OCV conditions. EIS was tested and recorded over a frequency range of 10^6 to 0.1 Hz with a signal amplitude of 10 mV.

Fig. 2.1 shows the experiment setup. This experimental setup was built for investigating the Ni-YSZ anode SOFCs degradation due to D4 contamination in different atmospheres. A certified cylinder which includes pure N_2 carrier gas with precise concentration of D4 (5.743 ppm_v) was purchased and utilized. In order to adjust the D4 concentration in the fuels, but not change the other gas concentrations, the N_2+D4 gas

was mixed with research grade N_2 gas to keep the total flow rate of N_2+D4 constant. In the experiment setup, the Brooks Delta II smart mass flow controllers (MFCs) interfaced with LabView software were utilized to mix the H_2, CO, N_2 and N_2+D4 with certain ratio at atmospheric pressure. The NE-300 Just Infusion syringe pump (PumpSystems Inc.) was utilized for supplying water into fuel deliver pipe. A heater was wrapped around the rest of gas deliver pipe for water vaporization. To confirm all the water was converted to steam and kept in gas phase, T-type thermocouples (Omega) were used to monitor the temperature of delivery pipe, which should be kept above 120 °C. To reduce the possibility of reactions between D4, water and the other gas components, D4 was incorporated into the mixture after the water heater and close to the furnace entrance.

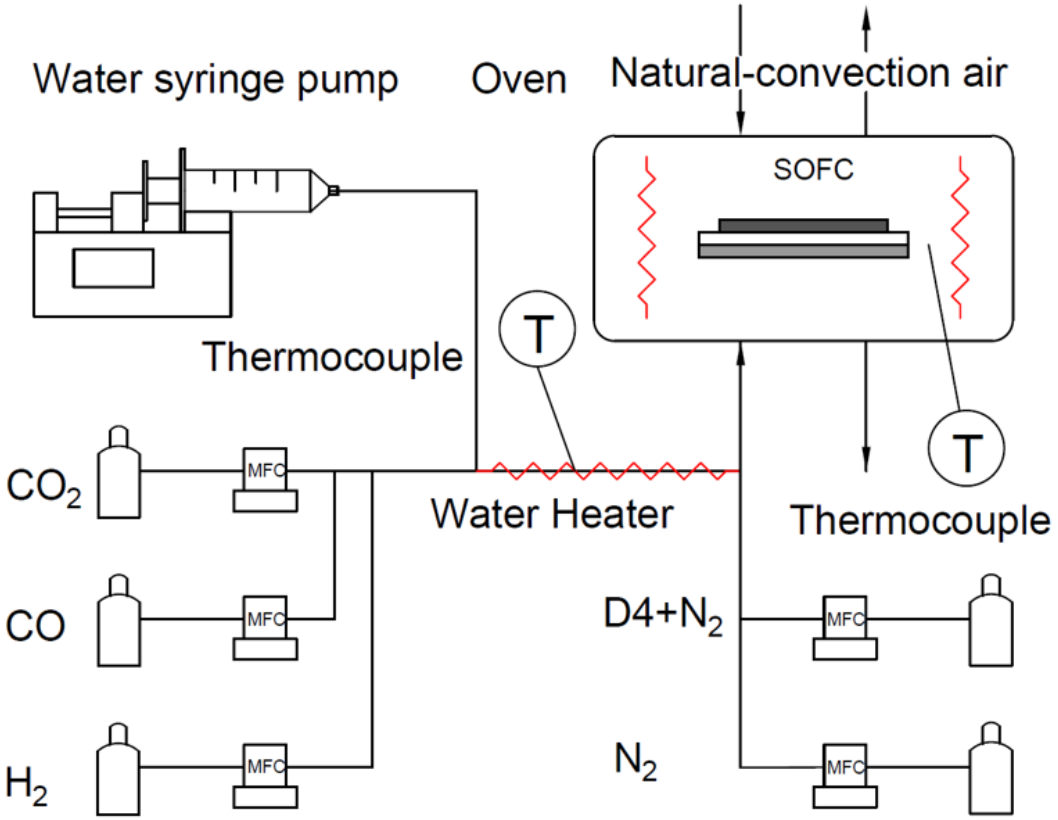

Figure 2.1 Schematic of experiment setup to investigate fuels influence of degradation process.

Table 2.2 shows the gas flow rates, whose unit is standard cubic centimeters per minute (sccm), fed to anode side in different experiments. The total gas flow rate in anode side was fixed at 20 sccm to keep the same Reynolds number of flows. For all the experiments, to ensure the same number of electrons available for electrochemical conversion from the fuels, the H_2 + CO total flow rate was kept at 7 sccm. Except the flow of N_2, the flow rates of H_2, CO, H_2O and CO_2 in all experiments were following the same component ratio in bio-syngas after reformer [72], respectively. For the cathode side, the air was supplied by natural convection through the vertical furnace.

Table 2.2 Flow rate of anode side gases for the impact of fuels experiments

Flow rates (sccm)	H_2	CO	CO_2	H_2O	N_2 (D4 conc. 0/1/0.4/2.5 ppm)	D4+N_2 (D4 conc. 0/1/0.4/2.5 ppm)
H_2+H_2O	7	NA	NA	2	11/11 /11/11	NA/NA/NA/NA
H_2+D4	7	NA	NA	NA	13/9.517 /11.607/4.294	NA/3.483/1.393/8.706
H_2+CO+D4	5	2	NA	NA	13/9.517 /11.607/4.294	NA/3.483/1.393/8.706
H_2+H_2O+D4	7	NA	NA	2	11/7.517 /9.607/2.294	NA/3.483/1.393/8.706
H_2+H_2O+CO+CO_2+ D4	5	2	1	2	10/6.517 /8.607/1.294	NA/3.483/1.393/8.706

For each experiment, a different Ni-YSZ anode SOFC was sealed on a quartz tube with silver paste. The setup was placed in a vertical tubular furnace, which was heated to 750 °C at 5 °C per minute. The experimental temperature was fixed at 750 ° C for all the tests. The silver and steel wire were used for current collection and voltage measurement for the anode and cathode sides. A K-type thermocouple placed outside the SOFC was used for measuring the operating temperature. The anode of SOFCs were reduced roughly 3 hours by 10 sccm H_2 and 10 sccm N_2.

After experiments, the fuel cell samples were crosscut to expose the cross-sections. Then the samples were embedded in epoxy to fill the pores in the anode. Cross-section sides were polished. SiC papers (from 46 μm to 16 μm) were used for coarse polishing. Fine polishing was achieved by water-based diamond suspension and colloidal silica diamond suspension (from 15 μm to 0.0415 μm). The cross section and

micrographs of fuel cells' anode was conducted by a field emission scanning electron microscope (FESEM, JEOL JXA-8530F electron microprobe) with wavelength-dispersive spectrometers (WDS) which permits the measurement of elements from B through U, and provides qualitative silicon-trace analysis. In addition, this instrument is also equipped with an energy-dispersive spectrometer (EDS), which is capable of X-ray count rates in excess of 200k counts per second and has high-speed X-ray mapping and quantitative microanalytical capabilities that rival the WDS. The SEM, EDS and WDX analysis were performed at 15 kV at 5×10^{-8} A beam current for the fuel cells' cross-section graphs and 15 kV at 2×10^{-8} A beam current for micrographs of anodes.

2.3 Electrochemical Characterizations

H. Madi et al. [15,65,72] reported that initial fuel cell degradation occurs prior to exposure to siloxane contamination and named this phenomenon as intrinsic degradation because of sources such as nickel grain growth and impurities in raw materials. The intrinsic degradation was also observed in this study. In order to reduce the impact of intrinsic degradation, the SOFCs were operating at their corresponding operating current densities for 50 hours with clean fuel (i.e., no siloxane) to stabilize the performance before starting formal experiments. In order to concentrate on the degradation caused by D4, the voltage during reduction and intrinsic degradation during the first 50 hours of operation was not shown. Then, except for the H_2+H_2O experiment, D4 with three different concentrations were mixed into the fuel with the sequence 1ppm$_v$, 0.4 ppm$_v$ and

2.5 ppm_v. To investigate how the concentration of siloxane impacts the degradation process, the sequence is neither increment nor decrement. The increment or decrement sequence which has been used in studies of H. Madi et al. [15,65,72] may not eliminate the time depended degradation influence on the experiment. Before and after each concentration, the polarization (I-V curve) and EIS tests were conducted. The SOFCs' operating voltage changes (V-t curve) at constant current density were recorded during the entire experiment. In previous SOFC siloxane degradation studies completed by H. Madi, D. Papurello, K. Haga et al. [60,72,74] , the voltages selected for constant current density tests were relatively close to OCV (around 0.8~1 V), but not SOFCs' more common operating conditions (0.5~0.7 V). In this study, the current density was selected for the voltage range 0.5~0.7 V. In order to keep all SOFCs in similar electrochemical reaction equilibrium and voltage changes in real operating region, the initial operating voltages were fixed at ~0.65 V. The cell was then operated with clean fuel for 50 hours, as discussed previously. Based on the fixed initial operating voltage, current densities for H_2+H_2O, H_2+H_2O+D4, H_2+D4, H_2+CO+D4 experiments were around 300-350 mA cm^{-2}. The current density was fixed at 200 mA cm^{-2} in the SOFC degradation experiment with H_2+H_2O+CO+CO_2+D4 as the fuel. The characterization tests results show in **Fig. 2.2**, **Fig. 2.3**, **Fig. 2.4**, **Fig. 2.5** and **Fig. 2.6** correspond to H_2+H_2O, H_2+H_2O+D4, H_2+D4, H_2+CO+D4 and H_2+H_2O+CO+CO_2+D4 experiments, respectively. **Fig. 2.2**, which assesses degradation with only H_2+H_2O, provides a baseline for comparison because no

D4 is present.

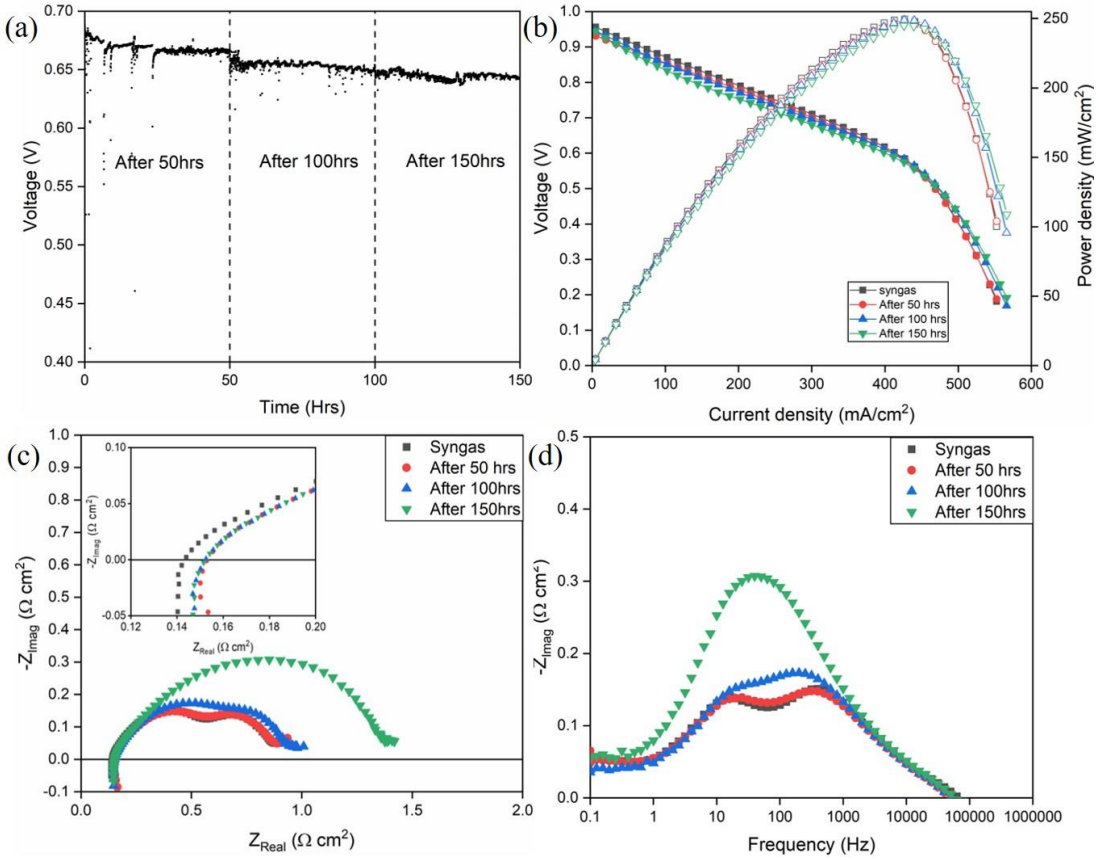

Figure 2.2 Performance degradation of the SOFC under H_2+H_2O experiment. (a) The SOFC voltage at constant current density (350 mA cm^{-2}); (b) polarization curve; (c) Nyquist plots of EIS measurements; (d) Bode plots of EIS measurements. The clean fuel composition is H_2+ H_2O+N_2 with no D4.

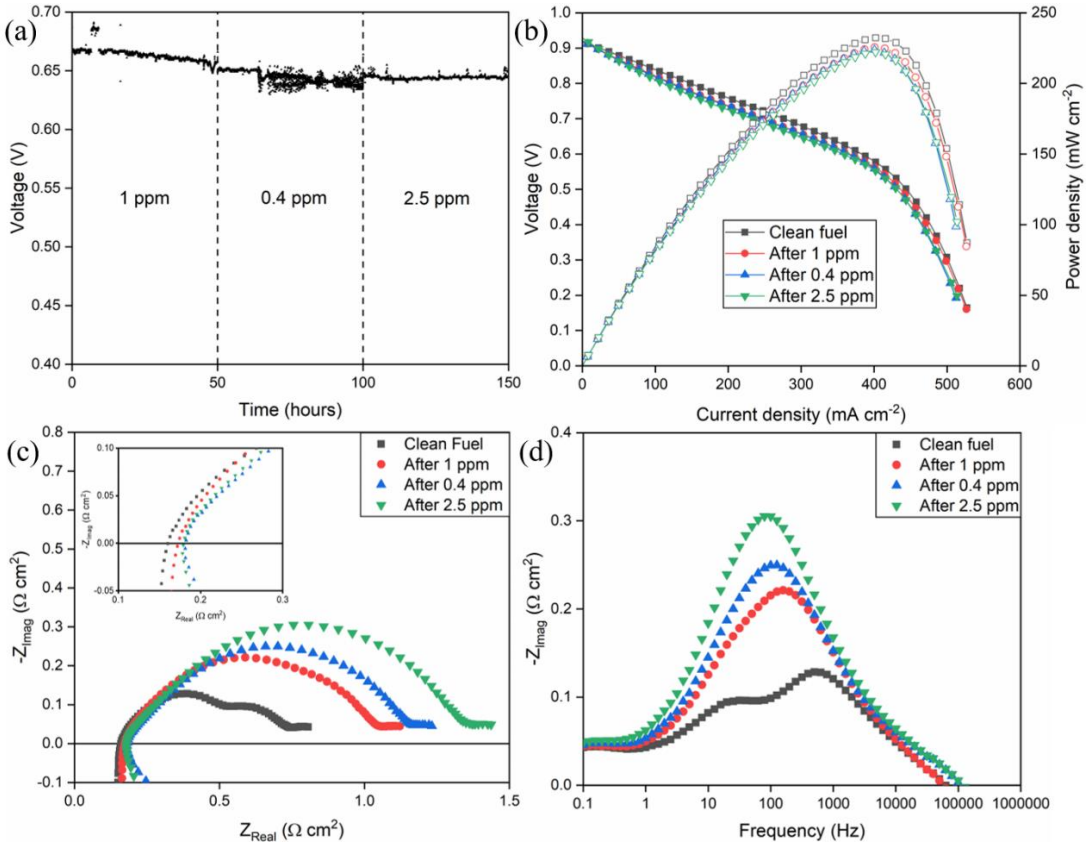

Figure 2.3 Performance degradation of the SOFC under H_2+H_2O+D4 experiment. (a) The SOFC voltage at constant current density (300 mA cm^{-2}); (b) polarization curve; (c) Nyquist plots of EIS measurements; (d) Bode plots of EIS measurements. The clean fuel composition is H_2+H_2O+N_2 with no D4.

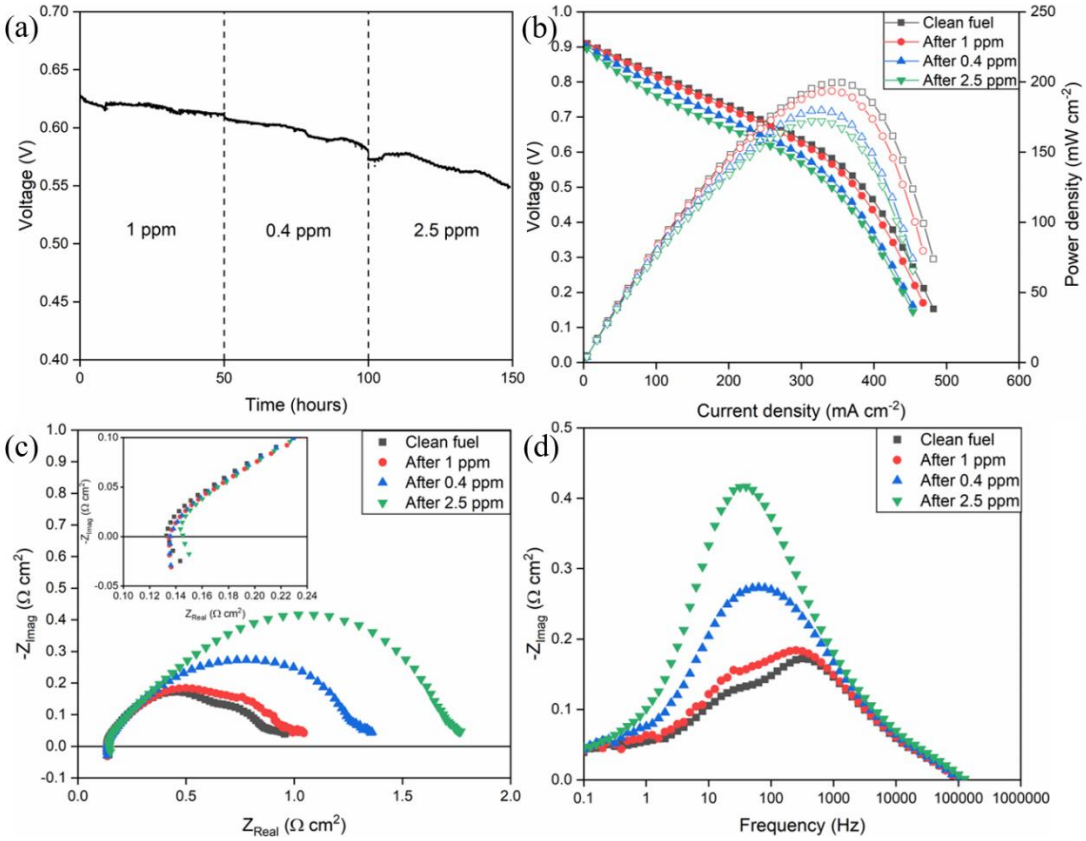

Figure 2.4 Performance degradation of the SOFC under H_2+D4 experiment. (a) The SOFC voltage at constant current density (300 mA cm^{-2}); (b) polarization curve; (c) Nyquist plots of EIS measurements; (d) Bode plots of EIS measurements. The clean fuel composition is H_2+N_2 with no D4.

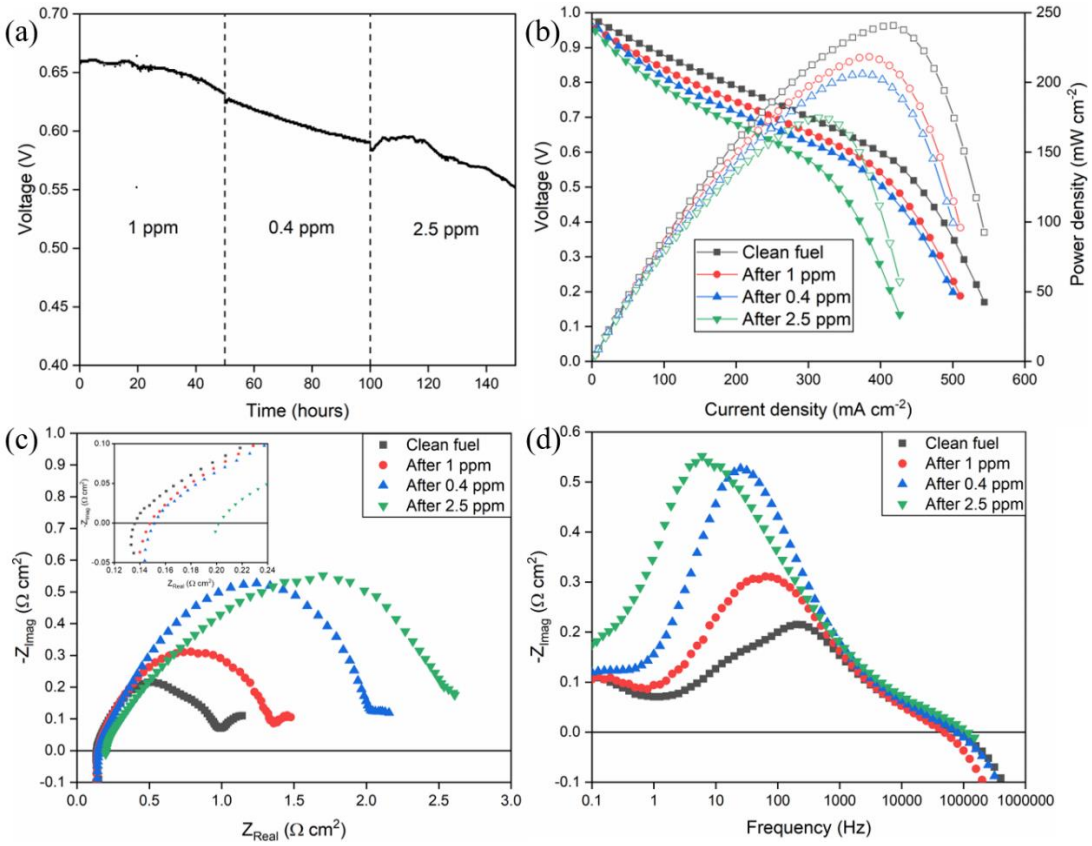

Figure 2.5 Performance degradation of the SOFC under H_2+CO+D4 experiment. (a) The SOFC voltage at constant current density (350 mA cm^{-2}); (b) polarization curve; (c) Nyquist plots of EIS measurements; (d) Bode plots of EIS measurements. The clean fuel composition is H_2+CO+N_2 with no D4.

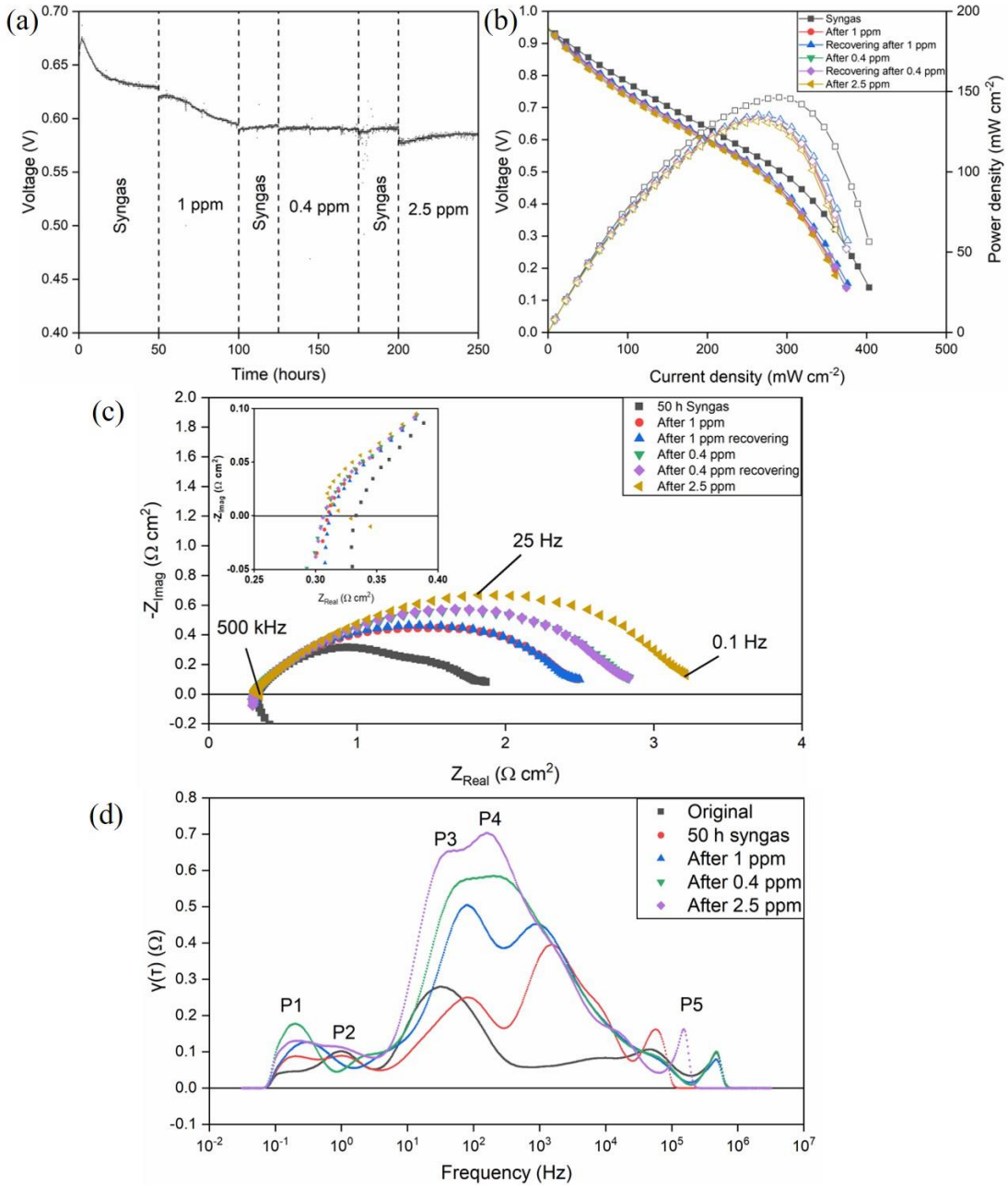

Figure 2.6 Performance degradation of the SOFC. (a) The SOFC voltage at constant current density (200 mA cm^{-2}); (b) polarization curve; (c) EIS measurements; (d) DRT plot.

In each figure, the SOFCs' performance degradation under D4 contamination can be noticed clearly from power density decrease and resistance increase. From the Nyquist

plots part (c) and Bode plots part (d) in **Fig. 2.2**, **Fig. 2.3**, **Fig. 2.4**, and **Fig. 2.5**, a small increase in mass transfer can be noticed at the low frequency arc ~ 1 Hz. Meanwhile, a small increase in ohmic resistance can be detected at high frequency. The main impedance increase occurred around 100 Hz which is attributed to anode activation degradation. An obvious impedance increase at cathode contribution frequency ~ 40 kHz [85] was not observed. In this case, no obvious LSCF cathode degradation influences this study. Generally, H_2+H_2O experiment has the lowest degradation and H_2+CO+D4 experiment has the highest degradation.

For siloxane contaminated bio-syngas experiment with H_2+H_2O+CO+CO_2+D4 as the fuel, a clean fuel phase was also added to investigate the recovery of the anode degradation. **Fig. 2.6a** shows the SOFC voltage decreases at constant current density even without D4 inside the fuel in the first 50 hours. The voltage degradation rate was relatively high initially. After 30 hours in the self-degradation phase, it decreased to 1.19% / 1000 hours which is lower than the average Ni/YSZ SOFCs' degradation rate without any contamination (2% / 1000 hours) [19]. As a result, the initial intrinsic degradation is considered to be stabilized sufficiently in order to start the contamination experiment. After initial intrinsic degradation and stabilization of the voltage, D4 was introduced into the fuel as show in **Fig. 2.6a**. From the increase of the resistance and decrease of power density, apparent SOFC performance degradation under D4 contamination can be detected. According to the EIS measurements in **Fig. 2.6c**, the

major impedance increase appears around 25 Hz which indicates degradation due to anode deactivation. From high frequency EIS results, considering the impedance accuracy of the EIS measurement at high frequency (±3 %), no significant change in ohmic resistance is detected. Simultaneously, there is the increase of impedance at the low frequency ~1 Hz attributed to mass transfer degradation. In this study, the impact of LSCF cathode degradation can be ignored because obvious cathode degradation impedances increase, typically occurring around 50 kHz, has not been noticed [85]. To separate the overlapping anodic and cathodic polarization process in EIS results, DRT analysis was conducted. From **Fig. 2.6d**, DRT plot shows five main separated peaks (P1 ~ P5) ranging from 10^{-1} to 10^{6} Hz. According to previous literature for SOFC DRT analysis, the physical meaning of various polarization peaks can be interpreted [46,86,87]. The P1 (0.1 to 1 Hz) is related to the gas diffusion process for the air electrode (cathode). The P5 (> 10 kHz) is related to charge transfer. Due to the inconsistency of previous reports for medium frequency range (0.5 Hz to 10 kHz), the DRT result for the SOFC before the intrinsic degradation phase has been added to help distinguish the anode and cathode processes. Different from the DRT results after the intrinsic degradation and siloxane contaminations, the P4 cannot be observed in the original cell and only four peaks can be detected. In this situation, the P2 appears to be related to cathode process and the P3 and P4 are attributed to anode process. This relaxation processes distribution is consistent with the report from J. Hong et al. [46]. In

this regard, from the DRT plot in **Fig. 2.6d**, the main degradation of the SOFC is due to anode processes (P3, P4). Generally, the P2 for cathode remained unchanged. The gas diffusion process for cathode increased slightly during the experiment (P1). No huge change of charge transfer process was noticed (P5). To assess performance recovery after operating with 1 ppm D4 for 50 hours, D4 was not supplied for 20 hours prior to starting the 0.4 ppm of D4 siloxane experiment. From **Fig. 2.6a**, the V-t curve shows no obvious performance recovery. The J-V curve, EIS measurement in **Fig. 2.6b** and **c**, all illustrate that the curves before and after recovery are almost overlapping. All these results support that performance degradation resulting from D4 cannot be recovered in clean fuel and indicate the degradation process is irreversible.

To reveal the process of siloxane deposition, quantitative analysis is necessary. In order to compare the degradation between different experiments and between different concentrations in the same experiment, degradation rates were calculated and presented in **Table 2.3**, **Table 2.4**, **Table 2.5** and **Table 2.6**. The voltage degradation rates and resistance increase rates were used to evaluate the extent of degradation. In **Table 2.3**, the voltage degradation rates from V-t curves, which are directly correlated to the power densities' decrease, were used to represent the degradation rates of the SOFCs' performances.

Table 2.3 Degradation rates calculated from V-t curve for the impact of fuels experiments

Experiment	50 h ($mV.h^{-1}$)	100 h ($mV.h^{-1}$)	150 h ($mV.h^{-1}$)	Average ($mV.h^{-1}$)
H_2+H_2O	0.08	0.1	0.08	0.08

Experiment	1 ppm D4/50 h ($mV.h^{-1}$)	0.4 ppm D4/100 h ($mV.h^{-1}$)	2.5 ppm D4/150 h ($mV.h^{-1}$)	Average ($mV.h^{-1}$)
H_2+H_2O+D4	0.3	0.3	–	0.2
H_2+ D4	0.2	0.5	0.5	0.4
H_2+CO+ D4	0.5	0.8	0.8	0.7

– No obvious voltage decrease.

In **Table 2.4**, area specific resistance (ASR) is reported from EIS results. The rate of resistance increase was calculated by equation (2.1) as follows:

(Final Resistance Value – Initial Resistance Value) / Experiment Time (2.1)

After comparing all SOFCs' degradation results for different concentrations, a significant relationship between the D4 concentration and the degradation rate including voltage decrease and resistance increase have not been observed. To exclude the possibility that degradation originated from other sources beside D4, the H_2+H_2O, H_2+H_2O+D4 experimental results can be compared as evidence. Considering the voltage degradation rates, at 1 ppm and 0.4 ppm D4 concentration, the H_2+H_2O+D_4 has a higher degradation rate. Furthermore, the total voltage degradation rate of the H_2+H_2O experiment is also smaller. The EIS results are another essential factor to compare. The results from **Table 2.4** show that for the H_2+H_2O+D4 experiment, the rate of ASR increase is larger than the H_2+H_2O experiment. This indicates that D4 is the reason for

the degradation. The reason why the concentration of siloxane did not result in a clearly observed change in degradation rate, which didn't appear in experimental results of H. Madi et al. [72], can be explained in different ways. Some of the degradation may be due to the LSCF cathode and SDC buffer layer used in this study which have non-negligible degradations during long-term operation [88], but that was not observed as a significant factor in the EIS results. As the cathode type and experimental conditions were the same in all experiments including the H_2+H_2O baseline experiment, the influence of cathode or buffer layer degradation can be excluded as a major contributing factor for the increased degradation with D4 exposure. The relatively short time operating with only hydrogen prior to D4 testing (~50 hours) may be insufficient. The size of SOFCs whose active area is 0.712 cm^2 in this study is much smaller than previous studies from H. Madi et al. [72] with 12.5 cm^2 active area. The SOFCs' size difference may influence the siloxane deposition speed as well. Although the connection between D4 concentrations and degradation was not observed, the degradation due to siloxane poisoning in different experiments shows time dependent behavior, generally.

Table 2.4 Area specific resistance (ASR) increasing rates calculated from EIS results for the impact of fuels experiments

Experiment	50 h ($m\Omega\ cm^2\ h^{-1}$)	100 h ($m\Omega\ cm^2\ h^{-1}$)	150 h ($m\Omega\ cm^2\ h^{-1}$)	Average ($m\Omega\ cm^2\ h^{-1}$)
H_2+H_2O	0.1	1.1	9.5	3.6
Experiment	1 ppm D4/50 h ($m\Omega\ cm^2\ h^{-1}$)	0.4 ppm D4/100 h ($m\Omega\ cm^2\ h^{-1}$)	2.5 ppm D4/150 h ($m\Omega\ cm^2\ h^{-1}$)	Average ($m\Omega\ cm^2\ h^{-1}$)
H_2+H_2O+D4	6.4	2.2	3.6	4.1
H_2+D4	1.8	6.3	8.1	5.4
H_2+CO+D4	7.4	13.7	11.3	10.8

According to **Table 2.3** and **Table 2.4**, the H_2+D_4 and H_2+D4+CO experiments shared the similar degradation trend that degradation rates were relatively small at the beginning and increased with time. One interesting result can be pointed out is that changes in the ohmic resistance followed the D4 concentration trends. This can be proved by calculation results shown in **Table 2.5**. For H_2+H_2O+D_4 experiment and the baseline H_2+H_2O experiment, there was relatively large degradation rate initially which decreased with time. The high concentration of water in the fuel may react with D4 in the anode and this may be responsible for the initial, more rapid degradation. Comparing the H_2+H_2O+D4 experiment which contains water with the fuel, the H_2+D4 and H_2+D4+CO experiment have dry fuel and the only source of water is the electrochemical reaction of hydrogen and oxygen in the SOFC.

Table 2.5 Ohmic resistance increasing rates calculated from EIS results for the impact of fuels experiments

Experiment	50 h ($m\Omega\ cm^2\ h^{-1}$)	100 h ($m\Omega\ cm^2\ h^{-1}$)	150 h ($m\Omega\ cm^2\ h^{-1}$)
H_2+H_2O	0.2	–	0.03

Experiment	1 ppm D4/50 h ($m\Omega\ cm^2\ h^{-1}$)	0.4 ppm D4/100 h ($m\Omega\ cm^2\ h^{-1}$)	2.5 ppm D4/150 h ($m\Omega\ cm^2\ h^{-1}$)
H_2+H_2O+D4	0.2	0.2	–
H_2+D4	0.04	0.02	0.3
H_2+CO+D4	0.2	0.07	1.1

– No obvious ohmic resistance increase.

Besides investigating the degradation in each individual experiment, degradation comparison among different experiments is also significant in this study. The voltage degradation rate and the ASR increasing rate from **Table 2.3** and **Table 2.4** were used as the standard for comparisons. Combined results from polarization and EIS tests indicate the extent of degradation follows the sequence below:

H_2+D4+CO experiment > H_2+D4 experiment > H_2+H_2O+D4 experiment > H_2+H_2O experiment

As expected, the H_2+H_2O experiment which was selected as a baseline without D4 had the smallest degradation. However, the dry CO and H_2 fuels with D4 had higher degradation rates than wet H_2 with D4. According to the previous siloxane deposition mechanism, equation (1.4) and (1.5), this result is unexpected. More details will be discussed in morphology analysis section.

For the bio-syngas recovery experiment, detailed quantitative analysis calculated

from the results in **Fig. 2.6** is presented in **Table 2.6**. The voltage degradation rates, which are proportional to the power densities, were obtained from the slope of V-t curve in **Fig. 2.6a**. According to the EIS results, the area specific resistance (ASR) increase can be calculated by equation (2.2) shown below:

(Final Resistance Value – Initial Resistance Value) / Initial Resistance Value (2.2)

Both the voltage degradation rate and increase in ASR were utilized to evaluate the performance degradation and recovery of the SOFC. Considering the voltage degradation rate and increase in ASR, there is no obvious relationship between the D4 concentration and the performance degradation. This result contradicts previous research [72] in which performance degradation followed the siloxane concentration. There are some significant differences in this study which may cause the differences in results. First, as described before, the concentration sequence in this study is neither increment nor decrement. Second, the cathode of the SOFC used in this study was LSCF with SDC buffer layer. This is different from the previous study in which LSM cathode was utilized. Third, the size of the SOFC may also have an effect on the degradation rate. The active area of SOFC in the previous study [72] was much larger than this work. As observed previously [84], the performance degradation is much closer to time dependent rather than D4 concentration dependent considering the voltage degradation rates and increase in ASR. Generally speaking, the degradation was relatively large initially. Then declined with time and kept stable eventually. Minute voltage recovery was detected when switching to

clean fuel between different concentrations. However, it still cannot be compared with the initial degradation.

Table 2.6 Voltage degradation rate and increase in area specific resistance (ASR) calculated from characterization results

	Original	1ppm	Recovery after 1ppm	0.4ppm	Recovery after 0.4ppm	2.5ppm
Voltage decreasing rate (mV h^{-1})		0.6	-0.2	0.02	-0.2	-0.2
ASR (Ω cm^2 h^{-1})	1.87	2.49	2.50	2.83	2.83	3.21
Percentage Increase in ASR (%)		33.26	0.31	13.41	-0.18	13.70

2.4 Morphology and Composition Analysis

Figure 2.7 shows silicon element distribution over the entire anode cross section in which left side is electrolyte and right side is the bottom of anode (fuel inlet). Due to relative weak signal of silicon, the contrast and the brightness of the **Fig. 2.7** has been increased to present results clearly. The brightness of the pixels can only be used for silicon distribution analysis and qualitative comparison. The SOFC tested by H_2+H_2O fuel without D4 can be used as a reference sample shown in **Fig. 2.7a**. From the figure, there are some silicon spots randomly distributing over the anode's cross section. Those silicon spots are likely due to contamination during fuel cell fabrication instead of D4 deposition. A similar pattern of silicon spots was detected in all of the cross sections. From all the WDS mapping of samples involving D4 in the fuel (**Fig. 2.7b, 2.7c, 2.7d**),

silicon deposition can be detected. The silicon distribution patterns are similar with the bottom of the anode having higher concentration of silicon which gradually decreases in the middle of the anode. From the **Fig. 2.7d**, some silicon was observed at the electrolyte/anode interface. Higher concentration of silicon around the bottom of the anode, which is near the fuel inlet, indicates that the majority of the silicon is directly deposited after entering fuel cell, far from the active region near the electrolyte. This phenomenon can be explained by higher siloxane concentration around anode bottom, but may also give a hint that the silicon deposition is influenced by the anode materials.

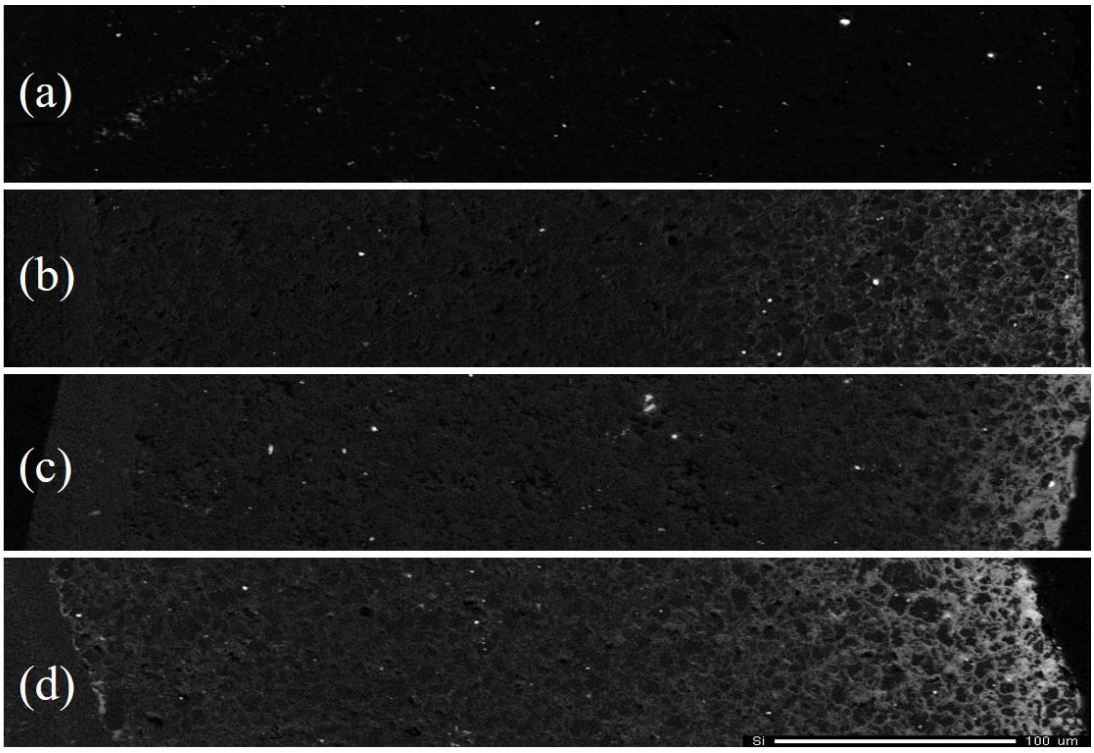

Figure 2.7 SEM-WDS mapping of silicon element distribution cross the entire anode after: (a) H_2+H_2O experiment; (b) H_2+D4 experiment; (c) H_2+CO+D4 experiment; (d) H_2+H_2O+D4 experiment. The left sides are YSZ electrolytes and right sides are bottom of anode (fuel inlet).

Figure 2.8 shows WDS maps of the silicon distribution at small sections of the anode from each experiment. FESEM conditions were kept consistence for all samples to obtain consistent signals. As a result, the silicon deposition around triple boundary areas (**Fig. 2.8a, 2.8c, 2.8e**) are similar across all experiments. However, the anode bottom areas (**Fig. 2.8b, 2.8d, 2.8f**) have stronger signal. This result coincided with **Fig. 2.7** that silicon was mainly deposited on the bottom of anode. Comparing silicon signals between the **Fig. 2.8b, d, f**, the fuel cell sample after H_2+ D4 experiment has the strongest silicon signal. The silicon signal in the H_2+H_2O+D4 experiment is weaker and H_2+CO+D4 has the weakest signal for silicon deposition. Part of that trend is consistent with polarization and EIS tests results which showed H_2+D4 experiment degradation rate is higher comparing with H_2+H_2O+D4 experiment.

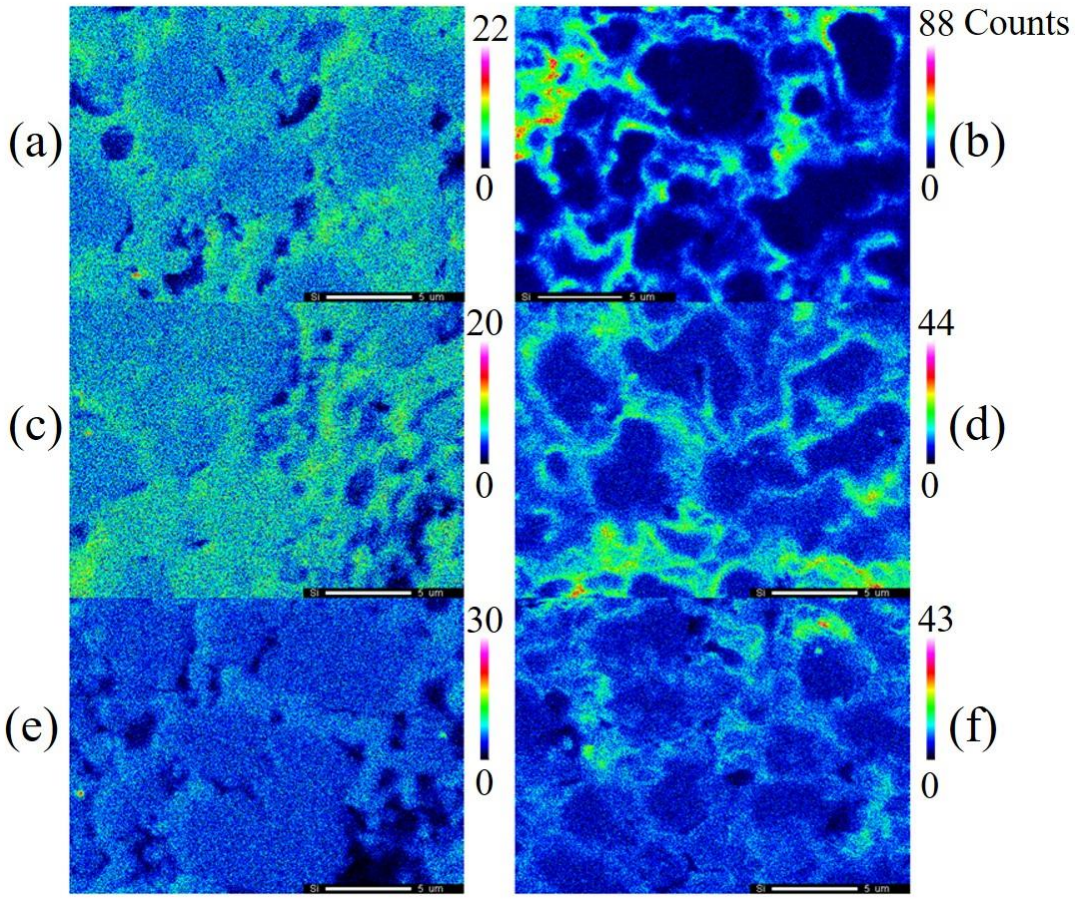

Figure 2.8 SEM-WDS mapping of the silicon deposition after experiment on anode: (a) near the triple phase boundary exposed to H_2+D4; (b) near the bottom of anode exposed to H_2+ D4; (c) near the triple phase boundary exposed to H_2+H_2O+D4; (d) near the bottom of anode exposed to H_2+H_2O+D4; (e) near the triple phase boundary exposed to H_2+CO+D4; (f) near the bottom of anode exposed to H_2+CO+D4.

These results contradict the previous siloxane deposition mechanisms in equation (1.4), which demonstrate that siloxane reacts with water forming othosilicic acid, and then othosilicic acid dissociates to the silicon dioxide. In this case, the silicon deposition in H_2+H_2O+D4 experiment was expected to be most significant. However, the polarization curves, EIS and SEM-WDS analysis all indicate that the anode will have more degradation due to silicon deposition in H_2+D4 experiment in which the only water

source is the product of hydrogen and oxygen reaction. To investigate this phenomenon, 6 μm level SEM-EDS/WDS elemental mapping for anode bottom after H_2+D4 experiment is shown in **Fig. 2.9**. It has to be mentioned that when using EDS for the anode, there is signal overlapping between the Y and Si which could cause an overestimate of the Si amount. **Fig. 2.10** shows the WDS profile comparison of the anode in a region of low silicon concentration and in high concentration area of silicon to ensure proper silicon detection and separation from Y. For this reason, WDS was used as critical technique to map the location and quantity of the Si in the anode.

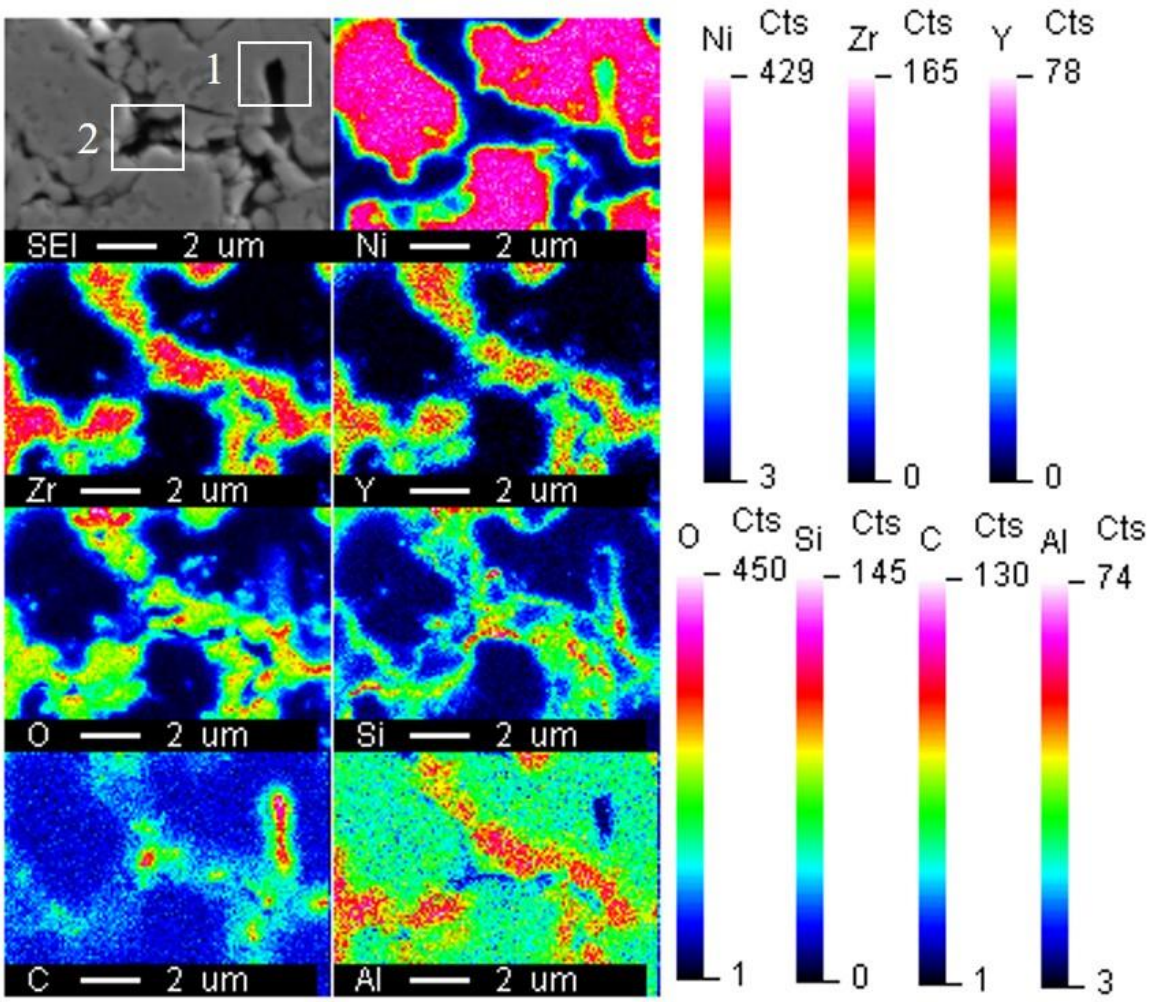

Figure 2.9 SEM-EDS/WDS elemental mapping of anode bottom after H_2+ D4 experiment.

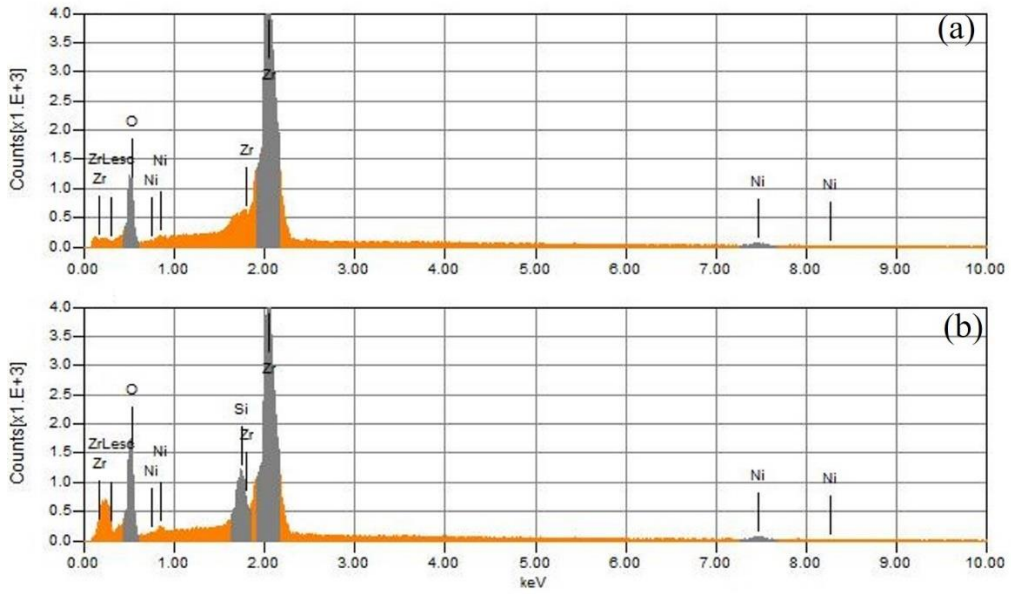

Figure 2.10 Comparison of WDS profiles of anode after H_2+ D4 experiment: (a) near triple phase boundary; (b) near the bottom.

From **Fig. 2.9**, most carbon and silicon elements are deposited in the pores of the anode. The carbon element is deposited around nickel element significantly. This is verified by examining region 1 labeled in **Fig. 2.9**. Compared with the carbon, the silicon element is associated with yttrium, zirconium, oxygen and nickle. From **Fig. 2.9**, the carbon and silicon deposition are noted both coincidentally and separately. Region 2 in **Fig. 2.9** has a large silicon and carbon signal, which may provide a hint that the existence of Si-C bond or compounds containing carbon and silicon elements. There is also a large oxygen signal in region 2. To demonstrate the association of silicon, carbon and oxygen and to expose more details, **Fig. 2.11** is presented. In this figure, due to relatively strong signal of oxygen compared with the other two elements, the signal of carbon and silicon

were enhanced. As a result, the brightness of each element in this figure can be used for concentration comparison to the relative elements themselves in the same experiment, but not across experiments.

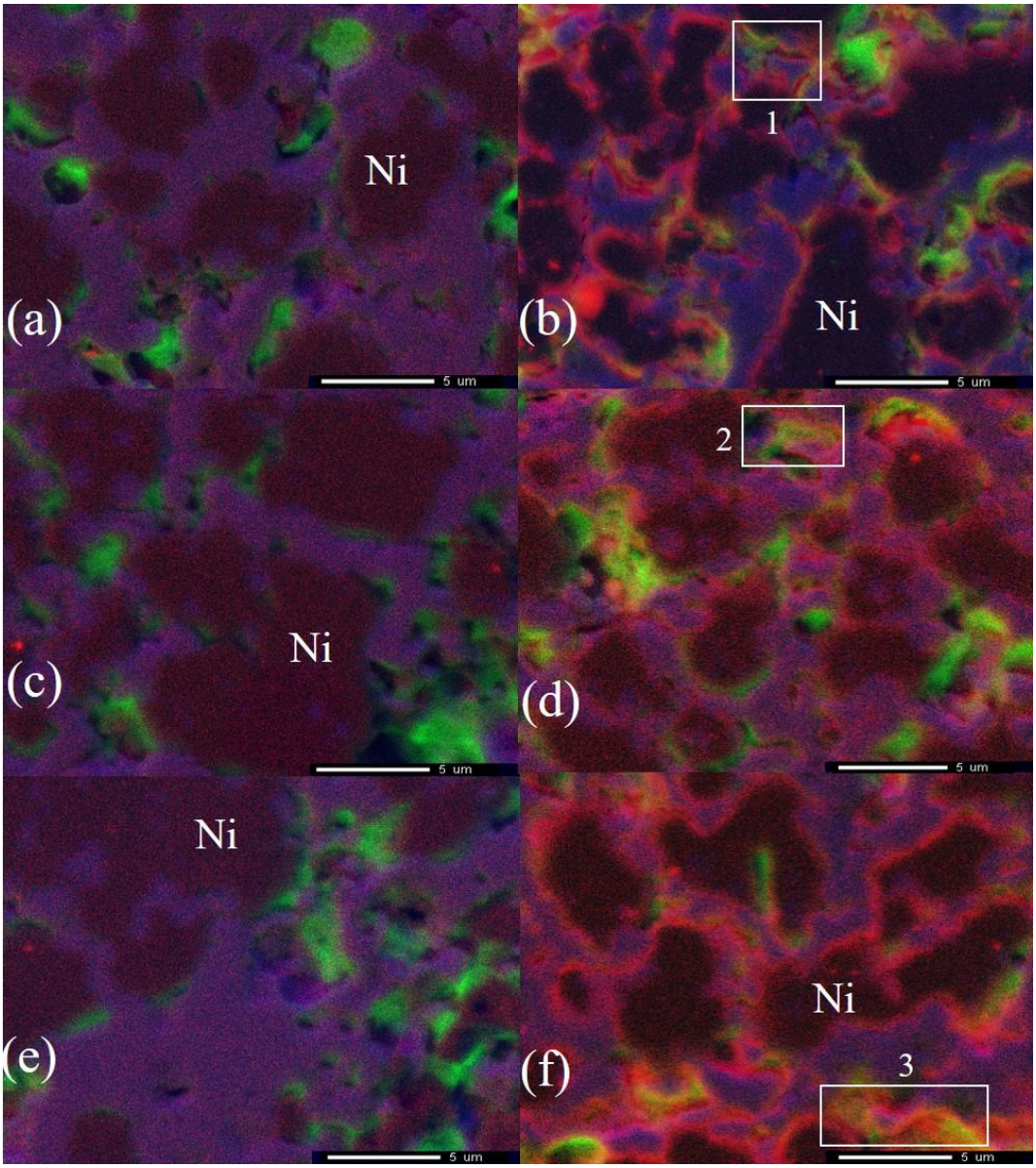

Figure 2.11 SEM-EDS/WDS elemental combination mapping after experiment on anode: (a) near the triple phase boundary exposed to H_2+D4; (b) near the bottom of anode exposed to H_2+ D4; (c) near the triple phase boundary exposed to H_2+CO+D4; (d) near the bottom of anode exposed to H_2+CO+D4; (e) near the triple phase boundary exposed to H_2+H_2O+D4; (f) near the bottom of anode exposed to H_2+H_2O+D4. The area of this EDS/WDS map is marked to red color for silicon, blue for oxygen and green for carbon. Dark regions are nickel.

From **Fig. 2.11**, the silicon and carbon distributions follow a similar pattern even under three different experiments. Similarly to **Fig. 2.9**, **Fig. 2.11** shows that silicon and

carbon may deposit individually and coincidentally. Region 1, 2, and 3 in **Fig. 2.11** refer to the bottom of the anode corresponding to H_2+D4, H_2+CO+D4 and H_2+H_2O+D4 experiments, respectively. The overlap of silicon, carbon and oxygen elements can be detected. This result indicates compounds with silicon, carbon and oxygen may still exist in anode. One possibility is that siloxane, which contains C-Si-O bonds, remains intact and directly deposits on the anode. There are also regions that contain only silicon and regions that contain only carbon. Comparing the region near the anode triple boundary layer and anode bottom, the extent of carbon deposition is similar. By contrast, the silicon was mainly deposited on the bottom of anode. This can also be approved by **Fig. 2.7.**

For the stimulating bio-syngas experiment with H_2+H_2O+CO+CO_2+D4 as the fuel, **Fig. 2.12** shows SEM with WDS elemental mapping over the anode cross section near the fuel inlet where most of the silicon deposition occurs based on previous studies [72,84]. According to the region I in **Fig. 2.12**, carbon is more associated with the nickel particles. Silicon element is mainly deposited around Ni-YSZ interface (i.e., tripe phase boundary (TPB)). Confirmed by the region II and III labeled in **Fig. 2.12**, the overlapping of silicon, carbon and oxygen signals can be observed which indicates the existence of deposition compounds with silicon, carbon and oxygen elements. Based on previous siloxane deposition studies [80], D4 siloxane composed of Si, C and O, may only partially decompose or not decompose at all. The overlapping signals of Si, C and O may confirm that previous result.

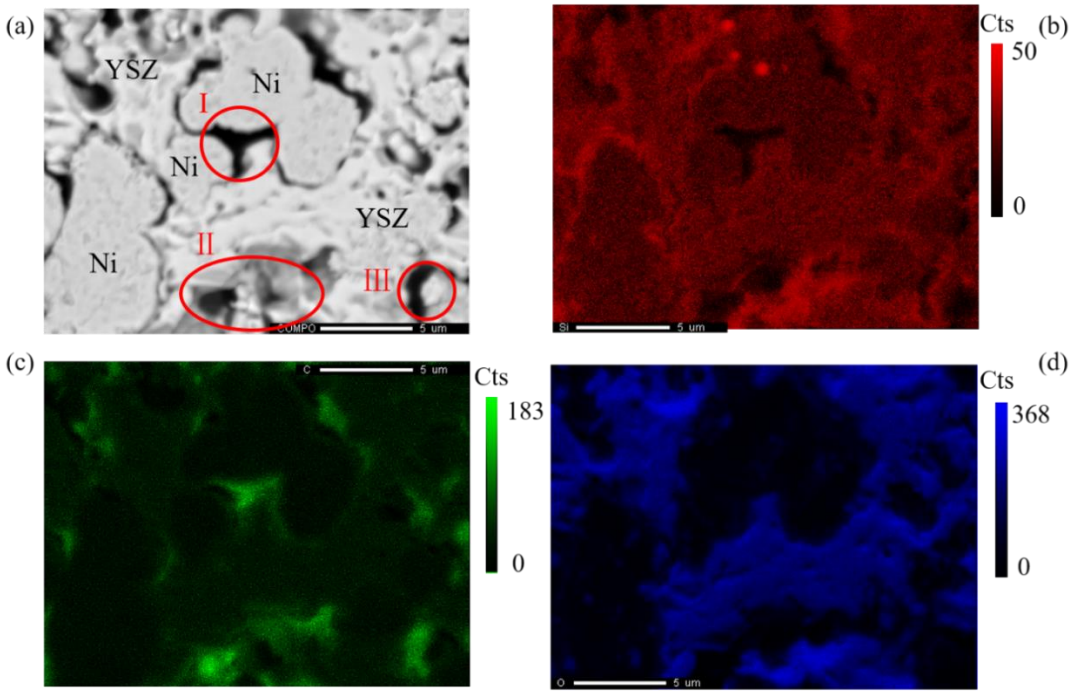

Figure 2.12 SEM-EDS/WDS elemental mapping near bottom of anode (fuel inlet side) after experiment: (a) SEM morphology; (b) silicon elemental mapping marked by red color; (c) carbon elemental mapping marked by green color; (d) oxygen elemental mapping marked by blue color.

Silicon element deposition in the anode can be confirmed by SEM with WDS in **Fig. 2.12.** This result has also been reported by H. Madi, K. Haga et al [72,74]. According to the WDS profile in **Fig. 2.13b**, silicon can be detected and separated from the Y peak. Beside SEM and WDS to confirm the compositions of the deposition, XRD tests have been conducted on the bottom surface of anode (**Fig. 2.13a**) and the results are shown in **Fig. 2.13c**.

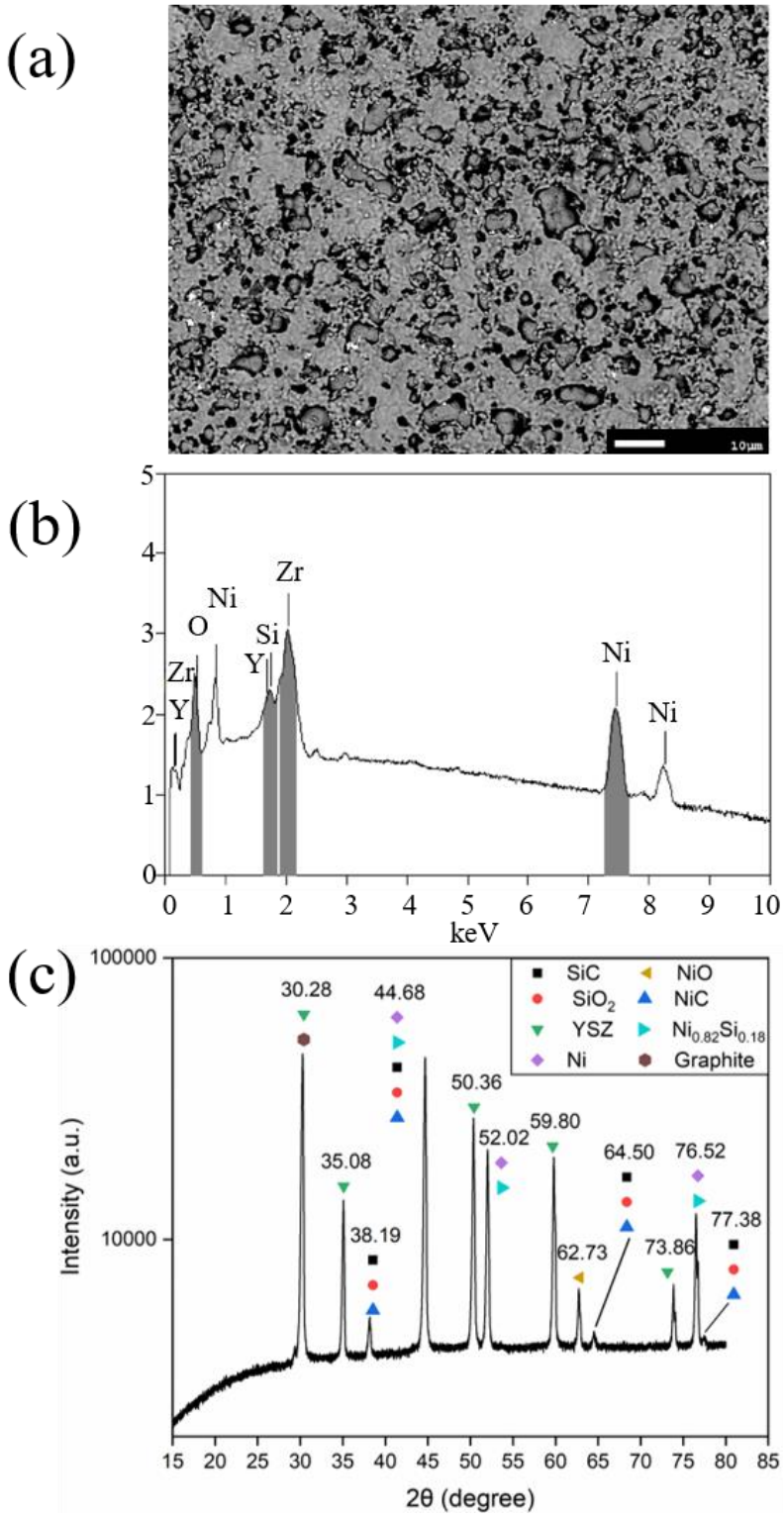

Figure 2.13 Tests on the anode bottom (fuel inlet side) surface. (a) SEM morphology of anode bottom surface; (b) WDS signal profile; (c) XRD spectrum of anode bottom surface.

The XRD result presented in **Fig. 2.13c** shows significant peaks of YSZ and nickel with a smaller NiO peak. Although thermodynamic based Factsage calculations suggest the only form of nickel silica likely to be found is Ni_7Si_{13}, from the XRD results the spectrum reveals no Ni_7Si_{13} remaining in the anode after cooling down. As the $Ni_{0.82}Si_{0.18}$ peak is overlapped with Ni, and the peak of graphite may also overlap with YSZ, their presence cannot be confirmed. The main deposition composition peaks are 38.19°, 64.50°, 77.38° in two theta spectrum because they are not in the raw materials. Considering the existing elements in the anode, SiC, SiO_2 and NiC are the most likely compositions. According to the study of H. He et al. [89], NiC is unstable above 600 °C. However, it may also be formed during the cooling down process. Due to the overlapping peaks, the components cannot be determined with certainty.

2.5 Discussions

The results of this study including characterization tests and morphology analysis provide some evidence that contradicts the previously reported mechanism for anode poisoning from siloxane which was mainly attributed to silicon dioxide deposition on the triple phase boundary areas [72,74]. In previous studies it has been shown that as a main product of the thermal degradation of polydimethylsiloxane (PDMS), D4 can exist at high temperature with steam because of its thermodynamic stability [66,82,90]. According to chemical reaction equation (1.4), a higher concentration of water should

accelerate the siloxane deposition and SOFCs' degradation process. However, comparing H_2+H_2O+D4 and H_2+D4 experimental results, feeding with dry fuels with D4 led to more serious degradation and silicon deposition. From these results, the siloxane poisoning behaviorin SOFCs' anode needs to be discussed again. As valuable references, the mechanism of siloxane deposition on certain metal oxides, like γ-alumina, was investigated previously for biogas cleaning [80]. It is well known that alumina is a good adsorbent of siloxane and has been utilized in industry for siloxane removal. Experimental results indicate that siloxane is first adsorbed to the surface of the metal oxide and the methyl radical in siloxane forms methane according to equation (2.3) [80].

$$Siloxane\ (g) + \ bAl_2O_3(s)_{active} \rightarrow \ silicated\ Al_2O_3(s)_{inert} + xCH_4 \quad (2.3)$$

Then the other methyl groups in siloxane are converted to methane and replaced by hydroxyl groups. Eventually the siloxane converts to amorphous crystal silicon dioxide [81]. Finocchio and Vaiss et al. [82,83] reported that in the siloxane chemical adsorption process, the surface hydroxyl groups of metal oxide play an important role as shown in equation (2.4).

$$\gamma\text{-}Al_2O_3\text{-}8OH + \frac{7}{4}[SiO(CH_3)_2]_4 + 3H_2O \rightarrow \gamma\text{-}Al_2O_3\text{-}Si_7O_{18} + 14CH_4 \quad (2.4)$$

These studies provide evidence for a possible anode degradation explanation under siloxane contamination. As was shown in **Fig. 2.12**, the silicon deposition is associated with the YSZ and the Ni particles. According to studies from Kogler et al. [91], Y_2O_3 which accounts for 8 mol% in the YSZ used in this study, has a strong initial

hydroxylation degree on the surface in a hydrogen atmosphere. In this situation, it shares similar surface hydroxylation properties with Al_2O_3. After dehydroxylation of the Y_2O_3 surface, there are also some mechanisms to recover the hydroxyl groups by hydrogen electro-oxidation reaction on Ni-YSZ anode. The hydrogen spillover mechanism [92] may provide a source of hydroxyl groups shown in equation (2.5), (2.6), and (2.7) [93]. In this circumstance, an alternative explanation for Ni-YSZ SOFC anode degradation under siloxane contamination is proposed. The first step of the deposition process is the chemisorption of siloxane on the YSZ surface. The process is shown in **Fig. 2.14** and its chemical reaction equation is given in equation (2.8).

$$H_2(g) + 2(Ni) \rightleftharpoons 2H(Ni) \quad (2.5)$$

$$H_2(g) + 2O^{2-}(YSZ) \rightleftharpoons OH^-(YSZ) \quad (2.6)$$

$$H(Ni) + O^{2-}(YSZ) \rightleftharpoons (Ni) + OH^-(YSZ) + e^-(Ni) \quad (2.7)$$

$$[(CH_3)_2SiO]_4(g) + 4OH^-(YSZ) \rightleftharpoons Si_4O_8H(CH_3)_5(YSZ) + 3CH_4(g) \quad (2.8)$$

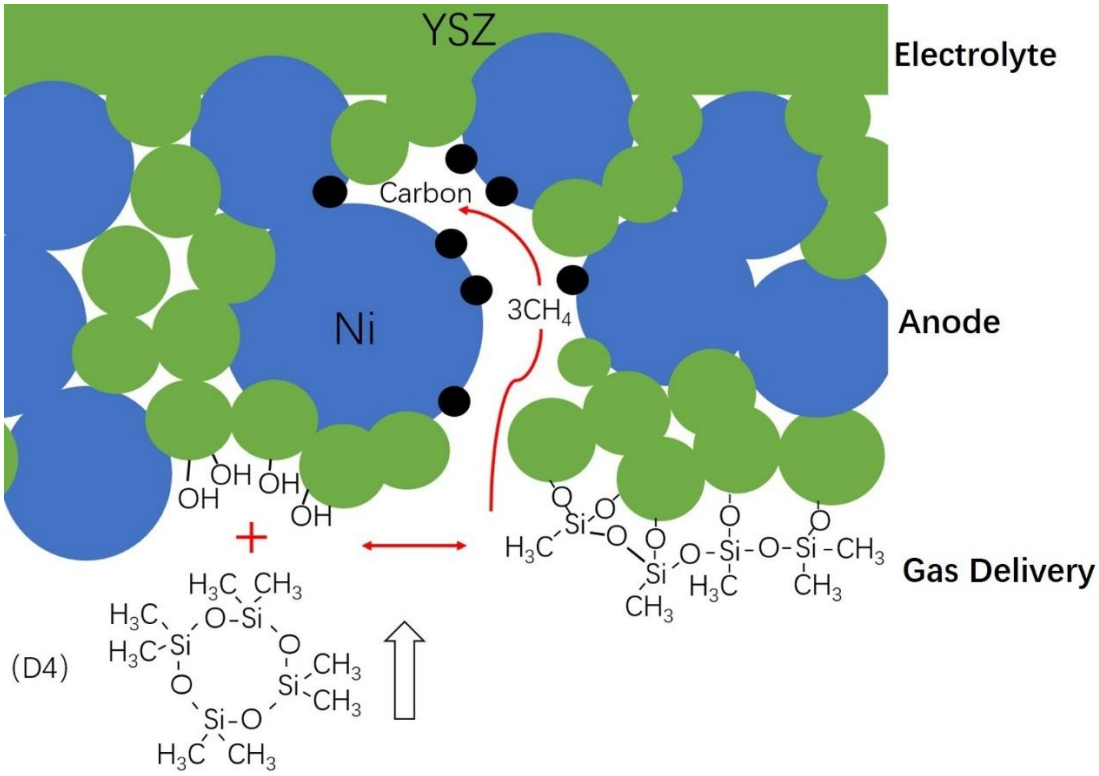

Figure 2.14 The early step of assumed Ni-YSZ SOFC anode degradation under siloxane contamination.

In the second step, the siloxane adsorbed on the surface of Ni-YSZ particles keeps reacting with hydroxyl groups and releasing methane. Eventually it converts to bulk SiO_2 with surface species SiOH, $Si(OH)_2$, ≡ $SiCH_3$, =$SiOHCH_3$, =$Si(CH_3)_2$, $Si(OX)_4$, $Si(OSi)_3(OX)$ and $Si(OSi)_2(OX)_2$ in which X could be H, Si, Y or Zr. The surface hydroxyl groups provide sites for more siloxane adsorption which eventually lead to SiO_2 as the methyl groups are removed. A similar process has been reported by Kellberg and Pérez-Romo et al. for siloxane deposition on alumina [94,95]. This assumption is supported by the regions of silicon, carbon and oxygen shown in **Fig. 2.9**, **Fig. 2.11** and **Fig. 2.12**. These regions may represent siloxane that is partially intact. Eventually all of

the methyl groups are removed leading to silicon rich (no carbon) regions in **Fig. 2.7**. Finocchio et al. [83] reported that the presence of water can strongly reduce metal oxide adsorption capacity of siloxane even though it may provide more hydroxyl groups. One reason is that water has a higher tendency to adsorb compared to siloxane [72,83]. A higher concentration of water may also block hydroxyl group recovery path shown in equation (2.5), (2.6), and (2.7). More detailed mechanisms have not been revealed and still require further investigations. This phenomenon can explain the morphology analysis results in **Fig. 2.8** which illustrates that dry H_2+D4 experiment has more silicon deposition at the bottom of the anode than H_2+H_2O+D4 experiment. According to oxygen spillover mechanism [92], the CO electro-oxidation path is show in equation (2.9), (2.10), and (2.11) [96,97]. In this case, a higher concentration of CO can occupy sites on the Ni surface and block hydroxyl group recovery path in H_2 adsorption shown in equation (2.5). Less hydroxyl groups on the YSZ surface would reduce the siloxane adsorption and finally reduce the deposition. This also explains why less silicon deposition was observed in the H_2+CO+D4 experiment as shown in **Fig. 2.8**.

$$CO(g) + (Ni) \rightleftharpoons CO(Ni) \tag{2.9}$$

$$O_O^x(YSZ) + (YSZ) \rightleftharpoons O^-(YSZ) + V_O^{\cdot\cdot}(YSZ) + e^-(Ni) \tag{2.10}$$

$$CO(Ni) + O^-(YSZ) \rightleftharpoons CO_2 + (Ni) + (YSZ) + e^-(Ni) \tag{2.11}$$

Based on the siloxane adsorption mechanism for alumina and the electrochemical reactions in a Ni+YSZ anode, the proceeding discussion and experimental results provide

evidence for reaction equation (2.8). This mechanism can also explain the regions with only carbon deposition (no silicon deposition) observed in the experiments. Carbon deposition from direct use of methane with a Ni based anode is widely reported. Methane released from siloxane can result in carbon deposition on Ni. The possible deposition equation is shown in equation (2.12) [98,99]. It also can be supported by the carbon deposition region near the nickel particles in **Fig. 2.9** region 1. Methane, as the product of siloxane chemical adsorption and demethylation in equation (2.8), has an ability to penetrate through the anode and deposit on nickel even in the vicinity of YSZ electrolyte where there is more active electrochemical reactions. This possibility is supported by the existence of carbon deposition near the electrolyte in **Fig 2.11**. The carbon deposition can also provide an explanation for the large degradation in the H_2+D4 experiment which suffered more degradation compared with H_2+H_2O+D4 experiment. According to research by Koh et al. [100], supplying dry methane to Ni-YSZ anode would cause irreversible carbon deposition. In contrast, wet methane results in reversible deposition. Ni is also considered as an excellent catalyst for methane reforming reaction shown in equation (13), in which carbon in methane is converted to CO, thus avoiding deposit directly [101]. In this regard, H_2+H_2O+D4 experiment involving water in the fuel would have less carbon deposition and less anode degradation. All EIS results with dry fuel including H_2+D4 and H_2+CO+D4 experiment show that the rate of increase of ohmic resistance is proportional to the D4 concentrations. This can be explained by the proposed

step as carbon deposits on Ni which acts as the conductor in anode. Carbon deposition between the grain boundaries of Ni can lead to this increase in ohmic resistance.

$$CH_4 \rightarrow 2H_2 + C \quad (2.12)$$

$$CH_4 + H_2O \rightarrow 3H_2 + CO \quad (2.13)$$

The siloxane deposition investigation in this study suggests multi-step silicon deposition and also highlights the importance of carbon deposition. As shown, the complexity of the entire degradation process is enhanced dramatically. The degradation results should be analyzed comprehensively, not with silicon or carbon deposition individually. Under this premise, some inexplicable results presented before can be assessed. According to **Fig. 2.7** and **Fig. 2.11**, the silicon is mainly deposited near the bottom of the anode near the fuel inlet. However, significant carbon deposition is observed inside the anode due to methane transportation. The chemical adsorption of siloxane on the YSZ surface is the first step which should be responsible for initial anode degradation. Following the adsorption process, the siloxane is gradually converted to SiO_2. From the second step, the pores around the bottom of the anode shrink, which hinders gas delivery. Although these two steps cause anode degradation, compared with carbon deposition their position is far from the electrolyte where the main electrochemical active region is located. This may explain why the experiment with dry fuel had relative low degradation rate initially and higher degradation rate later due to carbon deposition. Water inhibits the carbon deposition which reduces the degradation

rate of experiments with wet fuel. The H_2+CO+D4 experiment has less silicon deposition, but the most performance degradation. This phenomenon may also result from carbon deposition originating from CO. Carbon deposition from CO can result from two different pathways shown in equation (2.14) and (2.15) [6].

$$2CO \rightarrow CO_2 + C \quad (2.14)$$

$$CO + H_2 \rightarrow H_2O + C \quad (2.15)$$

2.6 Conclusions

As a conclusion, in order to reveal the Ni-YSZ anode degradation behavior exposed to siloxane (D4), which is one of main impurities in biogas, long term experiments with H_2+H_2O, H_2+H_2O+D4, H_2+D4 and H_2+CO+D4 as fuels are reported. The electrochemical characterization and morphology results of different experiments were analyzed and compared to investigate the degradation phenomenon.

Based on electrochemical characterization results, the degradation rates of different experiments followed the sequence: H_2+D4+CO experiment > H_2+D4 experiment > H_2+H_2O+D4 experiment > H_2+H_2O experiment. The results also show that the initial degradation rates were more likely time dependent rather than D4 concentration dependent. Research on the reversibility of the deposition was also completed by inserting clean fuel recovery phases between different D4 concentrations with simulated bio-syngas (H_2+H_2O+CO+CO_2) as the fuel. As a result, the electrochemical and material characterization results show that the SOFCs performance degradation caused by D4

contamination is irreversible under clean bio-syngas.

According to morphology analysis the silicon deposition, which mainly occurred around bottom (fuel inlet) side of anode can be detected when the fuels were mixed with D4. The H_2+D4 experiment with dry fuel has more serious silicon deposition compared with H_2+H_2O+D4 experiment. The H_2+CO+D4 experiment has the lowest silicon deposition extent besides the H_2+H_2O experiment. Similar amounts of carbon deposition were also detected both at the bottom (fuel inlet) side and in vicinity of YSZ electrolyte. Except silicon and carbon depositing individually, the overlap of silicon, carbon and oxygen was also noticed, which indicated the combination of these elements possibly as intact siloxane.

The results presented contradict the previous Ni-YSZ SOFC anode degradation mechanism by siloxane, in which siloxane reacts with water and then deposits in the anode. The SOFC in the H_2+H_2O+D4 experiment of this study has less performance degradation and less silicon deposition than H_2+D4 experiment. In this situation, a multi-step degradation process could occur that involves siloxane adsorption and deposition in the anode. The methane released from siloxane adsorption process would cause carbon deposition on the Ni surface. More details and evidence for these steps are discussed in the following chapters. Generally, this chapter identifies the contradictions present in the previous studies and also provides some indirect evidence for degradation analysis. Furthermore, the silicon and carbon deposition are both considered as essential factors

resulting in anode degradation.

3 INFLUENCE OF Ni, YSZ, ZrO_2, AND Y_2O_3 FROM SOFC ANODES ON THE SILOXANE DEPOSITION PROCESS

3.1 Introduction

As discussed in the prior section, the fuel composition has a significant impact on the anode degradation process. Moreover, the anode material where the siloxane deposits is another essential factor requiring further investigation. The anode material may influence the siloxane deposition in electrochemical and catalytic aspects. The electrochemical oxidation of siloxanes may accelerate their deposition process in the anode [102]. However, the electrochemically active region of the anode supported SOFCs used in previous studies was far from the surface layer of the anode where the silicon mainly deposited. In this situation, it can be extrapolated that the catalytic reactions on the surface of porous anode are critical in siloxanes deposition process in addition to the electrochemical reactions. Further work is needed to understand the surface reactions occurring when siloxane is in the presence of common anode materials.

Ni-YSZ (yttria-stabilized zirconia) anode is selected as the research target anode in this study because of its wide application. In the Ni-YSZ anode, Ni provides excellent characteristics with high electronic conductivity and good catalytic activity for hydrogen/ oxygen reactions [33]. YSZ, which is the same material used for the electrolyte, can provide excellent mechanical strength and extended triple phase boundary (TPB) [72]. Based on the properties of Ni and YSZ, they may contribute to both the catalytic

reactions of the siloxane deposition and electrochemical reactions. Ni based catalysts are widely used in methane steam reforming and steam cracking in the petroleum industry [103,104]. Due to its suitable stability and mobility of absorbed atomic hydrogen and oxygen, it may also serve as a good catalyst for the reforming reaction of the methyl group and also Si-O and Si-C bond cleavage [33]. YSZ is rarely used directly as a catalyst. However previous research suggested that mixing YSZ with Ni as the catalyst promoter can improve the CH_4 and CO_2 conversion in reforming reactions attributing to surface oxygen vacancies increasing [105].

Besides YSZ, selectivity enhancement toward H_2 and CO have also been observed with the addition of Y_2O_3 in the Ni catalyst [106]. ZrO_2 supported Ni catalyst shows high catalytic activity and stability for CO_2 reforming of methane [107]. Vaiss and Finocchio reported that the hydroxyl groups on the metal oxide surface are critical to siloxane surface adsorption [82,83]. From M. Kogler et al. [91], the surface hydroxylation extents are different for YSZ, Y_2O_3 and ZrO_2, in which the hydroxylation degree of Y_2O_3 is much higher compared with YSZ and ZrO_2. As a result the catalytic properties of ZrO_2, Y_2O_3 and Ni for the siloxane deposition process should be studied individually. Identifying the material with the highest catalytic activity toward siloxane deposition may lead to the selection of alternative materials that can be utilized to avoid or relieve silicon poisoning.

Several techniques are available to assess the extent of siloxane deposition on ZrO_2, Y_2O_3, YSZ and Ni. For ZrO_2, Y_2O_3 and YSZ, due to compact structure, siloxanes are

deposited on the pellets' surface directly. The deposition extent can be compared with surface morphology techniques such as scanning electron microscope (SEM) combined with an energy-dispersive spectrometer (EDS) or wavelength-dispersive spectrometer (WDS) [8]. However, for the porous Ni pellet, the surface morphology analysis techniques such as SEM and WDS cannot be utilized as the single standard for deposition estimate due to siloxane penetrating through the pores. For an actual porous Ni-YSZ anode, H. Madi [65,72] and our previous study discussed in chapter 2 [84,108] had the SEM and WDS analysis on the SOFC cross-section to reveal the siloxanes deposition across the whole anode. Instead of the two-dimensional stereology method, J. R. Wilson et al. [109] firstly utilized Focused ion beams (FIBs)-SEM technique to obtain the three-dimensional Ni-YSZ microstructure. P. R. Shearing et al. [110] also applied FIB-SEM to reconstruct 3D microstructure of the SOFC anode and obtained geometric parameters for SOFC performance evaluation. In one anode degradation study, Z. Jiao et al. [111] investigated the initial fast degradation phenomena of SOFC anode performance by FIB-SEM 3D reconstruction. A. Zekri et al. [112] showed that FIB-SEM can offer reliable quantitative microstructure parameter analysis during anode degradation such as porosity and tortuosity increase and TPB density decrease. For silicon contamination, Y. Liu et al. [113] found SiO_2 segregation and accumulation around TPB due to ~100 ppm_v siloxane contamination using FIB and TEM. However, these imaging techniques are not cost-effective. Moreover, in-situ analysis cannot be achieved, and fuel cell samples must be

destroyed for 3D reconstruction studies. Some studies focused on quantitative analysis of SOFC anode microstructure by electrochemical impedance spectroscopy (EIS). Y. Zhang et al. [114] calculated the tortuosity factor of the anode gas diffusion process for the anode supported SOFCs by distribution of relaxation time (DRT) of EIS. Leonide et al. [53] estimated the ratio of porosity to tortuosity factor of Ni-YSZ anode using the Warburg element resistance which was attributed to the diffusion process in the anode and obtained by equivalent circuit model from EIS results. The modelling process has been optimized by combination with distribution of relaxation times which can separate individual polarization mechanism from the overall polarization resistance [49,53,115]. The EIS analysis, which can reveal the electrode microstructure characterization, can also be a supplemental reference for the siloxane deposition in the porous Ni material besides morphology analysis.

To improve the composition analysis and help reveal the underlying deposition process, pure Ni and YSZ pellets were exposed to the simulated biogas-reformate fuel with D4 contamination for deposition analysis. Besides YSZ, to develop a deeper understanding of how individual components in Ni-YSZ anode influence the siloxane deposition process, the ZrO_2, Y_2O_3 and Ni pellets were exposed to different gas mixtures with siloxane contamination. To utilize EIS to analyze the microstructure change during the siloxane deposition process, a YSZ and silver layer were added on the porous Ni pellet as the electrolyte and cathode, respectively. D4, as a typical siloxane used for

SOFCs contamination studies, was selected as the contamination source. Humidity as the variable utilized in our previous Ni-YSZ anode SOFCs and YSZ siloxanes contamination studies was also investigated in this work. In this regard, two gas mixtures fed to the YSZ, ZrO_2, Y_2O_3 and Ni were distinguished as H_2+N_2+H_2O+D4 (wet) and H_2+N_2+D4 (dry).

3.2 Fabrication and Methodes

Y_2O_3 (Yttrium oxide, 99.99% trace metals basis, Sigma-Aldrich), ZrO_2 (Zirconium oxide 99% trace metals basis, Sigma-Aldrich) and 8YSZ ($(ZrO_2)_{0.92}(Y_2O_3)_{0.08}$, Fuelcellmaterials) were die pressed to pellets. Then the YSZ pellet was sintered at 1400 °C for 4 hours to have a similar property with the YSZ in the SOFC's anode. For the pure Y_2O_3 and ZrO_2, stable sintered pellets are hard to obtain due to the large volume change from tetragonal to monoclinic phase. The Y_2O_3 and ZrO_2 pellets were calcinated at 1050 °C for 4 hours to ensure the pellets structural stability and identical initial surface conditions. After calcination, the Y_2O_3, ZrO_2 and YSZ pellets have ~ 300 μm thickness and ~ 16mm diameter. For the Ni pellet, NiO (NiO-F:NiO-S = 50:50 wt%, Fuelcellmaterials) were die pressed and pre-sintered at 1100 °C for 4 hours. Then the surface of the NiO pellet was sprayed by YSZ ($(Y_2O_3)_{0.08}(ZrO_2)_{0.92}$, spray dried grade powder, Fuelcellmaterials). The YSZ layer can serve as the electrolyte for the EIS test and also ensures that the NiO can be totally reduced to Ni during the testing without O_2

gas penetrating. The NiO and YSZ layers were co-sintered at 1400 °C for 4 hours. The YSZ layer on the NiO pellet was around 10 μm thick. Silver ink was printed on the YSZ layer surface with 0.712 cm^2 active area as the current collector and the cathode for EIS test.

The electrochemical impedance of the Ni pellet was measured by an electrochemical impedance analyzer (Solartron Analytical Energylab XM) utilizing four-probe method. The impedance measurements were conducted under open circuit condition (OCV) over a frequency range from 10^6 Hz to 0.1 Hz with 10 mV signal amplitude. After the measurement, the DRT method was applied to separate the transport and reaction processes from the EIS data. A MATLAB GUI program (DRTtools) was utilized for the DRT analysis [50,116,117]. In order to ensure good resolution and also avoid artificial peaks, the regularization parameter λ was selected from 10^{-4} to 10^{-2} based on the residual root-mean-square error (RMSE) value of the DRT calculation [44]. The sample number was 2000 for the Bayesian run.

As depicted in **Fig. 3.1**, the Ni, Y_2O_3, ZrO_2 and YSZ pellets were sealed on the top of a quartz tube with silver paste. As shown in **Fig. 3.1a** for the Ni pellet, the silver wires were connected to the Ni anode and silver cathode for the electrochemical characterization. The gas mixture of H_2 (ultra-high purity grade, Airgas), N_2 (ultra-high purity grade, Airgas), CO (ultra-high purity grade, Airgas), CO_2 (ultra-high purity grade, Airgas) and certified D4 (5.358 ppm_v, balanced with N_2, Airgas) were fed to the bottom

side of the pellets (anode side for the Ni pellet) to simulate the fuel of the SOFC. The steam was generated by vaporization of deionized H_2O which was controlled by a syringe pump (PumpSystems Inc.). To provide heat for the vaporization and maintain the gas phase, a resistive heater was wrapped on the H_2O delivery pipe. The delivery gas temperature was maintained at 120 °C and monitored by T-type thermocouples (Omega). The gas compositions and gas flow rate were controlled by Brooks Delta II smart mass flow controllers (MFCs) with LabView interface.

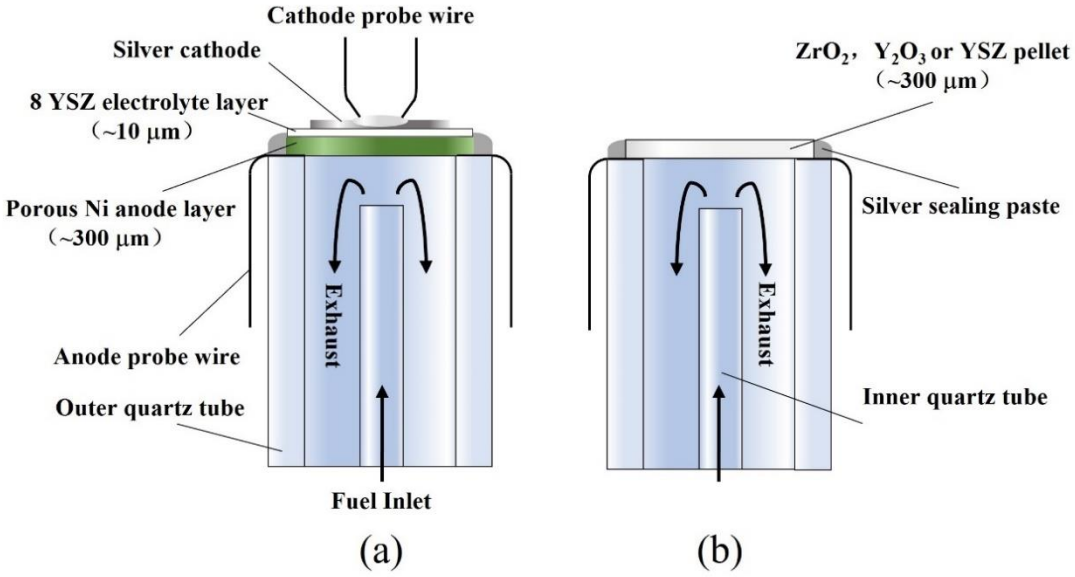

Figure 3.1 Schematic of pellet experiment setup (a) for Ni pellet and (b) for YSZ, ZrO_2 and Y_2O_3 pellet.

For the first step Ni and YSZ pellets bio-syngas experiment, the flow rates of H_2, H_2O, CO, and CO_2 were fixed at 5, 2, 2, and 1 standard cubic centimeter per minute (sccm), respectively. Those flowrates correspond to the gas component ratio of a

simulated biogas-reformate fuel [15]. To investigate the degradation process the sequence used is neither increment nor decrement. Three different concentrations were explored in the sequence of 1 ppm_v for 50 hours, 0.4 ppm_v for 50 hours and 2.5 ppm_v for 50 hours. The detailed concentrations of each component are show in **Table 3.1**. The NiO pellet was reduced for 3 hours with H_2 and N_2 mixture at flow rates of 10 sccm each. For the Ni pellet experiment the process was the same as the SOFC experiment. The YSZ pellet experiment skipped the reduction and intrinsic degradation phases.

Table 3.1 Flow rate of anode side gases for the anode materials experiments

Flow rates (sccm)	H_2	CO	CO_2	H_2O	N_2 (D4 conc. 0/1/0.4/2.5 ppm)	D4+N_2 (D4 conc. 0/1/0.4/2.5 ppm)
Ni pellet	5	2	1	2	10/6.517/8.607/1.294	NA/3.483/1.393/8.706
YSZ pellet	5	2	1	2	10/6.517/8.607/1.294	NA/3.483/1.393/8.706

For the subsequent study, the Ni, Y_2O_3 and ZrO_2 pellets were exposed to H_2+N_2+H_2O+D4 and H_2+N_2+D4 gas mixtures to investigate the impact of water on the siloxane depositions process. The gas composition and flow rates for both experiments are shows in **Table 3.2**. The total flow rate of the gas mixture was fixed at 20 standard cubic centimeters per minute (sccm) for each experiment. The D4 contamination was diluted to 2.5 ppm_v in this case. For all experiment, the top side of the pellets (cathode side for Ni pellet) were exposed to air. The quartz tube reactor was placed in the center of a vertical tubular furnace and heated to 750 °C at 5 °C per minute and held constant for

all experiments. Before starting the Ni pellet experiments, 20 sccm pure H_2 was fed to the anode side for 8 hours at 750 °C to ensure complete reduction of the Ni pellets.

Table 3.2 Flow rate (sccm) of anode side gases supplied to the pellets during the anode materials experiments

Pellets	Experiment conditions	H_2	H_2O	N_2	D4+N_2 Balance (2.5 ppm_v D4)
Ni	H_2+ N_2+D4	7	NA	3.67	9.33
	H_2+N_2+H_2O+D4	7	2	1.67	9.33
ZrO_2	H_2+ N_2+D4	7	NA	3.67	9.93
	H_2+N_2+H_2O+D4	7	2	1.67	9.93
Y_2O_3	H_2+ N_2+D4	7	NA	3.67	9.93
	H_2+N_2+H_2O+D4	7	2	1.67	9.93

A field emission scanning electron microscope (FESEM, JEOL JXA-8530F electron microprobe) equipped with an energy-dispersive spectrometer (EDS) and wavelength-dispersive spectrometer (WDS), was used for morphology analysis of the anode. The sample preparation process for morphology analysis has been reported in previous study [84]. WDS was selected for element mapping because of the overlapping of Y and Si signals in EDS. For the SEM and WDS analysis, 15 kV at 5×10^{-8} A was applied for the electron beam.

To characterize the silicon deposition phase, the samples were analyzed by X-ray diffractometer (XRD) system. The X-ray diffractometer (PANalytical X' Pert Pro MRD) with a Cu Kα (K-Alpha2/ K-Alpha2=0.5) source at 45 kV and 40 mA was used to scan continuously over the fuel cell anode surface in a 2 theta angle range 15-85° with 0.02° steps.

3.3 Thermodynamic Calculations

In order to determine the siloxane depositon composition theoretically, the software Factsage was utilized in this study. Due to functional limitations of Factsage and complexity of the siloxane depositon reactions in the SOFCs, predominance area diagrams of the Ni-O-Si-C-H and Zr-Y-O-Si-C-H systems at 750 °C are used to represent the D4 deposition reactions on the Ni and YSZ individually. The results are presented in **Fig. 3.2**. Ni_7Si_{13} is shown in **Fig. 3.2a** as the dominant silicon deposition product with Ni. From **Fig. 3.2b**, the formation of silicon deposits with ppm concentrations of D4 does not occur on YSZ. It is noteworthy that in both situations, the gas phase ketene (CH_2CO) can be generated following the solid phase deposition. This has not been reported in previous experiments likely due to instability of the ketene [118]. From the studies of siloxane deposition on metal oxides like alumina, mainly CH_4 is released in the process.

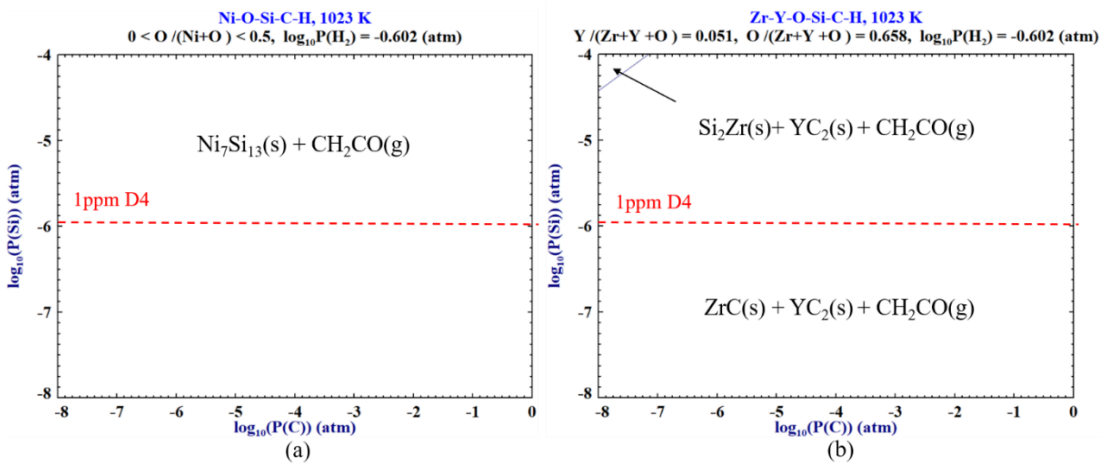

Figure 3.2 Predominance area diagrams at 750 °C for (a) the Ni-O-Si-C-H system and (b) the Zr-Y-O-Si-C-H.

3.4 Morphology and Composition Analysis

To investigate the deposition composition of siloxane in the SOFC's anode under the bio-syngas condition, XRD testing was utilized for the Ni and YSZ pellets before and after exposed to the H_2+H_2O+CO+CO_2+D4 mixed gases. As shown in **Fig. 3.3b**, the photo of the Ni pellet after the D4 exposure experiment, the color of the pellet has been converted from green as the NiO pellet in **Fig. 3.3a** to gray which indicates the NiO has been reduced to Ni. Furthermore, significant carbon deposition can be observed as the black shade in the middle of the pellet.

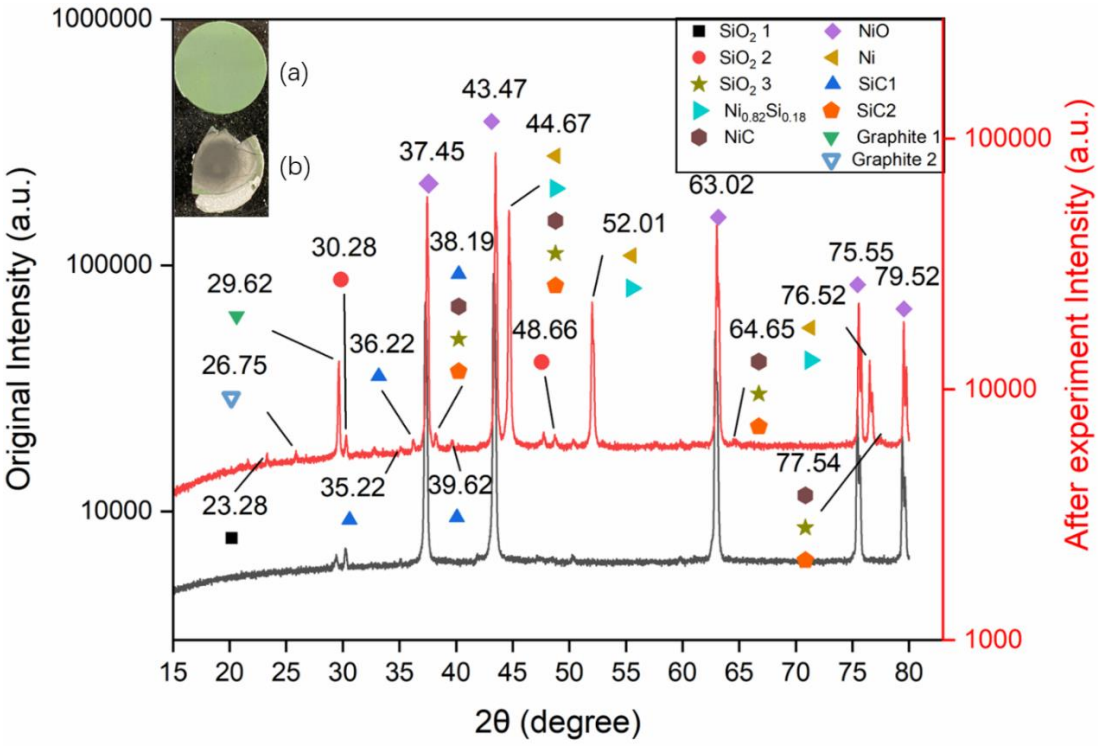

Figure 3.3 XRD patterns of Ni pellet bottom surface (fuel inlet side). Black line: before D4 exposure experiment. Red line: after D4 exposure experiment. (a) Figure of NiO pellet before the experiment. (b) Figure of Ni pellet after experiment.

Fig. 3.3 shows the XRD patterns of the Ni pellet before and after the D4 exposure experiment. The main diffraction peaks in the pellet sample before D4 exposure match with NiO (37.5°, 43.5°, 63.0°, 75.6° and 79.5° 2θ) very well. After the D4 exposure experiment, the Ni phase peaks at 44.7°, 52.0° and 76.52° (2θ) suggest that NiO was reduced, while the NiO peaks in the spectrum also means the co-existence of Ni and NiO phase. For the deposition composition, besides NiO/Ni, many weak peaks also can be observed in the spectrum in **Fig. 3.3**. The peak at 26.8° (2θ) appearing after experiment refers graphite. Meanwhile the largest peak for possible deposition is at 29.6° (2θ) also indicates graphite according to the methane reforming catalyst study of Ni [119]. These carbon peaks in XRD also can be proven by obvious black carbon deposition observed in the photo of pellet after experiment (**Fig. 3.3b**). For the silicon deposition, SiC, SiO_2 and $Ni_{0.82}Si_{0.18}$ are all possible from XRD result. Due to the overlap of $Ni_{0.82}Si_{0.18}$ and Ni peaks, the exist of this component cannot be verified. The peaks of two types of SiC can be detected after experiment at 35.2°, 36.2°, 38.2°, 39.6° (2θ) and 38.2°, 44.7°, 64.6°, 77.5° (2θ). Similarly, there are also three type of SiO_2 deposited on the pellet according to the relative peaks. After the experiment, the three new peaks at 23.3°, 30.3° and 48.7° (2θ) can be attributed to two types SiO_2, respectively. The third possible SiO_2 phase is overlapped with SiC at 38.2°, 44.7°, 64.6°, 77.5° (2θ). With same series of peaks at 38.2°, 44.7°, 64.6°, and 77.5° (2θ), NiC is also a candidate composition.

The photos of YSZ pellet before and after the D4 exposure experiment are show in

Fig. 3.4a and **b**. Compared with the pellet before experiment, a yellow color layer covered the bottom surface after the experiment. In **Fig. 3.4**, the XRD analysis of the YSZ pellets are also presented. The XRD patterns of the YSZ pellet before and after experiment show some interesting new peaks after experiment which may result from D4 deposition. Similar to the entire SOFC experiment, the new peaks located at 38.3°, 44.4°, and 64.47° (2θ) can be both attributed to SiO_2 and SiC. Other compositions like YC_2, ZrC and Si_2Zr, which are possible based on thermodynamic calculations, have not been found in XRD analysis.

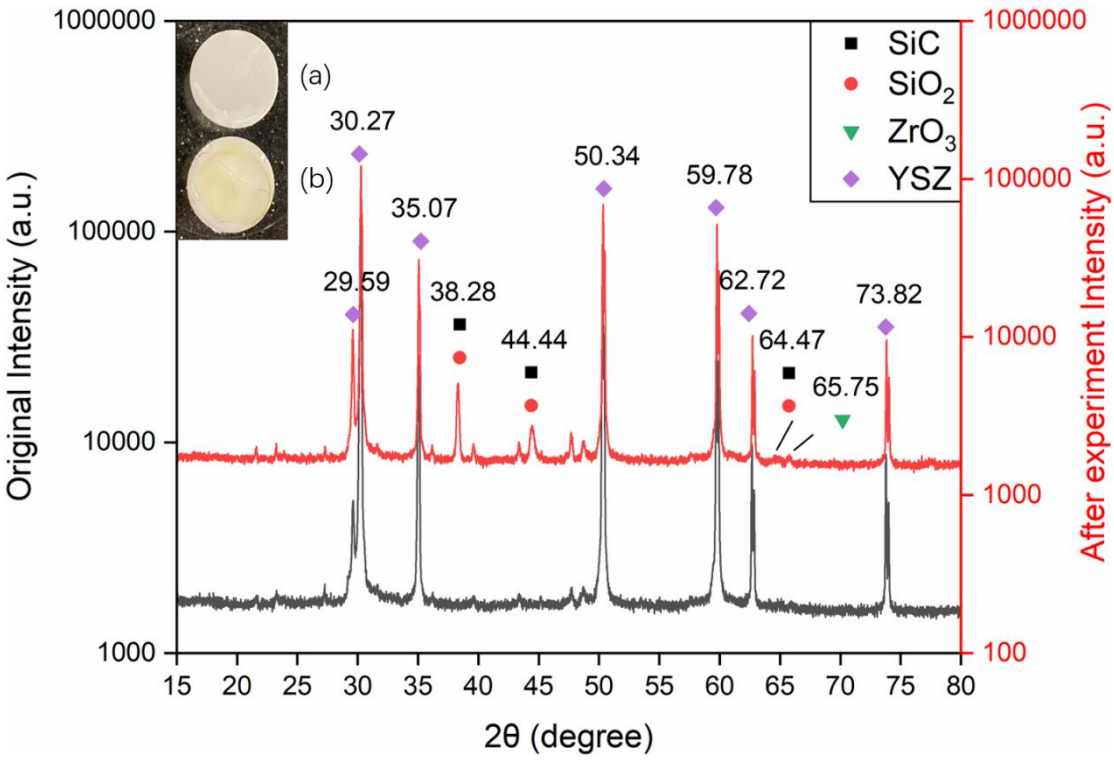

Figure 3.4 XRD patterns of YSZ pellet bottom surface (fuel inlet side). Black line: before D4 exposure experiment. Red line: after D4 exposure experiment. (a) Figure of YSZ pellet before the experiment. (b) Figure of YSZ pellet after experiment.

Besides XRD testing, thermodynamic calculations mentioned in previous section 3.3 may also be helpful for the deposition product determination. Due to lack of D4 thermodynamic property reference in Factsage, L2, the siloxane with simplest structure, is used as an alternative reactant in reaction calculation. The thermodynamic calculations in this part were also conducted by the software Factsage. **Table 3.3** shows the thermodynamic parameters of L2 and H_2O reactions which has been reported as the dominate siloxane deposition mechanism with γ-Al_2O_3 catalyst. For the products, several possible compositions were selected. Contradicted to the previous theories shown in **Table 3.3** equations (3.1a) in which CO is the final product for carbon oxidation, reaction equation (3.1b) shows that the reaction with CO_2 as the product has lower Gibbs free energy change at 1023 K. CH_4 also has be reported as the main gas phase product of the siloxane deposition with γ-Al_2O_3 catalyst and it has been approved by ^{13}C CP/MAS NMR test [82]. However, the Gibbs free energy change of reaction equation (3.1c) is still a littile bit larger than (3.1a) and (3.1b). Also considering the deposition compostions prediction by thermodynamic calculations in **Fig. 3.2**, the highest priority products cannot be found in XRD testing. All these realities which contradicted to the thermodynamic calculation demonstrate the CO_2 and SiO_2 may not be the only products for siloxane deposition reactions. Catalytic and kinetic factors may have a significant impact on the siloxane depostion reactions. In this situation, the reaction equation 3.1d in which the L2 depostion reaction with SiC as the product has much higher Gibbs free energy change

may also happen under these conditions.

Table 3.3 Thermodynamic parameters of L2 and H_2O reactions at 1023 K.

	Reactions	Δrxn G (kJ/mol)
3.1a	$C_6H_{18}OSi_2+9H_2O\rightarrow 6CO+2SiO_2+18H_2$	-1109.10
3.1b	$C_6H_{18}OSi_2+15H_2O\rightarrow 6CO_2+2SiO_2+24H_2$	-1122.59
3.1c	$C_6H_{18}OSi_2+3H_2O\rightarrow 6CH_4+2SiO_2$	-1045.85
3.1d	$C_6H_{18}OSi_2+7H_2O\rightarrow 4CO_2+2SiC+16H_2$	-520.73

Besides reacting with H_2O, siloxane can also participate in the electrochemical reaction in the SOFCs. **Table 3.4** shows the thermodynamic parameters of L2 electrochemical oxidation in the anode at 1023 K. Compared with H_2O reactions, L2 electrochemical oxidation reactions have much lower change of Gibbs free energy which indicates their higher priority thermodynamically. Similar to the H_2O reactions, the reaction with CO_2 and SiO_2 as products has the lowest Gibbs free energy change. However, reaction with CO and SiO_2 as products has the highest electrochemical potential which indicates the highest energy potential for each electron. Generally, reactions with SiC as the product have relatively low electrochemical potential comparing with SiO_2. From electrochemical perspective, with polarization voltage around 0.6 V, there would be sufficient O^{2-} supply on the YSZ surface in the fuel cell. SiO_2 should be the most likely silicon composition in this situation. Meanwhile some

researchers also reported that SiO_2 forms on the YSZ surface in electrochemical reactions with silicon compositions impurity contamination [120–122]. However, due to the complexity of siloxane electrooxidation reactions shown in **Table 3.4**, they are unlikely to occur in one step. Multi-step electrooxidation reactions may take place in this process. Ni as an outstanding C-H cleavage catalyst may promote dehydrogenation reactions of methyl groups in the siloxane shown in the reaction (3.3), (3.4) [123].

$$R - CH_3 \rightarrow R \equiv C + \frac{3}{2}H_2 \quad (3.3)$$

$$H_2 + O^{2-} \rightarrow H_2O + 2e^- \quad (3.4)$$

Table 3.4 Thermodynamic parameters of L2 electrochemical oxidation in the anode at 1023K.

	Reactions	Δrxn G (kJ/mol)	E (V)
3.2a	$C_6H_{18}OSi_2+12O_2 \rightarrow 6CO_2+2SiO_2+9H_2O$	-5715.75	1.23
3.2b	$C_6H_{18}OSi_2+8O_2 \rightarrow 4CO_2+2SiC+9H_2O$	-3582.39	1.16
3.2c	$C_6H_{18}OSi_2+9O_2 \rightarrow 6CO+2SiO_2+9H_2O$	-4553.97	1.31
3.2d	$C_6H_{18}OSi_2+6O_2 \rightarrow 4CO+2SiC+9H_2O$	-2807.98	1.21

In this situation, the dehydrogenation of methyl groups would result in carbon deposition and SiC formation around the Ni. This can be proven by the XRD results of Ni pellet (**Fig. 3.3**) in which graphite and SiC 1,2 without signal overlap can be observed.

From the pellet experiment XRD results and SOFC SEM/WDS results, they all point

out that the silicon deposition is more associated with YSZ which agrees with previous studies that show siloxane adsorbs on the surface of metal oxides like Al_2O_3. The carbon deposition from siloxane is associated with Ni. As mentioned before, the D4 deposition compositions in the SOFCs' anode at 38.19°, 64.50°, and 77.38° (2θ) cannot be determined because of the overlapping of SiC, SiO_2 and NiC. According to the XRD test results of Ni and YSZ pellets, the same peaks also can be detected. Due to absence of Ni element, the peaks cannot be NiC in pure YSZ pellet experiment. As a result, it is highly possible that the NiC does not exist in the anode of the SOFCs. Carbon deposition shown in **Fig. 3.3** at 29.6° is overlapping with YSZ in the entire SOFC's XRD results in **Fig. 2.13** in previous chapter indicating that graphite may also exist in the anode and YSZ pellet.

From section (b) of **Fig. 3.4**, the deposition appears as a yellow/brown color. Due to the interactions of light waves with atoms and their electrons, the color of one semi-conductor material can be determined by its band gap [124]. For 3C-SiC, which correlates to the XRD peaks with 3.26 eV bandgap value, its color should be in the range of yellow to green [125]. The color coincidence of SiC and deposition products suggests the possibility of the existence of SiC. SiO_2 is always reported as white or colorless crystalline. However, for the small particles, light scattering can also change the color to yellow. As a result, the existence of SiO_2 cannot be determined by color [126].

In this case, the carbon deposition shown in **Fig. 2.12** and the appearance of SiC in

XRD results instead of only pure SiO_2, which is more stable thermodynamically, indicate that carbon deposition is an essential factor in siloxane deposition. This is not surprising as there are more carbon atoms than silicon in D4 siloxane. In previous studies, only silicon deposition was the main consideration. In order to eliminate the influence of other carbon source such as CO and CO_2 in the fuel, a YSZ pellet experiment with only H_2, N_2, and D4 (2.5 ppm) as fuel was conducted for 48 hours of exposure. The bottom side (fuel inlet side) surface of spent YSZ pellet is shown in **Fig. 3.5**. Carbon deposition can be observed with black to yellow color which confirms the possibility of siloxane as a source of the carbon deposited.

Figure 3.5 Bottom (fuel inlet) side of YSZ pellet after 48 hours H_2+N_2+D4 (2.5 ppm) experiment at 750 °C.

From the XRD and thermodynamic analysis, the deposition of siloxane under bio-syngas (H_2+H_2O+CO+CO_2+D4) can be initially identified. However, there are also some uncertainties that remain. The siloxane deposition SiO_2 and SiC can both be detected from Ni and YSZ pellet by XRD testing. The roles YSZ and Ni play in siloxane deposition reaction still need to be investigated. To reveal more details in the siloxane deposition process, Ni, ZrO_2, and Y_2O_3 pellets were exposed to H_2+N_2+H_2O+D4 (wet) and H_2+N_2+D4 (dry) gas conditions to investigate their affinity and tolerance for siloxane degradation. In this case, surface morphology analysis of these pellets after long-term and high concentration siloxane contamination was conducted. In general, ZrO_2 has low surface hydroxylation extent and inactive catalytic properties [91]. As shown in **Fig. 3.6**, only subtle silicon and carbon deposition on the pellet can be noticed after exposure to the D4 contamination for 72 hours at 750 °C. Comparing the H_2+N_2+H_2O+D4 (**Fig. 3.6 a**) and H_2+N_2+D4 (**Fig. 3.6 b)** experiments, the WDS elemental mapping shows there is heavier silicon and carbon deposition after involving water in the simulated fuel. In **Fig. 3.7**, there is also limited silicon and carbon deposition observed in the SEM-WDS results for Y_2O_3 pellets. The silicon and carbon signals for the pellet after the H_2+N_2+H_2O+D4 experiment are slightly stronger than the pellet after the H_2+N_2+D4 experiment which are presented in **Fig. 3.7 a** and **Fig. 3.7 b**, respectively. Comparing the morphologies of ZrO_2 and Y_2O_3 pellets after H_2+N_2+H_2O+D4 and H_2+N_2+D4 experiments with the clean pellets in **Fig. 3.8**, the microstructures didn't show significant change during the experiments,

although carbon and silicon signal is higher for the ZrO_2 and Y_2O_3 pellets in the wet fuel experiment.

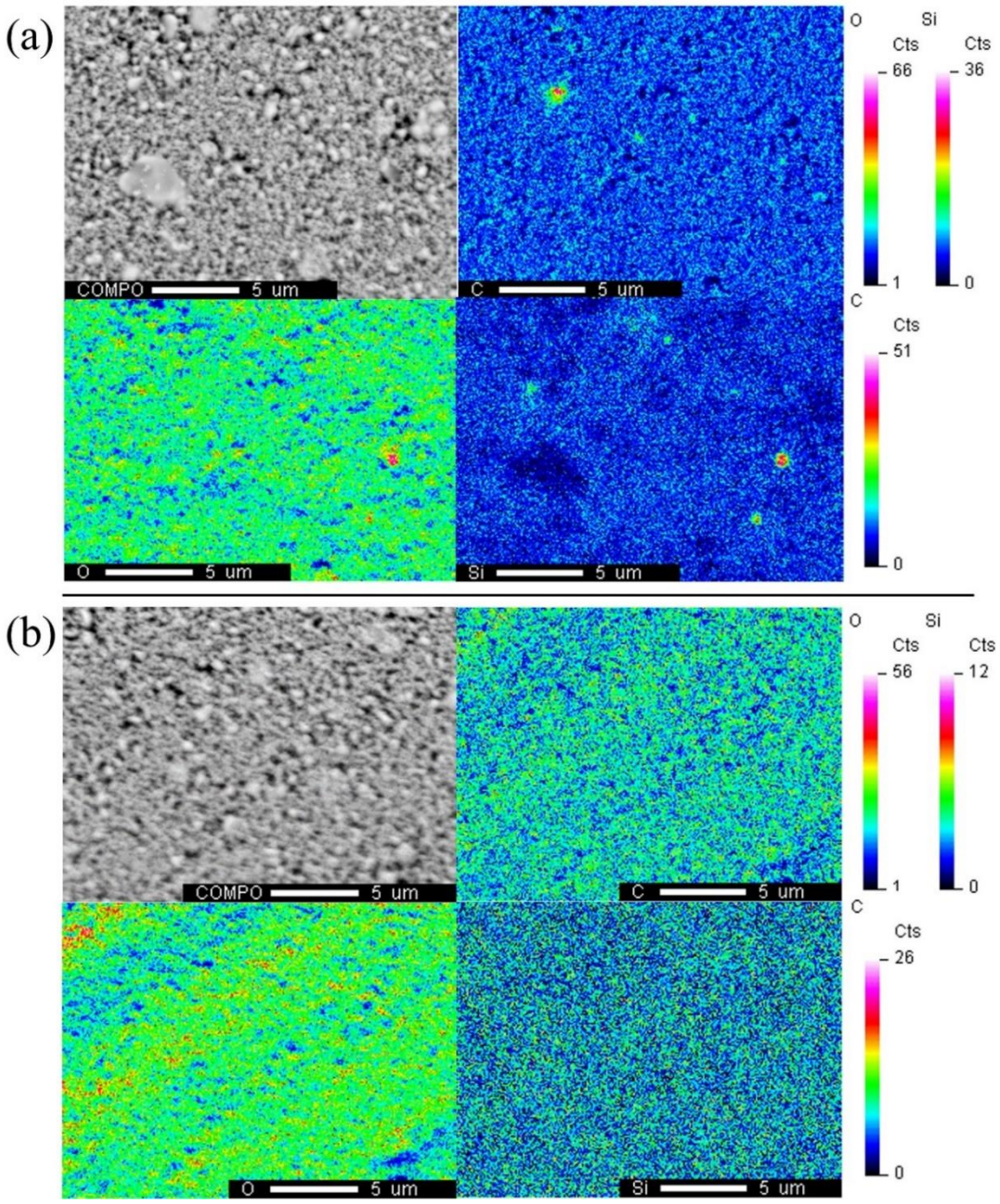

Figure 3.6 SEM/WDS elemental mapping of the surface of the ZrO_2 pellets after 72 hours (a) H_2+N_2+H_2O+D4 and (b) H_2+N_2+D4 experiments at 750 °C.

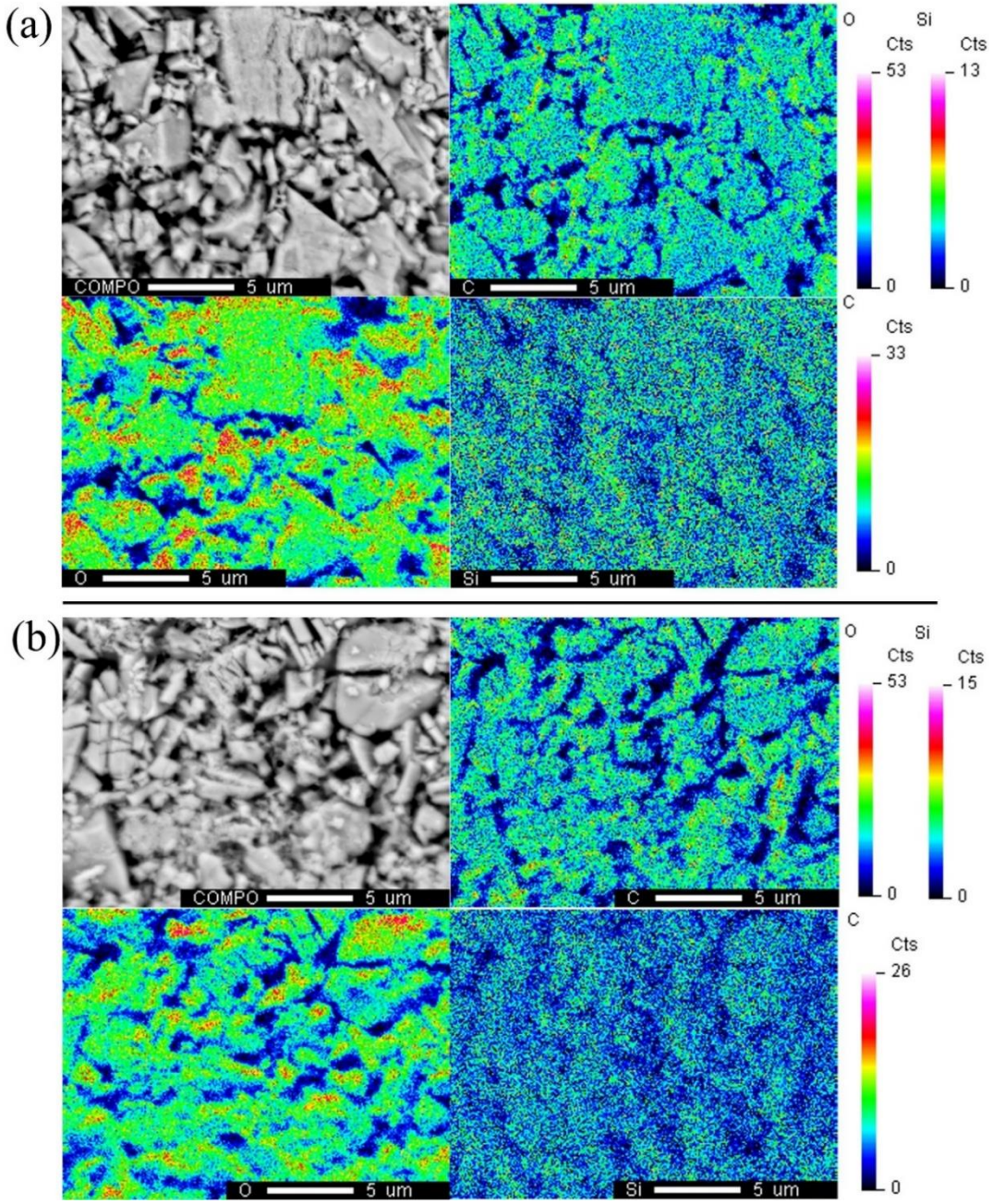

Figure 3.7 SEM/WDS elemental mapping of the surface of the Y_2O_3 pellets after 72 hours (a) H_2+N_2+H_2O+D4 and (b) H_2+N_2+D4 experiments at 750 °C.

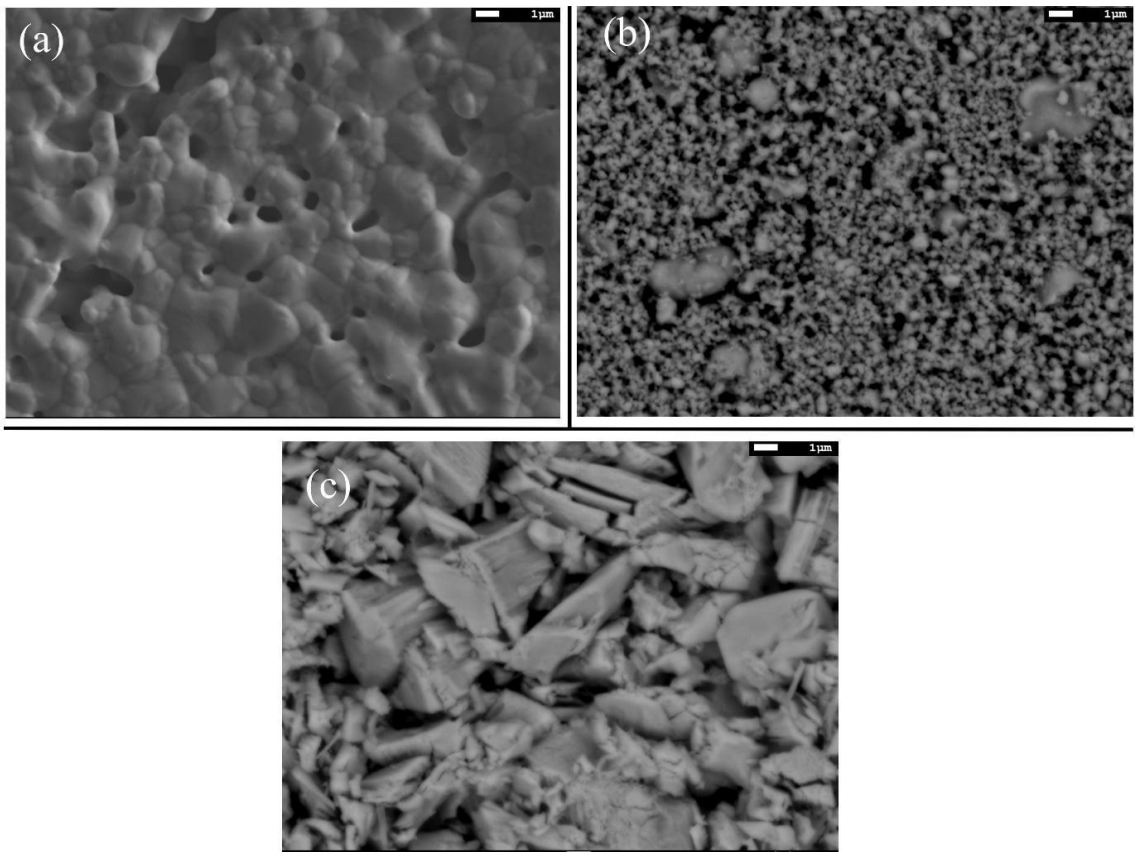

Figure 3.8 SEM image of (a) clean Ni pellet, (b) clean ZrO_2 pellet and (3) clean Y_2O_3 pellet.

Fig. 3.9a shows the surface morphology and element distribution for the Ni pellet after exposure to the H_2+N_2+H_2O+D4 mixture gas. Similar to the ZrO_2 and Y_2O_3 pellets, only limited amounts of silicon and carbon deposition can be found. However, in the dry fuel (H_2+N_2+D4) Ni pellet experiment, significant microstructure difference can be noticed from the SEM result in **Fig. 3.9b** compared with the clean pellet in **Fig. 3.8**. The 2-dimensional micrometer level flake crystals were growing on the surface of the Ni pellet. From the WDS results, the composition of the crystal should be SiO_2. The location of the SiO_2 crystal appears to be aligned with the porous substrate layer. The overlapping

carbon, silicon and oxygen signals indicate that the substrate layer may consist of partially decomposed siloxanes adsorbed on the surface of the Ni pellet which includes Si-O-C elements.

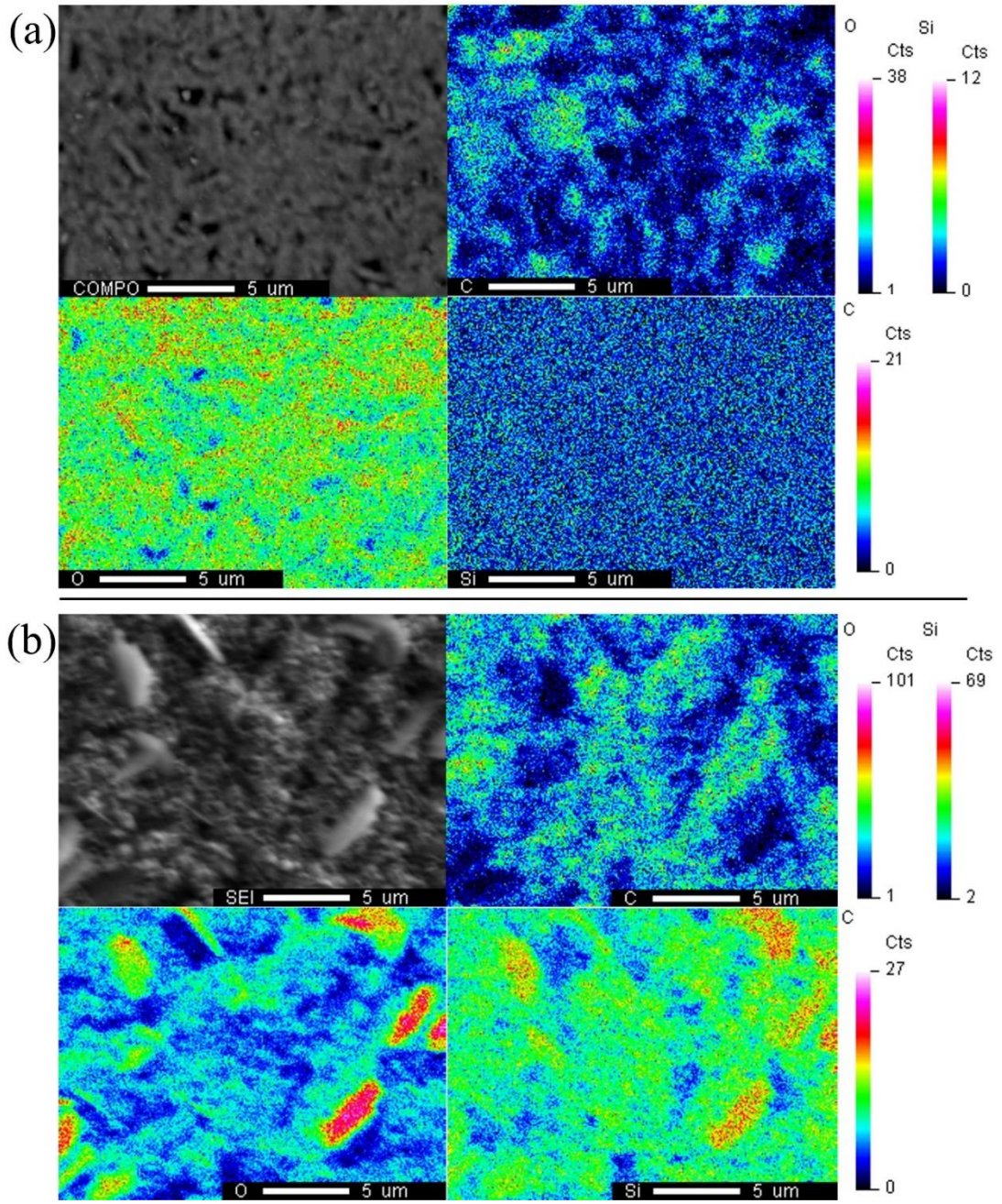

Figure 3.9 SEM/WDS elemental mapping of the surface of the Ni pellets after 72 hours (a) H_2+N_2+H_2O+D4 and (b) H_2+N_2+D4 experiments at 750 °C.

3.5 Electrochemical Characterizations

For the first step bio-syngas experiment, due to the complexity of the NiO-YSZ anode composition, the siloxane deposition and related processes cannot be revealed adequately with only thermodynamic analysis of the anode. To overcome these challenges, Ni and YSZ, as two main components of the anode, were fabricated as pellets and used in siloxane exposure experiments. D4 was mixed into syngas and the concentration was varied throughout the test with the sequence of 1 ppm_v, 0.4 ppm_v and 2.5 ppm_v. The EIS results of pellet experiments are shown in **Fig. 3.10**. Even though the main purpose of the pellet experiment is for XRD testing, the EIS results of the pellet experiment under the same test conditions as the SOFC can illustrate the electrolyte and anode changes during the degradation process. The degradation of pellets under D4 contamination can be observed clearly by impedance increase on the Nyquist plots. One phenomenon observed at low frequency is the Ni pellet experienced a large resistance increase compared to YSZ results. The obvious ohmic resistance increase for the Ni pellet experiment is likely due to the carbon deposition process reported by previous carbon deposition studies for the SOFC [127,128]. For the YSZ pellet the ASR increase may be attributed to the barrier of oxygen ion conduction because of the silicon and carbon composition coverage of the pellet surface. In the SOFC, similarly to the pellet, the YSZ part in the triple phase boundary may also be covered, eventually, resulting in the performance degradation.

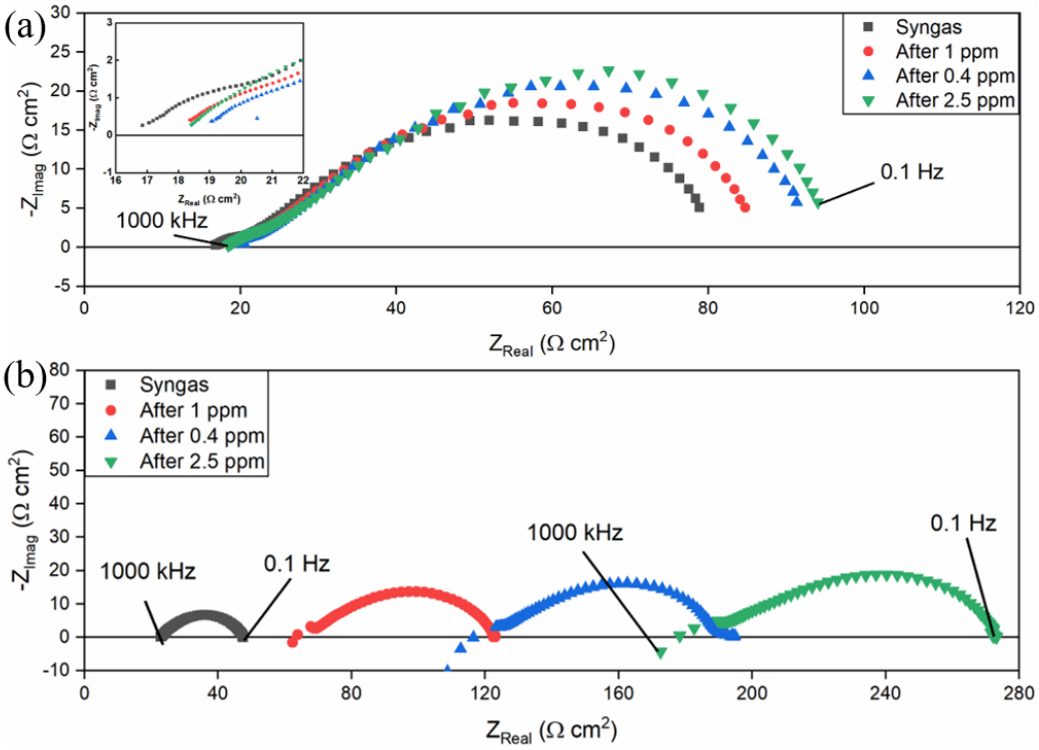

Figure 3.10 EIS results of the pellets. (a) Nyquist plots of YSZ pellet EIS measurements; (b) Nyquist plots of Ni pellet EIS measurements.

Table 3.5 and **Table 3.6** are the detailed EIS quantitative analysis based on the data in **Fig. 3.10**. Similar to SOFC's experiment results, the degradation showed greater time dependence rather than D4 concentration dependence. For the Ni pellet experiment, the percent increase of ASR in different concentrations are almost identical. The ohmic resistance percentage increase declined with time. The ASR and ohmic resistance increase for YSZ were relatively large initially and decreased with time.

Table 3.5 Area specific resistance (ASR) percent increase calculated from Ni and YSZ pellets characterization results

ASR increasing percentage (%)	1ppm	0.4ppm	2.5ppm
Ni pellet experiment	158.66	58.05	40.49
YSZ pellet experiment	7.39	7.8	2.95

Table 3.6 Ohmic resistance percent increase calculated from Ni and YSZ pellets characterization results

Ohmic resistance increasing percentage (%)	1ppm	0.4ppm	2.5ppm
Ni pellet experiment	179.34	82.15	53.08
YSZ pellet experiment	9.01	3.72	-3.37

3.6 Deconvolution by Distribution of Relaxation Times Technique

The electrochemical characterizations of Ni and YSZ pellet under H_2+H_2O+CO+CO_2+D4 gases demonstrated the rough degradation trend due to siloxane deposition. In this section, the Ni pellet degradation process under the H_2+N_2+H_2O+D4 (wet) and H_2+N_2+D4 (dry) gas conditions can be analyzed with assistance of DRT technique.

Although the Ni pellet's SEM results have already shown the microstructure and morphological changes from different experimental conditions, they can only exhibit the surface properties instead of overall porous structure change. To gain a further understanding of how siloxane deposition influences the performance of porous SOFC anodes whose main component is Ni, EIS was applied for Ni pellet degradation analysis. A thin layer of YSZ electrolyte and silver cathode were added to Ni pellet to form an

entire cell for the test. According to the accuracy characterization of the electrochemical impedance analyzer, the measurement uncertainty of EIS results is ± 0.2% at operation frequency range and impedance. **Fig. 3.11** and **Fig. 3.12** show the electrochemical analysis results for the Ni pellet experiments with H_2+N_2+H_2O+D4 and H_2+N_2+ D4, respectively. From **Fig. 3.11b** and **Fig. 3.12b**, the apparent impedance increase as a result of D4 contamination can be verified. With the same trend of SEM-WDS results, the cell exposed to H_2+N_2+D4 has much larger impedance increasing compared with the cell exposed to H_2+N_2+H_2O+D4.

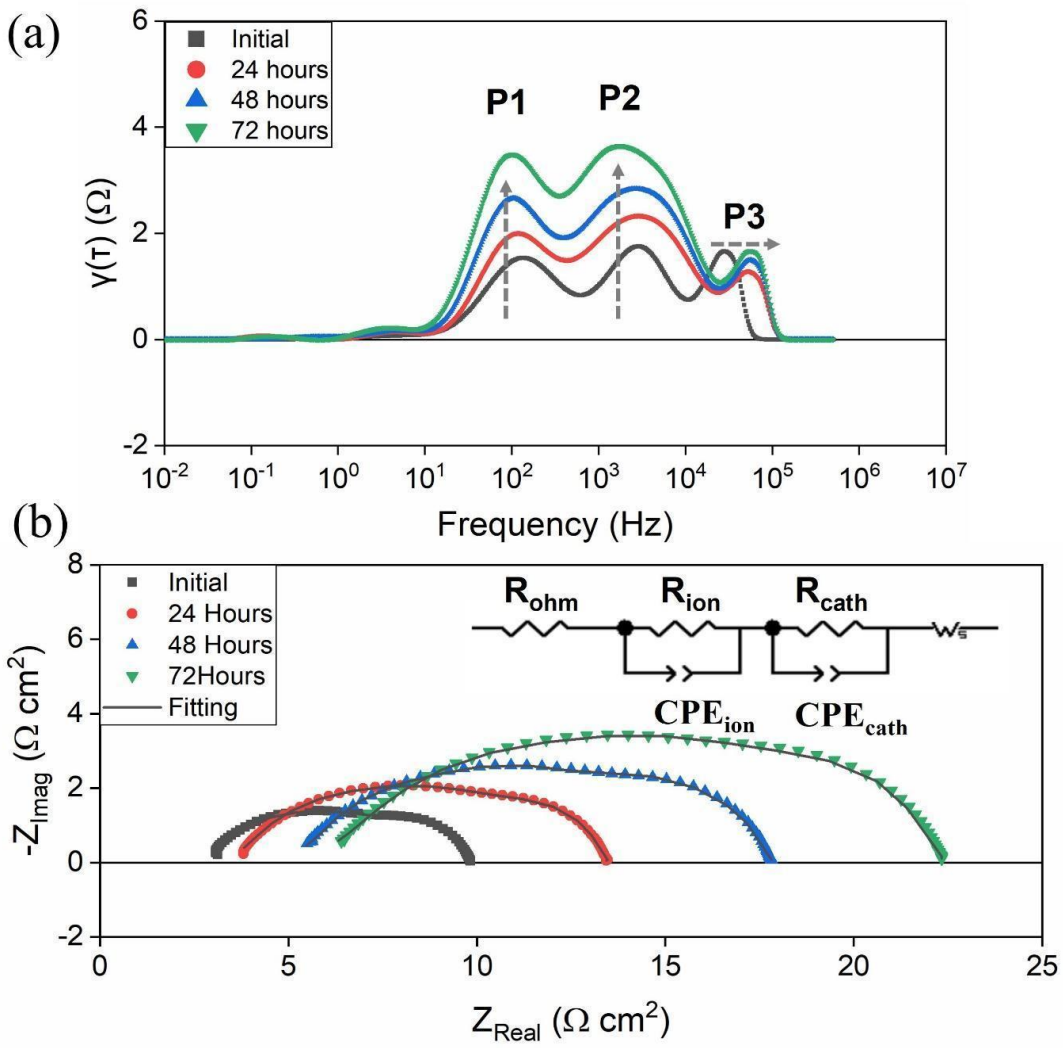

Figure 3.11 Electrochemical analysis of the Ni pellet during the H_2+N_2+H_2O+D4 experiment at 750 °C. (a) DRT plot; (b) EIS and equivalent circuit fitting results.

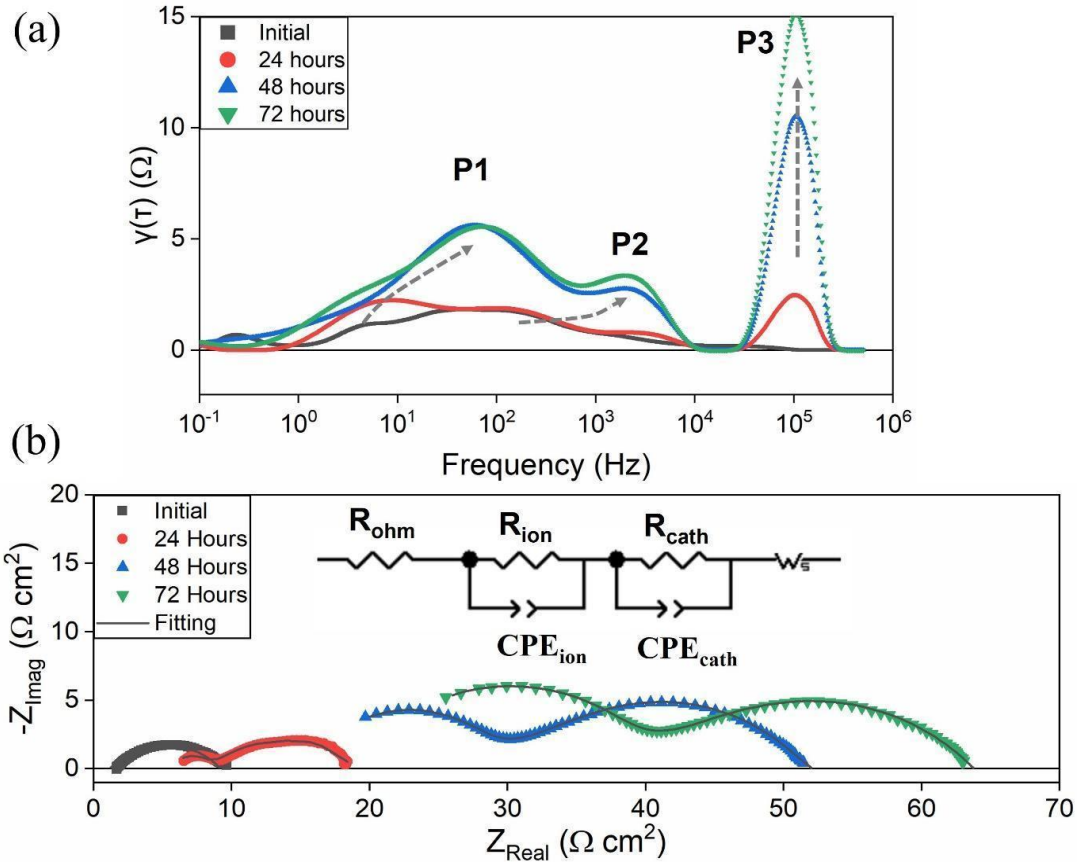

Figure 3.12 Electrochemical analysis of the Ni pellet during the H_2+N_2+D4 experiment at 750 °C. (a) DRT plot; (b) EIS and equivalent circuit fitting results.

Due to the combination of transfer and reaction processes merging together in the impedance spectrums, DRT analysis was utilized to separate these processes. As a result, three distinguished peaks were identified, namely P1, P2 and P3. Regarding the Ni pellet experiment, which can be comparable to an anode supported SOFC, the high anode diffusion polarization loss was expected due to slow gas diffusion process in thick, porous anode. Moreover, the anode was made by pure Ni without any YSZ which means the anode support layer (ASL) must be much thicker than anode active layer (AAL). In this situation, also considering the very thin electrolyte and cathode, the anode diffusion

process must be the largest and the slowest in DRT results. Also according to the frequency (10-100 Hz), P1 can be considered as the gas diffusion process for the anode [129]. Based on previous silver cathode SOFC and anode supported SOFC studies, the P2 at medium frequency (1 kHz to 10 kHz) is attributed to the cathode oxygen surface adsorption or bulk diffusion of O^{2-} [129–131]. As the fastest process, P3 at high frequency (> 10 kHz) is related to the ionic conductivity [46,86,87,129].

3.7 Equivalent Circuit Modeling Analysis

Based on the separation of the polarization processes from DRT analysis, an accurate equivalent circuit model consisting of four series connected elements can be developed (insert in **Fig. 3.11b** and **Fig. 3.12b**). The anode diffusion process P1 in the DRT results was modeled by a finite-length Warburg (FLW) element denoted Ws in the circuit. The processes P2 and P3 which represent the cathode diffusion/ oxygen surface adsorption and ionic conductivity were molded as the two RQ elements. They were denoted as R_{cath} and R_{ion}, respectively, in the circuit. A resistance R_{ohm} was added to the circuit for the ohmic loss of the Ni pellets. Besides three main peaks, one small peak at very low frequency (0.1 to 10 Hz) also can be noticed from the DRT results. According to a previous study [44], this peak can be attributed to the diffusion process due to the lowest frequency or the randomly distributed artificial peaks which always appear at very high or low frequency. Considering its small peak area compared with other three main peaks, the influence of these small peaks can be ignored for the equivalent circuit analysis. As a

result, it was not considered in the modeling process.

The nonlinear least squares (CNLS) algorithm fitting of EIS results was carried out by a commercial software ZView. As the CNLS-fitting results are highly initial value dependent, the approximated initial fitting parameters of each individual element needs to be estimated [53]. In this work, the initial resistance values for each element were pre-determined according to their peak area percentages in DRT results which should be proportional to the resistance of the corresponding processes [132]. The fitting results are shown in **Fig. 3.11b** and **Fig. 3.12b** with EIS results. For all ECM fitting results, χ^2 values were below 0.001. The detailed resistance values of each element are listed in **Table 3.7**. From **Fig. 3.11a** and **Table 3.7**, the polarization resistances of H_2+N_2+H_2O+D4 experiment related to the anode diffusion process P1 and cathode diffusion/ oxygen surface adsorption process P2 increase linearly following time. No obvious trend in ionic conductivity process (P3) polarization resistance is observed. For the Ni pellet with H_2+N_2+D4 fuel supplied, according to **Fig. 3.12a** and **Table 3.7**, a significant resistance increase is observed for the anode diffusion process (P1) during 0 to 48 hours degradation. However, from 48 to 72 hours, the anode diffusion resistance increased slowly. The cathode related process (P2) for the dry fuel experiment kept increasing following time similar to the H_2+N_2+H_2O+D4 experiment. The ionic conductivity process (P3) for the H_2+N_2+D4 experiment needs further analysis and discussion. Unlike the H_2+N_2+H_2O+D4 experiment in which the value kept relatively stable during the 72

hours, the ionic conductivity polarization resistance increased dramatically with the dry fuel. Connected with the much larger anode diffusion polarization resistance increase for the dry fuel experiment, it can be inferred that the deposition of the siloxanes may penetrate the whole anode supported layer and reach the active anode layer near the YSZ electrolyte. Meanwhile, the unchanged ionic conductivity process for wet fuel experiment may demonstrate that the deposition of the siloxanes only happened near the surface region of the Ni pellet. The ohmic resistance increasing can also be noticed both in H_2+N_2+H_2O+D4 and H_2+N_2+D4 experiment. Similar to polarization resistances, the dry fuel experiment also has larger ohmic resistance increasing than wet fuel experiment. This can be explained by the deposition of siloxanes on Ni who acts as the conductor in anode. In this regard, siloxane deposition between the grain boundaries of Ni can block conductive network and lead to the ohmic resistance increasing.

Table 3.7 Equivalent circuit fitting results from EIS results

Experiment Conditions	Time	R_{ohm} (Ω)	R_{ion} (Ω)	R_{cath} (Ω)	R_W (Ω)	τ/ε
Ni+H_2+N_2+ H_2O+D4	Initial	3.62	2.25	4.25	3.69	659
	24 h	4.93	1.61	7.63	5.10	913
	48 h	6.67	1.82	9.9	6.84	1230
	72 h	8.02	2.00	13.32	8.91	1590
Ni+H_2+ N_2+D4	Initial	1.71	2.71	7.27	1.38	802
	24 h	7.45	3.83	7.48	7.28	4230
	48 h	21.83	15.67	9.66	25.78	15000
	72 h	22.90	24.03	10.76	31.6	18400

Besides simply comparing the gas diffusion resistance R_W from FLW elements in an

equivalent circuit model, the microstructure change of porous Ni pellets during siloxane contamination can be revealed from calculation. The Stefan-Maxwell diffusion mechanism is dominant in the process when the gas mixture diffuses through the SOFC porous anode [114]. As a result, the polarization resistance for gas transport at open circuit can be theoretically given by equation (3.3) and equation (3.4) which applies for H_2-N_2 and H_2-H_2O-N_2 systems, respectively [53,114].

$$R_W = \frac{\tau}{\varepsilon}\left(\frac{RT}{2F}\right)^2 \frac{L}{P}\frac{1}{D_{H_2,N_2}}\left[\frac{1}{\chi_{H_2}} + \frac{1}{\chi_{N_2}}\right] \tag{3.3}$$

$$R_W = \frac{\tau}{\varepsilon}\left(\frac{RT}{2F}\right)^2 \frac{L}{P}\left[\frac{1}{\chi_{H_2O}}\left(\frac{\chi_{H_2}}{D_{H_2,H_2O}} + \frac{\chi_{H_2O}}{D_{H_2,H_2O}} + \frac{\chi_{N_2}}{D_{H_2O,N_2}}\right) + \frac{1}{\chi_{H_2}}\left(\frac{\chi_{H_2}}{D_{H_2,H_2O}} + \frac{\chi_{H_2O}}{D_{H_2,H_2O}} + \frac{\chi_{N_2}}{D_{H_2,N_2}}\right)\right] \tag{3.4}$$

Here τ is the tortuosity factor for anode diffusion process, ε is the porosity of Ni pellet, L is the diffusion length which is the thickness of the Ni pellet, P is the pressure of anode side gas (atmosphere pressure in this study), χ_{H_2}, χ_{H_2O}, χ_{N_2} are molar fraction of the H_2, H_2O, N_2 in the mixture gas, D_{H_2,N_2} is the binary diffusion coefficient between the H_2 and N_2 at 750 °C, D_{H_2,H_2O} is the binary diffusion coefficient between the H_2 and H_2O at 750 °C, and D_{H_2O,N_2} is the binary diffusion coefficient between the H_2O and N_2 at 750 °C. The values of D_{H_2,N_2}, D_{H_2,H_2O} and D_{H_2O,N_2} were selected as 1.96, 3.71, 1.12 cm^2s^{-1}, respectively, which can be obtained from the work accomplished by Y. Zhang et al. [114].

From the gas diffusion polarization resistance equations (3.3) and (3.4), the ratio of the tortuosity factor to porosity, τ/ε, is a valuable parameter for electrode microstructure

quantification and can be calculated. For the porous Ni pellet in this study, the tortuosity factor would be larger and porosity value would be smaller, if much heavier siloxanes deposition happened. This is expected because the silicon and carbon deposition would block the pores and extend the pathway for the diffusion process. In other words, the more serious deposition in the porous Ni pellet, the larger the τ/ε value would be. In **Fig. 3.13**, the change in the τ/ε with time and its corresponding resistance are shown. As expected, the τ/ε value is proportional to its related diffusion polarization resistance value. Much faster growth of τ/ε value for the Ni pellet in the H_2+N_2+D4 experiment is observed compared to the H_2+N_2+H_2O+D4 experiment demonstrating severe degradation and heavier deposition happened in the Ni pellet. This phenomenon can also be proved by the previous SEM/WDS results.

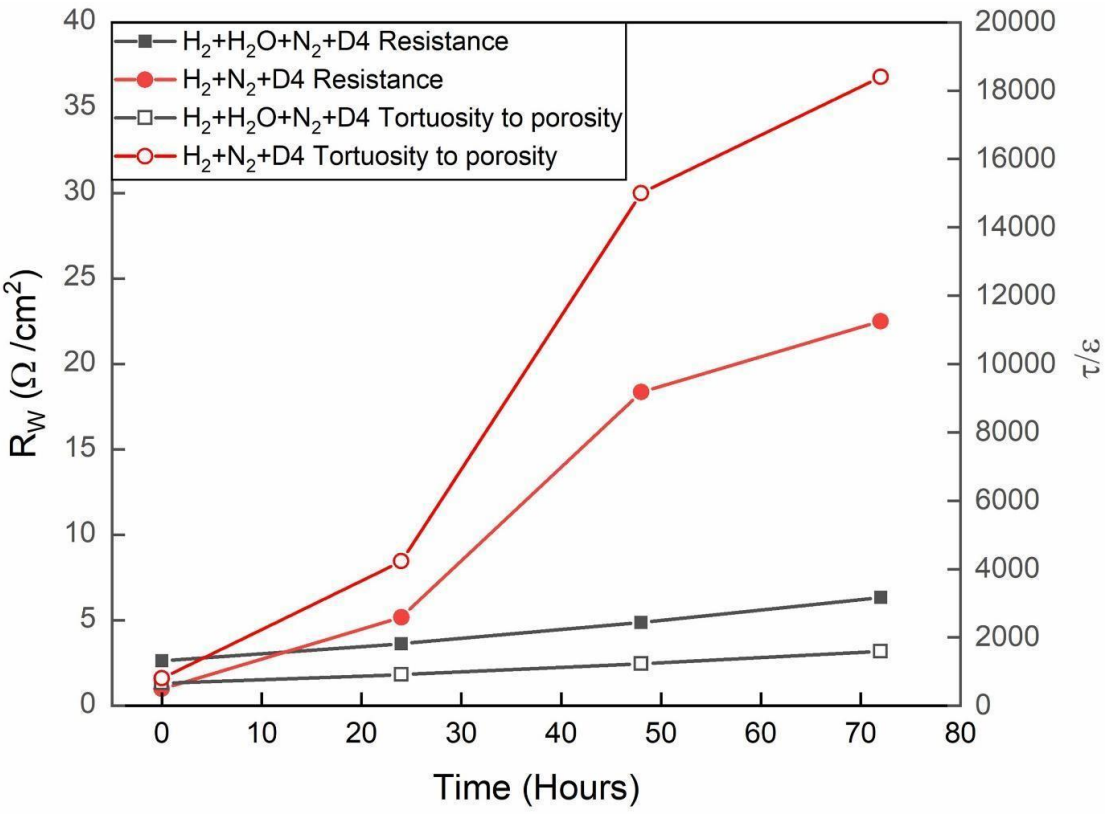

Figure 3.13 The FLW element resistance and relative tortuosity to porosity ratio change of the Ni pellet during H_2+N_2+H_2O+D4 and H_2+N_2+D4 experiments.

3.8 Discussions

For the siloxane deposition determination experiment in which Ni and YSZ pellets were exposed under bio-syngas with siloxane contamination. Although the predicted products such as Ni_7Si_{13} by thermodynamic calculation have not been found by XRD, the calculation results for L2+H_2O reaction indicate SiO_2 is more favorable than SiC under the experimental conditions for siloxane. However, for catalytic reaction perspective, previous siloxane metal oxide chemical adsorption literature points out that the formation of CH_4 following the adsorption process may provide the carbon source for deposition. From electrochemical reaction perspective, the electrochemical oxidation reactions have

higher priority than water reactions. In the siloxane partial electrooxidation process, the siloxane may be dehydrogenated on the Ni. This may also explain the formation of SiC and carbon.

Considering about the functions of Ni, YSZ, ZrO_2 and Y_2O_3 in siloxane deposition process. The pellets experiments under dry (H_2+N_2+D4) and wet fuel (H_2+N_2+H_2O+D4) conditions provide more valuable information. As a summary, considering the pellets' morphology changes and silicon and carbon element deposition extent before and after the contamination experiments, ZrO_2 and Y_2O_3, the main components of YSZ, didn't exhibit strong catalytic activity individually. Similar to our previous YSZ study [8], the presence of H_2O in the contamination fuel can accelerate the deposition of siloxane in both ZrO_2 and Y_2O_3. Compared with siloxane deposition on the pure ZrO_2 and Y_2O_3 in this study, the YSZ in our previous study [8] shows heavier siloxane deposition on its surface at the same experimental conditions. Regarding these results, the oxygen vacancy which exists in YSZ also play a critical factor in the siloxane deposition process especially at high temperatures. The surface structure may also pay a role in the process as the YSZ was relatively flat in comparison to the ZrO_2 and Y_2O_3 samples.

Compared with ZrO_2 and Y_2O_3, Ni shows much stronger catalytic activity for siloxane deposition reactions especially for the dry fuel experiment (H_2+N_2+D4). Significant deposition and surface morphology change can be observed in this case. The comparison of dry (H_2+N_2+D4) and wet fuel (H_2+N_2+H_2O+D4) experimental results for

Ni pellets also deserves special attention. In contrast to the YSZ, Y_2O_3 and ZrO_2 results, H_2O presents a strong ability to restrain the siloxanes deposition on the Ni pellet. It can be proven by the SEM/WDS and electrochemical analysis results including much less surface morphology change, silicon, carbon element deposition and diffusion polarization resistance increasing for the wet fuel experiment. This trend is similar to our previous Ni-YSZ anode SOFC degradation study (chapter 2) in which the performance degradation of SOFCs with wet D4 contaminated fuel was much lower compared with dry fuel after long-term test [84]. With the same trend of humidity influence on siloxanes deposition and more active catalytic properties, it can be inferred that Ni plays a more important role in catalytic siloxane depositions reactions for Ni-YSZ anode. From our previous work [84], this can be explained by the mechanism that sufficient H_2O in the fuel could prevent carbon deposition on the Ni surface who can be observed in **Fig. 3.9b** as the part of porous substrate layer for SiO_2 crystal growth.

In this study, extremely serious siloxanes deposition was noticed. The micrometer size flake shape SiO_2 crystal in **Fig. 3.9b** and **Fig. 3.14c** has never been reported in previous trace level siloxane contamination studies for SOFCs. One possible explanation is that pure Ni anode was utilized in this study instead of Ni-YSZ anode. This result demonstrates the importance of Ni in the siloxane deposition process. The porous Si-O-C composition substrate for SiO_2 crystal growth shown in **Fig. 3.9a** and **Fig. 3.14c** also provides evidence for a conclusion from our previous studies that surface adsorption of

siloxanes is a critical step for the deposition process [8,102]. The new discovery in study is that Ni exhibits a stronger accessibility for siloxanes adsorption instead of YSZ as previously assumed.

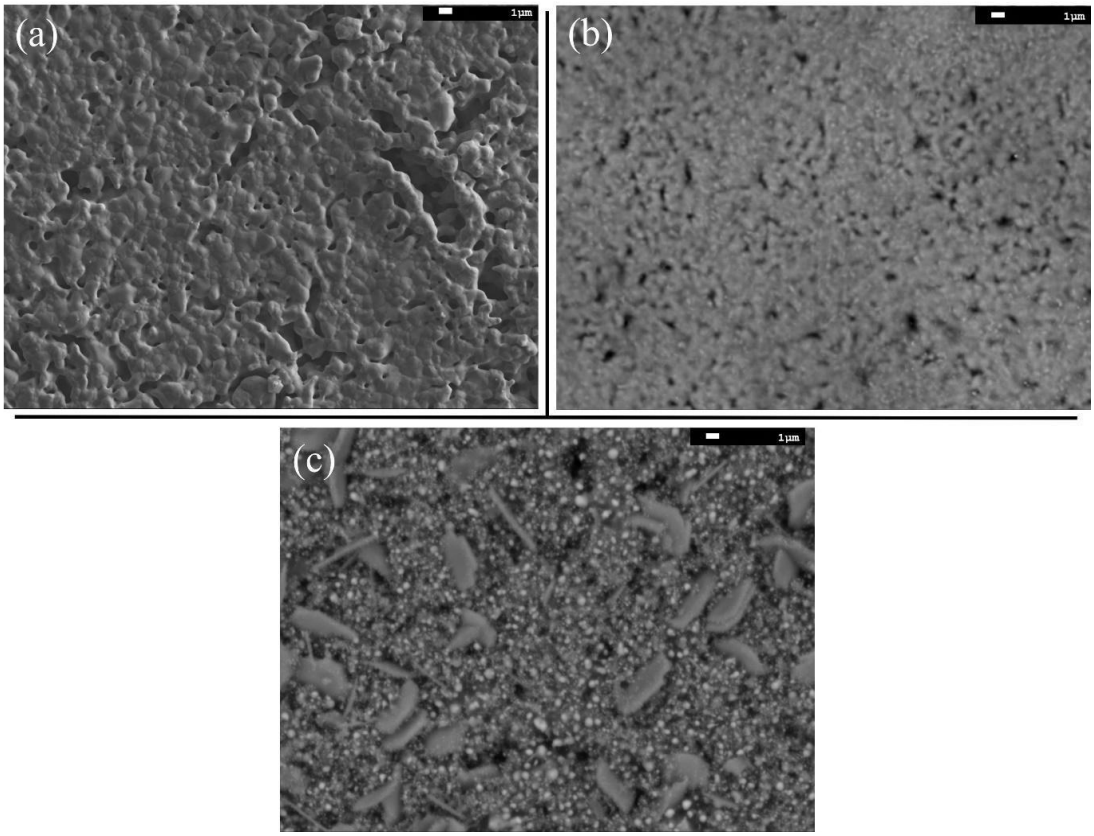

Figure 3.14 The morphologies of Ni pellets surface by SEM. (a) clean initial pellet, (b) after H_2+N_2+H_2O+D4 contamination and (c) after H_2+N_2+D4 contamination experiment.

Besides SEM/WDS, EIS testing results and related DRT optimized ECM were also applied to investigate the siloxane deposition in porous Ni pellets. From the DRT and ECM results, the Warburg element representing the anode diffusion process has been separated and its resistance values were utilized for deposition extent evaluation. As a result, its values fit the deposition trend obtained from SEM/WDS results well. A

microstructure parameter, tortuosity factor to porosity ratio τ/ε calculated from polarization resistance of anode diffusion process, provided valuable information for general microstructure change instead of surface morphology change from SEM/WDS. Actually, this method has been utilized for investigation of the anode support layer degradation and for the modeling of diffusion process of SOFCs' electrodes widely [52,53,114,129,133]. Compared with diffusion polarization resistance value, degradation evaluation by τ/ε value can eliminate several external factors such as gas composition and concentration difference, temperatures, pressure, and size of the porous materials from geometry features. For instance, for dry and wet fuel experiments in this study, even with different composition and concentration of the mixture gas, the initial values of τ/ε for clean cells are similar. Compared with τ/ε value obtained from A. Leonide et al. [53] (~71), S. Dierickx et al. [129] (~22) and Y. Zhang et al. [114] (~3), the initial value is much larger in this study. One possible explanation is that the fabrication method of the Ni pellet in this study is die-pressing instead of screen-printing or tape-casting which were utilized in previous studies for Ni-YSZ anodes. Die-pressing of Ni particles may generate more compact microstructure compared to other methods. N. Tikekar et al. [134] also reported hundreds level τ/ε values for die-pressing Ni-YSZ anode. In addition, pure Ni pellets were utilized in this study instead of Ni-YSZ from previous reported studies. This is also a reason for the larger τ/ε value. From **Fig. 3.13**, τ/ε increase rate of the dry fuel experiment is much larger than in the wet fuel experiment. Furthermore,

one phenomenon from the plot that can be noticed is the value of τ/ε increased slower after 48 hours for the dry fuel experiment. In comparison to the dry fuel experiment, for wet fuel, τ/ε value increased near linearly and slowly.

Combined with the morphology results from wet and dry experiments in **Fig. 3.14**, the deceleration of τ/ε growth may result from the almost total occupation of pores by siloxanes deposition in Ni pellets which can block gas diffusion process eventually. In this situation, complete blockage of the anode by the siloxane deposition process can be predicted by the τ/ε versus time curve. For the wet fuel experiment, assuming a constant τ/ε increase rate, the failure (deposition almost filling the pores) time can be expected at around 1109 hours which is near 23 times slower than the dry fuel experiment.

Generally, the electrochemical analysis of Ni pellets experiments also provides strong evidence to show the deposition of siloxanes in the Ni pellets and the depression function of H_2O on the deposition process. In this circumstance, considering the dominating factor of Ni attributing to the catalytic siloxane depositions, finding Ni- free or Ni-based modified anodes that have lower siloxane adsorption and affinity properties can be a direction to reduce siloxane poisoning of anodes in future.

3.9 Conclusions

For the siloxane deposition determination experiment in which Ni and YSZ pellets were exposed under bio-syngas with siloxane contamination. Based on morphology and

XRD analysis, silicon and carbon deposition were both detected coincidentally and separately. From XRD results, large amounts of carbon and trace silicon compositions can be observed on pure Ni pellet. For pure YSZ pellets and entire SOFC, the products at 38.19°, 64.50°, 77.38° (2θ) were considered the main deposition products which could be either SiO_2, SiC or both. Considering thermodynamic and electrochemical analysis, SiO_2 is more favorable. From the color of the deposition, the existence of C and SiC are possible. These results provide direct evidence for SiO_2 formation and infer carbon deposition in the anode.

To investigate how individual SOFC Ni-YSZ anode components influence the siloxane deposition process, Ni, ZrO_2, Y_2O_3 were fabricated to pellets and exposed to H_2+N_2+H_2O+D4 and H_2+N_2+D4 gas mixtures at 750 °C. After 72 hours with 2.5 ppm_v D4 contamination, SEM/WDS surface morphology analysis of pellets demonstrated that Ni has much stronger catalytic activity for siloxane deposition reaction than ZrO_2 or Y_2O_3. Furthermore, much heavier siloxane deposition with micrometer size flake shape SiO_2 crystal has been observed in dry fuel Ni pellet experiment (H_2+N_2+D4) than wet fuel (H_2+N_2+H_2O+D4) experiment. This phenomenon coincided with a previous study of an entire Ni-YSZ anode SOFC in which H_2O can reduce the performance degradation caused by siloxanes contamination. Meanwhile H_2O, which can increase the surface hydroxylation extent, was reported to accelerate siloxanes deposition on YSZ.

For the EIS testing results analysis, an equivalent circuit model was developed and

optimized by the DRT method. Gas diffusion process in the Ni pellets has been identified from the equivalent circuit model as the Warburg element. From CNLS fitting, the diffusion polarization resistance value for dry fuel experiment is much larger than wet fuel. A microstructure parameter, tortuosity factor to porosity ratio τ/ε, was calculated from diffusion polarization resistance to eliminate the external influences beside materials' microstructure features. This ratio was utilized to estimate siloxanes deposition extent in the Ni pellets. The change in τ/ε with time also confirmed that the siloxane deposition rate on the pellet with the dry fuel is much faster than with wet fuel. Comprehensively considering the SEM/WDS and electrochemical analysis, it can be concluded that Ni is the dominating composition contributing to the catalytic siloxane depositions reactions in Ni-YSZ anode.

4 DEGRADATION COMPARISION OF CYCLIC AND LINEAR SILOXANE CONTAMINATION ON SOFC NI-YSZ ANODE

4.1 Introduction

Besides the fuel composition and anode materials discussed in previous two chapters, the type of the siloxane in the contaminated fuel may also influence the SOFC's anode degradation process. There are many different kinds of siloxane that exist in biogas and they can be sorted based on cyclic or linear structure. Cyclic siloxanes are designated by a 'D' for cyclic structure and a number indicating how many silicon atoms per molecule. Hexamethylcyclotrisiloxane (D3), Octamethylcyclotetrasiloxane (D4) and Decamethylcyclopentasiloxane (D5) are the cyclic structure siloxanes typically found in biogas with the highest concentration. Linear siloxanes are designated by a 'L' for linear structure and a number indicating how many silicon atoms per molecule. For linear siloxanes, trace levels of hexamethyldisiloxane (L2), octamethyltrisiloxane (L3) and decamethyltetrasiloxane (L4) can be detected in biogas [64].

The concentration of each type of siloxane in biogas from wastewater treatment plants differs significantly. For example, smaller molecule siloxane, like D3, L3, and L2, can only exist in a limited amount because of high volatility which leads to vaporization prior to the anaerobic digester. There are also only small amounts of larger siloxane, such as D6, in biogas due to low volatility and low partial pressure in the active sludge [135]. As a result, cyclic siloxanes D5 and D4, which have stable molecular structure, typically have higher concentration and thus are often selected to represent all siloxanes in biogas

for SOFCs contamination studies.

The previous studies only focus on SOFC degradation due to cyclic siloxanes instead of linear siloxanes. This is due to the higher concentration of cyclic siloxanes (D4 and D5) and the fact that linear siloxanes are considered to be decomposed easier than cyclic structure in the digester due to instability. However, the concentration of smaller linear siloxanes in landfill gas are comparable or can be higher than cyclic siloxanes such as D4 and D5 [136,137]. For biogas from a wastewater treatment plant, siloxane concentration is also influenced by multiple factors such as digester type, location, and season. In some cases, high concentrations of linear structure siloxanes were also reported [15]. To improve the utilization of biogas from landfill and wastewater treatment plants, investigation of SOFC degradation due to linear siloxane contamination is necessary.

In this study, linear structure siloxane, L4, was selected as the contamination source and is compared with a cyclic siloxane, D4. L4 and D4 were chosen as they have different structure, but the same number of silicon atoms per molecule of siloxane. Stability tests are conducted to compare SOFC degradation and contamination on YSZ pellets. The experimental results of D4/L4 were analyzed and compared to reveal more information of the SOFC degradation due to different siloxane contamination.

4.2 Fabrication and Methods

The SOFCs were fabricated with LSCF ($(La_{0.60}Sr_{0.40})_{0.95}Co_{0.20}Fe_{0.80}O_{3-x}$, Fuelcellmaterials) + SDC ($Sm_{0.20}Ce_{0.80}O_{2-X}$, mid grade powder, Fuelcellmaterials)

cathode (7:3 w/w), SDC buffer layer, YSZ ($(Y_2O_3)_{0.08}(ZrO_2)_{0.92}$, spray dried grade powder, Fuelcellmaterials) electrolyte and NiO (standard grade powder, Fuelcellmaterials) + YSZ anode (60:40 w/w). NiO /YSZ was dry pressed and pre-fired (final thickness of 380 μm). The YSZ electrolyte and SDC buffer layers were sprayed on the surface of NiO/YSZ green body and sintered at 1400 °C with ~10 μm and ~3 μm thickness, respectively. LSCF + SDC cathode was hand sprayed on the SDC buffer layer and sintered at 1100 °C (final thickness ~17 μm). More details about the fabrication method can be found in previous literature [84]. YSZ pellets (380 μm thick) were also dry pressed and sintered to investigate the process of siloxane deposition.

Fig. 4.1 shows the experimental setup which was built for investigating the influence of the type of siloxane (cyclic or linear) contamination on the Ni-YSZ SOFC anode. According to previous work [84], dry fuel mixed with siloxane can increase SOFC performance degradation compared to adding H_2O. As a result, for the SOFC test, H_2 (ultra high purity grade, Airgas) + N_2 (ultra high purity grade, Airgas) + siloxane was selected as the fuel. To regulate the flow of H_2, N_2, L4 and D4, Brooks Delta II smart mass flow controllers (MFCs) with LabView interface were utilized. The H_2 flow rate was fixed at 7 standard cubic centimeters per minute (sccm). The certified D4 (5.358 ppm_v, Airgas) and L4 (5.034 ppm_v, Airgas) cylinders balanced with N_2 were mixed with research grade N_2 to fix the concentration of D4 and L4 to 2.5ppm. The total gas flow rate to the anode was 20 sccm for all experiments. For YSZ pellet experiments, which

included tests with steam, water was delivered by a syringe pump (PumpSystems Inc.). Resistive heaters wrapped on the fuel delivery pipe were used to vaporize the deionized water and maintain vapor phase. To ensure the steam remained in vapor phase, T-type thermocouples (Omega) were mounted on the pipe to monitor the temperature. Air was delivered to the cathode through the vertical furnace by natural convection.

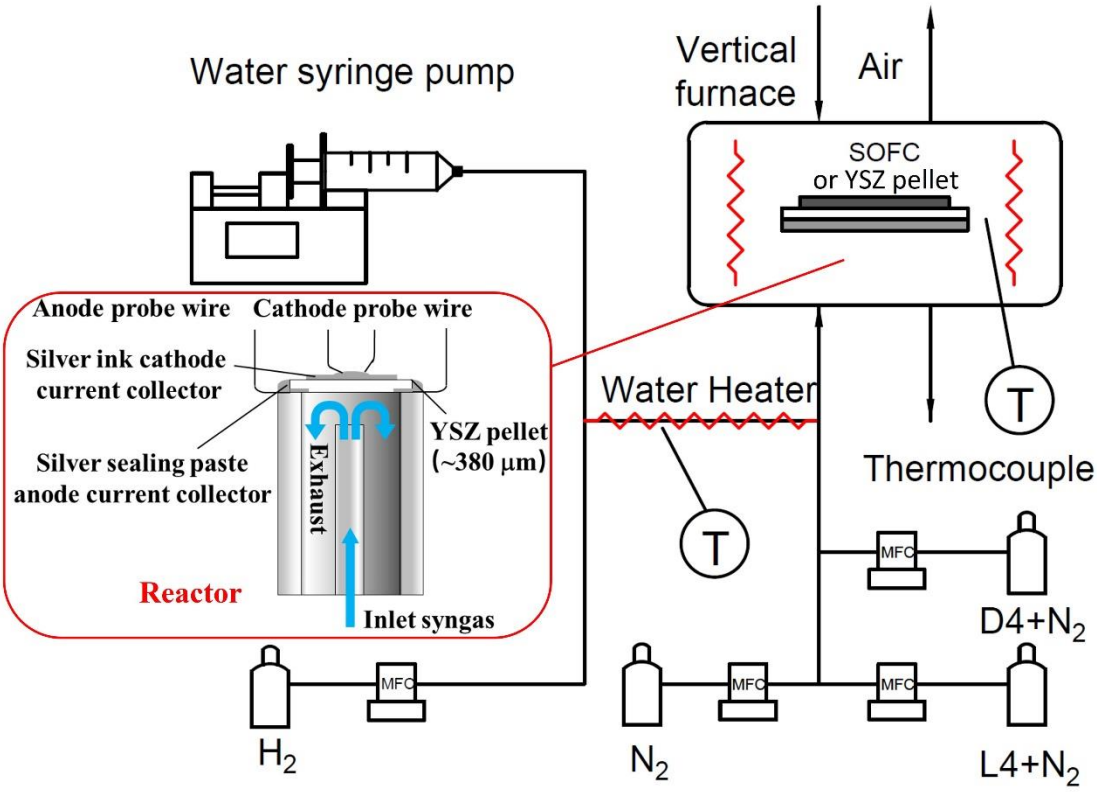

Figure 4.1 Schematic of experiment setup for the cyclic and linear siloxane comparison study.

Based on previous siloxane deposition studies [82,83], siloxanes prefer to chemisorb on metal oxide surfaces, like γ-Al_2O_3, due to reactions with hydroxyl groups present. As a result, YSZ grains are hypothesized as one of the locations where siloxane deposits

initially in the Ni-YSZ anode. To test this theory, siloxane (L4/D4) deposition on a YSZ pellet was conducted. To control the amount of hydroxyl groups on the YSZ pellet surface, different gas compositions were chosen for L4 and D4 contamination studies. The details of these experimental conditions are show in **Table 4.1**. In order to remove hydroxyl groups present on the surface of YSZ pellets before the experiment, the pellets were heated to 850 °C and maintained at that temperature for 1 hour with 20 sccm pure N_2 on the bottom side.

Table 4.1 Flow rate (sccm) of anode side gases supplied to YSZ pellet during the cyclic and linear siloxane comparison study

Experiment conditions	H_2	H_2O	N_2	Siloxane+ N_2
N_2+D4	NA	NA	10.67	9.33
H_2+ N_2+D4	7	NA	3.67	9.33
H_2+N_2+H_2O+D4	7	2	1.67	9.33
N_2+L4	NA	NA	10.07	9.93
H_2+ N_2+L4	7	NA	3.07	9.93
H_2+N_2+H_2O+L4	7	2	1.07	9.93

For the SOFC and YSZ pellet experiments, the SOFCs (or pellets) were sealed on a quartz tube with silver paste. The cathode (or the cathode side of the pellet surface) were

printed with silver ink as the current collector with an active area of 0.712 cm^2. Silver wires connected with the anode and cathode were utilized for the electrochemical characterization. The operating temperature was fixed at 750 °C with 5 °C per minute heating rate for all experiments.

In order to evaluate the performance degradation of SOFCs under L4 and D4 contamination, the fuel cells' polarization (I-V) curves were acquired by a digital SourceMeter (Keithley 2460) interfaced with LabView on the computer with four-probe technique. The electrochemical characterization of the entire SOFC and YSZ pellets were conducted by electrochemical impedance spectroscopy (EIS). The impedance spectra were obtained by an Electrochemical Impedance Analyzer (Solartron Analytical Energylab XM) with ac amplitude of 10 mV and a frequency range of 10^6 Hz to 0.1 Hz. The distribution of relaxation time (DRT) method was utilized to analyzed EIS data by a MATLAB GUI program (DRTtools) [50,116,117]. The regularization parameter is selected as 10^{-3} for DRT calculation.

Several techniques were used to characterize the morphology and composition of the silicon containing deposits. The morphologies of L4 and D4 deposition under different experimental conditions on YSZ pellets were conducted by a field emission scanning electron microscope (FESEM, JEOL JXA-8530F electron microprobe) equipped with an energy-dispersive spectrometer (EDS) and wavelength-dispersive spectrometer (WDS). As the Y and Si signals are not well separated with EDS, WDS was

utilized to obtain the elemental analysis of the sample. To determine the L4 and D4 deposition compositions on the YSZ pellets, X-ray diffractometer (XRD) system was utilized for the deposition crystalline structure characterization. The XRD patterns were obtained using the X-ray diffractometer (PANalytical X' Pert Pro MRD) with a Cu Kα (K-Alpha2/ K-Alpha2=0.5) radiation source. To obtain more composition information for the L4 and D4 deposition on the YSZ pellets, Raman test was conducted on an Acton 300i spectrograph and a back thinned Princeton Instruments liquid nitrogen cooled CCD detector with a 532 nm laser as excitation source. The power was kept at 6 mW.

4.3 SOFC Electrochemical Characterizations

As shown in **Fig. 4.2a**, the polarization curves of the SOFC after 20 hours and 40 hours D4 contamination are compared with the initial fuel cell performance after intrinsic degradation. In order to eliminate the influence of SOFCs' intrinsic degradation, the SOFCs haven been operated under clean fuel for 48 hours. This data, which is a useful reference without siloxane contamination, is show in **Table 4.2**. After 20 hours D4 contamination, the maximum power density of the fuel cell decreased from 211.5 mW cm^2 to 205.1 mW cm^2. In comparison, the maximum power density of the fuel cell during the next 20 hours (40 hours total contamination) decreased to 183.16 mW cm^2 from 205.1 mW cm^2. A similar trend of degradation was also observed in the EIS results. The obvious impedance increase after D4 contamination can be noticed from **Fig. 4.2c**. DRT analysis was conducted to identify the characteristic distribution of the SOFC EIS results.

Among the five main discrete peaks (P1 ~ P5) in **Fig. 4.2b**, P1 and P2 (0.1 to 1 Hz) at low frequency are considered as the gas diffusion process for the cathode, based on previous DRT analysis [102]. P3 and P4 at medium frequency (1 Hz to 10 kHz) are related to the gas diffusion process for the anode. P5 (> 10 kHz) at high frequency is attributed to charge transfer. With minor change of cathode and charge transfer process (P1, P2, P5), the main performance degradation of the SOFC results from anode processes (P3 and P4) [46,86,87].

Table 4.2 Maximum power density decrease and increase in area specific resistance (ASR) calculated from characterization results

	Original	Clean fuel 48 hours		After 20 hours	After 40 hours	Power density decrease after contaminations
D4 maximum power density ($mW\ cm^2$)	215.5	211.5		205.1	183.2	28.3
L4 maximum power density ($mW\ cm^2$)	229.6	226.0	Siloxane Added	225.0	222.8	3.2
						ASR increase after contaminations
D4 experiment ASR ($\Omega\ cm^2$)	0.75	0.87		1.32	1.85	0.98
L4 experiment ASR ($\Omega\ cm^2$)	0.60	0.67		1.03	1.18	0.41

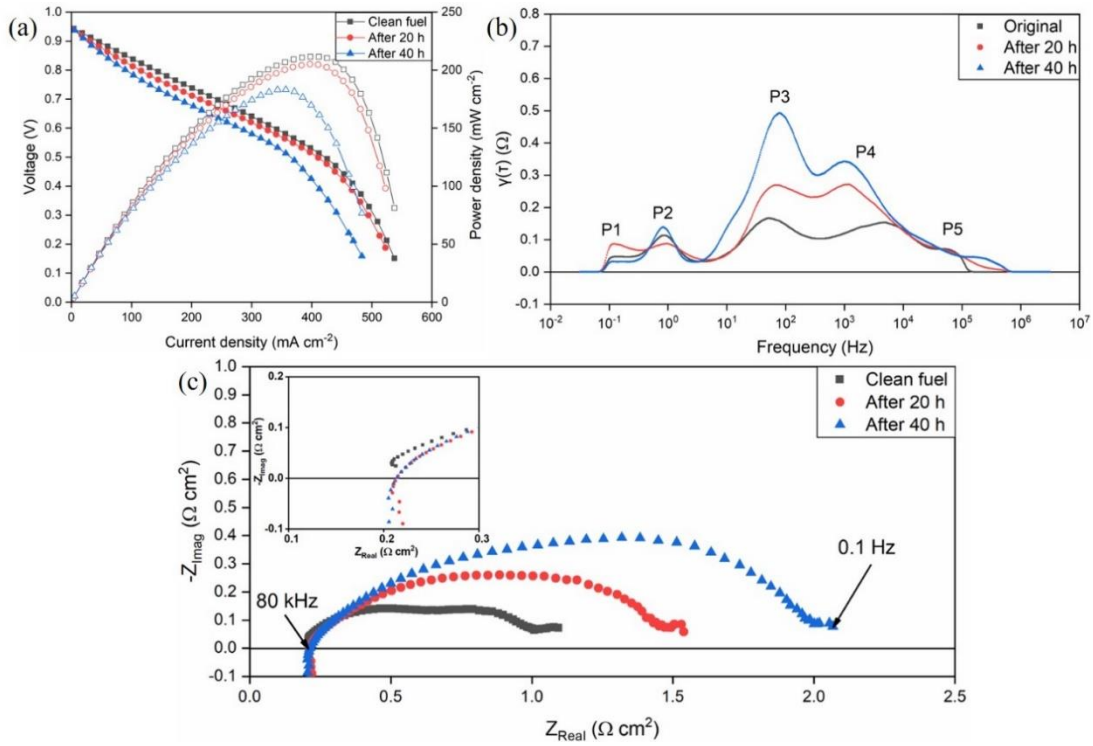

Figure 4.2 Performance degradation of the SOFC due to D4 contamination with H2+N2+D4 as the fuel at 750 °C. (a) polarization curve; (b) EIS measurements; (c) DRT plot.

The electrochemical characterization results for the L4 contamination experiment are show in **Fig. 4.3**. The obvious degradation rate difference from D4 and L4 can be observed in both power density and EIS results after 40 hours in **Fig. 4.3**. From **Fig. 4.3a**, no obvious degradation can be found in the polarization curve. From the EIS results in **Fig. 4.3c**, a relatively small impedance increase is observed. Similar to the DRT results from D4 contamination, L4 contamination results also illustrate the main degradation occurred in anode process as shown by P3 and P4 increase. More details comparing L4 versus D4 results are show in **Table 4.2**. From the results of **Table 4.2,** which show power density change and area specific resistance (ASR) increase, the SOFC under L4

contamination has noticeably less degradation than with D4 contamination. It is worth noting that even utilizing the SOFCs with same fabrication process and materials, the EIS and polarization results before D4/L4 contamination in two sets are also slightly different. In this situation, there are some experimental setup factors may influence the results such as current collector coating, cables, sealing etc. Considering the appearance of inductance in different sets, one possibility is that the cables which can introduce distortion by the inductance may influence this process which has been reported before [138].

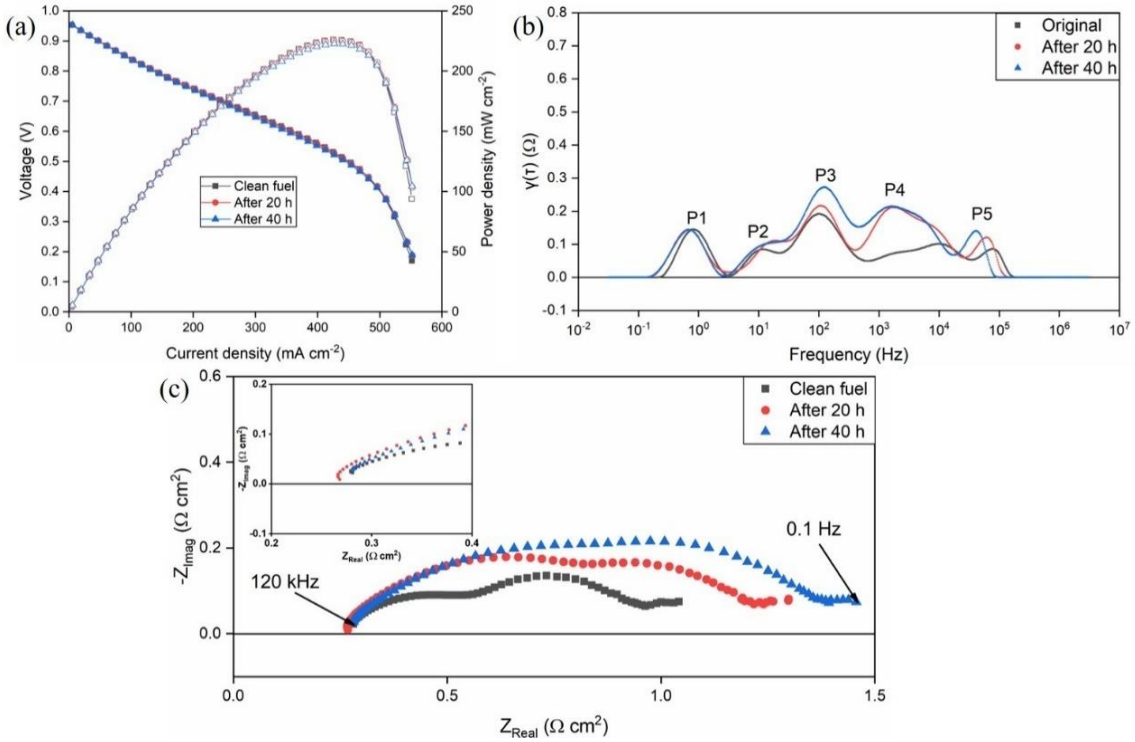

Figure 4.3 Performance degradation of the SOFC due to L4 contamination with H2+N2+L4 as the fuel at 750 °C. (a) polarization curve; (b) EIS measurements; (c) DRT plot.

4.4 YSZ Pellets Morphology Analysis

Fig. 4.4 shows photos of the YSZ pellets after the D4/L4 exposure experiments. The mechanical damage of SOFCs happened in the dismounting process from the silver sealing. As shown, the color of pellets, under certain conditions, has been converted from white (clean YSZ) to yellow/brown which indicates the deposition of siloxanes. Generally, the experiments with D4 as impurity had more deposition compared with L4. The siloxane deposition for the experiments with wet fuel (H_2+H_2O+siloxane) was larger than the experiments with dry fuel (H_2+ siloxane, N_2+ siloxane). Furthermore, some details shown in the photos should also be highlighted. For L4 contamination experiments, besides the test involving H_2O mixed with the fuel, there is little siloxane deposition on the YSZ pellets' surface. However, after adding H_2O, significant deposition was observed. For N_2+D4 experiment, there is no obvious deposition that can be noticed in the center of the pellet. However, siloxane was deposited on the edge of the pellet near the silver sealing/current collector.

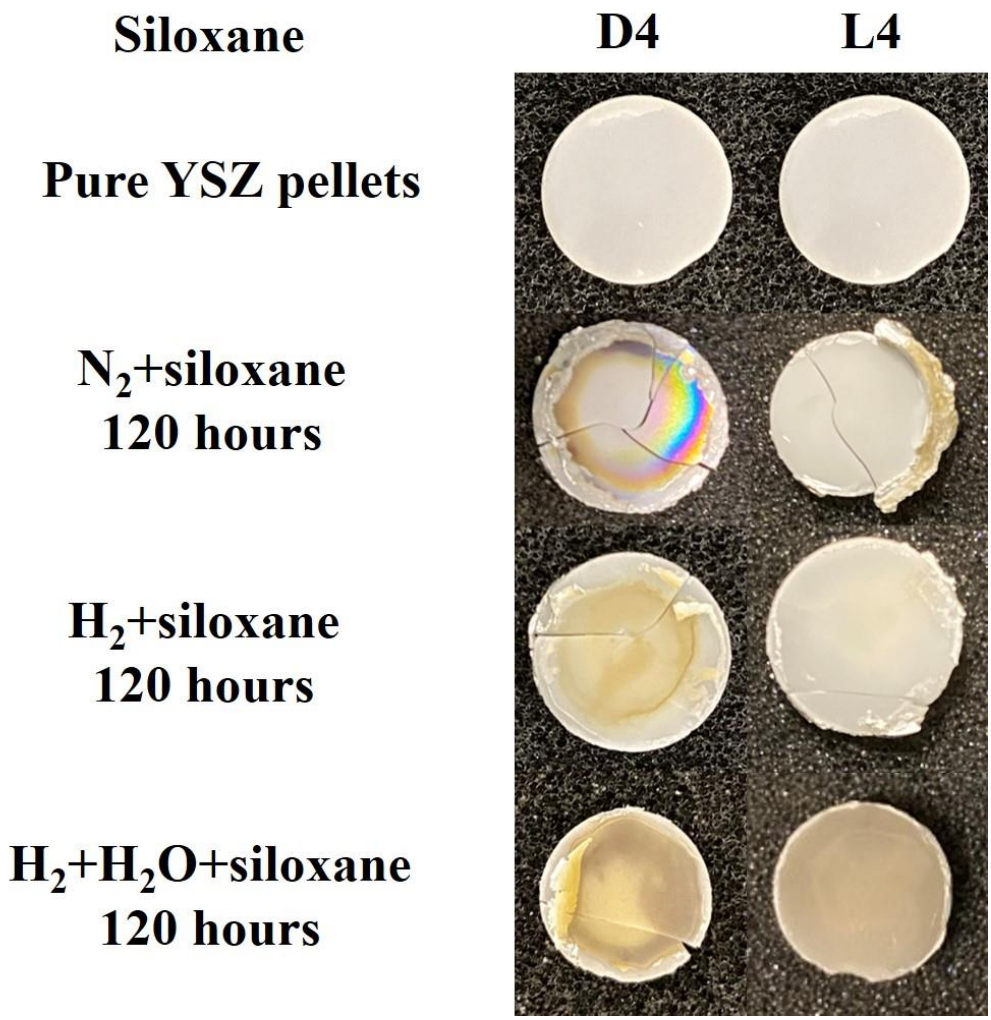

Figure 4.4 Figures of YSZ pellets after siloxane deposition experiments.

The morphology and elemental mapping of YSZ pellets were investigated after the contamination test utilizing SEM and WDS. **Fig. 4.5** shows the WDS map of the Zr, O and Si elements on the surface of the YSZ pellets under the H_2+N_2+D4/L4 conditions. As shown in **Fig. 4.5b**, which shows the surface after L4 contamination, the fine YSZ grains and grain boundaries can be observed and there is no obvious silicon deposition. In comparison the sphere shape depositions in **Fig. 4.5a** whose diameters are around 1 μm completely covered the surface of the YSZ pellet after D4 contamination experiment.

Thus, the clear grains and grain boundaries shown in **Fig. 4.5b** cannot be detected. The presence of strong overlapping signals of Si and O was observed with WDS elements mapping, indicating silicon dioxide formation in the H_2+N_2+D4 experiment.

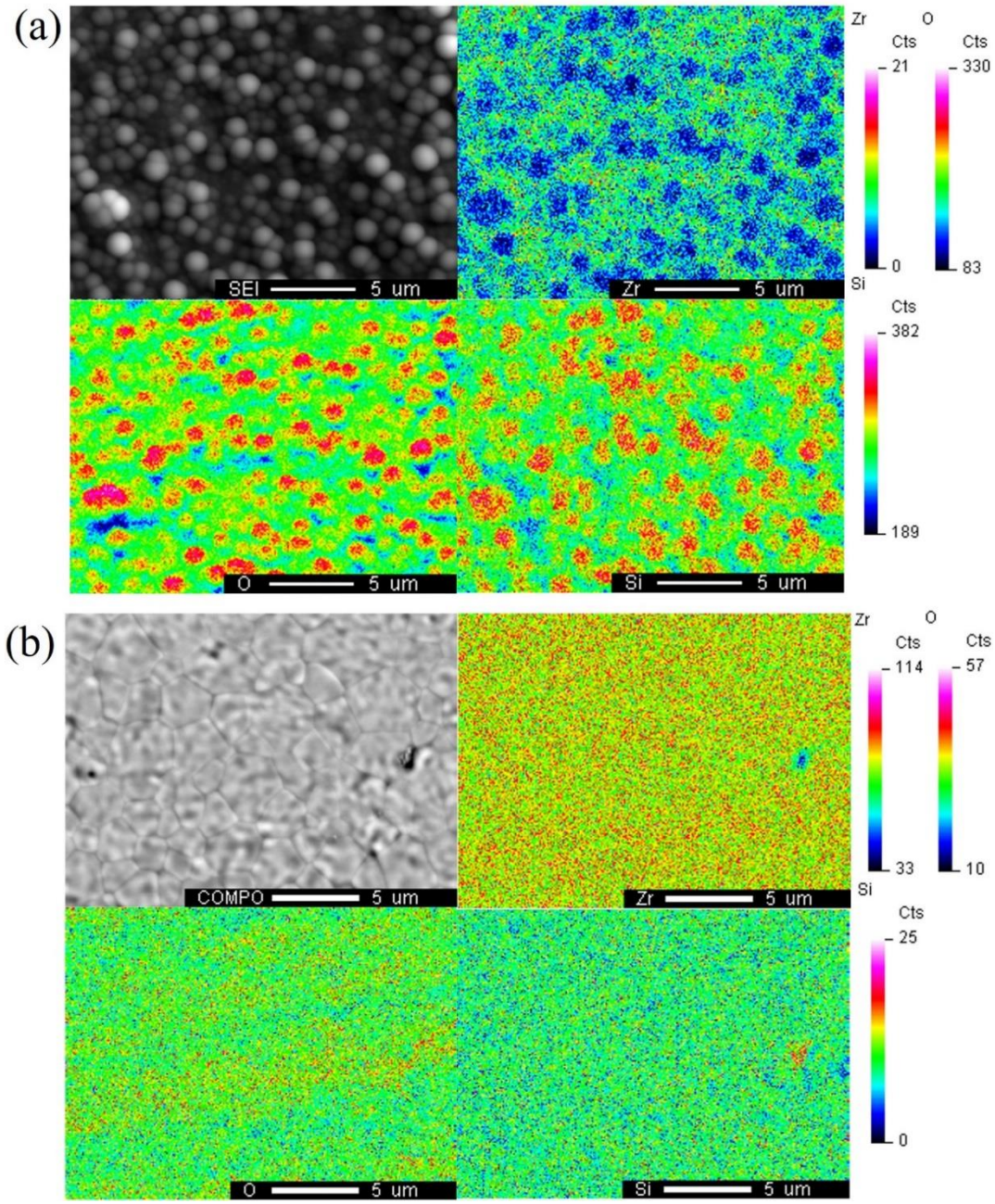

Figure 4.5 WDS elemental mapping of the surface of YSZ pellet with H_2+N_2+siloxane contamination after (a) D4 contamination and (b) L4 contamination at 750 °C.

For the H_2+N_2+H_2O+D4/L4 experiments, generally, heavier siloxane deposition on the pellet can be noticed than the H_2+N_2+D4/L4 experiments. Similar to the H_2+N_2+D4 experiment, overlapping silicon and oxygen signals can also be found in element mapping for H_2+N_2+H_2O+D4 experiment in **Fig. 4.6a** which indicates the composition is silicon dioxide. Compared with the regular sphere deposition observed in **Fig. 4.5a**, irregular or less structured deposition was formed with wet fuel likely due to more total deposition on the surface. For the H_2+N_2+H_2O+L4 experiment, also like the dry fuel experiments, less total deposition was observed than the D4 experiment. In **Fig. 4.6b**, the surface grain boundaries of YSZ can be detected. Silicon deposition was observed after the H_2+N_2+H_2O+L4 experiment primarily at the grain boundaries where small Si/O deposits initiate.

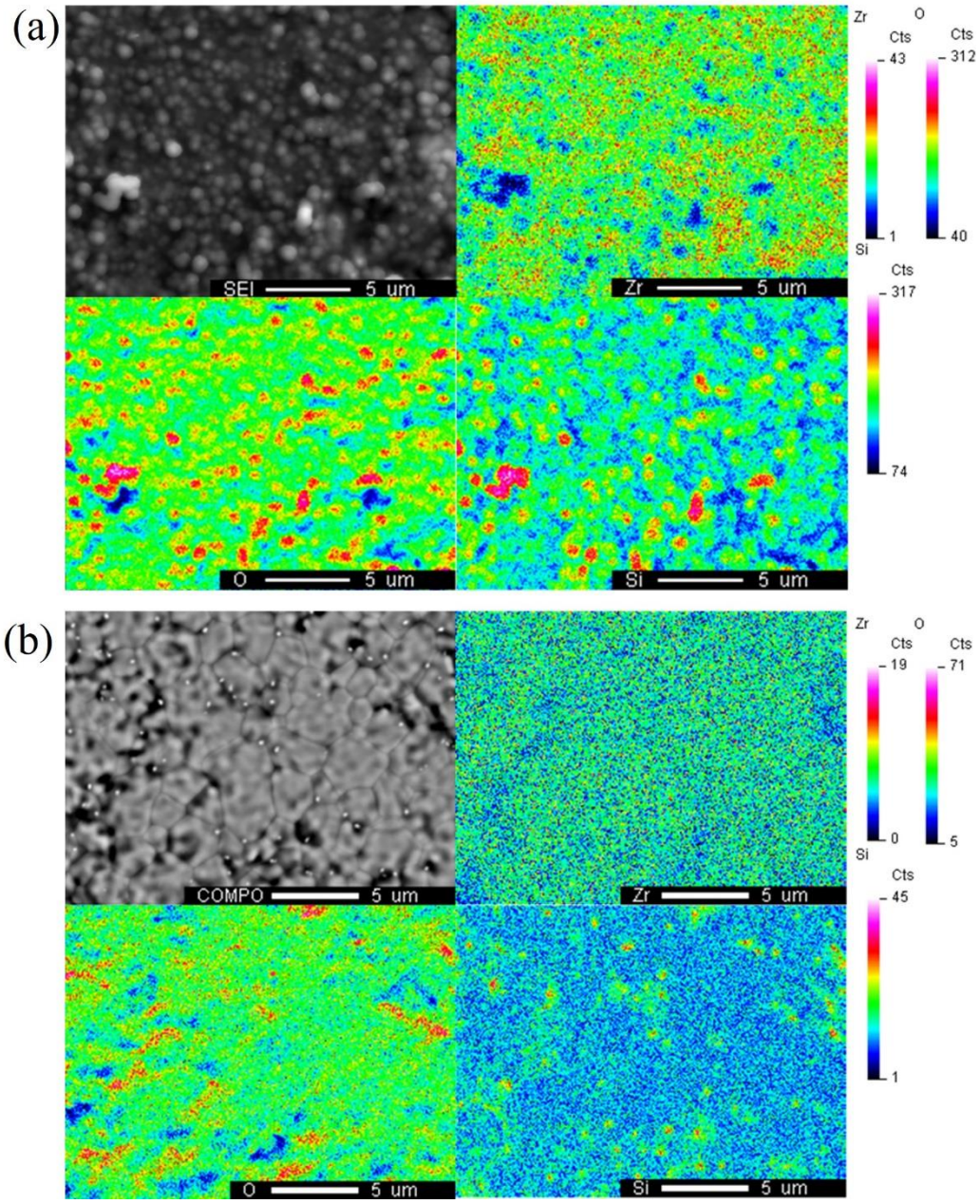

Figure 4.6 WDS elemental mapping of the surface of YSZ pellet with H_2+ H_2O+N_2+siloxane contamination after (a) D4 contamination and (b) L4 contamination at 750 °C.

4.5 Composition Analysis by XRD and Raman Spectroscopy for YSZ Pellets

Fig. 4.7 shows the XRD pattern of the YSZ pellet before and after exposure to the

fuel which was composed of H_2+N_2+H_2O+D4. New peaks appearing at 38.2°, 44.4°, 64.6°, and 77.5° (2θ) were found after contamination, which indicate siloxane deposition. Based on the Si, C and O present in siloxane, the deposition corresponding to the peaks can be attributed to both cubic crystal structure SiO_2 (melanophlogite, PDF#01-080-4051) and silicon carbide SiC (3C-SiC, PDF#00-049-1623).

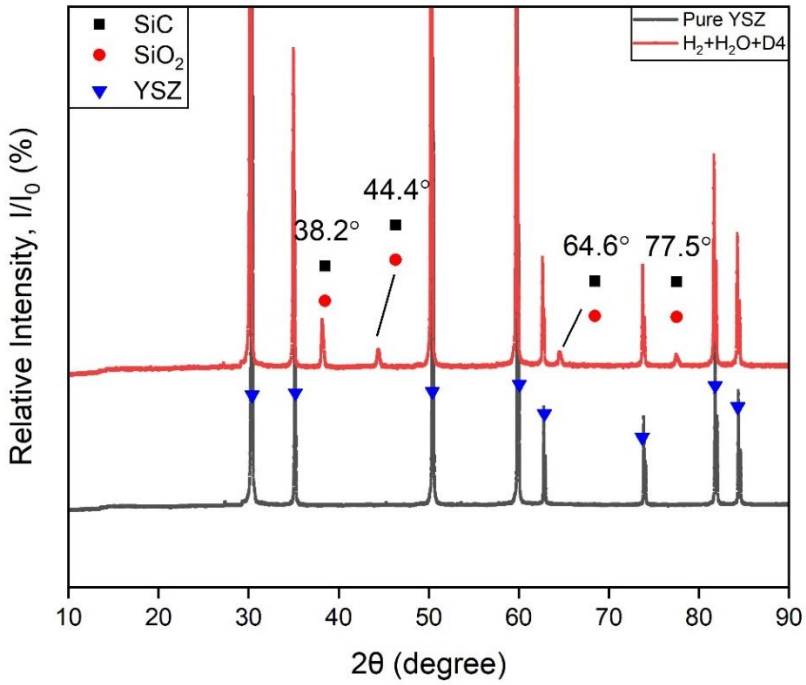

Figure 4.7 XRD patterns of the YSZ pellet bottom surface (fuel inlet side). Black color line: Pure YSZ sample. Red line: after 96 hours H_2+N_2+H_2O+D4 experiment at 750 °C.

According to the observed extent of deposition on the YSZ pellets in **Fig. 4.4** and SEM/WDS analysis, the deposition from L4 was much less compared with D4. Similar trends can also be found in the XRD result for the H_2+N_2+H_2O+L4 experiment. In **Fig.**

4.8, much weaker deposition peaks are observed at 23.1°, 36°, 43.2°, 48.6° and 57.2° (2θ) in the pattern. They correspond to a hexagonal crystal structure SiC (moissanite-18H, PDF#01-089-2217), a tetragonal structure SiO_2 (α- cristobalite, PDF#04-018-0233) and a cubic crystal structure SiO_2 (melanophlogite, PDF#01-080-4051). For two different polymorphs of SiO_2, melanophlogite which is always correlative to organic matter decomposition can exist steadily at 800 °C [139]. And α- cristobalite may originate from β- cristobalite after cooling below about 250 °C at ambient pressure from high temperature [140]. In this situation, these two kinds of polymorphs of SiO_2 can exist together in the siloxane deposition.

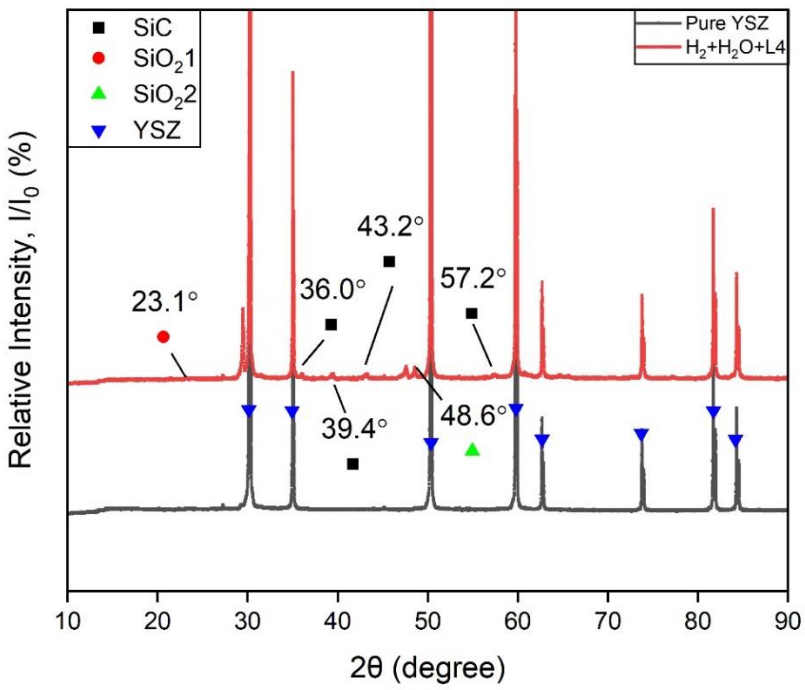

Figure 4.8 XRD patterns of the YSZ pellet bottom surface (fuel inlet side). Black color line: Pure YSZ sample. Red line: after 96 hours H_2+N_2+H_2O+L4 experiment at 750 °C.

There is a comparatively strong peak at 2θ = 29.4 in **Fig. 4.8**. Both considering its relative signal strength and the position, which is very close to the main peak of YSZ, it may be a result of the Zr, Y, O ratio change in the surface of YSZ pellet. There is also an unlabeled weak peak around 27 ° in both **Fig. 4.7** and **Fig. 4.8**. Considering this peak is present before and after siloxane contamination and without significant increase from the patterns, it should not be associated with siloxanes deposition process. It may originate from the noise or secondary peaks of main components.

Fig. 4.9a shows postmortem Raman spectra from the YSZ pellets after 120 hours D4 contamination with H_2+N_2+H_2O as fuel. For poly-aromatic hydrocarbons the appearance of D and G peaks in Raman spectroscopy are common. D peak originates from the breathing modes of sp2 atoms in rings. The G peak is generated by all pairs of sp2 atoms bond stretching in both rings and chains [141]. Compared with the pure YSZ pellet without D4 contamination, emergence of G peak observed in all sp^2 carbon systems near 1,600 cm^{-1} and D peak around 1350 cm^{-1} both indicate the presence of amorphous carbon deposition after exposure to D4 contamination. Besides the strong amorphous carbon signal, some weaker peaks corresponding to different chemical groups were observed as shown in **Fig. 4.9b**. Methyl/methylene (CH_x) group vibrational bands can be noticed at 2911 cm^{-1}. SiH_x, $(-C{=}C-)_n$ groups can be observed at 1948 and 2306 cm^{-1}. The secondary order D peak 2D can also be found at 2673 cm^{-1} [142–144].

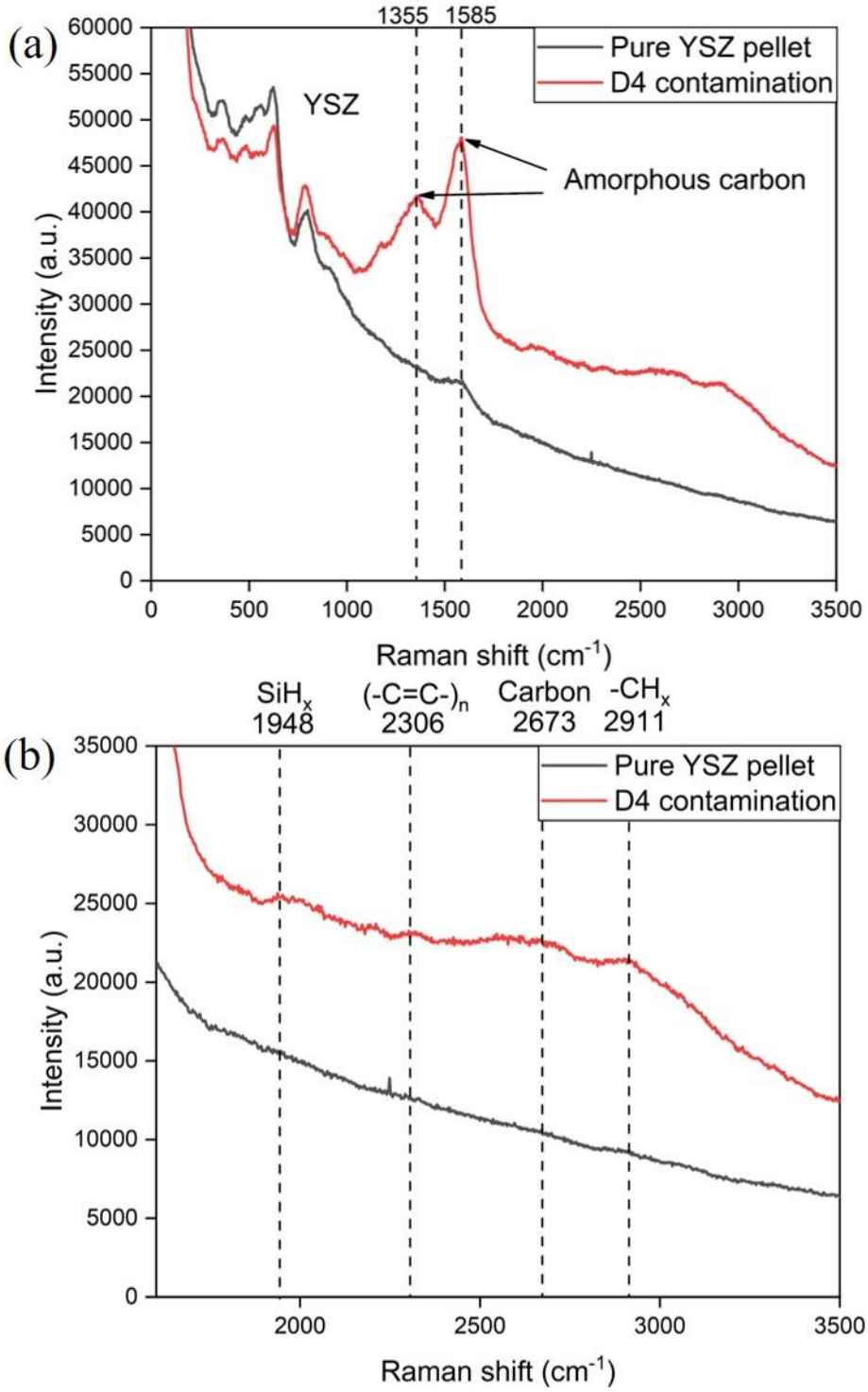

Figure 4.9 Postmortem Raman spectra acquired from the YSZ pellet after 120 hours D4 contamination at 750 °C versus pure YSZ pellet spectra. (a) Entire Raman spectra; (b) Raman spectra ranges from 2000-3500 cm^{-1}.

In **Fig. 4.10**, Raman spectra have been obtained from the YSZ pellet surface exposed to H_2+N_2+H_2O+L4 fuel. Besides YSZ, no strong signals like those observed in **Fig. 4.9a**, were detected. This also confirms the trend that D4 contamination has more deposition than L4. The band at 1604 and 2774 cm^{-1} are attributed to carbon deposition. Similarly in **Fig. 4.9b**, the $(-C=C-)_n$ groups can be also found at 2231 cm^{-1}. For the silicon deposition, Si-OH bond can be observed at 1000 cm^{-1} [15,145]. These results are important because they emphasize the role of carbon deposition in the siloxane deposition process.

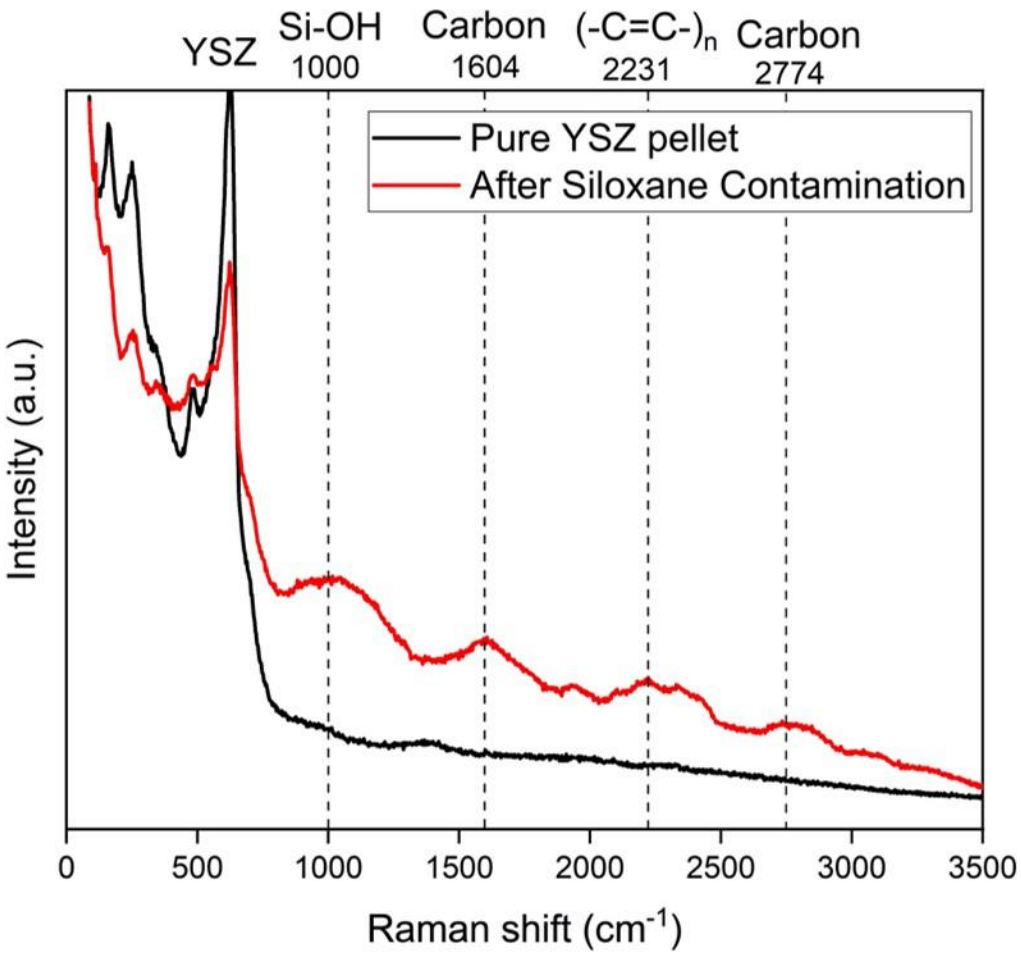

Figure 4.10 Postmortem Raman spectra acquired from the YSZ pellet after 120 hours L4 contamination at 750 °C versus pure YSZ pellet spectra.

4.6 Equivalent Circuit Modeling Analysis for YSZ Pellets' Experiment

Besides the deposition composition analysis, electrochemical analysis of the pellets experiment was also conducted to obtain more details about the degradation process. **Fig. 4.11** shows the Nyquist plots of the impedance of YSZ pellets under L4 contamination with H_2+N_2+H_2O as fuel at 750 °C. An obvious impedance increase can be observed after siloxane contamination. The EIS results were also fitted based on an equivalent circuit with the program LEVM embedded to Solartron Analytical Energylab XM software

[146]. The CPE is a constant phase element, whose characterization can be determined by two parameters, T and n. The effective capacitance, C, for the RQ circuit was calculated by equation (4.1) [147]. T is the frequency-independent constant, and n represents the non-ideal factor. The electrochemical process for the YSZ pellet can be reflected in the magnitude of C [148].

$$C = (R^{1-n}T)^{\frac{1}{n}} \quad (4.1)$$

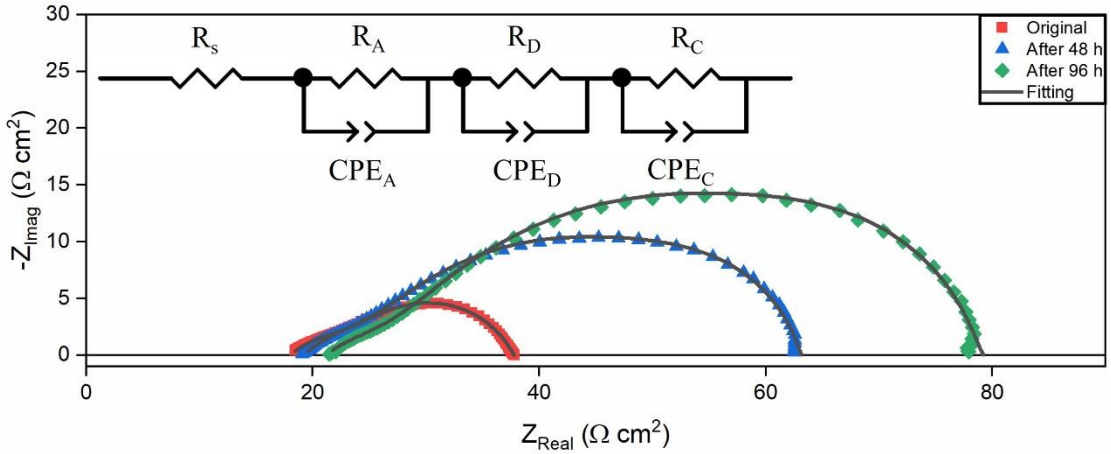

Figure 4.11 EIS and equivalent circuit fitting results of YSZ pellets with porous Ag electrodes under L4 contamination with H2+H2O+N2+L4 as the fuel at 750 °C.

According to previous EIS studies of YSZ pellets [130,149–151], there are two semicircles assigned to the impedance response of the gases chemisorption on the silver electrode, diffusion of gases through the silver electrode and gases conversion process in the silver electrode, respectively. The intercept R_s with the real axis at high frequency is related to the YSZ electrolyte resistance. Fitting the experimental impedance spectra with an equivalent circuit, the resistances and capacitances from diffusion (R_D and C_D),

chemisorption (R_A and C_A) and conversion (R_C and C_C) are shown in **Table 4.3** (Yan et al., 2013).

Consistent with a previous study [130], the resistance corresponding to the gas diffusion through electrodes is much larger than chemisorption resistance and gas conversion resistance. Resistance increase is observed in all the elements in the equivalent circuit after L4 contamination. The diffusion resistance increase is more dominant than the other types. This illustrates that besides deposition on the pellets' surface, the siloxane deposition also prefers to cover the silver current collector which is also the electrode in this setup. As a result, the diffusion process through the electrode is blocked due to siloxane deposition around silver, eventually causing a significant increase in the diffusion impedance. Beside diffusion process, the slight ohmic resistance and gas convection loss resistance increase can also be noticed from the change of R_s and R_C. For ohmic resistance, it is likely due to the obstruction of the conductive network among the silver electrodes associated with the siloxane deposition process. When the gas concentration cannot be maintained in the electrodes, the gas conversion loss appears. The increase of the gas conversion resistance indicates the concentration change of gases supplied to the surface of the electrode. The siloxane deposition may prevent the sufficient flow of gases through the electrodes. This is also in good agreement with the results found in **Fig. 4.4** that show siloxane deposition is more significant around the edge of the pellet covered by silver.

Table 4.3 Equivalent circuit fitting results from EIS results

Experiment Conditions	R_S (Ω)	R_A (Ω)	C_A (10^{-3} F)	R_D (Ω)	C_D (10^{-5} F)	R_C (Ω)	C_C (10^{-6} F)
Original	25.56	13.53	0.21	9.75	3.35	4.18	1.40
48 h	26.97	15.23	1.71	38.04	9.11	8.58	2.80
96 h	29.65	16.93	2.60	51.08	13.21	13.62	5.83

4.7 Discussion

Based on the SOFC siloxane contamination studies, the experiment with L4 as contamination source had less performance degradation compared with D4. To confirm this phenomenon and also investigate the reason causing cyclic and linear structure siloxane deposition, the YSZ pellet experiments were completed. From previous siloxane adsorption studies [82,83], hydroxyl groups play an important role in the siloxane chemical adsorption process. It has been established in previous research that YSZ has hydroxyl groups on its surface [91]. To assess the role of hydroxyl groups on the YSZ surface in the siloxane chemisorption process, different fuel mixtures were prepared. Based on the experimental conditions, the quantity of hydroxyl groups on the YSZ pellets' surface should follow the sequence: H_2+N_2+H_2O+siloxane > H_2+N_2+siloxane > N_2+siloxane. Hydroxyl groups can be formed on YSZ, based on equation (4.2) and (4.3), through reduction of YSZ by hydrogen, which only occurs near the surface, or through reaction with oxygen ions transported through the YSZ [92]. Alternatively, H_2O can form hydroxyl groups directly according to equation (4.4) at a faster rate compared to the

previous mechanism.

$$O_2 + (YSZ) \rightleftharpoons 2O(YSZ) \quad (4.2)$$

$$H_2(g) + 2O(YSZ) \rightleftharpoons 2OH(YSZ) \quad (4.3)$$

$$H_2O(YSZ) \rightleftharpoons OH(YSZ) + H(YSZ) \quad (4.4)$$

Based on the photos of YSZ pellets after experiments (shown in **Fig. 4.4**) and the SEM/WDS results (shown in **Fig. 4.5**, **4.6**), the extent of surface hydroxylation influences the siloxane deposition. The experiment with H_2+N_2+H_2O+siloxane as the fuel, which is considered to have the maximum hydroxyl groups among all conditions, had the most serious siloxane deposition on the pellets' surface. In comparison, with N_2+siloxane as the fuel, which does not result in any surface hydroxyl groups, no significant siloxane deposition is observed in the middle of the YSZ pellet surface. This demonstrates that siloxane chemical adsorption is essential to the entire deposition process.

Following the same trend with the SOFC results, L4 contamination experiments also had less siloxane deposition on the YSZ pellet surface than D4. This phenomenon can also be verified by XRD and Raman results in **Fig. 4.5** to **Fig. 4.10**, in which the YSZ pellet with D4 deposition always resulted in stronger signal during characterization than the YSZ pellet with L4 deposition. From a chemical reaction perspective, L4 as a linear structure siloxane is less stable compared with D4, with its cyclic structure [152]. As a result, L4 as a linear structure siloxane can be dissociated more easily compared to the stable D4 structure [152]. However, the results are opposite of what might be expected.

Considering the influence of hydroxyl groups on the siloxane deposition, the chemical adsorption process should be the rate determining step for the siloxane deposition reaction. This can also be proved by results in **Fig. 4.4**.

The deposition in **Fig. 4.4** appears a yellow/brown color. The visual inspection of the color change may only provide qualitative analysis. From XRD results in **Fig. 4.7** and **Fig. 4.8**, SiC and SiO_2 can be both deposition compositions of siloxanes. Considering the interaction of atoms and their electrons with light waves, the band gap of a semiconductor material can determine its color. For 3C-SiC, which correlates to 3.26 eV bandgap value, its color should be in the range of yellow to green [125]. In this case, the color of deposition may determine the extent of SiC deposition. However, SiO_2 is always reported as white or colorless crystalline. Different colors can also be found because of light scattering for the small particles. In this case, further quantitative analysis of deposition extent may still be needed in future.

For the experiment with H_2+N_2+siloxane and N_2+siloxane as the fuel, which had lower hydroxylation of the surface, deposition resulting from L4 is much less than from D4. After introducing H_2O in the fuel, which results in more hydroxyl groups, the chemical adsorption process accelerated and the extent of L4 deposition increased significantly.

M. Schweigkofler et al. reported that compared with linear siloxanes, many types of absorbents, including silicon and carbon-based material, show higher adsorption

ability for cyclic siloxanes [153]. Besides the adsorption process, linear siloxanes also have much higher desorption efficiency than cyclic siloxanes because linear siloxanes can also be absorbed physically without any transformation. In some cases, large molecule linear siloxanes can convert to L2 after desorption from absorbents [154]. Based on this insight, the assumed L4 and D4 adsorption and desorption processes on the YSZ pellet surface are presented in **Fig. 4.12**. The D4 contamination is believed to result in more degradation for SOFCs' anode due to its high adsorption and low desorption ability on YSZ compared to L4. The pellets' XRD results with D4 and L4 contamination in **Fig. 4.7** and **Fig. 4.8** show the different peak positions SiO_2 and SiC as depositions. It refers to the crystalline difference of D4 and L4 deposition even with the same composition. This may also be explained by the adsorption and desorption process difference for D4 and L4 on the YSZ pellets. As the initial step of siloxane deposition, the adsorption process difference may cause the significant divergence in next deposition reaction steps.

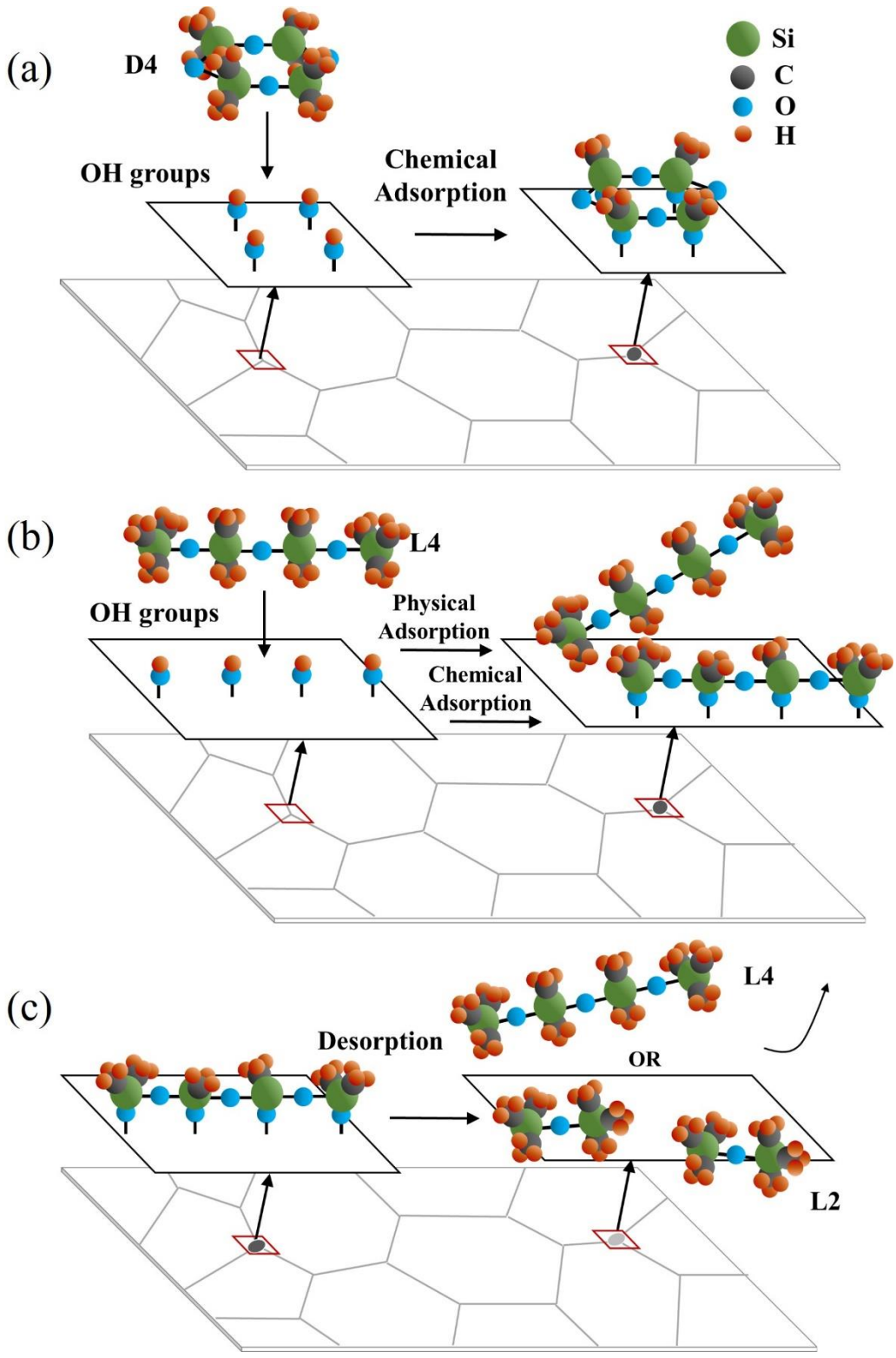

Figure 4.12 D4/L4 chemical adsorption and desorption on the YSZ pellet surface.

Besides the differences in D4 versus L4 deposition, there are other interesting results to discuss. For siloxane pellet experiments, introducing H_2O to the fuel accelerates the siloxane deposition which can be explained from the chemical adsorption process as discussed in the previous section. However, this can't explain why the wet fuel reduces performance degradation with siloxane contamination which has been reported in previous work [84]. There must be other factors also resulting in Ni/YSZ anode degradation besides siloxane deposition on the YSZ. Our previous work [84] suggested that sufficient H_2O in the fuel could prevent carbon deposition on the Ni which is considered as a good catalyst for hydrocarbon reforming reactions [101]. In this study, some evidence can also be provided. For siloxane deposition composition analysis tests, XRD and Raman tests both show carbon-based compounds, such as SiC in XRD tests and strong amorphous carbon signals in Raman test after D4 deposition. Existing $(-C{=}C-)_n$ and CH_x groups on YSZ surface are also evidence of early stages of carbon deposition.

Besides carbon deposition, degradation of silver current collector (also considered as electrode for pellet experiments) due to siloxane contamination is also demonstrated by this study. Silver, also known as an interaction catalyst of oxygen [155], can also be attacked by carbon and silicon, like Ni in the anode. From **Fig. 4.4**, the siloxanes prefer to deposit around the silver/YSZ interface. The degradation of silver current collector/electrode can also be verified by electrochemical characterization analysis from

Fig. 4.11 in which an obvious impedance increase can be noticed after siloxane contamination. Direct evidence of siloxane deposition near the silver current collector also can be provided by **Fig. 4.13**. A SEM/WDS mapping results of the pellet experiment with H_2+N_2+H_2O+D4 as fuel provides evidence that the silicon is deposited around silver grain. These results all suggest that silver is extremely vulnerable to siloxane contamination. Moreover, for the setup in this study, the failure of the silver current collector not only leads to poor conductivity for electrochemical reactions, but also creates leakage around the anode. This can also cause a significant performance loss for the SOFC. In future work, siloxane deposition on silver and nickel still needs to be addressed.

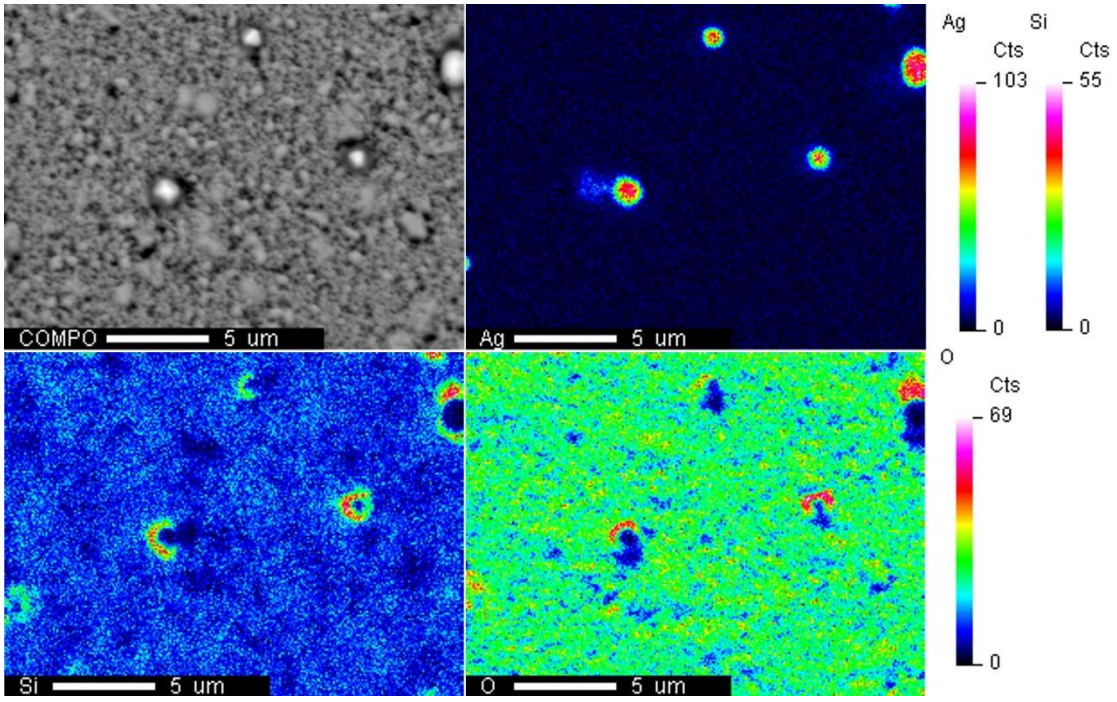

Figure 4.13 Siloxane deposition around silver grain.

4.8 Conclusions

In this study, D4 and L4 are used to represent cyclic and linear structure siloxanes, respectively, to investigate contamination of SOFCs utilizing biogas. SOFC degradation experiments with H_2+N_2+L4/D4 as the fuel were conducted. According to polarization curves and EIS results, the SOFC in the experiment with D4 as contamination source had higher degradation than with L4.

To reveal the reason causing the SOFC degradation difference by cyclic and linear structure siloxanes and also investigate the relationship between the chemical adsorption of siloxane and deposition process on YSZ, pure YSZ pellet experiments with H_2+N_2+H_2O+D4/L4, H_2+N_2+D4/L4 and N_2+D4/L4 as the fuel were conducted. Postmortem analysis including SEM/WDS, XRD and Raman all indicated that the deposition from D4 was more significant than from L4, in general. Among these experiments with different surface hydroxylation extent, H_2+N_2+H_2O+D4/L4 experiment had the most deposition due to more hydroxyl groups. Considering that the siloxane deposition process is highly dependent on the extent of the surface hydroxylation, it can be concluded that the YSZ surface chemical adsorption process is a critical step. Thus, the high adsorption and the low desorption rates of cyclic siloxane compared with linear siloxanes on YSZ may explain the deposition and SOFC degradation. The importance of the siloxane adsorption in the degradation process has been emphasized again in this chapter.

Besides silicon deposition, carbon deposition including SiC and amorphous carbon was also noted from XRD and Raman results due to siloxane contamination. Electrochemical characterization results from the YSZ pellet experiments also support that silver current collector accelerated siloxane deposition which can cause the SOFC performance degradation.

5 FAILURE ANALYSIS OF SOLID OXIDE FUEL CELLS NI-YSZ ANODE DEGRADATION UNDER SILOXANE CONTAMINATION ANODE

5.1 Introduction

From the previous chapters, the degradation of the SOFC Ni-YSZ anode due to siloxane contamination has been investigated by exploring the role of the fuel compositions, anode materials and type of siloxanes. However, the entire anode failure process still needs investigation. Generally, the failure of SOFC anode can be attributed to the combination of different degradation mechanisms. For the solid oxide fuel cells (SOFCs') anode, several degradation mechanisms including intrinsic degradation, Ni-agglomeration, densification/sintering, sulfur poisoning, carbon and silicon deposition all contribute to the overall cell performance loss. Generally those mechanisms can be categorized into two types [36]. One type of degradation results in gradual performance decay such as intrinsic degradation, Ni-agglomeration and densification/sintering [37,38]. For external sources of contamination, mechanisms like sulfur poisoning or carbon and siloxane deposition, there is also the gradual/soft degradation period initially which is similar to the gradual degradation mechanism. However, an obviously even sudden failure occurs after the gradual decay over a relatively short period of time.

External sources of contamination like sulfur and carbon have been explored for many years [16,19,161,162,75,108,127,156–160]. For anode poisoning by hydrogen sulfide, Li et al. reported that the sudden failure due to H_2S poisoning mainly happened

after a 5 minutes stable period at 0.2% contamination [163]. During exposure to ppm level concentration of H_2S there are hundreds of hours of soft degradation period initially and then obvious failure happened within hours shown in the research from Rasmussen et al. [157]. Compared with H_2S, the anode degradation mechanism due to carbon deposition also exhibits separated soft and rapid degradation periods but comparably longer failure time. In the study from Koh et al. [100], with dry methane as the fuel, the SOFC experienced around 250 hours of relative stable/slow degradation and then a significant performance loss. Similarly, Dhir et al. [164] reported the failure event happened after nearly 4 hours of stable operation under 0.625 A cm^{-2} current density with pure methane fuel.

Similar to sulfur and carbon, the SOFC anode failure process for silicon from siloxane contamination should also follow a similar trend with other external contamination sources. However, there are only limited reports about SOFC failure process due to siloxane contamination. Madi et al. reported over 800 hours single cell and over 100 hours of stack gradual degradation with ppm level D4 siloxanes contamination [65,72]. Papurello et al. demonstrated 50 hours slow performance degradation process with ppb level of D4 siloxanes [60]. 100 hours of soft performance degradation of SOFCs has been reported by Kikuchi et al. [16] with ppm level D5 siloxanes contamination. Our previous research [84] with different fuels mixed with ppm level D4 siloxanes also showed the gradual degradation process over 150 hours. To date, most of the degradation

studies for siloxane contamination occurred in the slow degradation period. There is only one exception with Haga et al. [76] reporting the failure period of SOFCs with ppm levels of D5 siloxanes at different temperatures within 40 hours. However, no detailed failure analysis has been reported.

For some gradual anode degradation mechanisms whose degradation extents are proportional to the stress level, such as temperature and current density, the performance loss can be predicted by accelerated lifetime tests with aggravated stress [36,37]. However, anode aging especially with extrinsic contamination sources is hard to predict due to separated stable and rapid degradation processes with significantly different degradation rates. For industrial applications the fuel quality criteria with tolerances to different impurities under the certain concentrations is applied empirically to confirm the cleanliness of fuel and prevent short-term failure of cells [165]. However, reports on the tolerance concentration vary due to dependence on the type of cells and operation conditions [56]. The failure event (joint point between stable and fast degradation) is extremely important for degradation mechanism studies and degradation predictions related to external contamination sources. For hydrogen sulfide, an acceleration experiment suggests that the sulfur/sulfide composition, such as nickel sulfide, generated at the active layer of anode near anode/electrolyte interface causes the fast degradation and failure of SOFCs. No obvious sulfur deposition was found on the anode surface which indicates the diffusion layer of anode did not influence the sulfur poisoning

significantly [163]. However, for siloxane contamination, the studies mainly focus on the slow degradation step. Not enough SOFCs' failure analysis has been conducted.

In this study, an acceleration poisoning experiment is conducted with 0.5% D4 siloxane contamination to focus on the failure analysis of Ni-YSZ SOFC anode. To investigate the influence of electrochemical polarization on the failure of the SOFC due to siloxane contamination, the experiments were conducted at open circuit voltage (OCV) and 50 mA cm^{-2} current density conditions. Simultaneously, exhaust gas component analysis is implemented to verify the previously proposed degradation process.

5.2 Fabrication and Methods

Electrolyte supported SOFCs were fabricated and utilized for the failure study. Most previous studies reported siloxane deposition occurred in the anode support layer (ASL) instead of the anode active layer (AAL) and utilized anode supported SOFCs [72,84]. With an anode supported SOFC and deposition occurring in the ASL it is difficult to investigate the influence of the electrochemical reactions on the siloxane deposition process. The thin anode layer in this study can reduce the impact of gas diffusion-related processes by shortening the effective diffusion thickness. This is considered an important feature of this study as diffusion limitations and changes in the microstructure of the electrochemical active region have been cited previously as the cause of degradation from siloxane contamination [74,75]. The supported yttria-stabilized zirconia (YSZ, $(ZrO_2)_{0.92}(Y_2O_3)_{0.08}$,

Fuelcellmaterials) electrolyte was prepared by die pressing and pre-sintered at 1100 °C for 4 hours. The wet power spray technique was utilized for the NiO+YSZ (60:40 w/w, Fuelcellmaterials) anode layer. The YSZ electrolyte and NiO-YSZ anode were co-sintered at 1400 °C for 4 hours. Strontium-doped lanthanum manganite (LSM, $(La_{0.80}Sr_{0.20})_{0.95}MnO_{3-x}$, Fuelcellmaterials) + YSZ (50:50 w/w) cathode was deposited on the electrolyte by wet powder spray. LSM-based cathode was chosen due to its low degradation rate compared to other cathodes in order to ensure the degradation observed in the fuel cell performance is primarily a result of siloxane contamination [88]. The cell was sintered at 1100 °C for 2 hours in air. After sintering, the thickness of electrolyte, cathode and anode are ~ 380 μm, ~ 20 μm and 17 μm, respectively.

For electrochemical characterization, electrochemical impedance spectroscopy (EIS) measurements were carried out with an Electrochemical Impedance Analyzer (Solartron Analytical Energylab XM) in a frequency range from 10^6 Hz to 0.1 Hz. All EIS measurements were conducted under open-circuit voltage (OCV) with 10 mV signal amplitude. The SOFCs' performance was also evaluated with polarization (j-V), power density and constant current operation (V-t curve) curves. The data was measured with four-probe technique and recorded by a digital SourceMeter (Keithley 2460) interfaced with LabView on the computer.

Fig. 5.1 shows the experimental setup utilized for the SOFCs' failure study with D4 siloxane contamination. The SOFCs were placed on the top of a quartz tube and sealed

with silver paste. Silver ink was painted on the center of the cathode for current collection with 0.495 cm^2 active area. A pair of silver/steel wires were attached to the anode and cathode surface as probes for electrochemical measurements. For the anode fuel supply, H_2 and N_2 flow rates were controlled by Brooks Delta II smart mass flow controllers (MFCs) with LabView interface. To obtain the targeted siloxane concentration in the fuel, the liquid phase D4 siloxane was delivered to the fuel pipeline at a controlled flow rate by a syringe pump (PumpSystems Inc.). The D4 siloxane was vaporized with heat added from resistive heaters wrapped on the gas delivery pipe and carried to the SOFCs' anode by the H_2 and N_2 gases. To ensure the D4 siloxane maintained gas phase (D4 boiling point is about 176 °C) the T-type thermocouples (Omega) were mounted along the fuel delivery pipe for temperature inspection. The heat generation rate of the wrapped resistive heaters were adjusted individually to ensure the whole gas delivery pipeline maintained a stable temperature around 200 °C. The D4 siloxane flow rate was controlled at 0.1 standard cubic centimeters per minute (sccm). In order to have a good comparison with previous work [8,84,102], the H_2 flow rate was maintained constant at 7 sccm. The flow rate of N_2 gas was fixed at 12.9 sccm with the primarily purpose of diluting the concentration of the D4 siloxane, similar to previous experiments [84]. For the SOFC accelerated degradation or failure studies, the external contamination sources were always mixed into the fuel with relatively large concentrations compared to the real application to highlight their influences. For H_2S, generally, the contamination

concentration can be found in ppm level for the biogas application. To accelerate the degradation process and reaction in the SOFC anode, 0.2 to 10% were selected for some studies [163,166,167]. Similarly, the total flow rate of fuel gases (H_2, N_2, D4) was held at 20 sccm resulting in a D4 concentration of 0.5%. The cathode was exposed to the air in the vertical furnace and the air supply was implemented through natural convection.

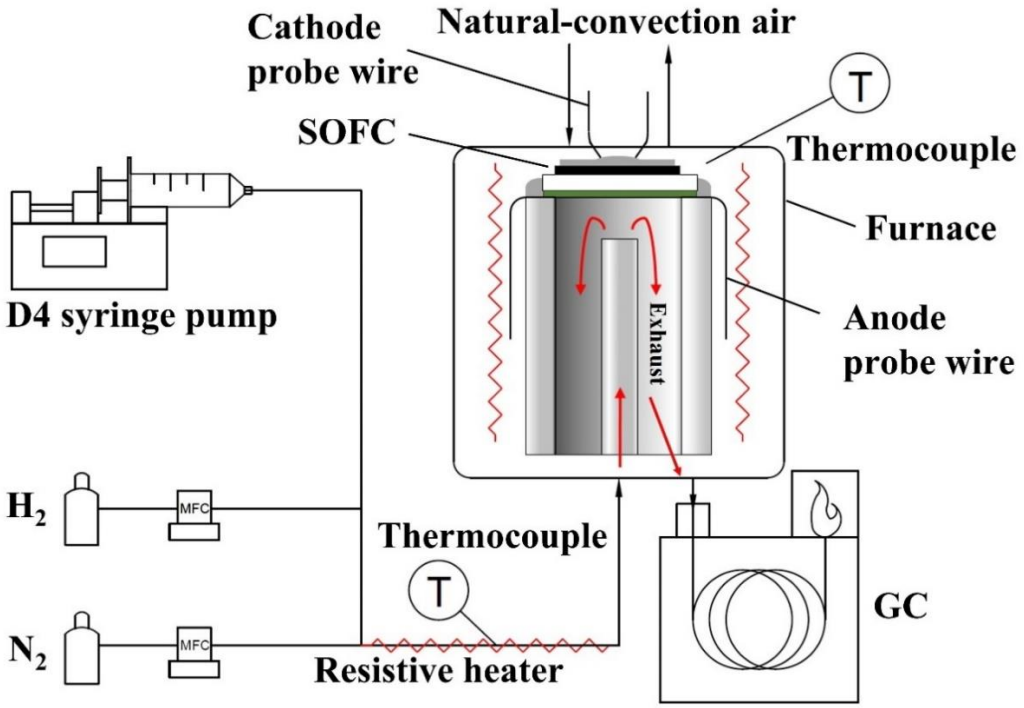

Figure 5.1 Schematic of the experiment setup for the failure study.

For all experiments in this study, the quartz tube reactor was fixed in the center of the vertical furnace. The furnace was heated at 5 °C per minute to an SOFC operating temperature of 800 °C. A K-type thermocouple inside the furnace near the SOFC was utilized to confirm the temperature. Before starting experiments, the YSZ-NiO SOFC

anode was supplied with H_2 and N_2 at flow rates of 10 sccm individually for 4 hours to reduce the NiO to Ni. To avoid the impact of anode intrinsic degradation which typically occurs in the first few hours of operation, the SOFC was operated with the same flow rate of H_2 and N_2 for 24 hours. After stabilizing the performance of the SOFC, D4 siloxane was added to the mixture and the flow rates were adjusted to the values previously described. To have a better understanding of the failure process of the anode by siloxane contamination, three different special points were analyzed during the failure process. The first point (i.e., point 1) is right after the siloxane contamination started. This point is the baseline for the failure process and also provides a chance to investigate the initial status of the degradation. The next and the most important point (i.e., point 2) is when the failure event begins because it may reveal the reason for the anode failure and detailed information about why the anode starts to degrade much faster after this point. The last point (i.e., point 3) is before the total failure of the SOFC. Comparison of this point with the second point at the failure initiation allows the rapid degradation and failure process to be analyzed. Electrochemical characterization tests were conducted with continuous V-t curves, and polarization and EIS results under both OCV and 50 mA cm^{-2} current density conditions were obtained at the three special points. For morphology and Photoelectron Spectroscopy (XPS) analysis, three samples obtained at each of the three different points are also necessary to represent the corresponding microstructure features. The exhaust gas composition was analyzed by a gas chromatograph (GC, Shimadzu FID-

GC2014) sample obtained at each point. In order to eliminate the disturbance that exhaust gas analysis could have on the electrochemical tests, they were conducted separately and both types of experiments were repeated several times with consistent results obtained each time. Considering that point 1 represents the initial status for the degradation process and should not have a significant difference in OCV and 50 mA cm^{-2} conditions, a single test for morphology, XPS and gas composition analysis was conducted instead of two to simplify the entire experimental process at this point. More details and description of these three special points can be found in the results section.

After the failure experiments, the samples obtained for morphology tests were crosscut and embedded in epoxy. The cross section of the samples were prepared by polishing with different grain size SiC papers, water-based diamond suspension and colloidal silica diamond suspension. More details about the sample preparation process can be found in our previous paper [84] which utilized similar techniques. The morphology of the SOFCs' cross section was investigated by a field emission scanning electron microscope (FESEM, JEOL JXA-8530F electron microprobe) equipped with wavelength-dispersive spectrometers (WDS). The electron beam was selected as 15 kV at 5×10^{-8} A for the SEM and WDS analysis.

5.3 Electrochemical Characterizations

For the SOFC D4 contamination failure experiments, nominally identical cells

following same fabrication processes were utilized for the OCV and 50 mA cm^{-2} conditions. The cells' voltage changes as a function of time under D4 contamination as shown in **Fig. 5.2**. The OCV of the SOFC is about 0.92V which has a good correspondence with the theoretical OCV calculation from Nernst equation based on diluted H_2 and O_2 as the fuel and oxidizer. Generally, the entire failure processes for the two experiments shared a similar pattern. As described in the introduction section, the SOFC failure process with siloxane contamination coincides appropriately with typical external contamination aging curves. The long and soft degradation period occurred at the beginning of the aging tests. The OCV declined from 0.92 V to 0.90 V during the first 95 minutes. For the SOFC operating at 50 mA cm^{-2}, the voltage decreased from 0.77 V to 0.73 V in 90 minutes. Subsequently, after the soft degradation period, the failure initiation events which have been marked as point 2 on the plot, appeared in both situations. Much higher degradation rates occurred after the initial failure point causing the sudden absolute failure of the SOFCs. Comparing the results from the OCV and 50 mA cm^{-2} experiments, the SOFC operating under polarization conditions had a faster failure process than when operating at OCV. This can be concluded from the fact that the 50 mA cm^{-2} experiment was about 5 minutes faster to reach the failure event point (point 2). Furthermore, from the initial failure event to complete failure, the 50 mA cm^{-2} experiment also has a higher degradation rate (0.04 V/min) compared to the OCV experiment (0.01 V/min). An interesting phenomenon can also be observed during the sudden failure

process when a short, relatively lower degradation rate process occurs around point 3 labeled in the plot in both 50 mA cm^{-2} and OCV cases. To confirm the reliability of the galvanostatic results, the uncertainty and repeatability analysis are presented in Appendix A.

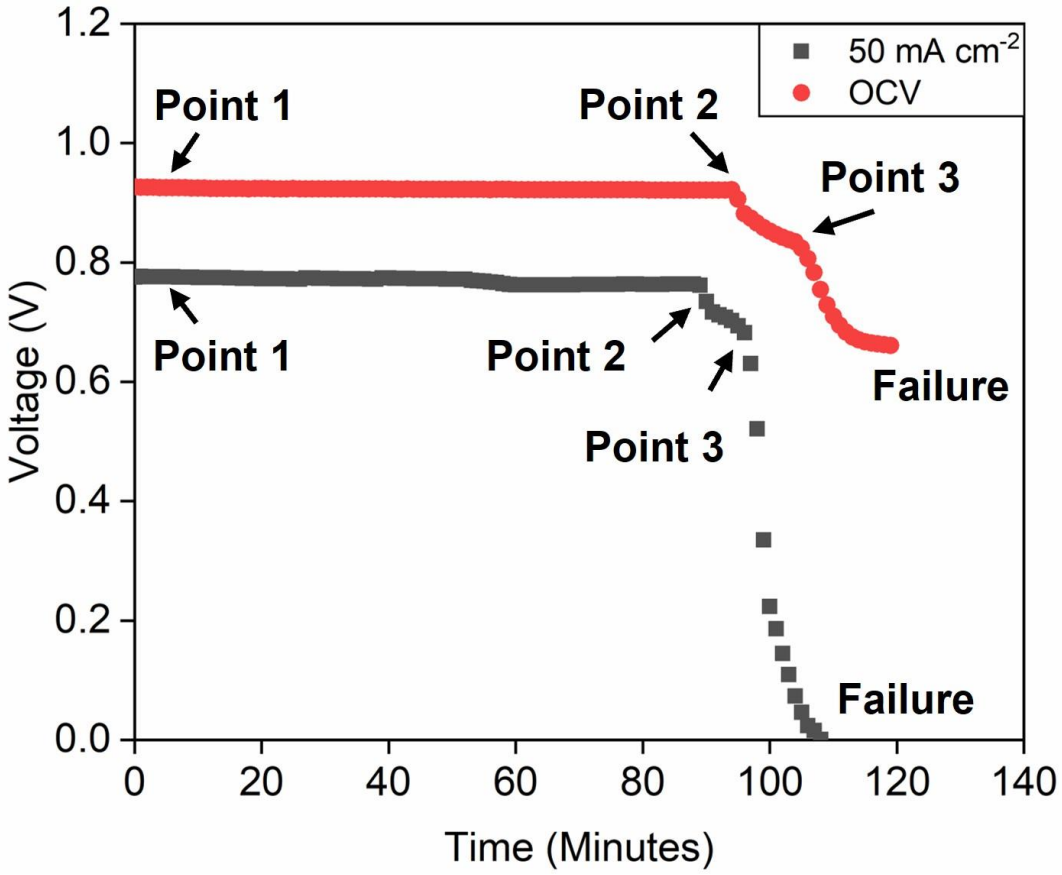

Figure 5.2 The voltage changes of SOFCs under OCV and 50 mA cm^{-2} with 0.5% D4 siloxane contamination at 800 °C.

Besides the constant current density test, polarization curves were also obtained to characterize the degradation as shown in **Fig. 5.3**. In order to have a quantitative investigation of the degradation processes at certain essential points such as initial

degradation, initial failure event, and the transition to sudden failure process, the measurements were implemented after point 1, 2 and 3. The maximum power density of the electrolyte supported SOFCs were reported from ~ 100 mW cm^{-2} to 300 mW cm^{-2} normally [168,169]. For this work considering the thickness of the electrolyte and the anode, the hydrogen concentration and total flow rate, the maximum power density at the point 1 was around 87 mW cm^{-2}. With a similar trend as the V-t curves in **Fig. 5.2**, the polarization curves in **Fig. 5.3** also demonstrate a relatively slow degradation process with less power density loss from point 1 to point 2 and larger power density decrease after the initial failure event (point 2) corresponding to the faster degradation process. For the OCV experiment, from point 1 to point 2, the maximum power density loss is about 8.86 mW cm^{-2}. In contrast, the SOFC maximum power density in the 50 mA cm^{-2} constant current density experiment decreased 41.44 mW cm^{-2} between point 1 and 2. This larger loss in power density is believed to be connected to the faster degradation rate after observing the initial failure event and is correlated with the higher voltage loss observed during the measurement process (**Fig. 5.2**).

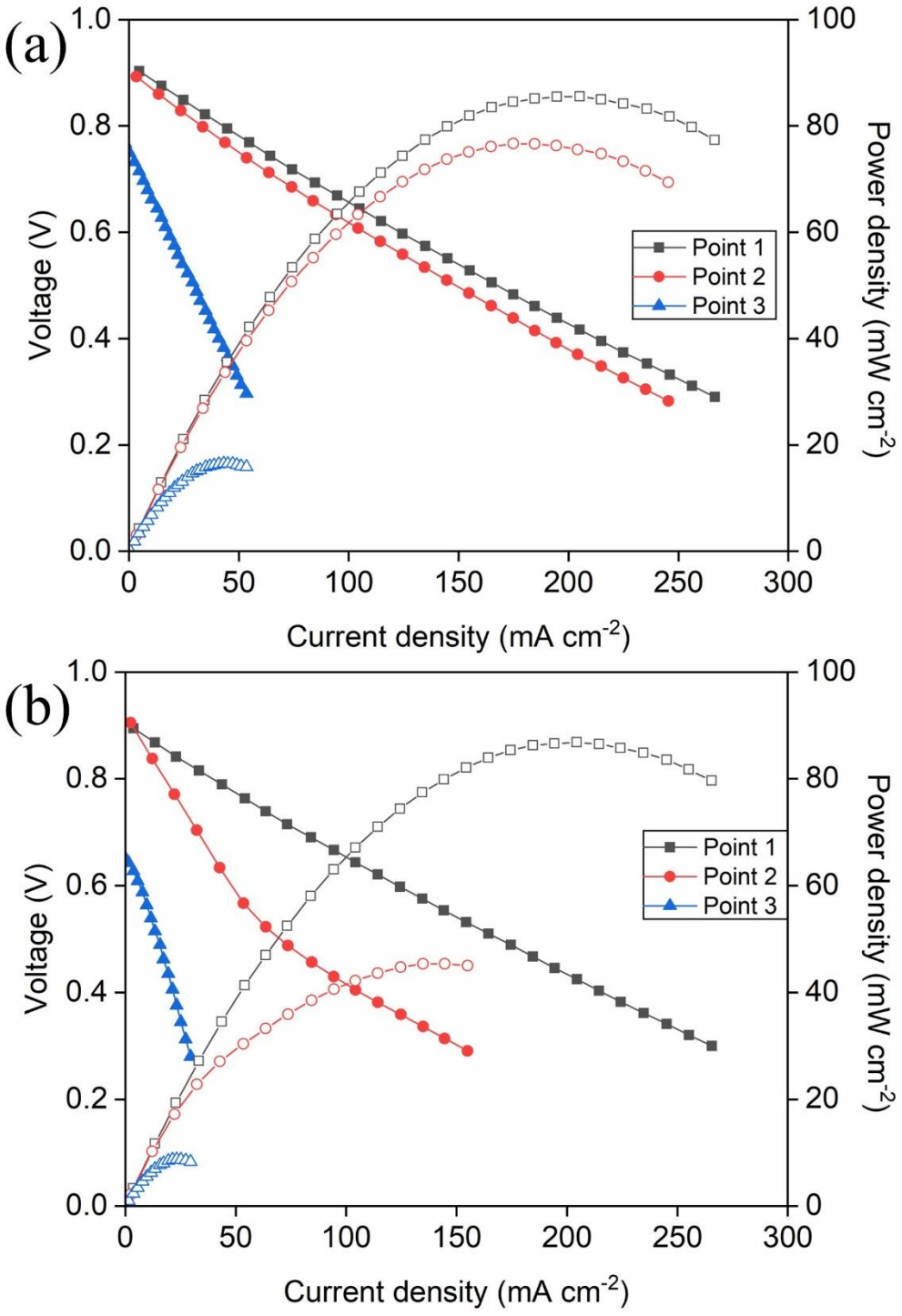

Figure 5.3 Characterization of SOFC performance degradation by polarization curve (a) under OCV and (b) 50 mA cm^{-2} current density operation.

5.4 Transmission Line Equivalent Circuit Modeling Analysis

In addition to the polarization curves, the EIS measurements were also utilized for the failure process analysis. From **Fig. 5.4**, obvious impedance increase can be noticed in both the OCV and 50 mA cm^{-2} current density experiments. With a similar trend to previous electrochemical characterization results, the total impedance increase for the 50 mA cm^{-2} constant current density experiment is much larger than the OCV experiment. In order to have a detailed quantitative analysis of the EIS results, an equivalent circuit model (ECM) was developed. Based on the SOFC with Ni-YSZ anode complex equivalent circuit models studies accomplished by Dierickx and Sonn et al. [44,49,129,170], the ECM was built up with one resistor for ohmic resistance polarization, one Gerischer element attributing to cathode process, one Warburg element representing the diffusion process and one two-channel transmission line model (TLM) for anode process. The TLM application in this study instead of the ordinary RQ element for the anode process can disclose more detailed information for the degradation of ionic transport and charge transfer in the failure process. Complex nonlinear least-squares (CNLS) fitting was utilized to analyze the impedance spectra with the commercial software Zview. For all ECM fitting results, χ^2 values were below 0.001. The TLM shown in the **Fig. 5.4** inserts is the distributed equivalent circuit element named "DX11-Bisquert 2" available in Zview. The model parameters for both OCV and 50 mA cm^{-2} show an excellent agreement with the other electrochemical results shown in **Fig. 5.2** to

Fig. 5.4. The specific resistance values for the anode degradation are listed in **Table 5.1** from the ECM. The ohmic resistance, ionic transport resistance, charge transfer resistance and gas diffusion resistance corresponding to anode are denoted by R_{ohm}, r_{ion}, r_{ct}, and R_W, respectively.

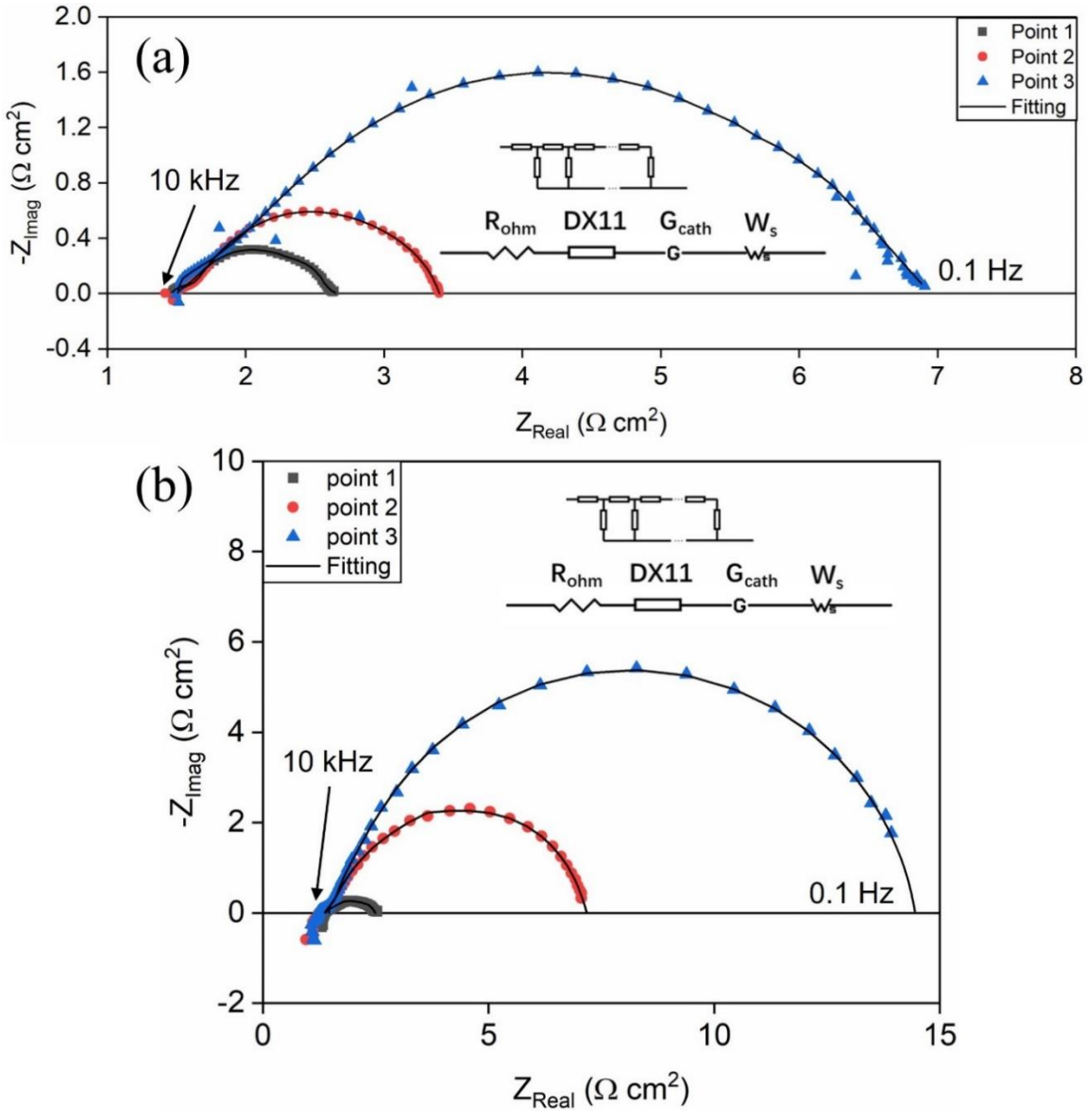

Figure 5.4 Electrochemical analysis of the SOFC failure process by EIS and related equivalent circuit model (a) under OCV and (b) 50 mA cm^{-2} current density operation.

Table 5.1 Equivalent circuit fitting results for anode degradation related polarization resistance.

Experimental Conditions	Time	R_{ohm} (Ω)	r_{ion} (Ω/μm)	r_{ct} (Ω μm)	R_W (Ω)
OCV	Point 1	2.98	0.042	1.23	1.69
	Point 2	3.08	0.049	1.96	1.83
	Point 3	3.08	0.055	2.64	6.33
50 mA cm^{-2}	Point 1	2.68	0.053	1.01	1.43
	Point 2	2.70	0.060	2.49	5.83
	Point 3	3.17	0.061	5.33	15.60

From **Table 5.1**, the ohmic resistance increase is observed in both the OCV and 50 mA cm^{-2} experiments. The larger ohmic resistance increasing for the SOFC operating at 50 mA cm^{-2} may be caused by more serious siloxane deposition which can jeopardize the Ni conductive network through grain boundaries. For ionic transport resistance, only limited increase is observed in both experimental conditions. This phenomenon may be explained by the bulk conduction of oxygen ions through the dense YSZ grains. Hence, the surface deposition of siloxane may not have significant influence on this process [150]. The significant charge transfer resistance increase shown in **Table 5.1** demonstrates the failure of triple phase boundaries (TPB). Besides charge transfer resistance, the most significant resistance increase is from the diffusion polarization. Furthermore, diffusion polarization resistance increase follows the same trend of degradation shown in **Fig. 5.2** and **Fig. 5.3** in which a slow degradation process occurred between point 1 and point 2 and sudden degradation happened after point 2. Similarly, the SOFC in the 50 mA cm^{-2} experiment has much larger diffusion impedance increase

compared to the OCV experiment. Based on the parameters from the ECM results, the degradation appears to be most correlated with the diffusion processes which may be primarily responsible for the failure process.

5.5 Morphology Analysis by SEM-WDS

Fig. 5.5 shows the morphology analysis results at the initial status around point 1 as the reference for the comparison with point 2 and point 3. The left side with the dense layer is the interface between the YSZ electrolyte and Ni-YSZ anode and the anode surface is on the right. From the figure, some random weak silicon signals can be observed in the anode while a thin layer of carbon deposition can also be noticed at the surface of anode. This illustrates that siloxane deposition happened rapidly even at the beginning of the experiment and the carbon deposition may occur at the outer anode surface even before significant silicon deposition. **Fig. 5.6** and **Fig. 5.7** depict the Si, C and O elements distribution over the entire anode cross section for OCV and 50 mA cm^{-2} experiments, respectively. For the OCV experiment in **Fig. 5.6**, compared with the initial status in **Fig. 5.5**, obvious silicon deposition can be detected, especially with silicon accumulation on the anode surface after the failure event (point 2). After point 3, a layer of silicon has been established on the surface of the Ni-YSZ anode (**Fig. 5.6b**). A slight increase in carbon signal can also be perceived from WDS results at point 2 and point 3 following the silicon deposition.

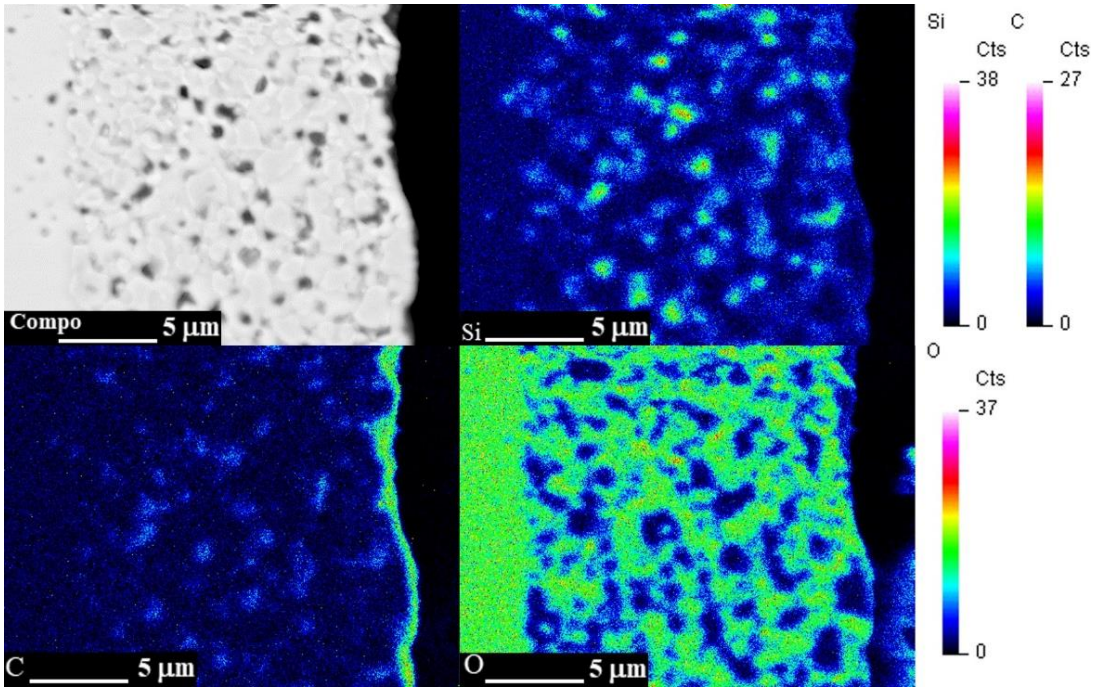

Figure 5.5 SEM /WDS elemental mapping of the SOFC anode after point 1.

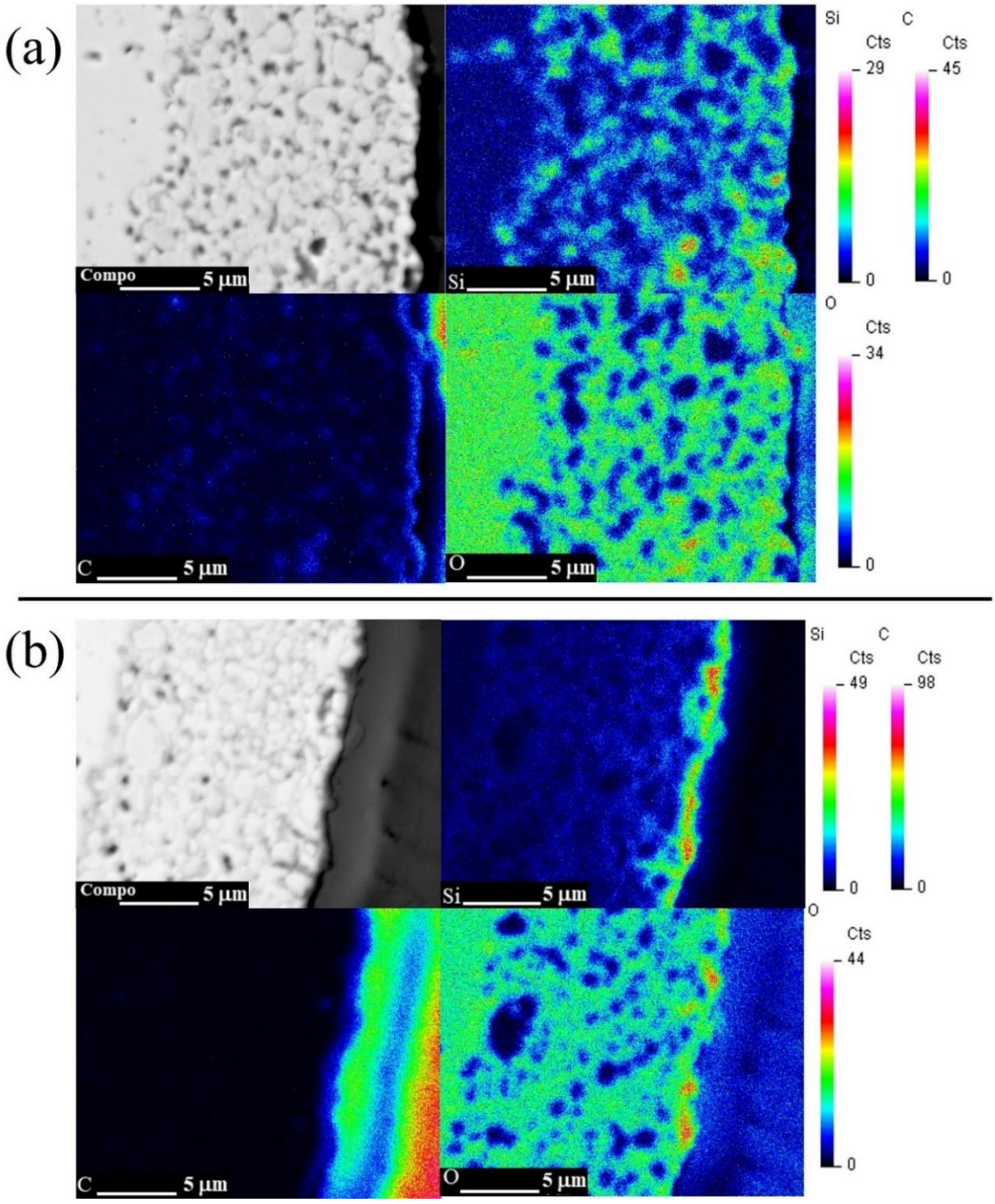

Figure 5.6 SEM /WDS elemental mapping of the SOFC anode during the OCV experiment (a) after point 2 and (b) after point 3.

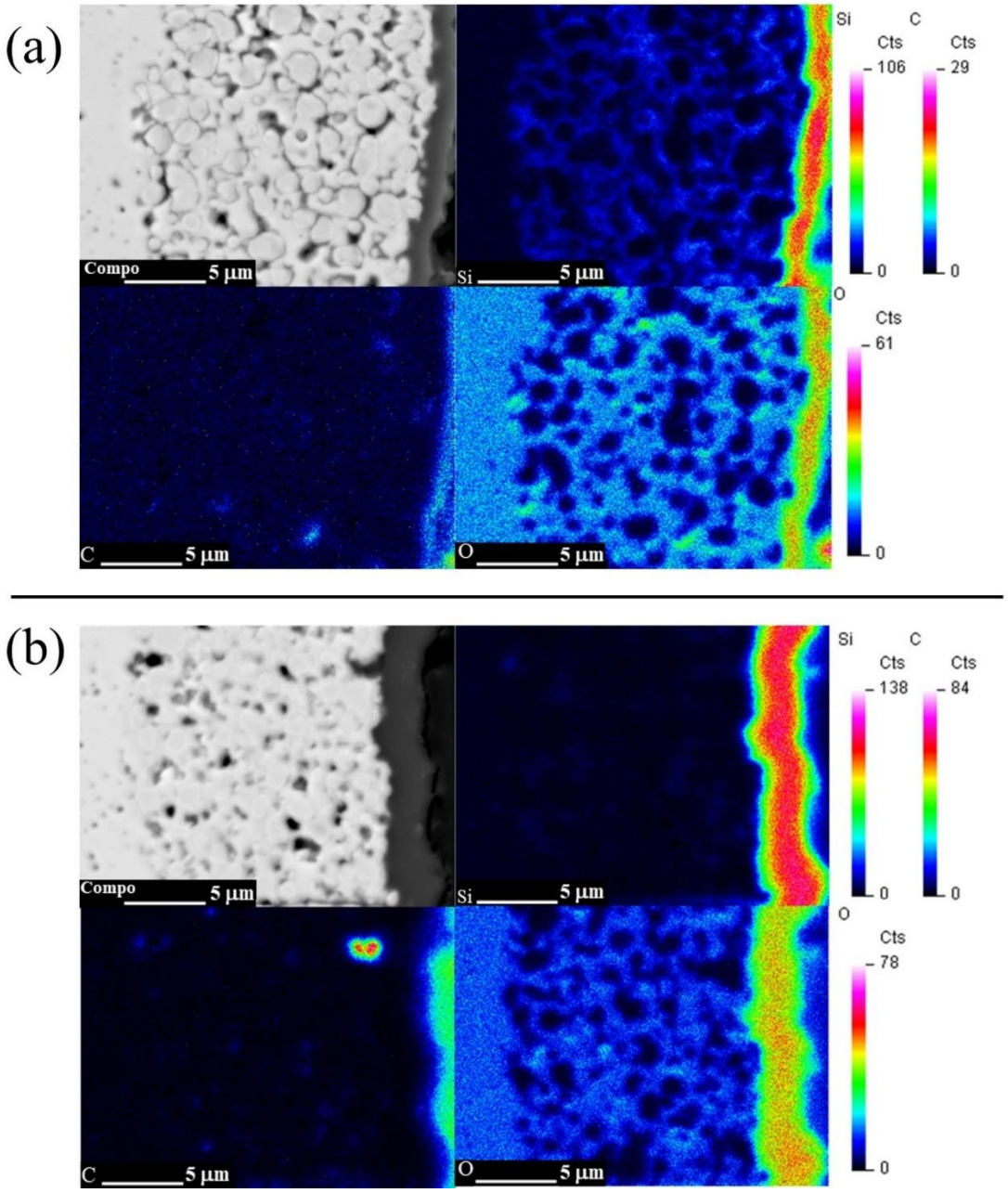

Figure 5.7 SEM /WDS elemental mapping of the SOFC anode during the 50 mA cm^{-2} current density experiment (a) after point 2 and (b) after point 3.

In contrast to the results from the OCV experiment, the experiment under 50 mA cm^{-2} current illustrates a much quicker failure process (**Fig. 5.7**). Even after point 2, a thick layer of silicon deposition appeared on the surface of the anode. The high correlation of

silicon and oxygen elements in the compact layer shown in morphology of the anode surface indicates silicon dioxide may be the composition of the dense layer. Comparing the elements distribution between point 2 and point 3, the surface deposition layer continued to grow until the absolute failure of the SOFC. More carbon deposition on the surface and inside the anode can also be observed compared to the OCV experiment. Comprehensively, the morphology results provide an excellent interpretation for the electrochemical results presented in **Fig. 5.2** to **Fig. 5.4**. The surface deposition layer formed after point 2 is interpreted as causing the sudden SOFC failure due to obstruction of the fuel diffusion path. The region with slightly lower degradation rate observed near point 3 on the V-t curve in **Fig. 5.2** may relate to the dense layer formation process. During the initial dense barrier layer formation phase, since the diffusion paths are not completely closed, the degradation continues at a comparatively slow speed. However, when the entire surface is almost covered by the dense silicon dioxide, dramatic degradation occurs until complete failure.

5.6 Composition Analysis by XPS

To determine the composition of the siloxane deposition, XPS analysis has been conducted on the surface of the Ni-YSZ anode after point 1, point 2, point 3 and complete failure in OCV experiments, respectively. For the contamination element detection, inspired by previous studies [8,84,102] and also the SEM/WDS results in this study, silicon, carbon and oxygen elements were selected as the targets for the spectra. **Table**

5.2 lists the results of XPS analysis of silicon, carbon and oxygen elements by atomic percentage. After point 1 in the OCV experiment, significant carbon deposition can be identified, and only limited silicon deposition can be found. This result is in good agreement with the morphology analysis results for point 1 presented in **Fig. 5.5**. Combining the XPS and morphology results, it can be concluded that at the initial state of siloxane deposition on Ni-YSZ anode, carbon is deposited first. Throughout the failure process the percentage of carbon on the surface continuously decreases. After the initial failure event (point 2), a significant increase in silicon is noted compared with the results after point 1. Coincidently, the sudden performance degradation happened after this initial failure event. From point 2 to complete failure, the silicon element increased gradually. While the percentage of oxygen is also increasing following the silicon, eventually, the ratio of Si:O is near 1:2 after complete failure. This provides strong evidence that the main composition of the deposition layer covering the anode surface is SiO_2. Considering the porous microstructure of carbon deposition [19,59,100,108,171], a relatively dense silicon dioxide layer can be considered as the cause of blocking the fuel diffusion into the anode and causing the sudden failure.

Table 5.2 Results of XPS analysis showing amount of deposition species on the surface in % for OCV experiment.

Elements	Point 1	Point 2	Point 3	Complete failure
Si	2.53	23.66	28.98	30.37
C	55.37	34.8	16.83	10.21
O	31.46	40.35	54.08	59.24

5.7 Exhaust Gas Analysis by GC

In order to reveal the siloxane deposition process on the Ni-YSZ anode, GC is also utilized for exhaust gas composition identification during the SOFC failure process. Besides H_2 and N_2, hydrocarbons and siloxanes can be detected in the exhaust as the compositions related to the products of the siloxane reaction on the anode. Due to the high concentration of siloxane (0.5%), several hydrocarbon components exist in the exhaust as the reaction products as shown in **Table 5.3**. From **Table 5.3**, the main gas phase product of siloxane deposition reaction is CH_4 and a relatively small amount of C_2H_6 and C_2H_4 were also observed. This result contradicts the previous siloxane mechanism shown in equation (1.5) which indicates CO should be the main component in exhaust gas besides H_2. No detectable level of CO was observed in the GC analysis results. The presence of a relatively high concentration of CH_4 also demonstrates the siloxane deposition process is similar to the chemical adsorption process on the anode material surface like equation (1.7) and our previous chapters suggest [8,84,102]. Specifically, the concentration of all hydrocarbons were below the GC calibration concentration after point 1. The highest concentration of CH_4 and other hydrocarbons was detected after point 2 when the fast degradation process occurred. At point 3, when the

SOFC is approaching complete failure, the methane concentration decreases.

Table 5.3 Results of the hydrocarbon compositions obtained from GC analysis of the SOFC exhaust during the OCV and 50 mA cm^{-2} degradation experiments.

OCV	Methane (%)	Ethane (%)	Ethylene (%)
Point 1	<0.6	<0.04	<0.018
Point 2	1.16	<0.04	0.052
Point 3	0.73	<0.04	0.045

In addition to the hydrocarbons, there are over 40 trace level species with detectable peaks in the GC spectra. The long retention time of those species in the spectra suggests they all belong to the heavy molecular weight compositions. Considering the inlet gas composition, there appears a high possibility that they also fall into the siloxane category. Due to the limitation of GC calibration, only 7 of the species having stronger signals can be identified as siloxane L2 to siloxane D5. In order to ensure there are no reactions before the D4 siloxane enters the SOFC, the GC results were also compared with the fuel mixture passing through the straight quartz tube reactor at ambient temperature and at 200 °C. Only 2.7% D4 loss has been detected when the D4 passes through the quartz tube indicating limited or no reactions occurring prior to the SOFC. In this case, all GC results for siloxane can be considered as products of the reactions occurring at high temperature in the reactor and SOFC. The unit of siloxane concentration is mg/m^3 due to the siloxane calibration method. From **Table 5.4**, unexpectedly, only a small amount of D4 can be found after passing through the high temperature SOFC/reactor compared with the inlet

concentration at 0.5% (~38215 mg/m^3) and a much higher concentration of D3, L4, L5 appeared which means D4 is extremely active. At point 1, linear structure siloxane L4 and L5 have been detected which may illustrate the ring-opening and polymerization process for D4 siloxane at the initial state of degradation. At point 2 when the failure event happened, GC results show the similar results to point 1. After point 3, L4 and L5 were replaced by D3 for the OCV experiment. More detailed explanation of the GC results will be discussed in the next part considering the electrochemical and morphology results.

Table 5.4 Results of the siloxane compositions from the GC analysis for the exhaust of OCV and 50 mA cm^{-2} degradation experiments.

OCV	L2 mg/m^3	L3 mg/m^3	D3 mg/m^3	D4 mg/m^3	L4 mg/m^3	L5 mg/m^3	D5 mg/m^3	Total mg/m^3
Point 1	2.25	<0.3	2.12	4.99	69.40	32.81	<3.85	111.56
Point 2	1.99	<0.3	1.93	5.03	73.94	36.30	<3.85	121.41
Point 3	0.94	<0.3	73.00	14.92	1.33	3.21	<3.85	93.39

5.8 Microstructure Parameters Calculation and Discussion

According to the morphology, XPS and electrochemical results analysis, the diffusion process obstruction by dense silicon dioxide deposition is primarily responsible for the failure of SOFC due to siloxane contamination. This conclusion contradicts the previous assumptions [74] that the blockage of the TPB causes the anode failure. Actually, the diffusion blockage failure has been implied by previous studies [65,72,84] which indicate the most severe siloxane deposition is located around the surface of the

anode, typically far from the TPB. Following the SOFC failure investigation, a lifespan prediction of the SOFC can be attempted by connecting microstructure parameters to the essential event in the failure process such as point 2 as the failure event. The microstructure parameters at failure event can also be utilized as a reference to recognize the cell conditions.

Three-dimensional Ni-YSZ microstructure and related geometric parameters have been investigated by focused ion beams (FIBs)-SEM technique for SOFC performance evaluation [109–111]. For the SOFC degradation studies, the FIB-SEM 3D reconstruction was utilized to have a trustworthy quantitative microstructure parameter analysis for electrode degradation including the tortuosity increase and the decrease of the porosity and the length of TPB [111,112]. For the SOFC anode degradation due to the intrinsic silicon contamination, the FIB-TEM technique was applied to the characterization of the SiO_2 segregation and accumulation at the anode/electrolyte interface and Ni/YSZ grain boundaries [113]. Recently, the in-situ, economical and non-destructive electrochemical method was proposed for the electrode's microstructure quantitative analysis. The electrochemical impedance spectra data was utilized for the ECM. Subsequently, the geometry parameters such as the tortuosity factor, length of TPB etc. can be calculated from the resistance values of the elements corresponding to the individual physicochemical process in ECM [53,114,115,129,170]. In this study, the electrochemical parameters obtained from the ECM can also be utilized for the anode microstructure

characterization. The anode transmission line model in this study can also provide more microstructure information which can be applied as the reference for cell performance prediction and also reveal the anode degradation behavior due to siloxane contamination.

Fuel diffusion through the porous Ni-YSZ anode can be simplified to a single Stefan-Maxwell diffusion mechanism governing process [114]. In this circumstance, the gas diffusion polarization resistance can be theoretically given by equation (5.1) for the H_2-N_2 system.

$$R_W = \frac{\tau}{\varepsilon} \cdot \left(\frac{RT}{2F}\right)^2 \cdot \frac{L}{P} \cdot \frac{1}{D_{H_2,N_2}} \cdot \left[\frac{1}{\chi_{H_2}} + \frac{1}{\chi_{N_2}}\right] \quad (5.1)$$

The polarization resistance for ionic transport process can be also calculated by equation (5.2) [129,170].

$$r_{ion} = \frac{1}{\sigma_{ion,8YSZ}} \cdot \frac{\tau_{YSZ}}{\varepsilon_{YSZ}} \cdot \frac{1}{A_{act}} \quad (5.2)$$

The charge transfer polarization resistance for corresponding process at TPB can be obtained by equation (5.3).

$$r_{ct} = \frac{LSR_{ct}}{l_{TPB} \cdot A_{act}} \quad (5.3)$$

In equation (5.1), τ is the tortuosity factor for the fuel diffusion process in Ni-YSZ anode, ε is the porosity of entire Ni-YSZ anode, L is the diffusion length which can be considered as the thickness of the Ni-YSZ anode in this study because the anode is relatively thin. Atmospheric pressure was selected as the pressure of fuel in anode side which was denoted as P in the equations. χ_{H_2}, χ_{N_2} represent the mole fraction of the H_2 and N_2 in the fuel. D_{H_2,N_2} is the binary diffusion coefficient between the H_2 and N_2. The

values of D_{H_2,N_2} was chosen as 2.10 cm^2s^{-1} [114].

For equation (5.2) as the ionic transport polarization resistance equation, $\sigma_{ion,8YSZ}$ is the theoretical oxygen ionic conductivity in 8YSZ. Similar to equation (5.1), τ_{YSZ} and ε_{YSZ} are tortuosity and porosity for the 8YSZ skeleton instead of the entire Ni-YSZ anode. The active electrode area of the anode is denoted by A_{act} in the equation.

The charge transfer polarization resistance can be calculated based on the equation (5.3). The LSR_{ct} represents the line specific resistance of the triple phase boundary in the Ni-YSZ anode and the value of LSR_{ct} can be obtained from the work accomplished by Utz et al. [121,172].

From the calculation based on previous equations, the ratio of porosity to tortuosity $\frac{\varepsilon}{\tau}$ can be obtained from the effective diffusion coefficient ($D_{theoretical} \cdot \frac{\varepsilon}{\tau}$) and effective oxygen ion conductivity ($\sigma_{theoretical} \cdot \frac{\varepsilon}{\tau}$) for the diffusion and ionic conduction polarization resistance. However, the porosity and tortuosity are both important geometric parameters for microstructure degradation investigation. Thus, the separation of these two parameters is necessary from the value of porosity to tortuosity ratio $\frac{\varepsilon}{\tau}$. Due to the fact that 3D microstructure reconstruction is not the purpose for this study, the rough 2D microstructure parameter investigation was conducted by morphology results for each point in the failure process. The porosity, as the relatively straightforward parameter to measure compared with the tortuosity, was acquired from the morphology results for the entire Ni-YSZ anode and YSZ skeleton. The porosity of each point is

presented in **Table 5.5.**

Table 5.5 Results of the anode and YSZ skeleton porosity analysis for the OCV and 50 mA degradation experiments.

OCV	Porosity of entire Ni-YSZ anode (%)	Porosity of YSZ skeleton in the anode (%)
Point 1	14.4	26.6
Point 2	12.7	22.7
Point 3	7.3	21.4

50 mA cm^{-2}	Porosity of entire Ni-YSZ anode (%)	Porosity of YSZ skeleton in the anode (%)
Point 1	14.4	26.6
Point 2	7.4	24.1
Point 3	3.0	21.4

From the ionic transport polarization resistance equations (5.2), the tortuosity of YSZ anode skeleton τ_{YSZ}, can be calculated from the r_{ion} value and porosity. The τ_{YSZ} values for OCV and 50 mA cm^{-2} experiments are around 2.7 and 3.3, respectively, during the failure period. They are all reasonable values compared with the results from previous studies which are 1.9 from Dierickx et al. [129,170] and 4.5 to 6 reported by Nenning et al. [173]. From **Fig. 5.8**, with similar value throughout the experiments, both YSZ porosity and tortuosity for OCV and 50 mA cm^{-2} failure experiments did not have a significant change. This is likely due to the fact that the compact YSZ grains may be impenetrable for siloxane deposition. This result also reveals that the siloxane deposition does not have a significant influence on the oxygen ion conduction process in the anode.

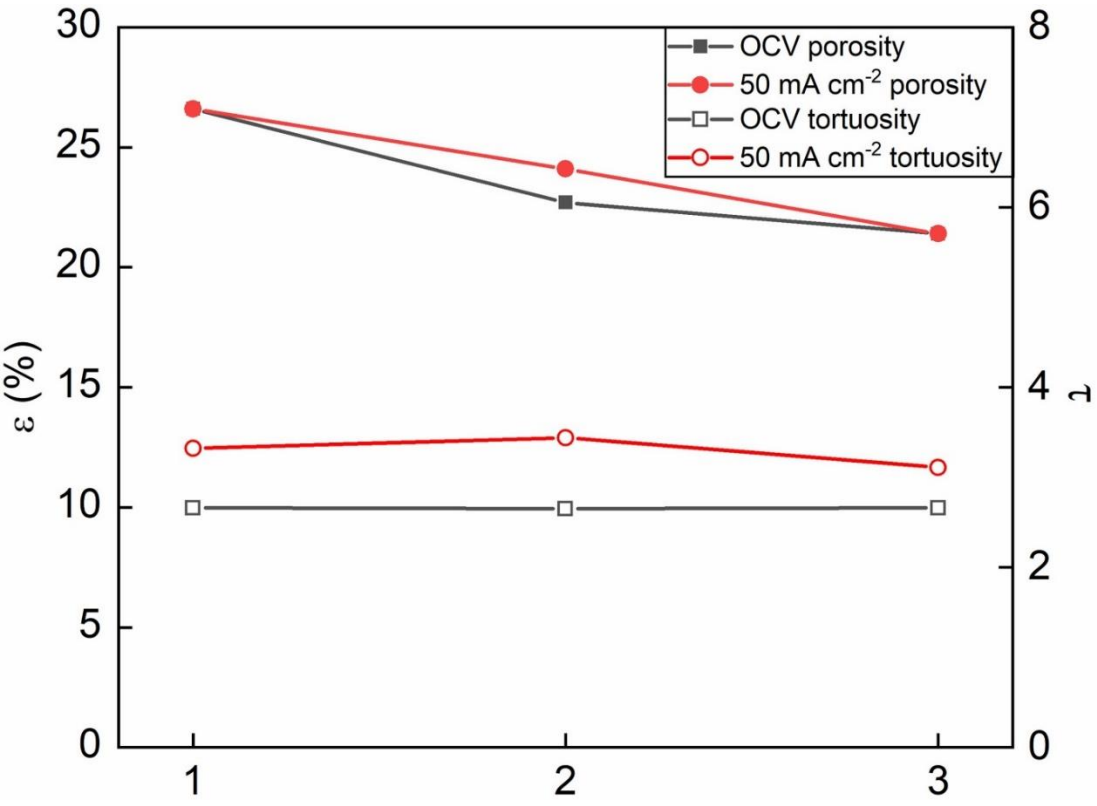

Figure 5.8 The porosity and corresponding tortuosity change of the YSZ anode skeleton during OCV and 50 mA cm^{-2} D4 contamination experiments.

The length of TPB of the Ni-YSZ anode can be obtained by equation (5.3). Shown in **Fig. 5.9**, due to the coverage of TPB by siloxane deposition, the decrease in the length of TPB can be detected. The values of the length of TPB before failure are 0.84 and 0.42 for OCV and 50 mA cm^{-2} experiments, respectively. They are much lower than the values reported by Dierickx et al. [129,170] which range from 1.61 to 2.061 for healthy fuel cells. However, in contrast to the sudden performance degradation of the SOFC after point 2, the TPB degradation process seems to be progressive. With a larger extent of TPB length decreasing, imposing polarization to the anode (under 50 mA cm^{-2}) can be considered as causing acceleration of the siloxane deposition process.

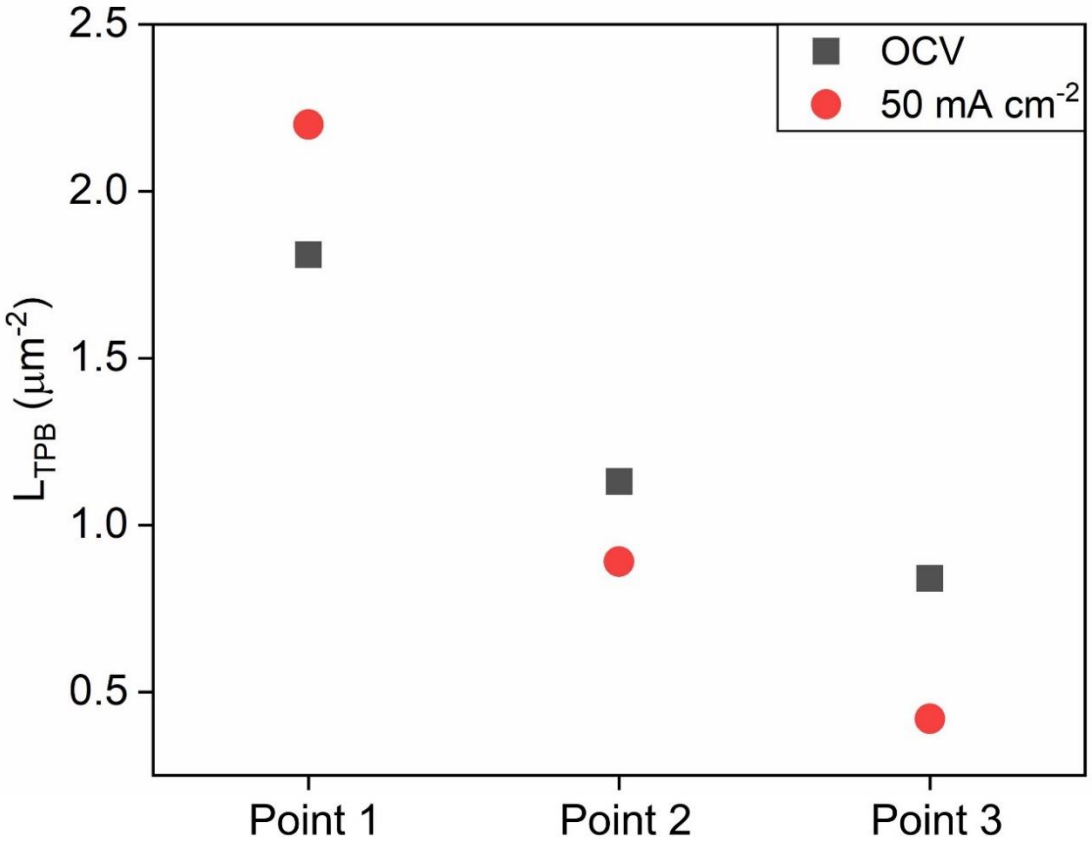

Figure 5.9 The length of triple phase boundary change of the Ni-YSZ anode during OCV and 50 mA cm^{-2} D4 contamination experiments.

For the fuel diffusion process, which is related the eventually failure of the SOFC, the tortuosity of entire anode τ, can be calculated from the R_w value and porosity ε. The change of tortuosity and porosity value of the anode corresponds to the electrochemical and morphology results satisfactorily (**Fig. 5.10**). Generally, the tortuosity decayed from around 2 to 6 for OCV and 50 mA cm^{-2} experiments. The tortuosity values before the total failure are much larger compared with normal values such as 3.034 from Dierickx et al. [129,170]; 1.36 suggested by Zhang et al. [114] and 1.42 to 1.56 reported by Zekri et al. [112]. For the OCV experiment, which had similar trends as the V-t Curve in **Fig. 5.2**

and slow performance degradation occurring from point 1 to point 2, the tortuosity and porosity doesn't change significantly. After the initial failure event (point 2), the microstructure started to decay tremendously in which porosity decreased and tortuosity increased dramatically. For the 50 mA cm^{-2} experiment, also with the same general trends, the decay of microstructure was much faster than the SOFC in the OCV experiment with larger porosity drop. All of these results demonstrate that the failure of Ni-YSZ anode is highly dependent on the degradation of gas diffusion process. One important observation is that the SOFC anode after the OCV and 50 mA cm^{-2} experiments have similar tortuosity values after point 3. It may demonstrate extremely serious coverage of the anode surface near the total blockage of the diffusion path. In this case, the two degraded anodes may share similar tortuosity.

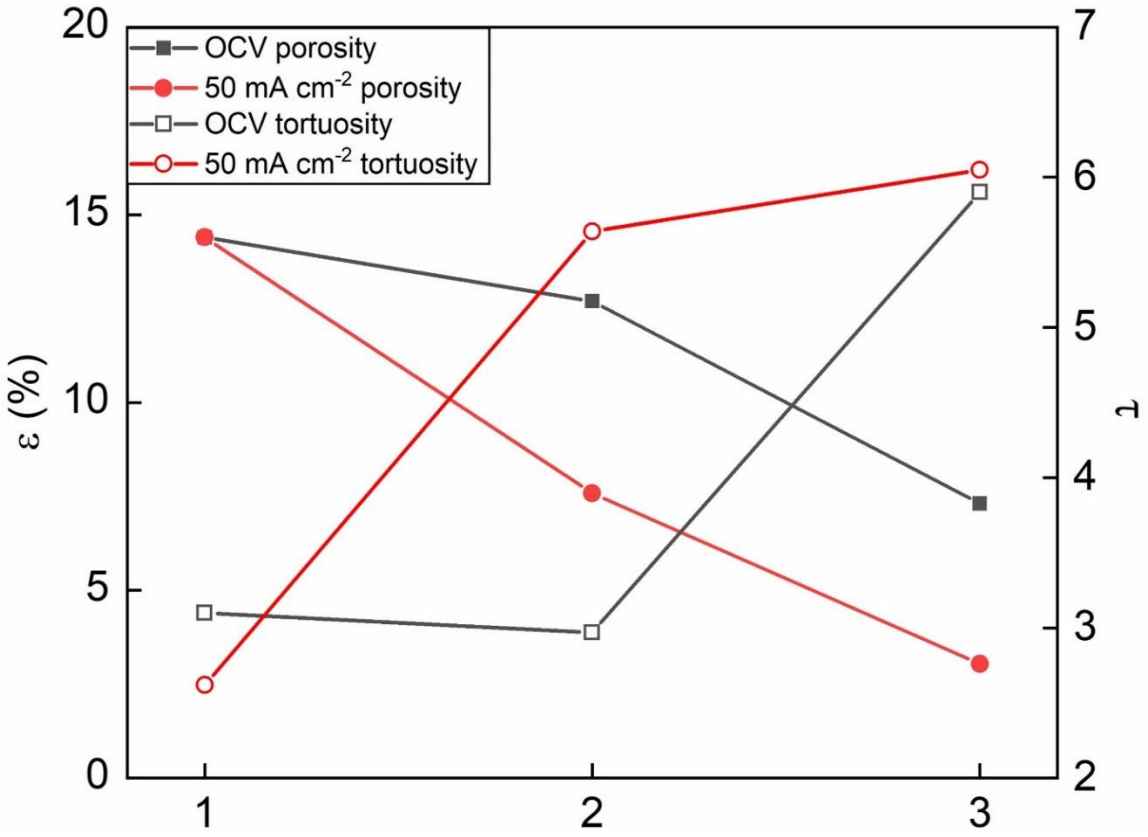

Figure 5.10 The porosity and corresponding tortuosity change of the entire anode during OCV and 50 mA cm^{-2} D4 contamination experiments.

As a summary, presenting those microstructure parameters and related electrochemical data during the SOFC failure process due to siloxane contamination can provide a useful reference for the anode lifetime prediction and also degradation behavior investigation. However, even without accurate 3D reconstruction the microstructure parameters calculated in this section are complementary to other results in this study.

5.9 Discussion

After considering the electrochemical, morphology and exhaust gas compositions

analysis results comprehensively, a more complete picture about the entire anode failure process for siloxane contamination has emerged. Combining the electrochemical and morphology results from **Fig. 5.2** to **Fig. 5.7**, the faster SOFC anode degradation process starting around point 2 is because of the blockage of the fuel diffusion pathway in the anode side. This conclusion can be supported by the much larger diffusion polarization resistance increasing compared with other polarization processes in the whole failure process. The dense layer of SiO_2 on the anode surface from the morphology results also suggests the severe obstruction of the diffusion process. Moreover, the attempted microstructure calculation results from **Fig. 5.9** depict the incomplete invalidation of length of TPB with linear decreasing trend instead of rapid degradation from point 2. This illustrates the TPB still remains active even with the absolute failure of the cells.

For the siloxane deposition studies, valuable information was also provided by the exhaust gas composition analysis from GC. The high concentration of methane and absence of the CO in the exhaust indicate that the siloxane chemical adsorption process assumed in our previous studies is more acceptable than the siloxane reforming mechanism in equation (1.5) in which CO is one of the main products. The carbon deposition from the methane generated by the siloxane adsorption process can form a thin layer on the Ni particle [84] which can be proved both from the SEM/WDS and XPS results at the point 1. The large amount of L4 and L5 siloxane existing at the initial state of siloxane contamination can provide strong evidence to the ring-opening reactions and

the polymerization of D4 siloxane into the anode. Cabrera-Codony et al. [174] also suggested that carbon surface can provide excellent sites for the adsorption and polymerization of cyclic siloxanes. In this case, the initial carbon deposition could accelerate the adsorption process further. Eventually, the amorphous silicon dioxide layer is formed upon the polymerized cyclic siloxanes layer [82]. From the GC results, the replacement of L4 and L5 by D3 may imply the end of the siloxane polymerization process and the starting of the silicon dioxide layer formation process. This step can also be verified by the fact that the appearance of the dense silicon dioxide layer in SEM/WDS always follows the high concentration of D3 generation in GC results for the point 3 in OCV experiment. The large concentration of D3 instead of D4 at the silicon dioxide layer formation phase maybe explained by the theoretical calculation from Vaiss et al. [82] that global silicon dioxide layer formation reactions from the D4 compound are more stable than from the D3. In this circumstance, D4 may directly deposit to silicon dioxide and the part of D4 may concert and remain to D3 due to higher stability of D3 than D4 from the thermodynamic consideration.

In this study, the faster failure process has been observed for the anode operating under polarization contrast with the OCV condition. It can be confirmed from the following results for 50 mA cm^{-2} experiment:

(1) Reaching the failure event faster in the V-t curve.

(2) Larger performance loss and polarization resistance in electrochemical tests.

(3) Starting to form the silicon dioxide layer early from the SEM/WDS results.

(4) Worse microstructure parameters during the whole failure process from the calculation.

Even with experimental uncertainty in the results, which is discussed in Appendix A, faster siloxane deposition for cells under polarization can be determined after considering the evidence comprehensively. Faster silicon dioxide formation may result from direct electrochemical oxidation of the siloxane. This can occur in this study because the siloxane can directly encounter the active layer of the anode due to only 17 μm thickness for the entire anode. Combined with the siloxane deposition behavior discussed before, the faster silicon dioxide formation may also be explained by the quicker adsorption and the establishment of the polymerized siloxane layer. The electrochemical reactions in anode under polarization such as equation (5.4) to (5.6) [92] can also offer different chemical groups. These groups may also accelerate the siloxane adsorption and polymerization process. Generally, much more siloxane compositions found in GC results for 50 mA cm^{-2} experiment can also demonstrate that reaction activity of the siloxane is improved under polarization.

$$O_2 \rightleftharpoons 2O(ad) \tag{5.4}$$

$$H_2(g) + 2O(ad) \rightleftharpoons 2OH \tag{5.5}$$

$$H_2O(ad) \rightleftharpoons OH(ad) + H(ad) \tag{5.6}$$

Enlighten by failure process investigation, the previous ppm level siloxane

contamination anode degradation studies should mostly lay down to the gradual degradation process which consists of the siloxane adsorption, polymerization and starting of silicon dioxide formation process for siloxane deposition around the point 1 to point 2 in this study. Thus, in order to reduce the siloxane deposition with ppm level siloxane contamination in practical applications, these initial steps should be explored more in the future. The blockage of the gas diffusion which is considered as the main anode failure reason in this study can also be relieved by special anode structure design such as separate anode supported and active layer with different porosity.

5.10 Conclusions

In order to investigate the failure process of the SOFCs' Ni-YSZ anode due to siloxane contamination, SOFCs were operated with D4 siloxane contaminating fuel under OCV and 50 mA cm^{-2} conditions at 800 °C. The sudden failure process of SOFCs can be observed after gradual degradation. The electrochemical characterization and morphology results indicate that the blockage of the fuel diffusion process in anode is the key factor resulting in fast failure of the SOFCs. The GC and XPS results at the different stages of the failure process can also provide a valuable reference to further understand the siloxane deposition behavior on the Ni-YSZ anode. The entire siloxane deposition processes including initial carbon deposition, siloxane polymerization and amorphous silicon dioxide deposition were proposed in this study based on morphology, XPS and

GC results. Compared with the OCV circumstance, the SOFCs operating under 50 mA cm^{-2} conditions experienced a faster failure process. This may be explained by the electrochemical processes in the anode under polarization conditions accelerating the siloxane adsorption and polymerization during the siloxane deposition. Generally, this chapter provides evidence for several steps of the siloxane deposition process. The carbon deposition and dense SiO_2 layer formation were confirmed by the SEM-WDS and XPS results. The polymerization of siloxane on the anode surface can also be assumed based on the large molecular siloxane formation by GC detection.

6 CONCLUDING AND OUTLOOK

6.1 Conclusions

Siloxanes, as a type of impurity in biogas, can poison the Ni-YSZ anode of SOFCs. The stable silicon compounds from siloxane deposition in the anode becomes one of the main barriers for SOFCs' biogas utilization. The previously assumed siloxane deposition process proposed in the literature was not verified completely and lacked some essential evidence. In this work, to investigate the SOFC Ni-YSZ anode degradation due to siloxane contamination, the research focused on four aspects: (1) influence of fuel compositions to siloxane deposition; (2) role of each material contained in Ni-YSZ anode on the siloxane deposition process; (3) influence of siloxane structure (cyclic and linear) on its deposition process in Ni-YSZ anode; and (4) entire failure process of Ni-YSZ anode under siloxane contamination.

With different gas compositions in the fuel, the possible reactants, products and the reaction path of the siloxane deposition may be extrapolated through deposition extent comparison. Thus, to investigate the influence of fuel compositions to siloxane deposition, four different experiments utilizing H_2+H_2O, H_2+H_2O+D4, H_2+D4, H_2+CO+D4 and H_2+H_2O+CO+CO_2+D4 as fuels at 750 °C is conducted in this study. The electrochemical characterization and morphology results are analyzed and compared for anode degradation phenomenon. The results contradict the previously proposed degradation mechanism as the experimental results show that water can inhibit the silicon

deposition and anode degradation. The recovery experimental results with simulated bio-syngas (H_2+H_2O+CO+CO_2+D4) show that the SOFCs performance degradation caused by D4 contamination is irreversible.

As the place where the siloxane deposition reaction occurs, the anode materials may also have significant influence on the siloxane deposition process. The function of pure Ni and YSZ in the siloxane deposition process was investigated. The pure Ni/YSZ pellets were exposed to a simulated biogas-reformate fuel with D4 contamination at 750 °C. Morphology and XRD results illustrate that silicon and carbon deposition can both be detected in the Ni and YSZ pellets. Graphite, SiC and SiO_2 are all possible products based on the results of XRD test. Moreover, further investigation of the individual components (Ni, ZrO_2, and Y_2O_3) of the anode on the siloxane deposition process was conducted. The results demonstrated that the heaviest siloxane deposition occurred on Ni pellets, and the deposition process on Ni was also sensitive to the humidity of fuels. For the ZrO_2, and Y_2O_3 pellets, no significant depositions have been noticed in both wet and dry fuels conditions. And electrochemical analysis including electrochemical impedance spectroscopy (EIS), related distribution of relaxation times (DRT) analysis and equivalent circuit modeling with complex nonlinear least square (CNLS) fitting were conducted. A microstructure parameter – tortuosity factor to porosity ratio τ/ε calculated by diffusion polarization resistance was utilized for siloxane deposition evaluation. After comparing pellets surface morphology changes before and

after experiments and τ/ε change following the contamination, Ni is considered as a major factor in siloxane deposition reactions in Ni-YSZ anode.

The type of siloxane may also influence the deposition process. The SOFC Ni-YSZ anode degradation due to different types of siloxane contamination is investigated in this work. Considering the properties difference of ring and linear structure siloxanes, comparison of the deposition results may also provide some evidence of the anode degradation process. In this case, a cyclic structure siloxane, D4, and a linear structure siloxane, L4, are mixed with H_2+N_2 as the fuel for SOFCs at 750 °C. The electrochemical characterization results after stability experiments suggest that the SOFC contaminated with cyclic siloxane, D4, had higher degradation. Pure YSZ pellets with different surface hydroxylation extents were also tested to investigate the D4/L4 adsorption and deposition process. Postmortem SEM/WDS, XRD and Raman analysis all indicate that cyclic siloxane has more deposition than linear siloxane on the anode. Further analysis demonstrates that high adsorption and low desorption rates of cyclic siloxane on YSZ are linked to the degradation. Besides the silicon deposition, SiC and amorphous carbon deposition were also observed from the XRD and Raman analysis.

Considering the previous studies only focus on the early degradation process, the entire failure process of the solid oxide fuel cell Ni-YSZ anode is investigated with D4 siloxane (octamethylcyclotetrasiloxane) contamination. In this regard, the anode degradation process is investigated. In order to evaluate the influence of the

electrochemical reaction on the siloxane deposition process, the SOFC experiments were operated at open circuit voltage (OCV) and 50 mA cm^{-2} conditions at 800 °C. During the failure process, electrochemical, morphology and exhaust gas component analysis testing are conducted at the critical points. Furthermore, the equivalent circuit model and corresponding microstructure parameter calculation for separated physicochemical processes were utilized for the quantitative analysis of the failure process. As a result, the failure of the anode was attributed to the gas diffusion blockage by dense silicon dioxide layer formation. The anode failure process with siloxane contamination is faster when the anode is operated under polarization.

Comprehensively considering the four different aspects of studies in this work, the siloxane deposition and Ni-YSZ anode failure process under siloxane contamination is proposed. The proposed adsorption degradation process for siloxane has been illustrated in **Fig. 6.1.**

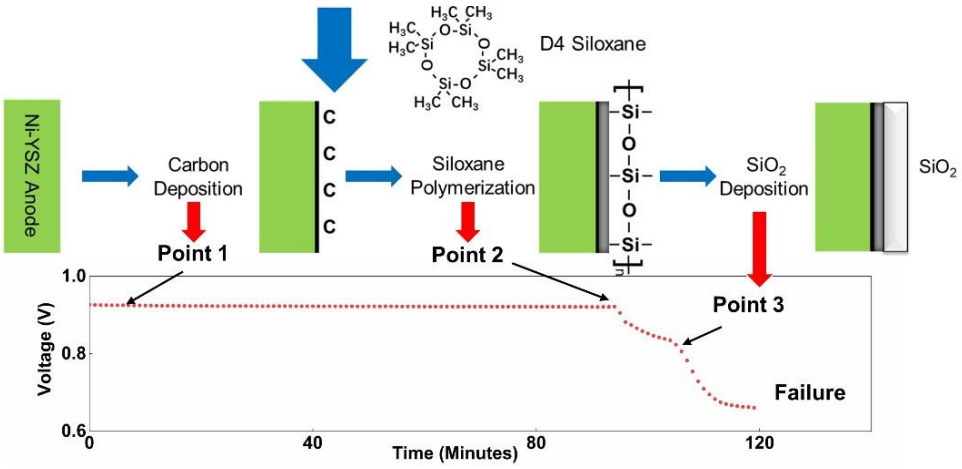

Figure 6.1 The porosity and corresponding tortuosity change of the entire anode during OCV and 50 mA cm^{-2} D4 contamination experiments.

Firstly, carbon generated by siloxane adsorption process can form a thin layer on the Ni particle. Besides the morphology evidence discussed in Chapter 2 and Chapter 5, the phenomenon that involve water in fuel preventing the siloxane deposition in Chapter 1 can also affirm this point. Water can reduce the carbon deposition and restrain the siloxane deposition. Besides the Ni particle, due to the existence of OH radicals on YSZ surface, the siloxanes can also adsorb on the YSZ particle inside the anode as demonstrated by SEM results in Chapter 3 and Chapter 4. The GC results in Chapter 5, the signal overlap of the Si, O and C elements and existance of SiC in deposition from multiple Chapters infer the existence of polymerization of siloxanes on anode surface. The comparison of linear and cyclic structure in Chapter 4 can also provide evidence for this step. The Low adsorption and the high desorption rates of linear siloxane compared with cyclic siloxanes can reduce the siloxane polymerization rate. As a result, linear structure siloxane deposition process is much slower than cyclic structure siloxane. The final step and also the step causing the failure of SOFCs is the dense layer of amorphous SiO_2 formation on the anode surface. The flake shape SiO_2 crystal observed by SEM in Chapter 5 can provide solid evidence for the last step. The SiO_2 also appeared in siloxane deposition composition analysis in multiple chapters in this work. Overall, this new understanding of siloxane deposition and anode degradation can serve as a reference for future SOFC studies

6.2 Future research

Although, some decent experimental and calculation results have been presented in this work, there are also some potential improvements that can be made in future work.

For the microstructure parameters evaluation, like in Chapter 3, Chapter 4 and Chapter 5, even with the assistance of the transmission line model or ordinary equivalent circuit model ECM, some preliminary values such as porosity are still necessary for other parameters calculation. Without the values, or only rough values, inaccuracy of the entire microstructure parameters evaluation results. In this work, D4 and L4 were selected as the representative siloxanes. In realistic applications, different kinds of siloxanes would all be involved in the bio-syngas. In this circumstance, the degradation process modeling corresponding with microstructure parameters can be hard to achieve only based on the results accomplished in this work. Thus, the precise lifetime prediction for the anode under siloxane contamination still needs more experiments with different types of siloxanes and different concentrations in the future. Simultaneously, the electrochemical and corresponding microstructure parameters acquired by 3D reconstruction techniques such as FIB-SEM should also be collected during the failure process.

For the adsorption siloxane deposition process proposed in this study, although it can be proven by evidence including the content discussed from Chapter 2 to Chapter 5, the direct evidence such as high spatial resolution imaging of the adsorption surface by techniques like transmission electron microscopy (TEM) is still necessary in future

research. The morphology and material characterization techniques such as SEM-WDS, XPS, XRD and Raman spectroscopy utilized in this work are all postmortem analysis. The in-situ studies such as in-situ XPS, SEM-WDS can also aid to have a more elaborate and precise understanding to the siloxane deposition process.

Based on the adsorption siloxane deposition investigation, the degradation of anode due to the siloxane contamination can be relieved by controlling the SOFC fuel and operation condition. As a conclusion from Chapter 1, the wet fuel can reduce the siloxane deposition and anode degradation because of suppression of carbon deposition and siloxane adsorption. The experiment in Chapter 5 also demonstrates that the anode degradation and siloxane deposition would be enhanced when the SOFC operates under polarization. In this regard, in future, the fuel fed to the SOFC, and the operating voltage/current can be optimized to avoid siloxane deposition. According to the siloxane degradation process, even the additive chemical compounds can be developed in future. Mixing proper additive chemical compounds to the fuel may obstruct the reaction path of siloxane deposition in the anode to prevent anode degradation.

Besides optimization of the fuel and operation conditions, developing the siloxane tolerant anode can also be an attractive research topic to solve the siloxane contamination problems in future. From Chapter 3, Ni has been identified as an essential component contributing to the catalytic siloxane depositions reactions in Ni-YSZ anode. Due to the high catalytic activity, Ni also has been found responsible for the anode degradation by

other external contamination sources such as hydrogen sulfide and carbon. In this situation, some poisoning resistant SOFC anode materials have been developed. For instance, Zurlo et al. reported Cu/CeO_2 based anode presents significant sulfur tolerance [175]. From research accomplished by Lu et al. and Grgicak et al. [176,177], Ni–Cu–YSZ cermet anode could avoid carbon deposition and sulfur poisoning during hydrocarbon cell application. Low et al. [178] also demonstrated that the sulfur corrosion and carbon deposition can be reduced by utilization of Cu coated Ni foam as the SOFC current collector. Moreover, Jiang et al. [179] also reported Sn and Ag doped Ni-YSZ have the better anti-coking ability than Cu. In this regard, Cu, Sn and Ag are all considered as potential elements for Ni-YSZ anode modification to increase the tolerance of siloxanes. From a thermodynamic perspective, doping Si to the anode materials may also increase the silicon deposition resistance. For instance, to reach lower affinity for sulfur absorption and improved sulfur tolerance, some sulfur doped materials were utilized in anode such as WS_2 and thiospinels ($CuNi_2S_4$, $CuCoS_4$, $CuFe_2S_4$, $NiCo_2S_4$ and $NiFe_2S_4$) [180]. Generally, the research about siloxane tolerant anode material development is not available in the literature and has huge potential in the future.

REFERENCES

[1] P. Weiland, Biogas production: Current state and perspectives, Appl. Microbiol. Biotechnol. 85 (2010) 849–860. https://doi.org/10.1007/s00253-009-2246-7.

[2] B.W. Ang, W.L. Choong, T.S. Ng, Energy security: Definitions, dimensions and indexes, Renew. Sustain. Energy Rev. 42 (2015) 1077–1093. https://doi.org/10.1016/j.rser.2014.10.064.

[3] N. Scarlat, J.-F. Dallemand, F. Fahl, Biogas: Developments and perspectives in Europe, Renew. Energy. 129 (2018) 457–472. https://doi.org/10.1016/j.renene.2018.03.006.

[4] J. Van Herle, Y. Membrez, O. Bucheli, Biogas as a fuel source for SOFC co-generators, J. Power Sources. 127 (2004) 300–312. https://doi.org/10.1016/j.jpowsour.2003.09.027.

[5] M. Gandiglio, A. Lanzini, M. Santarelli, M. Acri, T. Hakala, M. Rautanen, Results from an industrial size biogas-fed SOFC plant (the DEMOSOFC project), Int. J. Hydrogen Energy. 45 (2020) 5449–5464. https://doi.org/10.1016/j.ijhydene.2019.08.022.

[6] S. Farhad, F. Hamdullahpur, Y. Yoo, Performance evaluation of different configurations of biogas-fuelled SOFC micro-CHP systems for residential applications, Int. J. Hydrogen Energy. 35 (2010) 3758–3768. https://doi.org/10.1016/j.ijhydene.2010.01.052.

[7] D. Papurello, R. Borchiellini, P. Bareschino, V. Chiodo, S. Freni, A. Lanzini, F. Pepe, G.A. Ortigoza, M. Santarelli, Performance of a Solid Oxide Fuel Cell short-stack with biogas feeding, Appl. Energy. 125 (2014) 254–263. https://doi.org/10.1016/j.apenergy.2014.03.040.

[8] J. Tian, R.J. Milcarek, Degradation Comparison of Cyclic and Linear Siloxane Contamination on Solid Oxide Fuel Cells Ni-YSZ Anode, Front. Energy Res. 9 (2021) 1–13. https://doi.org/10.3389/fenrg.2021.749771.

[9] A.A. Bletsou, A.G. Asimakopoulos, A.S. Stasinakis, N.S. Thomaidis, K. Kannan, Mass Loading and Fate of Linear and Cyclic Siloxanes in a Wastewater Treatment Plant in Greece, Environ. Sci. Technol. 47 (2013) 1824–1832.

https://doi.org/10.1021/es304369b.

[10] C. Clark, R.G. Zytner, E. McBean, Analyzing volatile organic siloxanes in landfill biogas, Can. J. Civ. Eng. 39 (2012) 667–673. https://doi.org/10.1139/L2012-051.

[11] C. Zhang, M. Jin, S. Zhang, Z. Li, H. Li, Removal of cyclic and linear siloxanes in effluents from a cosmetic wastewater treatment plant by electrochemical oxidation, Int. J. Electrochem. Sci. 11 (2016) 6914–6921. https://doi.org/10.20964/2016.08.04.

[12] D. Papurello, L. Tomasi, S. Silvestri, Proton transfer reaction mass spectrometry for the gas cleaning using commercial and waste-derived materials: Focus on the siloxane removal for SOFC applications, Int. J. Mass Spectrom. 430 (2018) 69–79. https://doi.org/10.1016/j.ijms.2018.05.002.

[13] J. Wang, L. Liao, L. Wang, L. Wang, Influence of sampling methods and storage condition on volatile methyl siloxanes quantification in biogas, Biomass and Bioenergy. 158 (2022) 106347. https://doi.org/10.1016/j.biombioe.2022.106347.

[14] D. Papurello, L. Tognana, A. Lanzini, F. Smeacetto, M. Santarelli, I. Belcari, S. Silvestri, F. Biasioli, Proton transfer reaction mass spectrometry technique for the monitoring of volatile sulfur compounds in a fuel cell quality clean-up system, Fuel Process. Technol. 130 (2015) 136–146. https://doi.org/10.1016/j.fuproc.2014.09.041.

[15] A. Lanzini, H. Madi, V. Chiodo, D. Papurello, S. Maisano, M. Santarelli, J. Van herle, Dealing with fuel contaminants in biogas-fed solid oxide fuel cell (SOFC) and molten carbonate fuel cell (MCFC) plants: Degradation of catalytic and electro-catalytic active surfaces and related gas purification methods, Prog. Energy Combust. Sci. 61 (2017) 150–188. https://doi.org/10.1016/j.pecs.2017.04.002.

[16] Y. Kikuchi, J. Matsuda, Y. Tachikawa, Y. Shiratori, S. Taniguchi, K. Sasaki, Degradation of SOFCs by Various Impurities: Impedance Spectroscopy and Microstructural Analysis, ECS Trans. 78 (2017) 1253–1260. https://doi.org/10.1149/07801.1253ecst.

[17] K. Haga, Y. Shiratori, K. Ito, K. Sasaki, Chemical Degradation and Poisoning Mechanism of Cermet Anodes in Solid Oxide Fuel Cells, ECS Trans. 25 (2019) 2031–2038. https://doi.org/10.1149/1.3205748.

[18] H. Madi, Investigations into the Effects of Biofuel Contaminants on Solid Oxide Fuel Cells, 7161 (2016) 157. https://doi.org/10.5075/epfl-thesis-7161.

[19] M.S. Khan, S.B. Lee, R.H. Song, J.W. Lee, T.H. Lim, S.J. Park, Fundamental mechanisms involved in the degradation of nickel–yttria stabilized zirconia (Ni–YSZ) anode during solid oxide fuel cells operation: A review, Ceram. Int. 42 (2016) 35–48. https://doi.org/10.1016/j.ceramint.2015.09.006.

[20] K. Kubota, K. Kuroda, K. Akiyama, Present Status and Future Prospects of Biogas Powered Fuel Cell Power Units, Fuji Electr. Rev. 49 (2002) 68–72. http://www.fujielectric.com/company/tech/pdf/r49-2/08.pdf.

[21] W.G.C. Ryan O'hayre, Suk-Won Cha, Fuel Cell Fundamentals, 3. Edition, Wiley. (2005). https://doi.org/10.1017/CBO9781107415324.004.

[22] R.J. Milcarek, K. Wang, M.J. Garrett, J. Ahn, Performance investigation of dual layer yttria-stabilized zirconia-samaria-doped ceria electrolyte for intermediate temperature solid oxide fuel cells, J. Electrochem. Energy Convers. Storage. 13 (2016) 31–32. https://doi.org/10.1115/1.4032708.

[23] T. Suzuki, Z. Hasan, Y. Funahashi, T. Yamaguchi, Y. Fujishiro, M. Awano, Impact of Anode Microstructure on Solid Oxide Fuel Cells, Science (80-.). 325 (2009) 852–855. https://doi.org/10.1126/science.1176404.

[24] J.H. Shim, C.-C. Chao, H. Huang, F.B. Prinz, Atomic Layer Deposition of Yttria-Stabilized Zirconia for Solid Oxide Fuel Cells, Chem. Mater. 19 (2007) 3850–3854. https://doi.org/10.1021/cm070913t.

[25] H. Huang, M. Nakamura, P. Su, R. Fasching, Y. Saito, F.B. Prinz, High-Performance Ultrathin Solid Oxide Fuel Cells for Low-Temperature Operation, J. Electrochem. Soc. 154 (2007) B20. https://doi.org/10.1149/1.2372592.

[26] Z. Lu, X. Zhou, D. Fisher, J. Templeton, J. Stevenson, N. Wu, A. Ignatiev, Enhanced performance of an anode-supported YSZ thin electrolyte fuel cell with a laser-deposited $Sm_{0.2}Ce_{0.8}O_{1.9}$ interlayer, Electrochem. Commun. 12 (2010) 179–182. https://doi.org/10.1016/j.elecom.2009.11.015.

[27] H. Shi, R. Ran, Z. Shao, Wet powder spraying fabrication and performance optimization of IT-SOFCs with thin-film ScSZ electrolyte, Int. J. Hydrogen Energy. 37 (2012) 1125–1132. https://doi.org/10.1016/j.ijhydene.2011.02.077.

[28] R.J. Milcarek, K. Wang, R.L. Falkenstein-Smith, J. Ahn, Performance variation with SDC buffer layer thickness, Int. J. Hydrogen Energy. 41 (2016) 9500–9506. https://doi.org/10.1016/j.ijhydene.2016.04.113.

[29] N.H.M. and E.I.-T. J. Szasza, F. Wankmüllera, V. Wildeb, H. Störmerb, D. Gerthsenb, High-Performance Cathode/Electrolyte Interfaces for SOFC, ECS Trans. 68 (2015) 763–771. https://doi.org/10.1149/MA2015-03/1/138.

[30] A. Mai, V.A.C. Haanappel, F. Tietz, D. Stöver, Ferrite-based perovskites as cathode materials for anode-supported solid oxide fuel cells. Part II. Influence of the CGO interlayer, Solid State Ionics. 177 (2006) 2103–2107. https://doi.org/10.1016/j.ssi.2005.12.010.

[31] N. Jordan, W. Assenmacher, S. Uhlenbruck, V.A.C. Haanappel, H.P. Buchkremer, D. Stöver, W. Mader, $Ce_{0.8}Gd_{0.2}O_{2-\delta}$ protecting layers manufactured by physical vapor deposition for IT-SOFC, Solid State Ionics. 179 (2008) 919–923. https://doi.org/10.1016/j.ssi.2007.12.008.

[32] B. Shri Prakash, S. Senthil Kumar, S.T. Aruna, Properties and development of Ni/YSZ as an anode material in solid oxide fuel cell: A review, Renew. Sustain. Energy Rev. 36 (2014) 149–179. https://doi.org/10.1016/j.rser.2014.04.043.

[33] J. Rossmeisl, W.G. Bessler, Trends in catalytic activity for SOFC anode materials, Solid State Ionics. 178 (2008) 1694–1700. https://doi.org/10.1016/j.ssi.2007.10.016.

[34] S. Kakaç, A. Pramuanjaroenkij, X.Y. Zhou, A review of numerical modeling of solid oxide fuel cells, Int. J. Hydrogen Energy. 32 (2007) 761–786. https://doi.org/10.1016/j.ijhydene.2006.11.028.

[35] K. Gerdes, M.C. Williams, R. Gemmen, B. White, A Global Framework for Examination of Degradation in SOFC, ECS Trans. 57 (2013) 289–297. https://doi.org/10.1149/05701.0289ecst.

[36] A. Weber, J. Szász, S. Dierickx, C. Endler-Schuck, E. Ivers-Tiffée, Accelerated Lifetime Tests for SOFCs, ECS Trans. 68 (2015) 1953–1960. https://doi.org/10.1149/06801.1953ecst.

[37] M. Heneka, E. Ivers-Tiffee, Accelerated Life Tests for Fuel Cells, ECS Meet. Abstr. MA2005-02 (2006) 1206–1206. https://doi.org/10.1149/MA2005-

02/33/1206.

[38] W.Q. Meeker, L.A. Escobar, C.J. Lu, Accelerated Degradation Tests: Modeling and Analysis, Technometrics. 40 (1998) 89–99. https://doi.org/10.1080/00401706.1998.10485191.

[39] Orazem, Mark E. and Tribollet, B., Electrochemical impedance spectroscopy, New Jersey, 2008.

[40] D.D. MacDonald, Reflections on the history of electrochemical impedance spectroscopy, Electrochim. Acta. 51 (2006) 1376–1388. https://doi.org/10.1016/j.electacta.2005.02.107.

[41] E. Warburg, Uber das Verhalten sogenannter unpolarisirbarer Elektroden gegen Wechselstrom, Ann. Der Phys. Und Chemie. 67 (1899) 493–499.

[42] R. de Levie, Electrochemical Responses of Porous and Rough Electrodes, Adv. Electrochem. Electrochem. Eng. 6 (1967) 329–397.

[43] J.E. Bauerle, Study of solid electrolyte polarization by a complex admittance method, J. Phys. Chem. Solids. 30 (1969) 2657–2670.

[44] Sebastian, A. Weber, E. Ivers-Tiffée, How the distribution of relaxation times enhances complex equivalent circuit models for fuel cells, Electrochim. Acta. 355 (2020) 136764. https://doi.org/10.1016/j.electacta.2020.136764.

[45] M.E. Orazem, Advanced electrochemical impedance spectroscopy, in: 240th ECS Meet., Orlando, 2021: pp. 24–25. https://www.keysight.com/gb/en/assets/3121-1209/white-papers/Advanced-Electrochemical-Impedance-Spectroscopy-EIS-for-Battery-Testing.pdf.

[46] J. Hong, A. Bhardwaj, H. Bae, I. Kim, S.-J. Song, Electrochemical Impedance Analysis of SOFC with Transmission Line Model Using Distribution of Relaxation Times (DRT), J. Electrochem. Soc. 167 (2020) 114504. https://doi.org/10.1149/1945-7111/aba00f.

[47] E. Schweidler, Studien über die Anomalien im Verhalten der Dielektrika, Ann. Phys. 328 (1907) 711–770.

[48] A.G.Y. A .N. Tikhonov , A .V. Goncharsky , V.V. Stepanov, Numerical Methods

for the Solution of Ill-Posed Problems, Springer Netherlands, Dordrecht, 1995.

[49] V. Sonn, A. Leonide, E. Ivers-Tiffée, Combined Deconvolution and CNLS Fitting Approach Applied on the Impedance Response of Technical Ni/8YSZ Cermet Electrodes, J. Electrochem. Soc. 155 (2008) B675. https://doi.org/10.1149/1.2908860.

[50] F. Ciucci, C. Chen, Analysis of electrochemical impedance spectroscopy data using the distribution of relaxation times: A Bayesian and hierarchical Bayesian approach, Electrochim. Acta. 167 (2015) 439–454. https://doi.org/10.1016/j.electacta.2015.03.123.

[51] J.R. Macdonald, Impedance Spectroscopy, John Wiley & Sons, Hoboken, NJ, n.d.

[52] A. Leonide, Y. Apel, E. Ivers-Tiffee, SOFC Modeling and Parameter Identification by Means of Impedance Spectroscopy, ECS Trans. 19 (2019) 81–109. https://doi.org/10.1149/1.3247567.

[53] A. Leonide, V. Sonn, A. Weber, E. Ivers-Tiffée, Evaluation and Modeling of the Cell Resistance in Anode-Supported Solid Oxide Fuel Cells, J. Electrochem. Soc. 155 (2008) B36. https://doi.org/10.1149/1.2801372.

[54] Y. Shen, J.L. Linville, M. Urgun-Demirtas, R.P. Schoene, S.W. Snyder, Producing pipeline-quality biomethane via anaerobic digestion of sludge amended with corn stover biochar with in-situ CO2 removal, Appl. Energy. 158 (2015) 300–309. https://doi.org/10.1016/j.apenergy.2015.08.016.

[55] C. Goff, Combined Heat and Power at Wastewater Treatment Facilities : Market Analysis and Lessons from the EPA & Combined Heat and Power, 2011.

[56] D.M. Riley, J. Tian, G. Güngör-Demirci, P. Phelan, J.R. Villalobos, R.J. Milcarek, Techno-Economic Assessment of CHP Systems in Wastewater Treatment Plants, Environments. 7 (2020) 74. https://doi.org/10.3390/environments7100074.

[57] J. Roostaei, Y. Zhang, Spatially Explicit Life Cycle Assessment: Opportunities and challenges of wastewater-based algal biofuels in the United States, Algal Res. 24 (2017) 395–402. https://doi.org/10.1016/j.algal.2016.08.008.

[58] Y. Shen, J.L. Linville, M. Urgun-Demirtas, M.M. Mintz, S.W. Snyder, An overview of biogas production and utilization at full-scale wastewater treatment

plants (WWTPs) in the United States: Challenges and opportunities towards energy-neutral WWTPs, Renew. Sustain. Energy Rev. 50 (2015) 346–362. https://doi.org/10.1016/j.rser.2015.04.129.

[59] E. Rillo, M. Gandiglio, A. Lanzini, S. Bobba, M. Santarelli, G. Blengini, Life Cycle Assessment (LCA) of biogas-fed Solid Oxide Fuel Cell (SOFC) plant, Energy. 126 (2017) 585–602. https://doi.org/10.1016/j.energy.2017.03.041.

[60] D. Papurello, A. Lanzini, SOFC single cells fed by biogas: Experimental tests with trace contaminants, Waste Manag. 72 (2018) 306–312. https://doi.org/10.1016/j.wasman.2017.11.030.

[61] O. Jonsson, P. Erik, K. Jan, E. Rolf, S. Hakan, I. Staffan, Sustainable Gas Enters the European Gas Distribution, 1997. http://scholar.google.com/scholar?hl=en&btnG=Search&q=intitle:SUSTAINABLE+GAS+ENTERS+THE+EUROPEAN+GAS+DISTRIBUTION#0.

[62] E. Ryckebosch, M. Drouillon, H. Vervaeren, Techniques for transformation of biogas to biomethane, Biomass and Bioenergy. 35 (2011) 1633–1645. https://doi.org/10.1016/j.biombioe.2011.02.033.

[63] D. Papurello, A. Lanzini, D. Drago, P. Leone, M. Santarelli, Limiting factors for planar solid oxide fuel cells under different trace compound concentrations, Energy. 95 (2016) 67–78. https://doi.org/10.1016/j.energy.2015.11.070.

[64] C. Rücker, K. Kümmerer, Environmental chemistry of organosiloxanes, Chem. Rev. 115 (2015) 466–524. https://doi.org/10.1021/cr500319v.

[65] H. Madi, S. Diethelm, S. Poitel, C. Ludwig, J. Van herle, Damage of Siloxanes on Ni-YSZ Anode Supported SOFC Operated on Hydrogen and Bio-Syngas, Fuel Cells. 15 (2015) 718–727. https://doi.org/10.1002/fuce.201400185.

[66] F. Chainet, C.P. Lienemann, J. Ponthus, M. Courtiade, O.F.X. Donard, Development of heart-cutting multidimensional gas chromatography coupled to time of flight mass spectrometry for silicon speciation at trace levels in gasoline samples, J. Chromatogr. A. 1264 (2012) 80–86. https://doi.org/10.1016/j.chroma.2012.09.020.

[67] R. Dewil, L. Appels, J. Baeyens, Energy use of biogas hampered by the presence of siloxanes, Energy Convers. Manag. 47 (2006) 1711–1722.

https://doi.org/10.1016/j.enconman.2005.10.016.

[68] M. Arnold, VTT RESEARCH NOTES 2496 Reduction and monitoring of biogas trace compounds, 2006. http://www.vtt.fi/publications/index.jsp.

[69] D.D. Papadias, S. Ahmed, R. Kumar, Fuel quality issues with biogas energy – An economic analysis for a stationary fuel cell system, Energy. 44 (2012) 257–277. https://doi.org/10.1016/j.energy.2012.06.031.

[70] J. Álvarez-Flórez, E. Egusquiza, Analysis of damage caused by siloxanes in stationary reciprocating internal combustion engines operating with landfill gas, Eng. Fail. Anal. 50 (2015) 29–38. https://doi.org/10.1016/j.engfailanal.2015.01.010.

[71] E. Wheless, J. Pierce, Siloxanes in landfill and digester gas update, SCS Eng. Environ. Consult. Contract. (2004) 1–10. http://mercmail.scsengineers.com/Papers/Pierce_2004Siloxanes_Update_Paper.pdf .

[72] H. Madi, A. Lanzini, S. Diethelm, D. Papurello, J. Van herle, M. Lualdi, J. Gutzon Larsen, M. Santarelli, Solid oxide fuel cell anode degradation by the effect of siloxanes, J. Power Sources. 279 (2015) 460–471. https://doi.org/10.1016/j.jpowsour.2015.01.053.

[73] H. Wasajja, R.E.F. Lindeboom, J.B. van Lier, P.V. Aravind, Techno-economic review of biogas cleaning technologies for small scale off-grid solid oxide fuel cell applications, Fuel Process. Technol. 197 (2020) 106215. https://doi.org/10.1016/j.fuproc.2019.106215.

[74] K. Haga, S. Adachi, Y. Shiratori, K. Itoh, K. Sasaki, Poisoning of SOFC anodes by various fuel impurities, Solid State Ionics. 179 (2008) 1427–1431. https://doi.org/10.1016/j.ssi.2008.02.062.

[75] K. Sasaki, K. Haga, T. Yoshizumi, D. Minematsu, E. Yuki, R.-R. Liu, C. Uryu, T. Oshima, S. Taniguchi, Y. Shiratori, K. Ito, Impurity Poisoning of SOFCs, ECS Trans. 35 (2019) 2805–2814. https://doi.org/10.1149/1.3570280.

[76] K. Haga, Y. Shiratori, K. Ito, K. Sasaki, Chemical Degradation and Poisoning Mechanism of Cermet Anodes in Solid Oxide Fuel Cells, ECS Trans. 25 (2019) 2031–2038. https://doi.org/10.1149/1.3205748.

[77] S.H. Jensen, Solid oxide electrolyser cell, Risoe Natl. Lab. [Report] Risoe-R. (2006) 1–134.

[78] A. Hauch, J.R. Bowen, L.T. Kuhn, M. Mogensen, Nanoscale Chemical Analysis and Imaging of Solid Oxide Cells, Electrochem. Solid-State Lett. 11 (2008) B38. https://doi.org/10.1149/1.2828845.

[79] A. Hauch, S.D. Ebbesen, S.H. Jensen, M. Mogensen, Solid Oxide Electrolysis Cells: Microstructure and Degradation of the Ni/Yttria-Stabilized Zirconia Electrode, J. Electrochem. Soc. 155 (2008) B1184. https://doi.org/10.1149/1.2967331.

[80] A.C. Sonoc, C. Thurgood, B. Peppley, D.G. Kelly, Kinetic study of the thermal decomposition of octamethylcyclotetrasiloxane on activated gamma alumina, J. Environ. Chem. Eng. 5 (2017) 4858–4865. https://doi.org/10.1016/j.jece.2017.07.057.

[81] N.H. Elsayed, A. Elwell, B. Joseph, J.N. Kuhn, Effect of silicon poisoning on catalytic dry reforming of simulated biogas, Appl. Catal. A Gen. 538 (2017) 157–164. https://doi.org/10.1016/j.apcata.2017.03.024.

[82] V.S. Vaiss, C.G. Fonseca, F.P.N. Antunes, L.S. Chinelatto Jr., S.S.X. Chiaro, W.F. Souza, A.A. Leitão, Experimental and Theoretical Study of Deactivated HDT Catalysts by Si Species Deposited on their Surfaces: Models Proposition, Structural and Thermodynamic Analysis, J. Catal. 389 (2020) 578–591. https://doi.org/10.1016/j.jcat.2020.06.007.

[83] E. Finocchio, G. Garuti, M. Baldi, G. Busca, Decomposition of hexamethylcyclotrisiloxane over solid oxides, Chemosphere. 72 (2008) 1659–1663. https://doi.org/10.1016/j.chemosphere.2008.05.032.

[84] J. Tian, R.J. Milcarek, Investigating the degradation mechanism of the solid oxide fuel cell nickel-yttria stabilized zirconia anode under siloxane contamination, J. Power Sources. 480 (2020) 229122. https://doi.org/10.1016/j.jpowsour.2020.229122.

[85] C. Comminges, Q.X. Fu, M. Zahid, N.Y. Steiner, O. Bucheli, Monitoring the degradation of a solid oxide fuel cell stack during 10,000 h via electrochemical impedance spectroscopy, Electrochim. Acta. 59 (2012) 367–375. https://doi.org/10.1016/j.electacta.2011.10.080.

[86] P. Caliandro, A. Nakajo, S. Diethelm, J. Van herle, Model-assisted identification of solid oxide cell elementary processes by electrochemical impedance spectroscopy measurements, J. Power Sources. 436 (2019) 226838. https://doi.org/10.1016/j.jpowsour.2019.226838.

[87] H. Sumi, H. Shimada, Y. Yamaguchi, T. Yamaguchi, Y. Fujishiro, Degradation evaluation by distribution of relaxation times analysis for microtubular solid oxide fuel cells, Electrochim. Acta. 339 (2020) 135913. https://doi.org/10.1016/j.electacta.2020.135913.

[88] C. Sun, R. Hui, J. Roller, Cathode materials for solid oxide fuel cells: a review, J. Solid State Electrochem. 14 (2010) 1125–1144. https://doi.org/10.1007/s10008-009-0932-0.

[89] H. He, J.M. Hill, Carbon deposition on Ni/YSZ composites exposed to humidified methane, Appl. Catal. A Gen. 317 (2007) 284–292. https://doi.org/10.1016/j.apcata.2006.10.040.

[90] F. Chainet, M. Courtiade, C.P. Lienemann, J. Ponthus, O.F.X. Donard, Silicon speciation by gas chromatography coupled to mass spectrometry in gasolines, J. Chromatogr. A. 1218 (2011) 9269–9278. https://doi.org/10.1016/j.chroma.2011.10.047.

[91] M. Kogler, E.M. Köck, T. Bielz, K. Pfaller, B. Klötzer, D. Schmidmair, L. Perfler, S. Penner, Hydrogen surface reactions and adsorption studied on Y_2O_3, YSZ, and ZrO_2, J. Phys. Chem. C. 118 (2014) 8435–8444. https://doi.org/10.1021/jp5008472.

[92] K. Ong, J. Hanna, A.F. Ghoniem, Investigation of a Combined Hydrogen and Oxygen Spillover Mechanism for Syngas Electro-Oxidation on Ni/YSZ, J. Electrochem. Soc. 164 (2016) F32–F45. https://doi.org/10.1149/2.0161702jes.

[93] H. Zhu, R.J. Kee, V.M. Janardhanan, O. Deutschmann, D.G. Goodwin, Modeling Elementary Heterogeneous Chemistry and Electrochemistry in Solid-Oxide Fuel Cells, J. Electrochem. Soc. 152 (2005) A2427. https://doi.org/10.1149/1.2116607.

[94] L. Kellberg, P. Zeuthen, H.J. Jakobsen, Deactivation of HDT Catalysts by Formation of Silica Gels from Silicone Oil. Characterization of Spent Catalysts from HDT of Coker Naphtha Using ^{29}Si and ^{13}C CP/MAS NMR, J. Catal. 143 (1993) 45–51. https://doi.org/10.1006/jcat.1993.1252.

[95] P. Pérez-Romo, J. Navarrete-Bolaños, C. Aguilar-Barrera, C. Angeles-Chavez, G.C. Laredo, Morphological and structural study of the Si deposition on the sulfided NiMo/γ-Al_2O_3 catalyst: Effect on the support, Appl. Catal. A Gen. 485 (2014) 84–90. https://doi.org/10.1016/j.apcata.2014.07.038.

[96] J. Hanna, W.Y. Lee, A.F. Ghoniem, Kinetics of Carbon Monoxide Electro-Oxidation in Solid-Oxide Fuel Cells from Ni-YSZ Patterned-Anode Measurements, J. Electrochem. Soc. 160 (2013) F698–F708. https://doi.org/10.1149/2.136606jes.

[97] V. Yurkiv, D. Starukhin, H.-R. Volpp, W.G. Bessler, Elementary Reaction Kinetics of the CO/CO_2/Ni/YSZ Electrode, J. Electrochem. Soc. 158 (2011) B5. https://doi.org/10.1149/1.3505296.

[98] R.J. Milcarek, J. Ahn, Micro-tubular flame-assisted fuel cells running methane, propane and butane: On soot, efficiency and power density, Energy. 169 (2019) 776–782. https://doi.org/10.1016/j.energy.2018.12.098.

[99] E. Achenbach, Three-dimensional and time-dependent simulation of a planar solid oxide fuel cell stack, J. Power Sources. 49 (1994) 333–348. https://doi.org/10.1016/0378-7753(93)01833-4.

[100] J.H. Koh, Y.S. Yoo, J.W. Park, H.C. Lim, Carbon deposition and cell performance of Ni-YSZ anode support SOFC with methane fuel, Solid State Ionics. 149 (2002) 157–166. https://doi.org/10.1016/S0167-2738(02)00243-6.

[101] E.S. Hecht, G.K. Gupta, H. Zhu, A.M. Dean, R.J. Kee, L. Maier, O. Deutschmann, Methane reforming kinetics within a Ni-YSZ SOFC anode support, Appl. Catal. A Gen. 295 (2005) 40–51. https://doi.org/10.1016/j.apcata.2005.08.003.

[102] J. Tian, R.J. Milcarek, Siloxane Deposition on the Ni-YSZ Solid Oxide Fuel Cell Anode Exposed to Bio-Syngas, J. Electrochem. Soc. 168 (2021) 044503. https://doi.org/10.1149/1945-7111/abf21a.

[103] S. Ali, M.M. Zagho, M.J. Al-Marri, Y.I. Arafat, M.M. Khader, Development of Nickel-based Catalysts for Methane Steam Reforming, in: Proc. 4th Int. Gas Process. Symp., Elsevier, 2015: pp. 111–116. https://doi.org/10.1016/B978-0-444-63461-0.50011-0.

[104] J. Aguilhon, C. Boissière, O. Durupthy, C. Thomazeau, C. Sanchez, Nickel

nanoparticles with controlled morphologies application in selective hydrogenation catalysis, in: Stud. Surf. Sci. Catal., Elsevier Masson SAS, 2010: pp. 521–524. https://doi.org/10.1016/S0167-2991(10)75099-0.

[105] J.D.A. Bellido, E.M. Assaf, Effect of the Y_2O_3–ZrO_2 support composition on nickel catalyst evaluated in dry reforming of methane, Appl. Catal. A Gen. 352 (2009) 179–187. https://doi.org/10.1016/j.apcata.2008.10.002.

[106] W. Chu, Q. Yan, X. Liu, Q. Li, Z. Yu, G. Xiong, Rare earth promoted nickel catalysts for the selective oxidation of natural gas to syngas, in: Stud. Surf. Sci. Catal., Elsevier Masson SAS, 1998: pp. 849–854. https://doi.org/10.1016/S0167-2991(98)80538-7.

[107] H.S. Roh, K.W. Jun, W.S. Dong, S.E. Park, Y.S. Baek, Highly stable Ni catalyst supported on Ce-ZrO_2 for oxy-steam reforming of methane, Catal. Letters. 74 (2001) 31–36. https://doi.org/10.1023/A:1016699317421.

[108] B.B. Skabelund, H. Nakamura, T. Tezuka, K. Maruta, J. Ahn, R.J. Milcarek, Thermal partial oxidation of n-butane in a micro-flow reactor and solid oxide fuel cell stability assessment, Energy Convers. Manag. 254 (2022) 115222. https://doi.org/10.1016/j.enconman.2022.115222.

[109] J.R. Wilson, W. Kobsiriphat, R. Mendoza, H.Y. Chen, J.M. Hiller, D.J. Miller, K. Thornton, P.W. Voorhees, S.B. Adler, S.A. Barnett, Three-dimensional reconstruction of a solid-oxide fuel-cell anode, Nat. Mater. 5 (2006) 541–544. https://doi.org/10.1038/nmat1668.

[110] P.R. Shearing, J. Golbert, R.J. Chater, N.P. Brandon, 3D reconstruction of SOFC anodes using a focused ion beam lift-out technique, Chem. Eng. Sci. 64 (2009) 3928–3933. https://doi.org/10.1016/j.ces.2009.05.038.

[111] Z. Jiao, N. Shikazono, N. Kasagi, Quantitative Characterization of SOFC Nickel-YSZ Anode Microstructure Degradation Based on Focused-Ion-Beam 3D-Reconstruction Technique, J. Electrochem. Soc. 159 (2012) B285–B291. https://doi.org/10.1149/2.045203jes.

[112] A. Zekri, M. Knipper, J. Parisi, T. Plaggenborg, Microstructure degradation of Ni/CGO anodes for solid oxide fuel cells after long operation time using 3D reconstructions by FIB tomography, Phys. Chem. Chem. Phys. 19 (2017) 13767–13777. https://doi.org/10.1039/c7cp02186k.

[113] Y.L. Liu, C. Jiao, Microstructure degradation of an anode/electrolyte interface in SOFC studied by transmission electron microscopy, Solid State Ionics. 176 (2005) 435–442. https://doi.org/10.1016/j.ssi.2004.08.018.

[114] Y. Zhang, Y. Chen, F. Chen, In-situ quantification of solid oxide fuel cell electrode microstructure by electrochemical impedance spectroscopy, J. Power Sources. 277 (2015) 277–285. https://doi.org/10.1016/j.jpowsour.2014.11.123.

[115] A. Kromp, A. Leonide, A. Weber, E. Ivers-Tiffée, Electrochemical Analysis of Reformate-Fuelled Anode Supported SOFC, J. Electrochem. Soc. 158 (2011) B980. https://doi.org/10.1149/1.3597177.

[116] T.H. Wan, M. Saccoccio, C. Chen, F. Ciucci, Influence of the Discretization Methods on the Distribution of Relaxation Times Deconvolution: Implementing Radial Basis Functions with DRTtools, Electrochim. Acta. 184 (2015) 483–499. https://doi.org/10.1016/j.electacta.2015.09.097.

[117] M.B. Effat, F. Ciucci, Bayesian and Hierarchical Bayesian Based Regularization for Deconvolving the Distribution of Relaxation Times from Electrochemical Impedance Spectroscopy Data, Electrochim. Acta. 247 (2017) 1117–1129. https://doi.org/10.1016/j.electacta.2017.07.050.

[118] Ullmann's Encyclopedia of Industrial Chemistry, Wiley, 2000. https://doi.org/10.1002/14356007.

[119] S. Wang, G.Q. Lu, Reforming of methane with carbon dioxide over Ni/Al_2O_3 catalysts: Effect of nickel precursor, Appl. Catal. A Gen. 169 (1998) 271–280. https://doi.org/10.1016/S0926-860X(98)00017-9.

[120] A. Hauch, S.H. Jensen, J.B. Bilde-Sørensen, M. Mogensen, Silica Segregation in the Ni/YSZ Electrode, J. Electrochem. Soc. 154 (2007) A619. https://doi.org/10.1149/1.2733861.

[121] A. Utz, K. V. Hansen, K. Norrman, E. Ivers-Tiffée, M. Mogensen, Impurity features in Ni-YSZ-H_2-H_2O electrodes, Solid State Ionics. 183 (2011) 60–70. https://doi.org/10.1016/j.ssi.2010.12.014.

[122] K. Vels Jensen, Microstructural and chemical changes at the Ni/YSZ interface, Solid State Ionics. 144 (2001) 197–209. https://doi.org/10.1016/S0167-2738(01)00969-9.

[123] O.A. Marina, M. Mogensen, High-temperature conversion of methane on a composite gadolinia-doped ceria - gold electrode, Appl. Catal. A Gen. 189 (1999) 117–126. https://doi.org/10.1016/S0926-860X(99)00259-8.

[124] K.J. Dean, Waves and Fields in Optoelectronics: Prentice-Hall Series in Solid State Physical Electronics, Phys. Bull. 35 (1984) 339–339. https://doi.org/10.1088/0031-9112/35/8/023.

[125] G.L. Zhao, D. Bagayoko, Electronic structure and charge transfer in 3C- and 4H-SiC, New J. Phys. 2 (2000) 16–16. https://doi.org/10.1088/1367-2630/2/1/316.

[126] R. Bousbih, I. Haddadi, H.B.E.N. Zina, N. Alatawi, H. Ezzaouia, PURIFICATION OF TABUK SILICA USING CHEMICAL ATTACK AND THERMAL TREATMENT, J. Non-Oxide Glas. 12 (2020) 27–30.

[127] B. Stoeckl, V. Subotić, M. Preininger, H. Schroettner, C. Hochenauer, SOFC operation with carbon oxides: Experimental analysis of performance and degradation, Electrochim. Acta. 275 (2018) 256–264. https://doi.org/10.1016/j.electacta.2018.04.036.

[128] B. Stoeckl, V. Subotić, D. Reichholf, H. Schroettner, C. Hochenauer, Extensive analysis of large planar SOFC: Operation with humidified methane and carbon monoxide to examine carbon deposition based degradation, Electrochim. Acta. 256 (2017) 325–336. https://doi.org/10.1016/j.electacta.2017.09.026.

[129] S. Dierickx, J. Joos, A. Weber, E. Ivers-Tiffée, Advanced impedance modelling of Ni/8YSZ cermet anodes, Electrochim. Acta. 265 (2018) 736–750. https://doi.org/10.1016/j.electacta.2017.12.029.

[130] J. Van Herle, A.J. McEvoy, Oxygen diffusion through silver cathodes for solid oxide fuel cells, J. Phys. Chem. Solids. 55 (1994) 339–347. https://doi.org/10.1016/0022-3697(94)90230-5.

[131] T. Cavoué, A. Caravaca, I. Kalaitzidou, F. Gaillard, M. Rieu, J.P. Viricelle, P. Vernoux, Ethylene epoxidation on Ag/YSZ electrochemical catalysts: Understanding of oxygen electrode reactions, Electrochem. Commun. 105 (2019) 106495. https://doi.org/10.1016/j.elecom.2019.106495.

[132] D. Klotz, D.S. Ellis, H. Dotan, A. Rothschild, Empirical in operando analysis of the charge carrier dynamics in hematite photoanodes by PEIS, IMPS and IMVS,

Phys. Chem. Chem. Phys. 18 (2016) 23438–23457. https://doi.org/10.1039/C6CP04683E.

[133] T. Yang, J. Liu, H. Finklea, S. Lee, W.K. Epting, R. Mahbub, T. Hsu, P.A. Salvador, H.W. Abernathy, G.A. Hackett, An efficient approach for prediction of Warburg-type resistance under working currents, Int. J. Hydrogen Energy. 43 (2018) 15445–15456. https://doi.org/10.1016/j.ijhydene.2018.06.076.

[134] N.M. Tikekar, T.J. Armstrong, A. V. Virkar, Reduction and Reoxidation Kinetics of Nickel-Based SOFC Anodes, J. Electrochem. Soc. 153 (2006) A654. https://doi.org/10.1149/1.2167949.

[135] R. Dewil, L. Appels, J. Baeyens, A. Buczynska, L. Van Vaeck, The analysis of volatile siloxanes in waste activated sludge, Talanta. 74 (2007) 14–19. https://doi.org/10.1016/j.talanta.2007.05.041.

[136] N. Wang, L. Tan, L. Xie, Y. Wang, T. Ellis, Investigation of volatile methyl siloxanes in biogas and the ambient environment in a landfill, J. Environ. Sci. 91 (2020) 54–61. https://doi.org/10.1016/j.jes.2020.01.005.

[137] Y. Lu, T. Yuan, W. Wang, K. Kannan, Concentrations and assessment of exposure to siloxanes and synthetic musks in personal care products from China, Environ. Pollut. 159 (2011) 3522–3528. https://doi.org/10.1016/j.envpol.2011.08.015.

[138] J. Nielsen, J. Hjelm, Impedance of SOFC electrodes: A review and a comprehensive case study on the impedance of LSM:YSZ cathodes, Electrochim. Acta. 115 (2014) 31–45. https://doi.org/10.1016/j.electacta.2013.10.053.

[139] B. Skinner, D. Appleman, Melanophlogite, a cubic polymorph of silica, Am. Mineral. 48 (1963) 854–867. http://scholar.google.com/scholar?hl=en&btnG=Search&q=intitle:Melanophlogite,+a+cubic+polymorph+of+silica#0.

[140] R.T.Downs, D.C.Palmer, The pressure behavior of a cristobalite, Am. Mineral. 79 (1994) 9–14. https://doi.org/10.1088/0953-8984/27/30/305401.

[141] A.C. Ferrari, Raman spectroscopy of graphene and graphite: Disorder, electron–phonon coupling, doping and nonadiabatic effects, Solid State Commun. 143 (2007) 47–57. https://doi.org/10.1016/j.ssc.2007.03.052.

[142] Y. Yu, Y. Wang, K. Lin, N. Hu, X. Zhou, S. Liu, Complete Raman spectral assignment of methanol in the C-H stretching region, J. Phys. Chem. A. 117 (2013) 4377–4384. https://doi.org/10.1021/jp400886y.

[143] S.K. Jerng, D.S. Yu, J.H. Lee, C. Kim, S. Yoon, S.H. Chun, Graphitic carbon growth on crystalline and amorphous oxide substrates using molecular beam epitaxy, Nanoscale Res. Lett. 6 (2011) 1–6. https://doi.org/10.1186/1556-276X-6-565.

[144] H. Bouhamed, Improved structural stability and electrochemical performance of 8YSZ electrolyte by MxOy doping for low temperature solid oxide fuel cells (LT-SOFCs), Mater. Sci. Eng. B Solid-State Mater. Adv. Technol. 225 (2017) 182–188. https://doi.org/10.1016/j.mseb.2017.08.020.

[145] S.W. da Silva, R.C. Pedroza, P.P.C. Sartoratto, D.R. Rezende, A. V. da Silva Neto, M.A.G. Soler, P.C. Morais, Raman spectroscopy of cobalt ferrite nanocomposite in silica matrix prepared by sol-gel method, J. Non. Cryst. Solids. 352 (2006) 1602–1606. https://doi.org/10.1016/j.jnoncrysol.2006.01.054.

[146] J.R. Macdonald, J.A. Garber, Analysis of Impedance and Admittance Data for Solids and Liquids, J. Electrochem. Soc. 124 (1977) 1022–1030. https://doi.org/10.1149/1.2133473.

[147] P. Yan, A. Mineshige, T. Mori, Y. Wu, G.J. Auchterlonie, J. Zou, J. Drennan, Microanalysis of a grain boundary's blocking effect in lanthanum silicate electrolyte for intermediate-temperature solid oxide fuel cells, ACS Appl. Mater. Interfaces. 5 (2013) 5307–5313. https://doi.org/10.1021/am401195e.

[148] M. Yuan, W. Dong, L. Wei, Q. Liu, Y. Meng, X. Wang, B. Wang, B. Zhu, Stability study of SOFC using layered perovskite oxide $La_{1.85}Sr_{0.15}CuO_4$ mixed with ionic conductor as membrane, Electrochim. Acta. 332 (2020) 135487. https://doi.org/10.1016/j.electacta.2019.135487.

[149] P. Mondal, A. Klein, W. Jaegermann, H. Hahn, Enhanced specific grain boundary conductivity in nanocrystalline Y_2O_3-stabilized zirconia, Solid State Ionics. 118 (1999) 331–339. https://doi.org/10.1016/s0167-2738(98)00452-4.

[150] X. Guo, R. Waser, Electrical properties of the grain boundaries of oxygen ion conductors: Acceptor-doped zirconia and ceria, Prog. Mater. Sci. 51 (2006) 151–210. https://doi.org/10.1016/j.pmatsci.2005.07.001.

[151] X. Guo, Size dependent grain-boundary conductivity in doped zirconia, Comput. Mater. Sci. 20 (2001) 168–176. https://doi.org/10.1016/S0927-0256(00)00174-9.

[152] V.M. Gun'ko, M. V. Borysenko, P. Pissis, A. Spanoudaki, N. Shinyashiki, I.Y. Sulim, T. V. Kulik, B.B. Palyanytsya, Polydimethylsiloxane at the interfaces of fumed silica and zirconia/fumed silica, Appl. Surf. Sci. 253 (2007) 7143–7156. https://doi.org/10.1016/j.apsusc.2007.02.185.

[153] M. Schweigkofler, R. Niessner, Removal of siloxanes in biogases, J. Hazard. Mater. 83 (2001) 183–196. https://doi.org/10.1016/S0304-3894(00)00318-6.

[154] G. Soreanu, M. Béland, P. Falletta, K. Edmonson, L. Svoboda, M. Al-Jamal, P. Seto, Approaches concerning siloxane removal from biogas - A review, Can. Biosyst. Eng. / Le Genie Des Biosyst. Au Canada. 53 (2011).

[155] A. Nagy, G. Mestl, High temperature partial oxidation reactions over silver catalysts, Appl. Catal. A Gen. 188 (1999) 337–353. https://doi.org/10.1016/S0926-860X(99)00246-X.

[156] F.N. Cayan, M. Zhi, S.R. Pakalapati, I. Celik, N. Wu, R. Gemmen, Effects of coal syngas impurities on anodes of solid oxide fuel cells, J. Power Sources. 185 (2008) 595–602. https://doi.org/10.1016/j.jpowsour.2008.06.058.

[157] J.F.B. Rasmussen, A. Hagen, The effect of H2S on the performance of Ni–YSZ anodes in solid oxide fuel cells, J. Power Sources. 191 (2009) 534–541. https://doi.org/10.1016/j.jpowsour.2009.02.001.

[158] D.-W. Choi, M. Ohashi, C.A. Lozano, J.W. Vanzee, P. Aungkavattana, S. Shimpalee, Sulfur diffusion of hydrogen sulfide contaminants to cathode in a micro-tubular solid oxide fuel cell, Electrochim. Acta. 321 (2019) 134713. https://doi.org/10.1016/j.electacta.2019.134713.

[159] A. Lussier, S. Sofie, J. Dvorak, Y.U. Idzerda, Mechanism for SOFC anode degradation from hydrogen sulfide exposure, Int. J. Hydrogen Energy. 33 (2008) 3945–3951. https://doi.org/10.1016/j.ijhydene.2007.11.033.

[160] V. Yurkiv, Reformate-operated SOFC anode performance and degradation considering solid carbon formation: A modeling and simulation study, Electrochim. Acta. 143 (2014) 114–128. https://doi.org/10.1016/j.electacta.2014.07.136.

[161] J. Kuhn, O. Kesler, Carbon deposition thresholds on nickel-based solid oxide fuel cell anodes II. Steam:carbon ratio and current density, J. Power Sources. 277 (2015) 455–463. https://doi.org/10.1016/j.jpowsour.2014.07.084.

[162] M.B. Pomfret, J.C. Owrutsky, R.A. Walker, High-temperature raman spectroscopy of solid oxide fuel cell materials and processes, J. Phys. Chem. B. 110 (2006) 17305–17308. https://doi.org/10.1021/jp063952l.

[163] T.S. Li, W.G. Wang, T. Chen, H. Miao, C. Xu, Hydrogen sulfide poisoning in solid oxide fuel cells under accelerated testing conditions, J. Power Sources. 195 (2010) 7025–7032. https://doi.org/10.1016/j.jpowsour.2010.05.009.

[164] A. Dhir, K. Kendall, Microtubular SOFC anode optimisation for direct use on methane, J. Power Sources. 181 (2008) 297–303. https://doi.org/10.1016/j.jpowsour.2007.11.005.

[165] A. Chambers, I. Potter, Gas utilization from sewage waste, Carbon Energy Manag. Alberta Res. Counc. 1 (2002) 1–9. http://citeseerx.ist.psu.edu/viewdoc/download?doi=10.1.1.476.516&rep=rep1&type=pdf.

[166] C.M. Grgicak, R.G. Green, J.B. Giorgi, SOFC anodes for direct oxidation of hydrogen and methane fuels containing H_2S, J. Power Sources. 179 (2008) 317–328. https://doi.org/10.1016/j.jpowsour.2007.12.082.

[167] L. Aguilar, S. Zha, Z. Cheng, J. Winnick, M. Liu, A solid oxide fuel cell operating on hydrogen sulfide (H2S) and sulfur-containing fuels, J. Power Sources. 135 (2004) 17–24. https://doi.org/10.1016/j.jpowsour.2004.03.061.

[168] H.J. Ko, J.H. Myung, S.H. Hyun, J.S. Chung, Synthesis of LSM-YSZ-GDC dual composite SOFC cathodes for high-performance power-generation systems, J. Appl. Electrochem. 42 (2012) 209–215. https://doi.org/10.1007/s10800-012-0390-8.

[169] S. Masciandaro, M. Torrell, P. Leone, A. Tarancón, Three-dimensional printed yttria-stabilized zirconia self-supported electrolytes for solid oxide fuel cell applications, J. Eur. Ceram. Soc. 39 (2019) 9–16. https://doi.org/10.1016/j.jeurceramsoc.2017.11.033.

[170] S. Dierickx, T. Mundloch, A. Weber, E. Ivers-Tiffée, Advanced impedance model

for double-layered solid oxide fuel cell cermet anodes, J. Power Sources. 415 (2019) 69–82. https://doi.org/10.1016/j.jpowsour.2019.01.043.

[171] M.A. Buccheri, J.M. Hill, Methane Electrochemical Oxidation Pathway over a Ni/YSZ and $La_{0.3}Sr_{0.7}TiO_3$ Bi-Layer SOFC Anode , J. Electrochem. Soc. 159 (2012) B361–B367. https://doi.org/10.1149/2.001204jes.

[172] A. Utz, H. Störmer, A. Leonide, A. Weber, E. Ivers-Tiffée, Degradation and Relaxation Effects of Ni Patterned Anodes in H_2–H_2O Atmosphere, J. Electrochem. Soc. 157 (2010) B920. https://doi.org/10.1149/1.3383041.

[173] A. Nenning, M. Gerstl, M. Bram, A.K. Opitz, Mechanistic Insight into Porous Electrode Impedance: An Example of Ni+YSZ Cermet Anodes, ECS Trans. 91 (2019) 479–490. https://doi.org/10.1149/09101.0479ecst.

[174] A. Cabrera-Codony, M.A. Montes-Morán, M. Sánchez-Polo, M.J. Martín, R. Gonzalez-Olmos, Biogas upgrading: Optimal activated carbon properties for siloxane removal, Environ. Sci. Technol. 48 (2014) 7187–7195. https://doi.org/10.1021/es501274a.

[175] F. Zurlo, A. Iannaci, V.M. Sglavo, E. Di Bartolomeo, Copper-based electrodes for IT-SOFC, J. Eur. Ceram. Soc. 39 (2019) 17–20. https://doi.org/10.1016/j.jeurceramsoc.2018.02.029.

[176] Z. Lü, L. Pei, T. min He, X. qiang Huang, Z. guo Liu, Y. Ji, X. hai Zhao, W. hui Su, Study on new copper-containing SOFC anode materials, J. Alloys Compd. 334 (2002) 299–303. https://doi.org/10.1016/S0925-8388(01)01795-9.

[177] C.M. Grgicak, M.M. Pakulska, J.S. O'Brien, J.B. Giorgi, Synergistic effects of $Ni_{1-x}Co_x$-YSZ and $Ni_{1-x}Cu_x$-YSZ alloyed cermet SOFC anodes for oxidation of hydrogen and methane fuels containing H2S, J. Power Sources. 183 (2008) 26–33. https://doi.org/10.1016/j.jpowsour.2008.05.002.

[178] Q.X. Low, W. Huang, X.Z. Fu, J. Melnik, J.L. Luo, K.T. Chuang, A.R. Sanger, Copper coated nickel foam as current collector for H_2S- containing syngas solid oxide fuel cells, Appl. Surf. Sci. 258 (2011) 1014–1020. https://doi.org/10.1016/j.apsusc.2011.07.133.

[179] Z. Jiang, N.A. Arifin, P. Mardle, R. Steinberger-Wilckens, Electrochemical Performance and Carbon Resistance Comparison between Tin, Copper and Silver-

Doped Nickel/Yttria-Stabilized Zirconia Anodes SOFCs Operated with Biogas, J. Electrochem. Soc. 166 (2019) F393–F398. https://doi.org/10.1149/2.1011906jes.

[180] N.U. Pujare, K.J. Tsai, A.F. Sammells, An Electrochemical Claus Process for Sulfur Recovery, J. Electrochem. Soc. 136 (1989) 3662–3678. https://doi.org/10.1149/1.2096528.

APPENDIX A

UNCERTAINTY AND REPEATABILITY ANALYSIS FOR CHAPTER 5

To have an accurate and precise evaluation of the entire SOFCs failure process due to siloxane contamination, as discussed in Chapter 5, potential sources of error should be considered. The measured data in experiments was confirmed by uncertainty analysis. For this experimental study, the bias (systematic) error and precision (random) error are considered.

The bias error or systematic error causes an offset between the mean value of the data set and its true value. As are result, the uncertainty of the bias error cannot be estimated by statistical methods. In Chapter 5, the bias error for the galvanostatic results of entire failure process shown in **Fig. 5.2** is attributed to the resolution limit of the Solartron Analytical Energylab XM analyzer. In this situation, the resolution of the analyzer for the galvanostatic test can be obtained from the manual which is ±0.1% for the voltage measurement and 1 ms for time measurement.

Precision error is uncertainty that appears from a random effect. After repeated measurements of the variable, the random variations can be evaluated utilizing statistical methods. In Chapter 5, in order to obtain samples for morphology analysis and to eliminate the disturbance that exhaust gas analysis causes, the galvanostatic tests for the failure process were repeated several times for each point. Repetition of the study can be utilized for the uncertainty analysis of precision error. Three galvanostatic results of the failure experiment under OCV for point 2, point 3 and entire failure are show in **Fig. A1**. In this regard, the repeated measurement data for point 1, point 2 and point 3 can be

utilized for the uncertainty analysis.

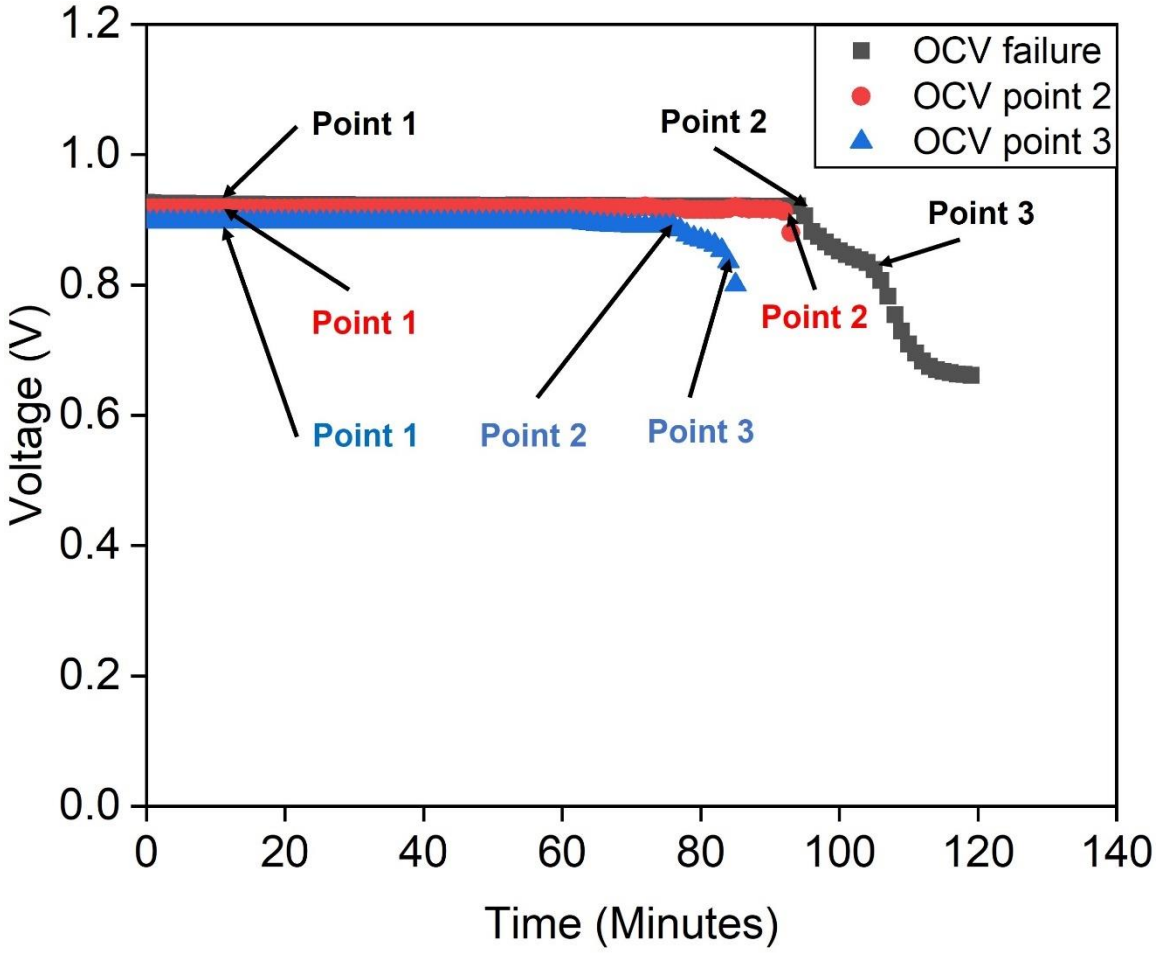

Figure A1 The voltage changes of SOFCs for point 2, point 3 and failure experiment under OCV with 0.5% D4 siloxane contamination at 800 °C.

Similarly, repeated measurement of the failure experiment under 50 mA cm^{-2} with 0.5% D4 siloxane contamination at 800 °C is reported in **Fig. A2**.

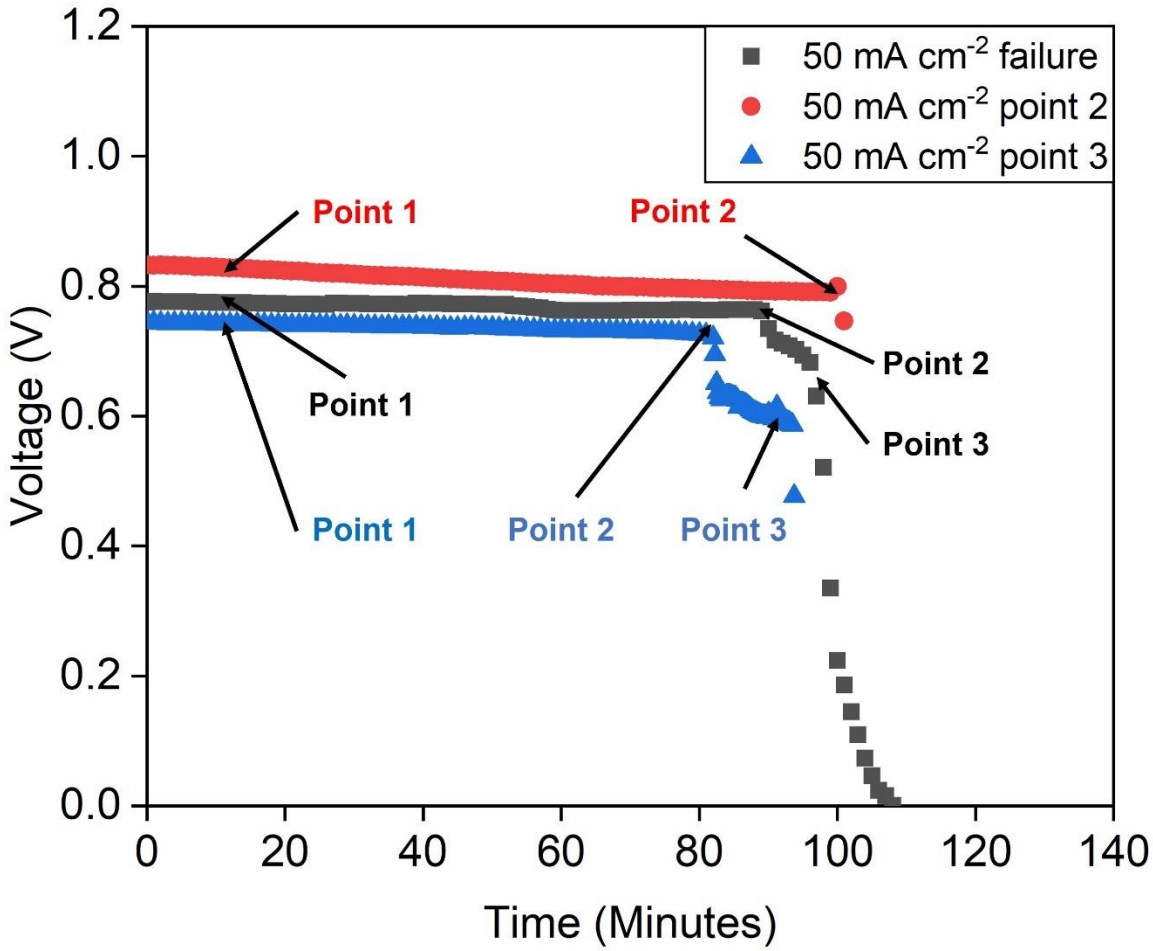

Figure A2 The voltage changes of SOFCs for point 2, point 3 and failure experiments under 50 mA cm^{-2} with 0.5% D4 siloxane contamination at 800 °C.

For OCV and 50 mA cm^{-2} experiments, there are three repeated measurements for point 1 and point 2, and two repeated measurements for point 3. In this circumstance, Student t-distribution is utilized as the statistical analysis method because the measurement was repeated less than 30 times. For Student t-distribution, the precision uncertainty in voltage and time can be calculated by equation (A1):

$$P = t_{0.1,\nu} \frac{S_x}{\sqrt{n}} \quad \text{(A1)}$$

For the uncertainty analysis, an 80% confidence interval was selected. n is the number of

repeated measurements. $\nu = n - 1$, represents the degrees of freedom. S_x is the sample standard deviation and $S_x = \sqrt{\frac{1}{n-1}\sum_{i=1}^{n}(x_i - \bar{x})^2}$. $\bar{x}$ is sample average and $\bar{x} = \sum_{i=1}^{n}\frac{x_i}{n}$. For t value calculation, $t = \frac{\bar{x}-\mu}{S_x/\sqrt{n}}$.

For point 2 and point 3, besides uncertainty in the voltage, the uncertainty in the time is also evaluated because the time when SOFCs reached the failure event is also important for the failure analysis. The uncertainty at each point is shown in **Table A1**.

Table A1 The random uncertainty of the voltage and time galvanostatic results of SOFCs failure experiments under OCV and 50 mA cm^{-2}

Time Uncertainty		(Minutes)
OCV	Point 2	10.74
	Point 3	32.32
50 mA cm^{-2}	Point 2	9.3
	Point 3	4.62
Voltage Uncertainty		(V)
OCV	Point 1	0.016
	Point 2	0.017
	Point 3	0.019
50 mA cm^{-2}	Point 1	0.027
	Point 2	0.04
	Point 3	0.14

After random uncertainty analysis, the total uncertainty can be calculated by combination of the bias uncertainty and the random certainty shown in equation (A2):

$$U_x = \sqrt{(B_x^2 + P_x^2)} \quad \text{(A2)}$$

Where B_x is the bias uncertainty and P_x is the random uncertainty. After calculations, the bias uncertainties from the analyzer resolution limit, which is 0.1% for voltage, and millisecond for time, can be ignored compared to the random uncertainties. The random uncertainty presented in **Table A1** can represent the total uncertainty for the experimental study. The total uncertainty for Galvanostatic results of SOFCs failure experiments are presented in **Fig. A3** with error bars.

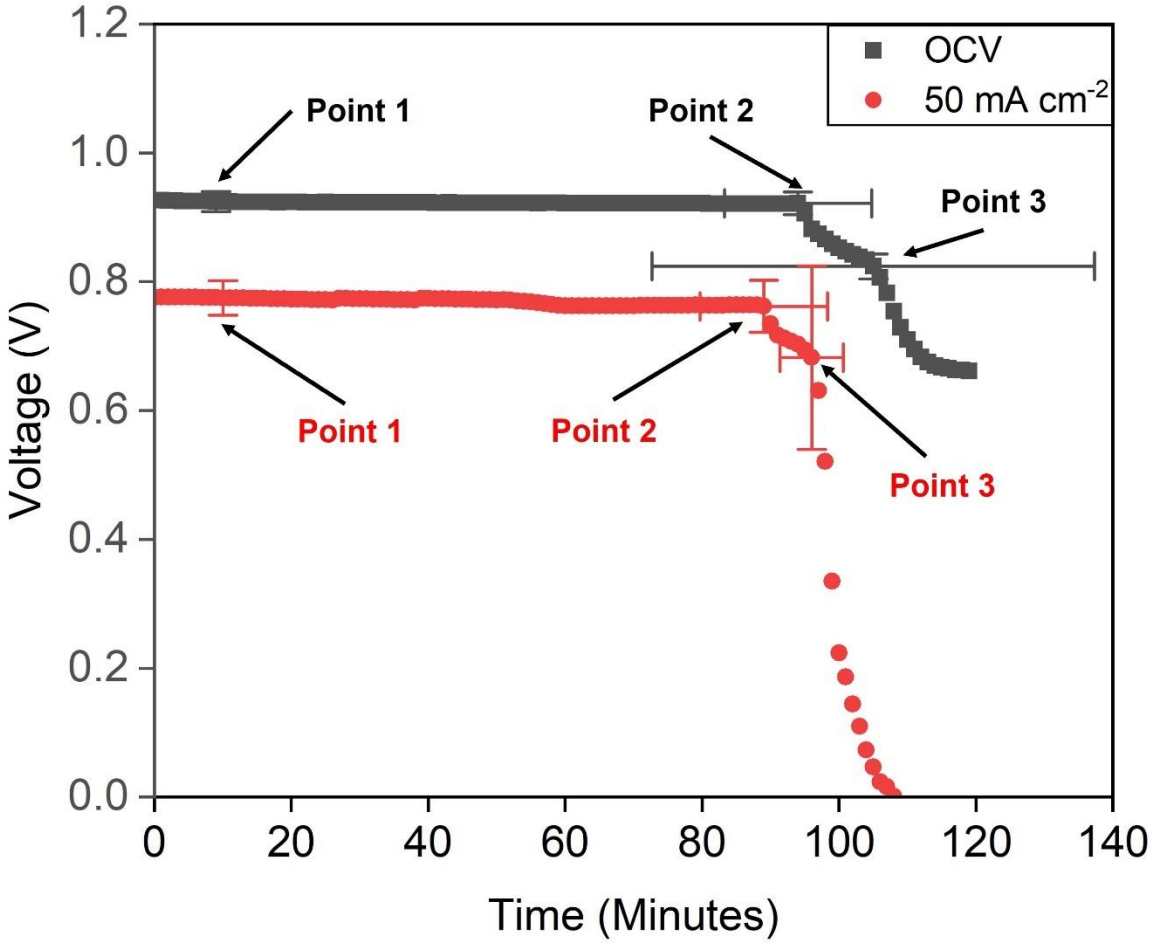

Figure A3 The uncertainty of point 1, point 2 and point 3 data in SOFCs failure process under OCV and 50 mA cm^{-2} with 0.5% D4 siloxane contamination at 800 °C.

From **Fig. A3**, the point 1 uncertainty results from OCV and 50 mA cm^{-2} experiments

both having relatively low errors compared with other points. Considering point 2 and point 3, the measurements from points 2 have much smaller uncertainties. In this situation, the data from point 2 where the SOFCs starts to decay faster is more convincing for the failure analysis. The large uncertainty of data from point 3 is caused by the large random variation of the voltage and time values and only 2 repeated measurements. Thus, it may only be utilized as a reference. Comprehensively considering the uncertainty analysis results, the experimental data from point 1 and point 2 have acceptable accuracy and precision for SOFCs failure analysis. In order to have a more convincible conclusion, the Galvanostatic test results still need to be reviewed combined with the other evidence such as morphology analysis results.

For repeatability analysis, the Galvanostatic results of SOFCs failure processes under OCV and 50 mA cm^{-2} have been tested repeatedly three times for point 1 and point 2, and twice for point 3. The results are shown in **Fig. A1** and **Fig. A2**. From the plots, the failure curves shared a similar pattern. The long and soft degradation period from point 1 to point 2 can be noticed at the beginning of the aging tests. From point 2 to the failure event, much higher degradation rates of SOFCs can be observed. Combined with the **Fig. A1** and **Fig. A2**, the pattern of entire failure process can be confirmed.

APPENDIX B

COPYRIGHT AND CO-AUTHOR APPROVAL

This statement is a declaration that the dissertation contents (e.g. figure, graph, table and textual material) includes some of the previous published and publishable work from Jiashen Tian as the first or second author and Ryan Milcarek as the corresponding author. The Detailed copyright permission is shown as below:

Chapter 1 includes previous published works with permission from Derall M. Riley, Jiashen Tian, Gamze Güngör-Demirci, Patrick Phelan, J. Rene Villalobos and Ryan J. Milcarek. "Techno-economic assessment of CHP systems in wastewater treatment plants." Environments 7.10 (2020): 74. DOI: 10.3390/environments7100074, Publication Date: September 26th 2020, Copyright © 2020 MDPI.

Chapter 2 includes previous published works with permission from Jiashen Tian and Ryan Milcarek. "Investigating the degradation mechanism of the solid oxide fuel cell nickel-yttria stabilized zirconia anode under siloxane contamination." Journal of Power Sources 480 (2020): 229122, DOI: 10.1016/j.jpowsour.2020.229122, Publication Date (Web): November 3rd 2020, Copyright © 2020 Elsevier B.V.. "Siloxane Deposition on the Ni-YSZ Solid Oxide Fuel Cell Anode Exposed to Bio-Syngas." Journal of the Electrochemical Society 168.4 (2021): 044503, DOI: 10.1149/1945-7111/ abf21a, Publication Date: April 6th 2021, Copyright © 2021 The Electrochemical Society ("ECS").

Chapter 3 includes previous published works with permission from Jiashen Tian and Ryan Milcarek. "Siloxane Deposition on the Ni-YSZ Solid Oxide Fuel Cell Anode Exposed to Bio-Syngas." Journal of the Electrochemical Society 168.4 (2021): 044503, DOI:

10.1149/1945-7111/ abf21a, Publication Date: April 6th 2021, Copyright © 2021 The Electrochemical Society ("ECS"). "Investigating the Influence of Ni, ZrO_2, and Y_2O_3 from SOFC Anodes on Siloxane Deposition." ECS Journal of Solid State Science and Technology 11.4 (2022): 044005, DOI: 10.1149/2162-8777/ ac63e2, Publication Date: April 12th 2022, Copyright © 2022 The Electrochemical Society ("ECS").

Chapter 4 is a previous published work with permission from Jiashen Tian and Ryan Milcarek. "Degradation Comparison of Cyclic and Linear Siloxane Contamination on Solid Oxide Fuel Cells Ni-YSZ Anode." Frontiers in Energy Research (2021): 689, DOI: 10.3389/fenrg.2021.749771, Publication Date: October 22nd 2021, Copyright © 2021 Frontiers Media SA.

Chapter 5 is a publishable work with permission from Jiashen Tian and Ryan Milcarek. " Failure Analysis of Solid Oxide Fuel Cells Ni-YSZ Anode under Siloxane Contamination.", Copyright © Jiashen Tian and Ryan Milcarek.